

---

Thomas Pilgerstorfer

# Mechanical Characterization of Fault Zones

## Doctoral Thesis

Department of Civil Engineering  
Graz University of Technology

Reviewers:

O.Univ.-Prof. Dipl.-Ing. Dr.mont. Wulf Schubert  
Institute for Rock Mechanics and Tunnelling  
Graz University of Technology

Professor Dr. Reşat Ulusay  
Department of Geological Engineering, Applied Geology Division  
Hacettepe University, Ankara, Turkey

Graz, February 2014

---

# Abstract

Alpine fault zones are often very complex structures, exhibiting highly heterogeneous rock mass conditions. When dealing with tunnels or underground structures in difficult ground conditions like fault zones, featuring intensely sheared, fractured material with low strength, the knowledge of the rock mass parameters is of utmost importance to ensure a sound and reliable selection of support and construction measures. In order to meet this goal a proper geomechanical characterization is imperative.

Tectonic faults are usually composed of lens-shaped, relatively competent rock blocks surrounded by finely grained cataclastic material and they are categorized as block-in-matrix rock (bimrocks) in terms of their mechanical behavior. Hence, their properties are highly anisotropic and depend on the degree of the regularity of the block orientation, the total volumetric amount of the competent lenses, as well as the properties of the matrix. Cataclasite, found in fault zones, in stress-released conditions appears as soil-like, finely grained, silty to clayey material. For the determination of the mechanical properties of such geo-materials, traditional soil mechanics testing procedures are usually adopted, although they just account for the properties of the matrix. Investigating the overall properties is currently a challenging task, originating from difficulties in sample acquisition during field investigation, sample preparation and laboratory testing.

The dissertation aims at addressing certain inherent mechanical issues of bimrocks. The thesis basically consists of three thematic parts. The first unit provides a review of the currently available research on bimrocks and identifies issues requiring additional research.

The second part deals with investigating the deformation properties of bimrocks. For the determination of deformability of faulted rock mass an in-situ testing program, consisting of double plate load tests was carried out in a test adit in the Lavanttal fault zone. The performed tests provide valuable information about the anisotropic deformation properties. In addition, the magnitude of the Young's modulus is assessed, allowing a reliable prognosis of system behavior. A new large oedometer test apparatus was developed, addressing the peculiarities of fault material. The influence of block orientation and block proportion on the overall deformability were studied and investigated on artificial bimrocks. The performed large oedometer tests provide insight into the stress dependency of the deformation properties, which are discussed in detail. Empirical relationships are developed, based on easily determinable bimrock properties, allowing a straightforward assessment of the overall deformability of bimrocks.

---

The third part focuses on the determination of strength properties of bimrocks. In order to gain insight into the overall strength properties of cataclasite-like material and to study the basic mechanical behavior of bimrocks an extensive laboratory program was carried out. Direct shear tests, performed on artificial bimrocks, cover a broad range of possible block orientations and block proportions. A straight forward evaluation method is presented and the results are discussed in detail, highlighting the effect of block orientation and block proportion on the shear behavior and shear strength of bimrocks. The gained knowledge about factors influencing the stress path and the stress-displacement behavior yields a qualitative characterization of a constitutive model for bimrocks.

---

# Kurzfassung

## Mechanische Charakterisierung von Störungszonen

Störungszonen in alpinen Regionen stellen oftmals ausgesprochen komplexe geologische Bedingungen mit ausgeprägt heterogenen Gebirgsverhältnissen dar. Bei Tunnels oder Untergrundbauwerken in schwierigen Gebirgsverhältnissen, wie es zum Beispiel bei Störungszonen mit intensiv zerschertem Material geringer Festigkeit der Fall ist, ist die Kenntnis der Gebirgseigenschaften von enormer Wichtigkeit um eine fundierte und zuverlässige Auswahl von Stützmitteln und Vortriebsmethoden zu gewährleisten. Einer ordnungsgemäßen und profunden geomechanischen Charakterisierung kommt daher ein immens hoher Stellenwert zu.

Tektonische Störungszonen sind oftmals aus linsenförmigen, relativ kompetenten Blöcken aufgebaut, welche von feinkörnigem, kataklastischem Material umgeben sind. Die Eigenschaften sind daher ausgeprägt anisotrop und hängen vom Einregelungsgrad der Blockorientierungen, dem volumetrischen Blockanteil sowie den Eigenschaften der Matrix ab. Kataklastit stellt sich in ausgebrochenem, spannungsfreiem Zustand als bodenähnliches, feinkörniges, schluffiges bis toniges Material dar. Zur Bestimmung der mechanischen Eigenschaften werden meist traditionelle bodenmechanische Versuchsprozeduren angewandt, wenngleich diese auch nur den Eigenschaften der Matrix Rechnung tragen. Die Untersuchung und Ermittlung der globalen Eigenschaften stellt zur Zeit eine noch enorm herausfordernde Aufgabe dar. Gründe dafür finden sich in den Schwierigkeiten der Probengewinnung bei Erkundungskampagnen, der Probenvorbereitung und der Laborversuchsmethoden.

Die vorliegende Dissertation zielt darauf ab, die inhärenten mechanischen Eigenschaften von Block-in-Matrix – Störungsmaterial (bimrocks) herauszuarbeiten und wissenschaftlich zu beleuchten. Die Arbeit gliedert sich grundsätzlich in drei Hauptteile. Der erste Teil beschäftigt sich mit einer umfassenden Literaturrecherche zu bis dato verfügbaren Forschungsarbeiten über bimrocks, wobei offene Fragenstellungen und weiterer Forschungsbedarf aufgezeigt werden.

Der zweite Teil befasst sich mit der Untersuchung der Vorformungseigenschaften von bimrocks. Für die Bestimmung der Verformbarkeit von Störungsmaterial wurde ein in-situ Versuchsprogramm, bestehend aus Doppellastplattenversuchen, in einem Versuchsstollen im Kernbereich der Lavanttaler Störungszone durchgeführt. Die durchgeführten Versuche liefern wertvolle Informationen über die anisotropen Verformungseigenschaften. Des Weiteren wird die Größenordnung des Elastizitätsmoduls ermittelt, was eine zuverlässige Prognose des

---

Systemverhaltens erlaubt. Es wurde ein neuer Großödometerversuch entwickelt, welcher auf die Charakteristik von Störungsmaterial zugeschnitten ist. Die Einflüsse der Blockorientierung und des Blockanteils auf die globale Verformbarkeit wurden anhand von künstlich hergestellten Block-in-Matrix Material untersucht und ermittelt. Die durchgeführten Großödometerversuche liefern Einblick über die Spannungsabhängigkeit der Verformungseigenschaften, welche eingängig in der Arbeit diskutiert werden. Basierend auf einfach zu bestimmenden bimrock-Eigenschaften werden empirische Zusammenhänge entwickelt. Diese Beziehungen erlauben eine unkomplizierte Abschätzung der Gesamtverformbarkeit von Block-in-Matrix Material.

Der dritte Hauptteil konzentriert sich auf die Bestimmung der Festigkeitseigenschaften von bimrocks. Um Einblick in die globalen Festigkeitseigenschaften von kataklasit-ähnlichem Material zu erlangen und um das grundsätzliche mechanische Verhalten von bimrocks zu untersuchen wurde ein umfangreiches Laborversuchsprogramm durchgeführt. Direktscherversuche an künstlich hergestellten bimrock-Probekörpern umfassten eine große Bandbreite an möglichen Blockorientierungen und Blockanteilen. Die Ergebnisse der Auswertung werden eingehend diskutiert, wobei der Einfluss von Blockorientierung und Blockanteil auf das Scherverhalten und die Scherfestigkeit von bimrocks besonders herausgearbeitet wird. Das so gewonnene Wissen um die Faktoren, welche den Spannungspfad sowie das Spannungs-Dehnungsverhalten beeinflussen, liefert eine qualitative Charakterisierung eines konstitutiven Modells für Block-in-Matrix Material.

---

# Contents

1	Introduction	12
2	State of the art	14
2.1	Structural and engineering geological features of tectonic faults	14
2.2	Geomechanical features of tectonic faults in terms of bimrock concept	21
3	Definition of objectives	32
4	Deformation properties of fault rocks	34
4.1	In-situ tests	34
4.1.1.1	Geological conditions	35
4.1.1.2	Position of test cross sections	38
4.1.1.3	Test set-up	39
4.1.1.4	Preliminary measures	40
4.1.1.5	Measurement of rock mass deformation	43
4.1.1.6	Test execution	45
4.1.1.7	Measurement data evaluation	47
4.1.1.8	Results	48
4.2	Laboratory tests	62
4.2.1	Large oedometer tests on artificial block-in-matrix samples	62
4.2.1.1	Test apparatus	62
4.2.1.2	Sample preparation	65
4.2.1.3	Test set-up and instrumentation	68
4.2.1.4	Test procedure	68
4.2.1.5	Data evaluation	71
4.2.1.6	Results and discussion	72

---

4.3	Influence of geological structures on deformation properties of fault material	85
4.4	Summary of influence of block proportion and block orientation on deformation properties of bimrocks	86
5	Strength properties of fault rocks	88
5.1	Direct shear tests on artificial block-in-matrix samples	88
5.1.1	Sample preparation	88
5.1.2	Test program	91
5.1.3	Test set-up	94
5.1.4	Test procedure	95
5.1.5	Data evaluation	96
5.2	Results and discussion	103
5.2.1	Shear behavior types	103
5.2.2	Influence of block proportion and block orientation on peak shear strength	110
5.2.3	Influence of block proportion and block orientation on the stress path and stress-displacement behavior	121
5.2.4	Influence of local block arrangement on the stress path and stress-displacement behavior	125
5.2.5	Engineering properties of intact bimrocks	132
5.2.6	Investigation of shear strength of “1”-block bimrocks	137
5.3	Summary of the influence of block proportion on strength properties of bimrocks	142
5.4	Summary of the influence of block orientation on strength properties of bimrocks	142
6	Conclusions	144
7	References	147

---

Appendix	A-1
Appendix A Performed loading schemes for the plate load tests	A-2
Appendix B Evaluated interval- and instant-moduli for the plate load tests	A-3
Appendix C Evaluated moduli for the large oedometer tests	A-5
Appendix D Compilation of test results for direct shear tests on artificial bimrocks	A-9



---

---

# Symbols and abbreviations

## Scalars

$c$	[MPa]	cohesion
$c_{ini}$	[MPa]	initial cohesion
$d$	[m]	diameter
$d_{max}$	[m]	length of the largest likely block
$E$	[MPa]	Young's modulus
$E_B$	[MPa]	Young's modulus of block
$E_{def}$	[MPa]	overall deformation modulus
$E_{inst}$	[MPa]	instant modulus
$E_{int}$	[MPa]	interval modulus
$E_M$	[MPa]	Young's modulus of matrix
$E_s$	[MPa]	constrained modulus, oedometer modulus
$E_{z_i}$	[MPa]	instant modulus
$E_{z_i-z_{i+1}}$	[MPa]	interval modulus
$F_v$	[kN]	activated vertical force
$F_n$	[kN]	normal force
$i$	[°]	dilation angle
${}^e k_n$	[MPa/m]	external normal stiffness
$k_{ni}$	[MPa/m]	initial normal stiffness
${}^i k_n$	[MPa/m]	internal normal stiffness
${}^i k_{n,hyp}$	[MPa/m]	hyperbolic part of the internal normal stiffness
${}^i k_{n,lin}$	[MPa/m]	linear part of the internal normal stiffness
$K_{tot}$	[MPa/m]	total normal stiffness
$K_{z_i}$	[1/m]	coefficient accounting for the corresponding depth from the surface $z_i$
$L_c$	[m]	characteristic engineering dimension
$m_i$	[-]	Hoek-Brown parameter for intact rock
$s$	[m]	shortening
$\Delta s_i$	[m]	displacement in the direction of the applied load
$t$	[m]	thickness
$t$	[min]	time
$r$	[m]	radius of the load plate
$u$	[m]	shear displacement
$du$	[m]	shear displacement increment
$v$	[m]	vertical normal displacement
$v_m$	[m]	maximal joint closure
$W$	[mm <sup>3</sup> ]	moment of resistance/inertia
$W$	[kJ/m <sup>2</sup> ]	shear energy
$W_{norm}$	[-]	normalized shear energy
$z_i$	[m]	depth of a point below the surface where displacements are measured

---

### ***Greek letters***

$\varepsilon_a$	[-]	axial strain
$\eta$	[-]	function parameter
$\varphi$	[°]	friction angle
$\varphi_b$	[°]	basic friction angle
$\kappa$	[-]	function parameter
$\nu$	[-]	Poisson's ratio
$\sigma_{ci}$	[MPa]	uniaxial compressive strength of intact rock
$\sigma$	[MPa]	stress
$\sigma_n$	[MPa]	normal stress
$d\sigma_n$	[MPa]	normal stress increment
$\sigma_v$	[MPa]	activated vertical stress
$\Delta\sigma_m$	[MPa]	mean normal stress on the loaded surface under the load plate
$\tau$	[MPa]	shear stress
$\tau_{max}$	[MPa]	shear strength
$\tau_{max,norm}$	[-]	normalized shear strength
$d\tau$	[MPa]	shear stress increment
$d\tau_{corr}$	[MPa]	corrected shear stress increment
$\omega$	[-]	coefficient for the calculation of the deformation modulus
$\psi$	[-]	ratio of moments of inertia

### **Abbreviations**

BIM		block in matrix
bimrock		block-in-matrix rock
BP	[%]	block proportion
ced	[m]	characteristic engineering dimension
CNL		constant normal load
CNS		constant normal stiffness
CWFS		cohesion-weakening – frictional-strengthening
DIP		digital image processing
EBP	[-]	equivalent block proportion
GSI	[-]	geological strength index
HBM		Hottinger Baldwin Messtechnik
LVDT		linear variable differential transducer
MS		measuring section
SC	[-]	strength contrast between blocks and matrix
TBM		tunnel boring machine
UCS	[MPa]	uniaxial compressive strength
UCS <sub>N</sub>	[-]	normalized uniaxial compressive strength
VBP	[%]	volumetric block proportion
VBC	[%]	volumetric block content

# 1 Introduction

Alpine fault zones are often highly complex structures, featuring pronounced heterogeneous rock mass conditions. During tunneling through fault zones frequently observed phenomena are large and anisotropic displacements, often accompanied by stability problems or violation of serviceability requirements. When dealing with tunnels or underground structures in difficult ground conditions, e.g. fault zones, featuring intensely sheared, fractured material with low strength, the knowledge of the rock mass parameters is of utmost importance for the selection of appropriate excavation and support measures. Sections with a high content of fault material or cataclasites form the most challenging stretches during tunneling, and a sound and reasonable geomechanical characterization is imperative. However, investigating the overall-properties of fault material is currently a challenging task. The problems originate from difficulties in sample acquisition, sample preparation and laboratory testing. In consequence, the ground model, constituting the basis for excavation and support design, is comprised by a plethora of uncertainties.

Faults and fault rocks, by governing rock mass strength and deformation behavior, play a major role in rock engineering and engineering (Brosch et al. 2006). Issues like the distinctive heterogeneity of the internal and external structure, mechanical and hydrological properties, and mineral composition and stress distribution feature geotechnically relevant peculiarities of faults. Hence, serious problems in geotechnical rock engineering and natural hazards are often closely related to (brittle) faults. However, the importance and severe complexity of faults make their investigation and characterization a challenging task (Brosch et al. 2006).

Usually, the mechanical properties of rock are determined through laboratory testing of core samples, hence representing generally the only source to rely on, unless back analyses from projects under similar conditions are available. Moreover, one has to be aware that a reasonable determination of rock parameters decreases significantly with increasing weakness of the rock concerned, since retrieving representative specimen from core drillings is often nearly impossible, for example due to disintegration by loss of confining pressure (spilling out of cohesionless material). Obtaining representative parameters is a challenging task, originating from the inherent risk of disturbing core samples, problems associated with sample preparation, and the often distinctive variation of test results.

Based on experience, Riedmüller et al. (2001), for example, suggest the utilization of drained direct shear tests on disturbed samples of grain size fractions  $< 40 \mu\text{m}$ , which ensures to be on the conservative side. However, many authors (Medley 1994, Medley 1999, Lindquist 1994, Goodman and Algren 2000) emphasize the vital importance of including blocks in the determination of strength and deformation properties of “block-in-matrix” rocks, since focusing only on the fine grained matrix ignores the potentially substantial mechanical contribution of blocks (Riedmüller et al. 2001). Therefore, it is stressed that in the geotechnical assessment of fault zones in general, the bimrock approach should be considered, instead of the classical approach, since fault zones often exhibit similarities with bimrocks in geotechnical sense.

## 2 State of the art

In this chapter, a brief review of research dealing with faults, fault material and bimrocks in terms of geomechanical characterization is provided. Evaluation of shortcomings and limitation of previous research allows a clear definition of the thesis' objectives and provides a basis for discussion of the results presented in the course of the thesis.

### 2.1 Structural and engineering geological features of tectonic faults

In structural geology, a distinction is made between brittle faults and shear zones, according to where the deformation occurred. According to Sibson (1977) ductile shear zones are generated in deeper parts of the earth crust, and the present metamorphism conditions lead to preservation of the material integrity during deformation. Main deformation mechanisms encountered in ductile shear zones are crystal plasticity, dynamic recrystallization, solution mass transfer, dislocation creep, diffusion creep and grain boundary sliding. On the other hand faults are common characteristics found in the upper crust, featuring complex structures, originating mainly from brittle fracturing deformation. Hence, faults pose the highest impact on the rock mass parameters (Riedmüller et al. 2001). Mechanical damaging processes, such as micro-cracking, fragmentation, grinding with rigid-body rotation and frictional wear, lead to grain size reduction, dilatancy and a dramatical drop in strength. The combination with low-temperature solution transfer, yielding neoformation of clay minerals or other secondary minerals (carbonates, oxides) results in cohesionless "soil-like" or cemented cataclastic rocks, such as gauge, cataclasites, breccia and pseudotachylite (Riedmüller et al. 2001).

Cataclasite, which is often associated with brittle faults, was first introduced by Waters and Campbell (1935) who determined the term "cataclastic rocks" as a collective name for all rocks of the gauge-breccia-cataclasite-mylonite kindred. Sibson (1977) deems this definition as a somewhat misleading implication that such rocks have developed solely by cataclasis. Strictly speaking cataclasis involves the brittle fragmentation of mineral grains with rotation of grain fragments accomplished by frictional grain boundary sliding and dilatancy (Sibson 1977). The term "cataclastic" is derived from the Greek word *cataclase* referring to purely mechanical deformation processes and the term "cataclastic rock" refers to rocks formed by dominant cataclastic deformation processes at non- to low-grade metamorphism conditions and relatively high strain rates, i.e. tectonically crushed rocks (Bürgi 2000, Habimana et al. 2002).

Fault zones typically feature considerable heterogeneity, comprising randomly appearing units of more or less undeformed, unaltered stiff and competent rock

fragments, surrounded by a weaker, mainly softer and less competent matrix (Riedmüller et al. 2001).

In literature, a plethora of geological names and terms for the fabric of hard rock blocks, embedded in a weaker matrix (gouge, breccia, tectonic chaos, etc.) as well as for the hard components (e.g. horses, knockers, clasts, tectonic inclusions, etc.) (Medley 2001, Laznicka 1988) can be found. To avoid confusion, Medley (1994) introduced the term “block-in-matrix rocks”, in a short form named “bimrocks”, which was originally introduced by Raymond (1984) to describe “block-in-matrix” mélanges and olistostromes. Attention has to be paid to the fact that the term “bimrock” has no geological or genetic connotations and is simply defined as “a mixture of rocks, composed of geotechnically significant blocks within a bonded matrix of finer texture”. The expression “geotechnically significant blocks” in this context signifies that there is a mechanical contrast between blocks and matrix. The proportion and size range of the blocks has influence on the overall mechanical properties of the competent block/weak matrix mixture at the scale of interest.

The characteristics of the internal structure of fault zones are influenced by a range of factors, resulting in a considerable variability in the properties and the appearance of fault zones. However, in many cases three structural elements can be found in brittle faults, which may also represent evolutionary steps in temporal development of a fault zone (Figure 1, Figure 2). The structural domains are (Brosch et al. 2006, Fasching and Vanek 2011):

- a) The protolith (host/country/parent rock), comprising intact rock mass bounding the fault related structure.
- b) The damage zone, being characterized by sets of minor shears, veins and a closely spaced fracture network; these structures are generally related to the processes of fault zone formation. The transition from host rock to the damage zone is gradual.
- c) The fault core, where shear displacement with particle rotation and grain size degradation is present. Fault rocks may obtain a characteristic grain size distribution. The internal structure of fault core, and reaching into the damage zone, is often characterized by a fractal (scale-independent) size and shape pattern of clasts and strings of sheared matrix.

Fasching and Vanek (2011) point out that damage zones can also occur at only one margin of the fault or not be present at all due to the possible variability in the formation of a fault zone. The thickness and type of shear zones can vary widely in the fault core zone (such as the size, shape, condition and frequency of shear bodies). Due to small scale variations of the rock and rock mass properties all fault zones can be considered as heterogeneous, showing anisotropic internal structures (Fasching and Vanek 2011).

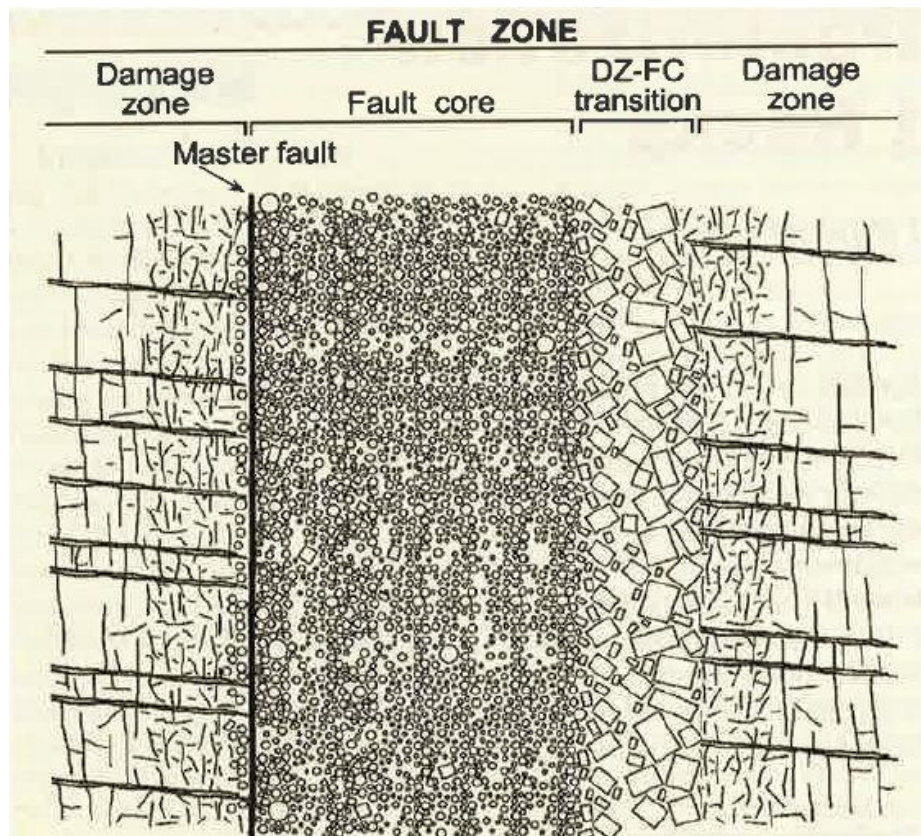


Figure 1: Sketch of general fault internal architecture (Brosch et al. 2006).

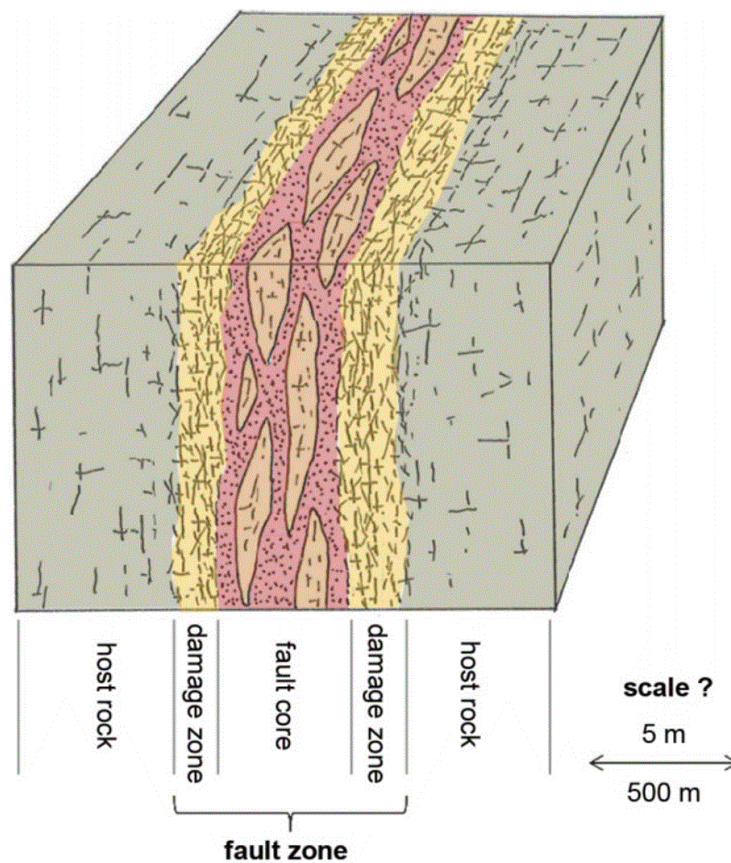


Figure 2: Model of internal architecture of a fault zone: host rock, damage zone, fault core (Fasching and Vanek 2011).



One important feature of block-in-matrix rocks is their self-similarity of the grain-size or block-size distribution over a broad range of scale. One can find these structures in fault zones in “all sizes”, ranging from millimeters up to hundreds of meters, hence there is no certain boundary where to distinguish between “block” and “matrix” and the discrimination of block sizes from matrix materials strongly depends on the engineering scale of interest. Block size distributions in brittle faults are often fractal and a pattern of shear and tensile fractures is evident. Thus reflecting the geometry of the displacement field during faulting, the lenticular shaped cataclasites and blocks are usually oriented towards the dominant direction of shearing (Figure 3).

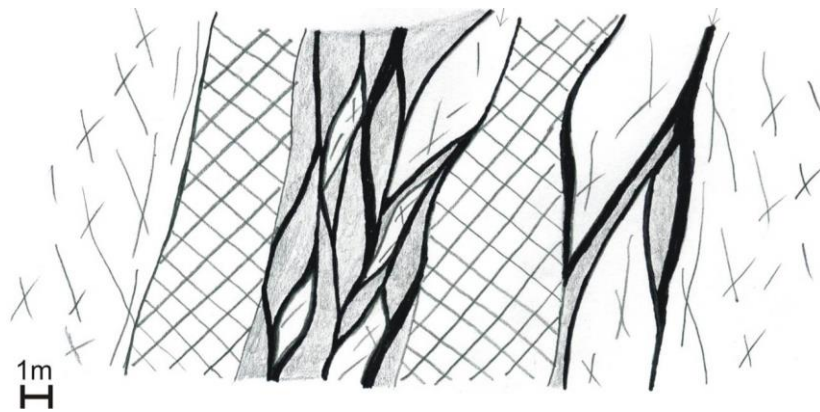


Figure 3: Sketch of a fault structure composed of alternating zones of intense fracturing and blocks embedded in finely and/or coarsely grained cataclastic material (courtesy of 3G ZT GmbH and ÖBB (3G Gruppe Geotechnik Graz ZT GmbH 2008)).

According to the volumetric proportion and distribution of the distinct zones of shear deformation various structural characteristics can result. Figure 4, taken from Fasching and Vanek (2011), shows on the left an anastomosing network of shear zones and fault structures mainly containing shear lenses. On the contrary Figure 4 on the right depicts a fault structure which is dominated by a cataclastic matrix in which individual intact shear bodies are embedded.

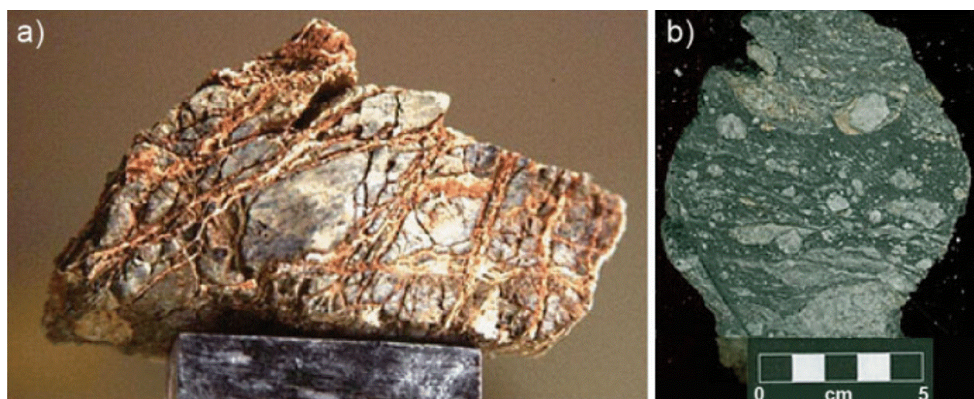


Figure 4: Different fault structures: a) dominance of shear bodies (hand sample), b) dominance of cataclastic matrix (polished section) (Fasching and Vanek 2011).

Despite the obvious heterogeneity of bimrocks, some geometric and geomechanical order, found by Medley (1999), was used to develop guidelines for the systematic characterization of bimrocks. Medley (1999) discovered that characterization of bimrocks must always take blocks into account due to the scale-independence of block-size distribution. Regardless of scale, blocks will always be found in bimrocks and blocks at one scale will be part of the matrix at a smaller scale. A size threshold between blocks and matrix for any volume of bimrocks must be related to the scale of engineering interest since blocks are found at all scales. Medley (1999) suggests that scaling dimensions may be the length of the largest likely block ( $d_{\max}$ , or equivalently,  $\sqrt{A}$ ), or a characteristic engineering dimension,  $L_c$ , (the “ced” of Medley (1994)) such as tunnel diameter, landslide height, or laboratory specimen diameter. He determined the block/matrix threshold to be about  $0.05 \cdot \sqrt{A}$  (or  $0.05 \cdot d_{\max}$ ) or else 5% of the characteristic engineering dimension ( $0.05 \cdot L_c$ ).

A comprehensive classification/characterization scheme for brittle faults is given by Riedmüller et al. (2001). They proposed a diagnostic functional classification, based on experience from investigations for, and construction of, rock engineering structures and on the results of research. In their basic classification for cataclastic rocks, they differentiate between the cohesive and non-cohesive character of the faulted rock. For cohesionless (soil-like) material the strength ratio between block and matrix is applied. Blocks are classified with regard to the volumetric block proportion, while the differentiation of the matrix basically follows standard soil mechanics classification procedures. Cohesive and cataclastic rocks are subdivided with respect to the type of cementation (Figure 5).

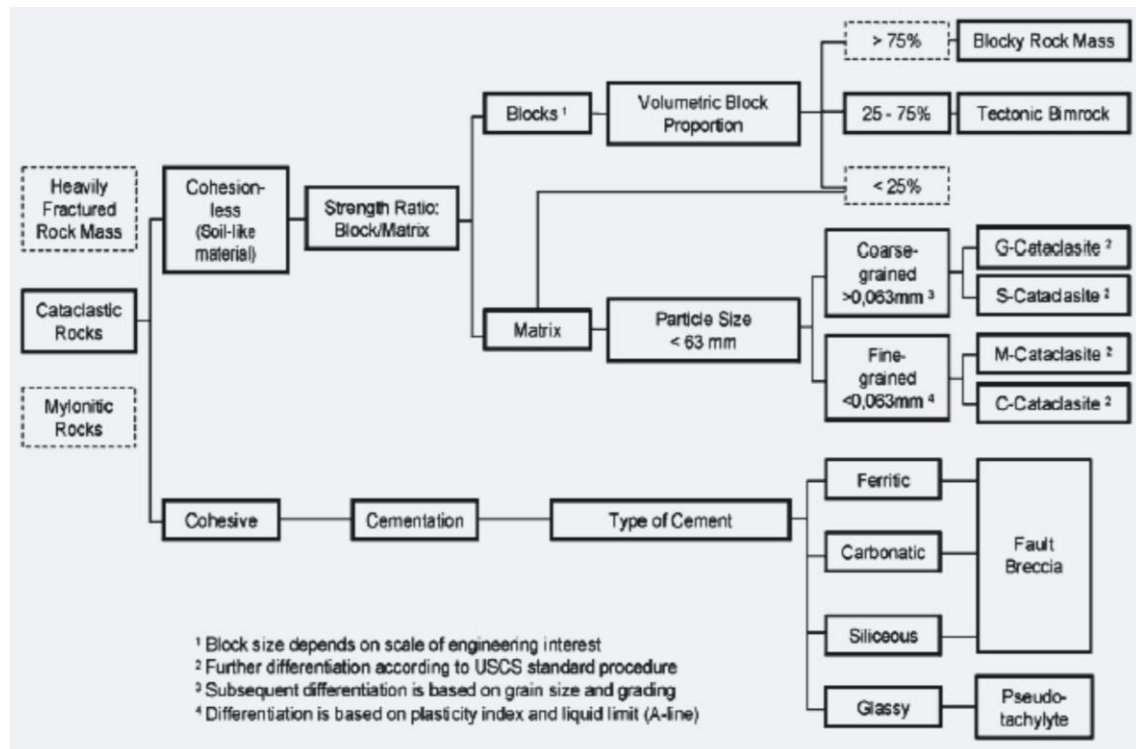


Figure 5: Engineering geological classification of cataclastic rocks (Riedmüller et al. 2001).

A more recent engineering geological characterization of fault rocks and fault zones is given by Fasching and Vanek (2011). These investigators introduced the essential definitions, representing a basic requirement for a comprehensible characterization of fault zone, cataclasis, categorization of fault rocks as soil or hard rock and factors influencing the genesis of fault zones, and give the general framework. The authors point out that comparing individual classification systems sometimes show an ambiguous use of terms and definitions. In practice, this leads to misinterpretation when project-specific definitions are introduced, which do not match with definitions used in other projects. The authors introduce a uniform classification system, based on existing literature and project experience. They emphasize the objective of a clear differentiation of geomechanically relevant rock structures and the provision of appropriate definitions and terms for fault rocks, which can be clearly distinguished from each other. Figure 6 shows the suggested classification scheme by Fasching and Vanek (2011). They classify fault rocks into “cemented” and “non-cemented” rocks, where for cemented fault rocks the degree of mineral formation is crucial, since it influences the rock strength notably. Non-cemented fault rocks are differentiated in fault rocks with and without blocks, which depends on the particle composition. Further differentiation is made between “cohesive” and “non-cohesive” material, where cohesive fault rocks form the group of cataclasites, while cohesionless fault rocks feature no fine-grained particles, or not enough to be mechanically significant. Fault rocks with blocks consider the volumetric block proportion as well as the grain size distribution.

In case of intermittent staged grain size distribution fault rocks are described as block-in-matrix rocks (term “BiM rock” in Figure 6), while widely graded particle composition is classified as “cohesive fault rock with blocks” and “non-cohesive fault rock with blocks”, respectively.

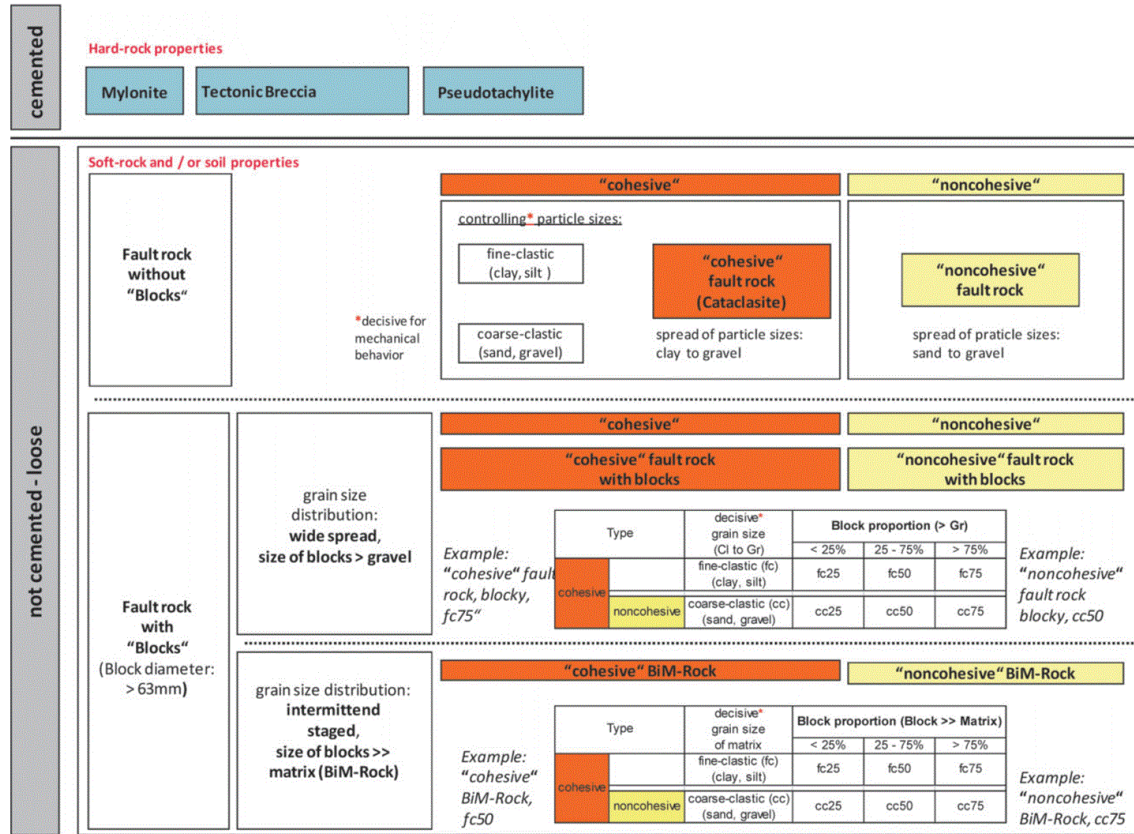


Figure 6: Classification system for fault rocks proposed by Fasching and Vanek (2011).

Fasching and Vanek (2011) further provide a description according to “ground types”, following the “Guideline for the Geotechnical Design of Underground Structures” (Austrian Society for Geomechanics 2010), where the internal architecture and the properties of the fault zone material are the most crucial characteristics to be described, besides the thickness of a fault zone and the orientation relative to the tunnel. Fasching and Vanek (2011) suggest providing a description of the parent rock and the geological setting of the fault zone, the properties of the shear zones, the shear lenses or preserved rock portions, and the internal architecture of the fault zone, describing the spatial layout of the zones of shear deformation and shear bodies (Figure 7).

ENGINEERING GEOLOGICAL CHARACTERISATION OF FAULT ZONES <sup>1</sup>			
		<i>description</i>	<i>parameters</i>
<b>geological environment</b>		parent rock and geological setting	-
<b>fault components</b>	<b>shear zones / fault rocks</b>	fault rocks, particle size distribution, compaction, mineralogy, permeability, ...	<i>friction angle, cohesion, Young's modulus, ...</i>
	<b>shear bodies / preserved rock portions <sup>2</sup></b>	rock properties, mineralogy, properties of discontinuity network, wear properties, ...	<i>strength parameters of rock, shear parameters of discontinuities, wear indices, ...</i>
<b>internal architecture</b>		thickness of shear zones, shape and size of shear bodies, volumetric proportion of shear bodies, anisotropy, ...	<i>size of shear bodies, block-matrix-ratio, ...</i>
<b>rock mass</b>	<b>rock mass parameters</b>	description of strength und deformability properties, comment on anisotropy of rock mass properties	<i>rock mass strength, friction angle, cohesion, Young's modulus, Poisson's ratio, ...</i>
	<b>additional. engin. geol. information <sup>3</sup></b>	permeability, grouting properties, swelling potential, wear properties, ...	<i>(as required)</i>

<sup>1</sup> according to "ground types" following the "Guideline for the Geotechnical Design for Underground Structures" (ÖGG, 2010)

<sup>2</sup> the properties of shear bodies usually can be characterised analogously to ground types of hard rock mass

<sup>3</sup> according to project requirements

Figure 7: Details required for a comprehensive engineering geological characterization of fault zones (Fasching and Vanek 2011).

## 2.2 Geomechanical features of tectonic faults in terms of bimrock concept

Although there is a plethora of geological descriptive terms for fault rocks, research dealing with geomechanical and geotechnical features of tectonic faults is limited to a small number of works so far. However, though it is “nice” to have sound and proper names for the “material” engineers have to work with, it is much more important and imperative to have sound knowledge about the properties and the behavior of the material of interest.

A comprehensive collection of published literature regarding strength and deformation properties of melanges (stronger, stiffer blocks in a weaker, softer matrix) is provided by Lindquist (1994). The major findings and conclusions of his literature review, where he distinguishes between research on melanges, other block-in-matrix rocks (conglomerate, tillite, sheared serpentinite and breccia), Portland cement concrete, and heterogeneous soils (clay matrix studies and clayless matrix studies) are as follows:

1. An increase in block proportion leads to an increase of the angle of internal friction. For almost all materials, this increase is perceptible beyond some threshold proportion of blocks or coarse particles. The reason for this occurrence is found in the increase of waviness or thickness of shear surfaces.

2. There is a somewhat diverse perception on how cohesion is influenced by block proportion. Most results indicate a decrease in cohesion with increasing block proportion. However, some results yield a conflicting pattern. Savely (1990) suggested that the cohesion of a boulder conglomerate mass should be assumed to be the same as that of the matrix material. On the other hand, results of Goodman and Ahlgren (2000), who conducted triaxial compression tests on samples of Franciscan melange in the foundation of Scott dam, draw a rather different picture where it is observed that cohesion actually increased with block proportion.
3. As expected, an increase in block or aggregate proportion yields an increase in rock mass or concrete stiffness, respectively. This result was mostly pronounced in experiments conducted on Portland cement concrete (Hirsch 1962, Stock et al. 1979).

Lindquist (1994) and Lindquist and Goodman (1994) performed an extensive laboratory test program on physical model melanges in order to study the effect of block proportion and block orientation on the mass strength and deformation properties. The model melanges, where a bentonite-portland cement mixture was used for the matrix and a sand-portland cement-fly ash mixture was used for the blocks, were tested triaxially to determine the Mohr-Coulomb strength parameters and to study the stress-strain behavior. Four different block orientations ( $0^\circ$ -,  $30^\circ$ -,  $60^\circ$ - and  $90^\circ$ -orientation related to the axial loading direction) with three different block proportions each (25%, 50% and 75%, respectively) were used. The results show that cohesion decreases with increasing block proportion, resulting in cohesion reduced by 50% for block proportions over 70%. The specimens with  $30^\circ$  block orientation, representing the most adverse orientation, yield the lowest values for cohesion. This finding is hardly surprising, since in the  $30^\circ$ -orientation configuration the blocks and thus the block-matrix contacts, constituting weakness surfaces, coincide with the failure plane ( $45 + \phi/2$ ) in triaxial tests. An opposite picture is drawn for the friction angle, which increases with increasing block proportion. Only a minor influence of the block orientation on the frictional resistance is observed for medium and high block proportion specimen. A remarkable result is that a threshold block proportion can be observed, below which the blocks have negligible influence on the overall strength. The authors determined this threshold value to be around 30% block proportion. This is in good accordance with the findings of Irfan and Tang (1993), who propose a threshold volumetric block proportion of 25% (Figure 14). By examination of the failed specimen it turned out that the failure surface only rarely passes through the blocks, yielding the conclusion that the strength of the mass is marginally governed by the strength of the blocks, as long as they are stronger than the matrix. Regarding the stiffness properties it is determined that the modulus of deformation increases with increasing block proportion. This behavior is expected, since increasing the

block proportion increases the volume of stiffer inclusions in the relatively weaker matrix, resulting in a stiffer model. Another finding was that the rate of increase in modulus is less pronounced for the horizontally and 60° aligned blocks. Lindquist and Goodman (1994) substantiate this appearance with the explanation that vertically aligned blocks attract more of the axial stresses, yielding a stiffer model.

Irfan and Tang (1993) conducted a laboratory study to investigate the effects of coarse fractions on the shear strength of colluvium and similar materials by using reconstituted soils containing large particles in a fine grained matrix. They performed triaxial tests using steel balls and aggregates as coarse contents, as well as large and small direct shear tests were conducted using aggregates only (Figure 14). For the matrix material, a completely decomposed granitic soil was used. As coarse fraction single size steel balls, 20 mm – 28 mm rock aggregates and 5 mm – 6.3 mm rock aggregates were used. The coarse fraction content was varied between 0% and 45%. As generally expected, their results show an increase in shear strength with increasing coarse fraction content. However, the pattern of increase depends on many factors, such as the type of test (triaxial or direct shear test), specimen size, and shape of the coarse aggregates or the applied stress level. It turned out that below about 10% coarse fraction content their effect is vanishingly low and negligible; hence the behavior is entirely controlled by the matrix properties. When increasing the coarse fraction content to 30%, different patterns for triaxial tests and direct shear tests are present. In direct shear tests, the behavior is highly stress dependent, expressed in larger strength increase obtained at lower normal stresses due to a much more pronounced freedom for the specimen to dilate. Less pronounced is the increase in shear strength in triaxial tests. This finding is attributed to the fact that in triaxial tests not many coarse particles may be located along the induced shear plane, generally following the weakest path, and hence the particle's contribution to shear strength (due to grain interlocking) is relatively low. Considering direct shear tests the orientation of the failure surface is pre-determined due to the test arrangement, therefore interlocking effects of larger grains are much more pronounced, expressed in mobilized shear resistance.

A comprehensive literature review about the effect of coarse particles on the strength properties is also given in the report of Irfan and Tang (1993). The literature cited therein is mostly covered by Lindquist (1994), hence these results and assertions are stated above.

Sönmez et al. (2004) studied the relationships between volumetric block proportion and overall uniaxial compressive strength (UCS) of a volcanic bimrock. They conducted UCS-tests on Ankara agglomerate. Their results show a pronounced scatter, when depicting the overall UCS over the equivalent block proportion (Figure 8). However, a trend of increasing strength with increasing block proportion is observable. The results also indicate a uniformly stronger

bimrock with less data scatter above 70% block proportion. This supports the suggestion of Medley (1999) that volumetric block proportions greater than 70% to 75% should be treated as blocky rock masses, for which conventional rock engineering methods should be used.

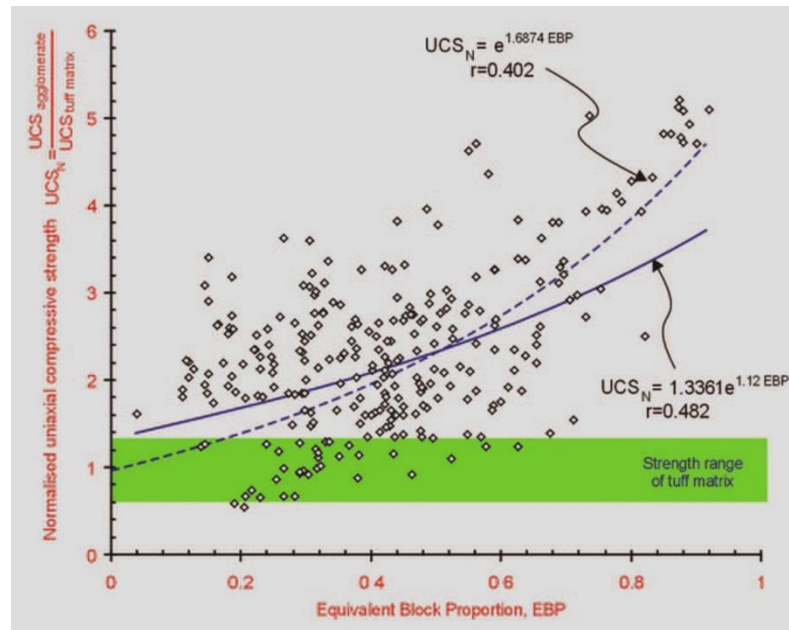


Figure 8: Relationship between equivalent block proportion (EBP) and UCS of Ankara agglomerate (Sönmez et al. 2004).

Kahraman and Alber (2006) examined the strength and deformation properties of fault breccia material, featuring weak blocks in a strong matrix, hence representing an inverse strength difference than usually found in bimrocks. The results of their studies yield a decreasing strength with increasing volumetric block proportion, which is reasonable and as expected. However, their results have to be treated with caution. These investigators conducted UCS tests on samples with diameter between 7.6 mm and 101.3 mm, where nearly 80% of the tested samples fall below the recommended minimum diameter threshold (approximately 50 mm), given by standards and guidelines for testing rock samples (DGGT 2004, ISRM 2007, ASTM 2010). There is no indication about the maximum or minimum block size given in their paper. One must be aware that scale effects play a major role when samples of different diameter are tested. They obtained relatively high values for UCS for the small diameter samples, which is ascribed to the low block proportion and thus high content of strong matrix. However, one must be aware that small samples inherently feature less pronounced natural planes of weakness, which reflects in higher strength values. If one compares the results for UCS versus volumetric block proportion (VBP) for a certain sample diameter solely, shown in Figure 9 for sample diameters where at least four tests were available, the “clear” dependence of VBP on the UCS nearly vanishes.



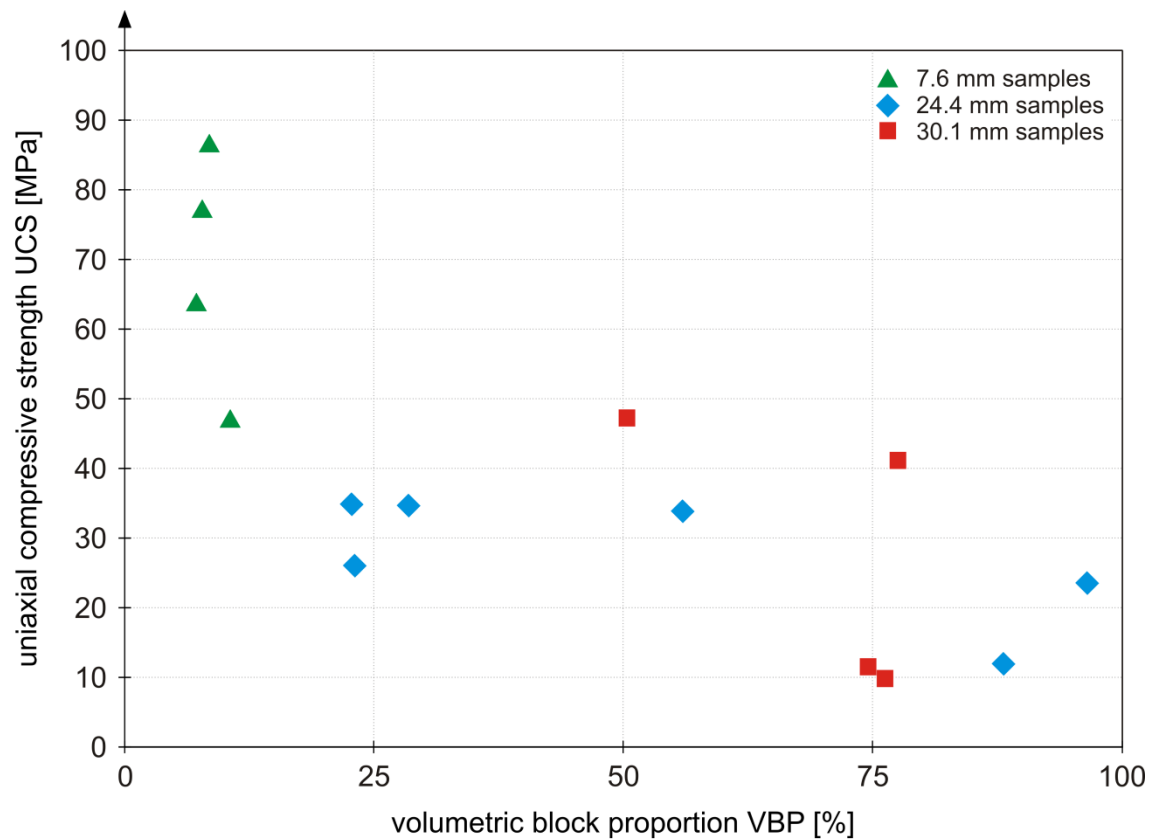


Figure 9: UCS vs. VBP of the results of triaxial tests of Kahraman and Alber (2006), depicted for certain sample diameter.

Sönmez et al. (2006) tried to develop an empirical approach for estimating the overall strength of a bimrock mass. Their empirical approach is based on an exhaustive database, developed by literature reviews and laboratory studies employed on artificial matrix and bimrock cores. Figure 10 gives a graphical illustration of the proposed approach. The results of the tests performed reveal that the UCS not only depends on the block proportion but also on the strength contrast between blocks and matrix. Therefore, the value of strength contrast between blocks and matrix (SC-value) for estimating the uniaxial compressive strength of Ankara agglomerate was introduced. The predictive performance of the conceptual approach is promising to a certain degree. However, the authors point out that the approach is open to improvement, since features influencing the overall strength of bimrocks, like shape and orientation of blocks were not accounted for in their study.

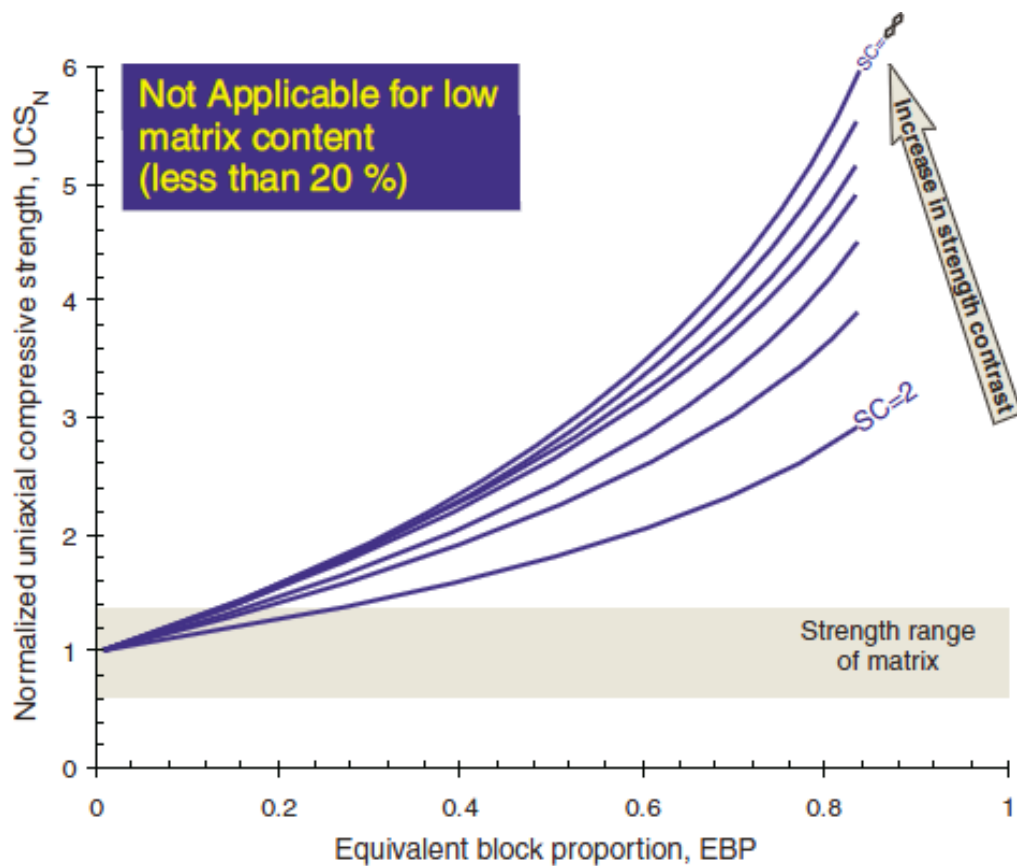


Figure 10: Schematic illustration of empirical approach proposed by Sönmez et al. (2006).

Numerical studies were performed by Barbero et al. (2007), Pan et al. (2008) and Coli et al. (2012). Barbero et al. (2007) conducted 2D-numerical triaxial and uniaxial compression tests on bimrocks with circular and elliptical blocks. Their results show a linear trend of both increasing stiffness and strength with increasing block proportion. These findings are in slight contrast to the research results stated above, where a block proportion threshold of 25% was determined, below which blocks have vanishingly low influence on the overall strength. Also the upper limit of about 75% block proportion, above which no considerable increase in stiffness or strength is observable, was not demonstrated by the numerical studies.

Pan et al. (2008) performed a series of numerical simulations as “virtual mechanical tests” in order to examine influencing factors which affect the mechanical properties of BIM-colluvium. The influencing factors such as block proportion, block inclination, and block aspect ratios were studied. Their major findings were that the strength of BIM-colluvium increases with increasing block proportion and that rock block inclination results in anisotropy of the mechanical behavior, while higher confining pressure reduces the anisotropic behavior. On the other hand, the block aspect ratio has a minor influence on the mechanical properties. Figure 11 and Figure 12 exemplarily depict the findings of Pan et al. (2008) mentioned above.

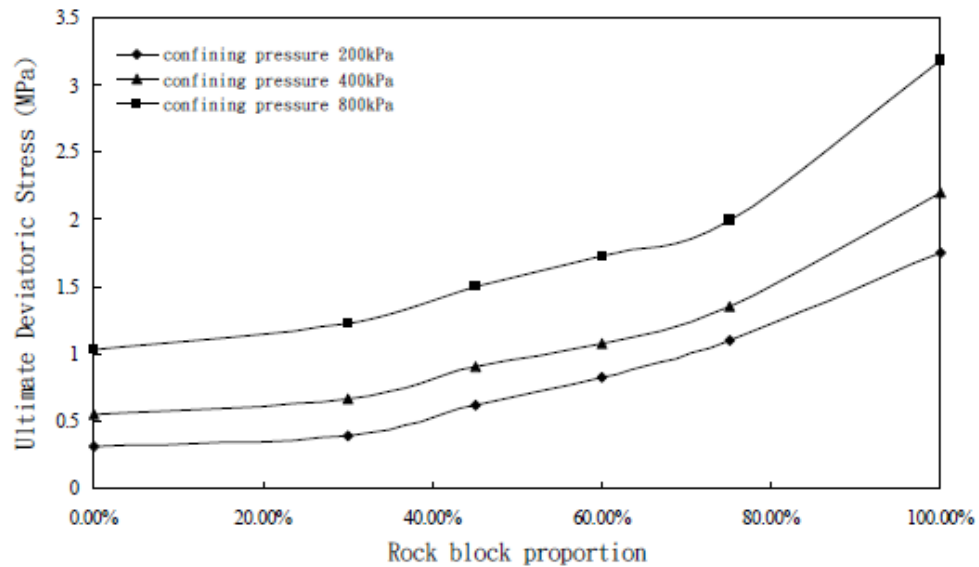


Figure 11: Results of numerical triaxial tests after Pan et al. (2008); ultimate deviatoric stress versus block proportion with aligned blocks (Pan et al. 2008).

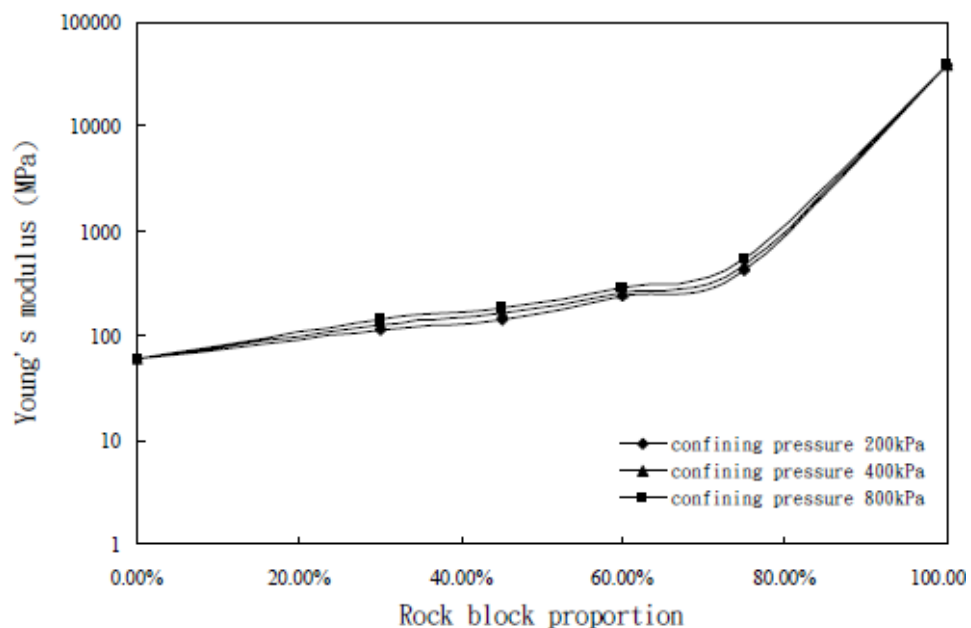


Figure 12: Results of numerical triaxial tests after Pan et al. (2008); Young's modulus versus block proportion with rock blocks without preferred orientation (Pan et al. 2008).

Coli et al. (2012) investigated the mechanical response of rock mixtures by utilizing a finite element approach. They performed numerical compression tests under uniaxial and triaxial conditions on virtual cylindrical specimen of both welded and unwelded bimrocks with spherical inclusions. For the purpose of having a basis for validation, the assigned material properties and the test configuration were in accordance with the assumptions made by Lindquist (1994). The investigators observed a pronounced correlation between volumetric block content and the mechanical parameters and their results were in good

agreement with the findings of Lindquist (1994). For welded specimens an increase of Young's modulus, UCS, friction angle and cohesion with VBC was evident, while cohesion showed a progressive decrease for unwelded specimen (Figure 13). Their findings back the common assumption of a block content threshold of about 20% - 25%, above which the blocks start to contribute to the overall mechanical behavior. Their results evidenced a negligible influence on strength and deformability properties for volumetric block content of 10%.

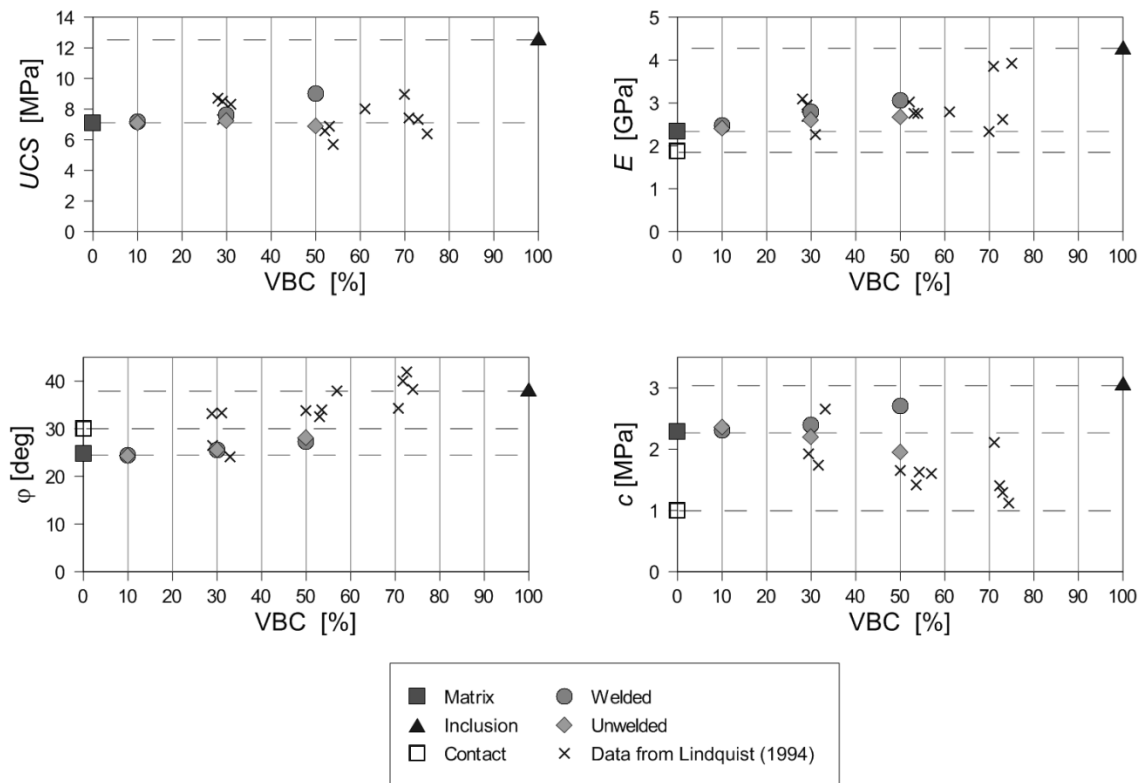


Figure 13: Influence of VBC on strength and deformability properties of virtual bimrock models. The physical test data from Lindquist (1994) on unwelded specimen are also shown (Coli et al. 2012).

Wen-Jie et al. (2011) and Coli et al. (2011) in their research focused on large scale in-situ tests. Wen-Jie et al. (2011) studied the shear strength of reconstituted soil-rock mixtures, taken from a slope in China (bedrock is Permian basalt, lithological composition of cobbles and gravels is widespread (limestone, sandstone, granite, etc.)) and performed direct shear tests in the field (sample size: 60/60/40 cm). Special attention was paid to the sample reconstitution process, by applying digital image processing (DIP) and statistical evaluation methods to determine proper block sizes and frequency distributions.

From the shear stress versus horizontal displacement curves it was observed that samples containing blocks show a kind of yield stage (or even several translation stages from yield to strain hardening) before reaching the peak strength. This behavior becomes more pronounced with increasing block proportion and increasing normal stress. As expected, the development characteristics of the

shear zone are related to the rock block proportion. With increasing block proportion the shear zone becomes wider and wider, the zone affected by the shear process increases in expansion and the failure surface becomes more tortuous. Their evaluation of friction angle and cohesion is in good agreement with the findings of Lindquist (1994) and Irfan and Tang (1993) (Figure 14). For block proportions in the range of 25% to 70% an approximately linear relationship between increment of friction angle and increase of block proportion is determined. A different picture is drawn for the cohesion. Cohesion decreases quite pronounced up to 30% block proportion, while above 30% cohesion tends to have a minor decrement with increasing block proportion.

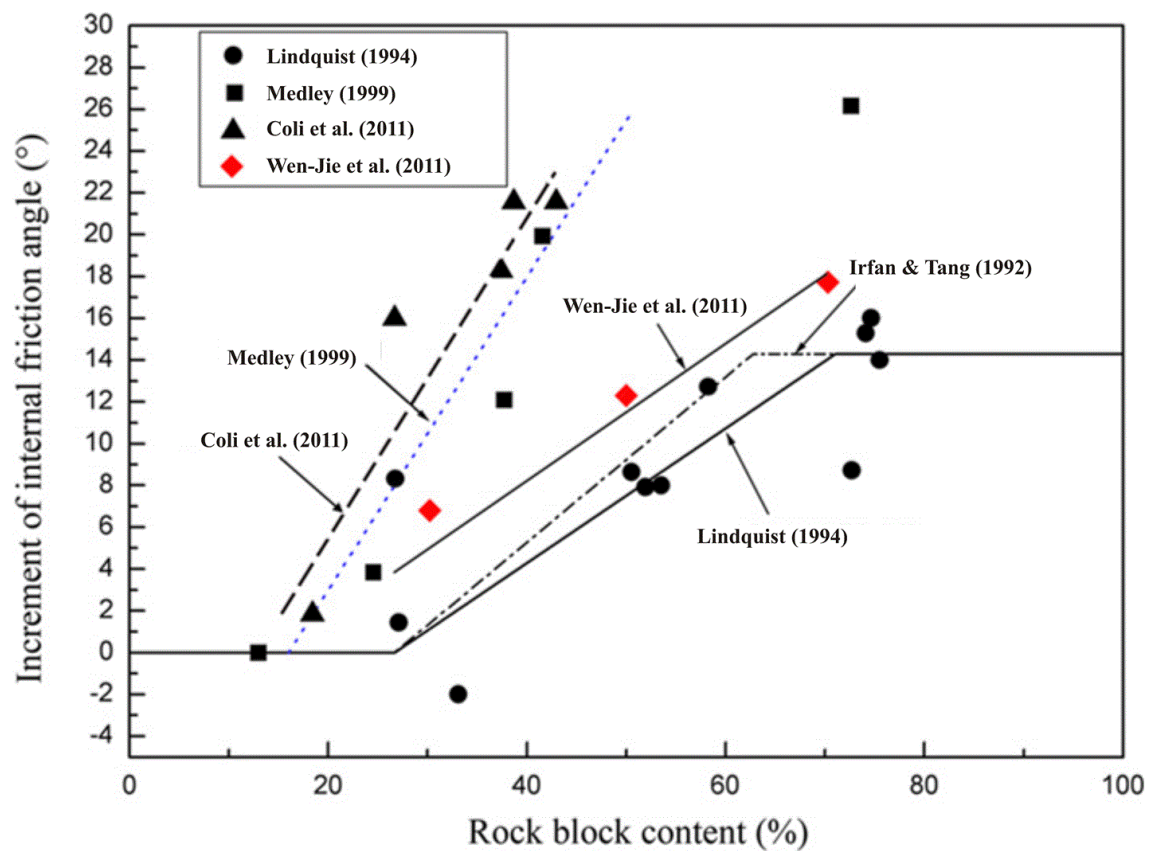


Figure 14: Relationship between the increment of internal friction angle and rock block content (modified from Wen-Jie et al. 2011).

Coli et al. (2011) performed in-situ shear tests on bimrocks, which were inspired by the work of Wen-Jie et al. (2011) and were improved in terms of testing apparatus and data acquisition system. A special feature of their test procedure is that the shear surface is not forced to develop along a pre-defined horizontal plane, but is free to develop in a tortuous way along block boundaries. Due to the high heterogeneity of the tested samples, very different deformational paths and shapes of force-displacement curves were observed. Strength parameters (friction angle  $\phi$ , cohesion  $c$ ) were determined for each test using a simplified limit equilibrium approach based on the measurements on the failure surfaces. Again, the friction angle increases with the volumetric block content (VBC) in a good

linear correlation ( $R^2=0.85$ ) (Figure 15). Determined values for cohesion are scattered for low block proportions ( $< 20\%$ ) and remain at a very low level, which is characterized by a negligible negative correlation with the volumetric block content (Figure 16). The sudden drop in cohesion between 20% and 25% of VBC is in accordance to the findings of many authors and represents the threshold value between a matrix-controlled and a block-controlled behavior. The performed tests yielded larger values for friction and lower values for cohesion, compared to the effective strength parameters of the clayey matrix. These investigators emphasize that the determined strength parameters of the bimrock material are not effective but operative parameters under natural conditions.

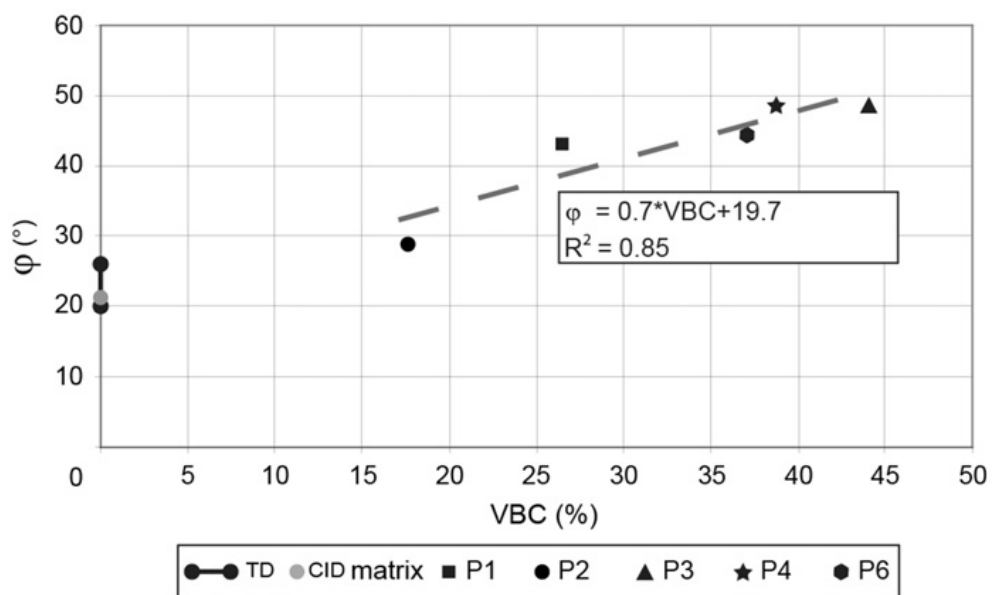


Figure 15: Correlation between friction angle and VBC (Coli et al. 2011).

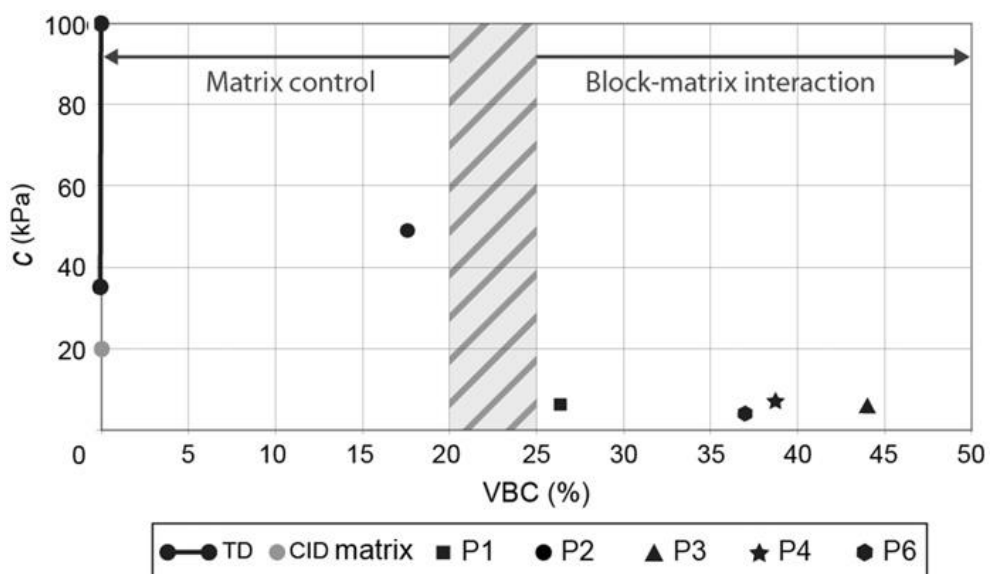


Figure 16: Correlation between cohesion and VBC (Coli et al. 2011).

Coli and Tanzini (2013) performed a geomechanical characterization of the “Chaotic Complex”, which is largely present in the Northern Apennines (Italy), where they utilized and compared three different approaches: a) the classical geotechnical approach; b) the GSI approach and c) the bimrock approach. The classical geotechnical approach is mainly based on the determination of the mechanical properties of the clayey matrix by utilizing laboratory tests on reconstructed samples. In the GSI approach the authors determined the Hoek-Brown failure criterion parameters (GSI,  $\sigma_{ci}$  and  $m_i$ ; Hoek et al. 2002) by back analysis based on radial strain values, gained by displacement monitoring at a tunnel project. Hence, the GSI approach, in the sense of their paper, is rather a back analysis method than an approach for the geomechanical characterization of bimrocks. The bimrock approach is based on the determination of cohesion and friction for the matrix and the UCS of the blocks by laboratory tests as well as on the determination of volumetric block proportion and angle of repose for blocks. The bimrock cohesion and friction angle was assessed by utilizing empirical solutions. The investigators showed in their comparative study, that the classical approach underestimates the shear strength of the rock mass. The reason for this finding was attributed to the difficulties of sample recovery in tectonically disturbed rock mass and the high sensitivity of pervasively fissured material to sampling disturbance. The bimrock approach yielded promising results for the determination of shear strength parameters, especially for slopes and shallow tunnels, while for deep tunnels an underestimation of cohesion was observed. In the authors opinion the GSI approach, in combination with laboratory tests on matrix and blocks, represents the method of choice for a proper characterization of bimrocks. However, as mentioned above, their GSI approach is based on back analysis of monitored displacements by utilizing the closed-form solution after Hoek et al. (2002). It is noted that performing a back analysis does not necessarily require the GSI as input, since utilizing a closed-form solution will instantaneously yield the overall bimrock properties. Moreover, the GSI system, in fact, was developed for certain geological rock mass conditions. The basic requirement is, that the rock mass behaves as an isotropic mass, composed of a sufficient number of discontinuities (Marinos et al. 2005). In addition, the intact rock properties and the joint properties have to be assessed independently. Therefore, applying the GSI approach for the prediction of the overall bimrock properties will lead to erroneous and misleading results. In sheared rock masses the GSI system reaches its limitations when a separate description of intact rock and joints is impossible. Goricki et al. (2006) emphasize that in such conditions direct testing of the rock mass in a proper scale or the bimrock approach should be utilized for the determination of the rock mass strength.

### 3 Definition of objectives

After performing a review of the state-of-the-art regarding geomechanical characterization of fault material, following issues requiring additional research effort and clarification associated with bimrocks have been identified:

- **In-situ testing of fault material:**  
There are a few works available in literature, which are dealing with in-situ-testing of fault material. However, they often do not account for the actual conditions given at site. The test procedure is mainly restricted to take undisturbed samples. The peculiarities of a certain rock mass zone of interest are often not accounted for, like stress regime, groundwater conditions, etc.
- **Laboratory techniques:**  
The currently available laboratory techniques for the determination of rock mass properties of fault material are still lagging behind the experience regarding the special features and treatment of highly heterogeneous rock samples.
- **Type of used laboratory tests:**  
Most of the available tests on bimrock material are performed utilizing uniaxial compression or triaxial compression tests. Although they yield information about the strength of materials, they often do not allow a proper assessment of the failure surface after the test. Hence a sound determination of the mechanical processes involved and occurring during the loading process is often not possible.

The dissertation pursues several objectives. For the determination of the deformability of faulted rock mass an in-situ testing program should be carried out. The test program should be conducted directly in a fault zone, hence accounting for the properties which are present in reality without making any concessions to simplifications in test set-up or test procedure. Fault material is often treated as soil-like material, since the aggregates are ascribed to clay, silt and sand or blocks and boulders. However, due to high primary stresses (especially for deep tunnels in Alpine fault zones), involved chemical processes, the presence of groundwater, etc., it is deemed as fairly certain that fault zones exhibit a quite different mechanical behavior than the pure aggregates.

Another objective is the development of a new laboratory test apparatus for the determination of deformation properties of real and artificial fault material samples. The focus is laid on a large oedometer test device, circumventing the shortcomings of currently available laboratory techniques for the determination of deformability properties. The new test apparatus should meet the requirements of allowing testing large samples and providing the possibility of testing different sample sizes. Additionally, the applicable load should cover a broad range of



stress magnitudes, accounting for test conditions with stress regimes found at tunnel level. The deformability of fault material, as with many porous and granular materials, shows high dependency on the stress magnitude. The testing device should account for this issue, allowing a sound assessment of stress dependent stiffness properties.

A key objective is to provide knowledge about the mechanical behavior of fault zones based on bimrocks concept, focusing on the influence of block proportion and block orientation. Since large displacement magnitudes are often observed in tunnels in weak rock mass, special attention should be paid to study the behavior of bimrocks exposed to large strains. A suitable test procedure should be utilized, allowing a proper investigation of the failure surface after the test, in order to gain information about the mechanical processes involved. The variation of block proportion and block orientation should cover a broad range, providing an overall picture and comprehensive understanding of possible mechanical behavior. The determined mechanical properties should provide a basis for a qualitative description of a constitutive law for bimrocks.

## 4 Deformation properties of fault rocks

Stress-strain – relationship or deformability in general is one of the most important engineering properties for describing rock masses. The determination of realistic values for the deformability of weak rock masses, i.e. block-in-matrix rocks, is challenging, since the “overall” or average deformability of a heterogeneous fault material depends both on the deformability of the pure matrix and the pure block and on the volumetric block proportion. Moreover, fault material or fault zones feature a high degree of anisotropy, since the block orientation significantly influences the deformation properties. In order to study the deformation behavior of fault material in principle and to gain knowledge about factors influencing the deformability following approach was chosen:

a) Determination of deformation properties through in-situ tests, conducted in a fault zone. The information about the behavior of weak rock mass under in-situ conditions (stress state, etc.) compared with laboratory test results of the same material, allows the evaluation of stress and scale dependency of the deformability. Comparing in-situ test results with laboratory test results allows determining of the “degree of deviation” between both results and the assessment of influencing factors.

b) To account for the anisotropic properties of fault material, the role of volumetric block proportion and block orientation on the deformability has to be investigated. An extensive laboratory program on artificial block-in-matrix rocks, in which the block proportion and orientation is varied, yields information about the degree of anisotropy. Varying the block proportion and block orientation in a reasonable manner allows for the applicability of the findings to a broad range of combinations.

### 4.1 In-situ tests

The 32.9 km long Koralmtunnel, currently the longest Austrian tunneling project, will pass a roughly 450 m long section of the Lavanttal fault zone, featuring intensively sheared, fractured, cataclastic material. In order to have a sound database and knowledge about the properties and the behavior of the surrounding rock mass, exploratory tunnels with a total length of 8 km were constructed in Carinthia between 2004 and 2010 (Figure 17).

Within the scope of an extended exploration program, a test adit was constructed in the core region of the Lavanttal fault system in order to conduct an extensive in-situ testing program. The in-situ testing program consisted of 3D displacement monitoring, an installation of a chain-inclinometer above the tunnel crown, installation of a face extensometer in the center of the test adit, strain gauges and temperature gauges in the shotcrete lining, plate load tests and direct shear tests

at the shotcrete shell. Within the scope of this thesis the plate load tests are considered and explained in detail. A detailed description of the entire in-situ testing program is given in Pilgerstorfer et al. (2011).

The instrumentation adit was excavated at chainage 1248.66 m of the exploratory tunnel Paierdorf, situated at a future cross passage between the northern and southern tube of the Koralm tunnel.

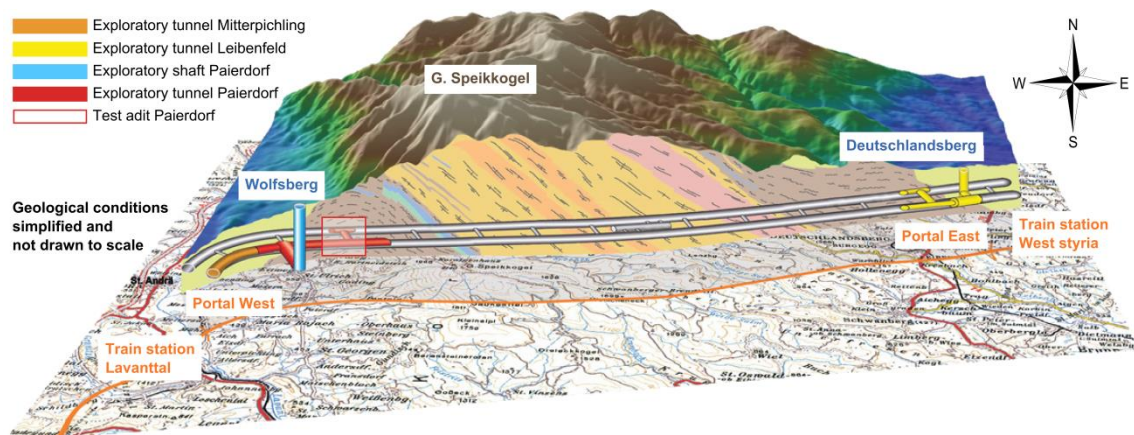


Figure 17: 3D model of the Koralm massif with geological longitudinal section and exploration structures; test adit marked with red square (modified after ÖBB-Infrastruktur AG 2013).

The instrumentation adit has a length of 20 m, where the first 6 m were excavated according to the typical cross section of the cross passage design and the remaining 14 m feature a circular excavation with an inner diameter of 4.15 m (Figure 18).

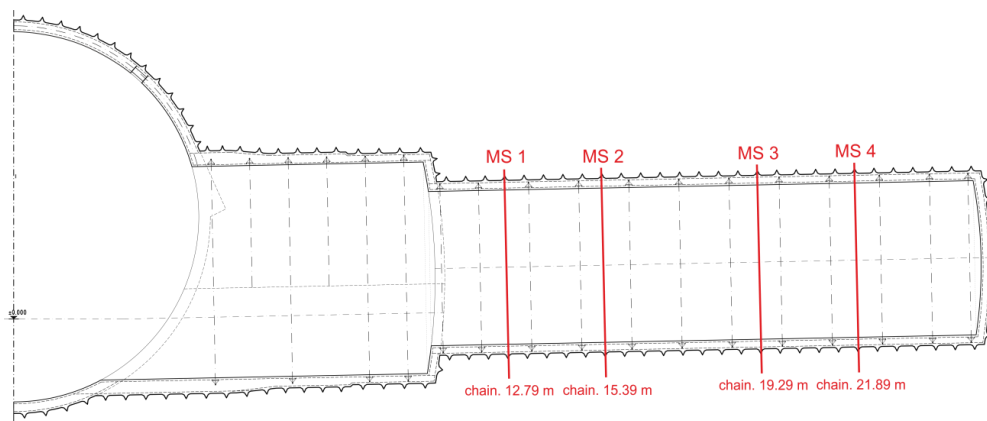


Figure 18: Longitudinal section of the instrumentation adit and the test cross sections MS 1 – MS 4.

#### 4.1.1.1 Geological conditions

The rock mass, surrounding the test adit, is composed of highly fractured and softened schistose gneiss and coarsely grained cataclasites accompanied by

erratically occurring lenticular insertions of moderately competent crystalline rock and shear bands with cataclastic fillings (silty-clayey), ranging from millimeters to centimeters (Figure 19). The rock mass features strongly varying intact rock strength (< 1 to 50 MPa), depending on the degree of tectonism and is moderately-to-highly (at cataclastic sections) fractured.

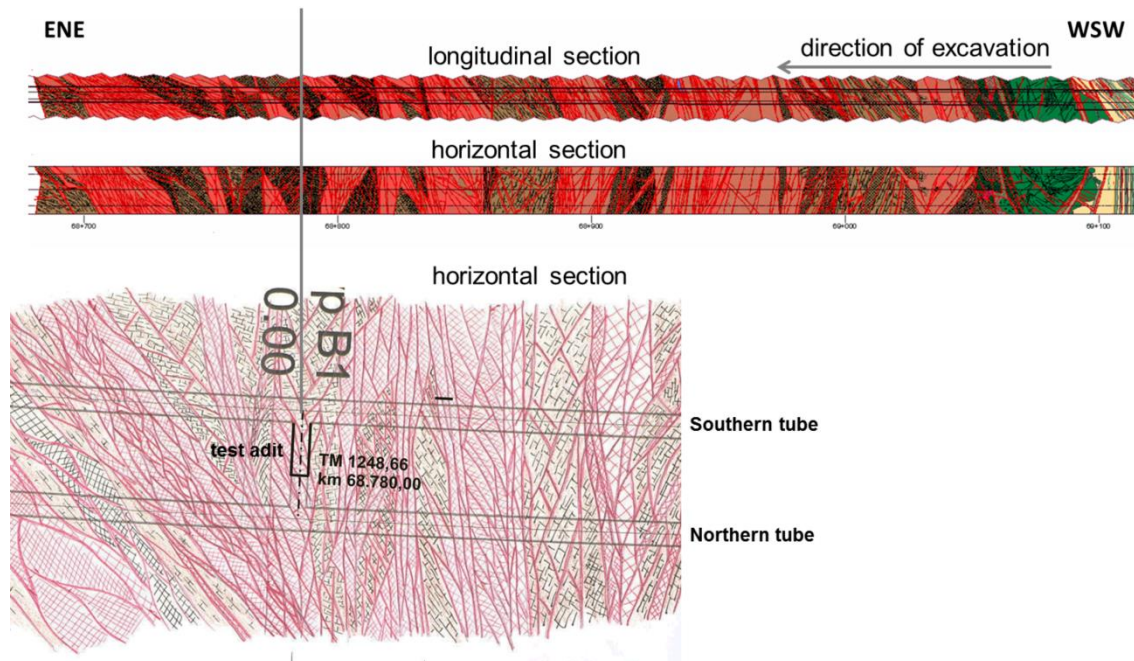


Figure 19: Geological conditions in the core region of the Lavanttal fault zone and location of the test adit with surrounding geological conditions.

The rock mass has been frequently sheared along the foliation, thus slickensides are usually oriented parallel to the foliation. The dominating discontinuity set (foliation and associated slickensides) shows low to moderate dip angles towards southeast to southwest.

Two further slickenside-sets and shear bands, respectively, being orthogonal to each other, dip moderately steep and strike mainly from northeast – southwest to south-southeast – north-northwest (Figure 20 and Figure 21, Table 1).

Table 1: Geological data of discontinuities at the test adit.

Discontinuity-type	Dip direction / dip [°]	Confidence cone [°] (confidence 99%)	Spherical opening angle [°]
SF	177/28	13	20
H1	249/33	7	17
H2	136/56	9	13

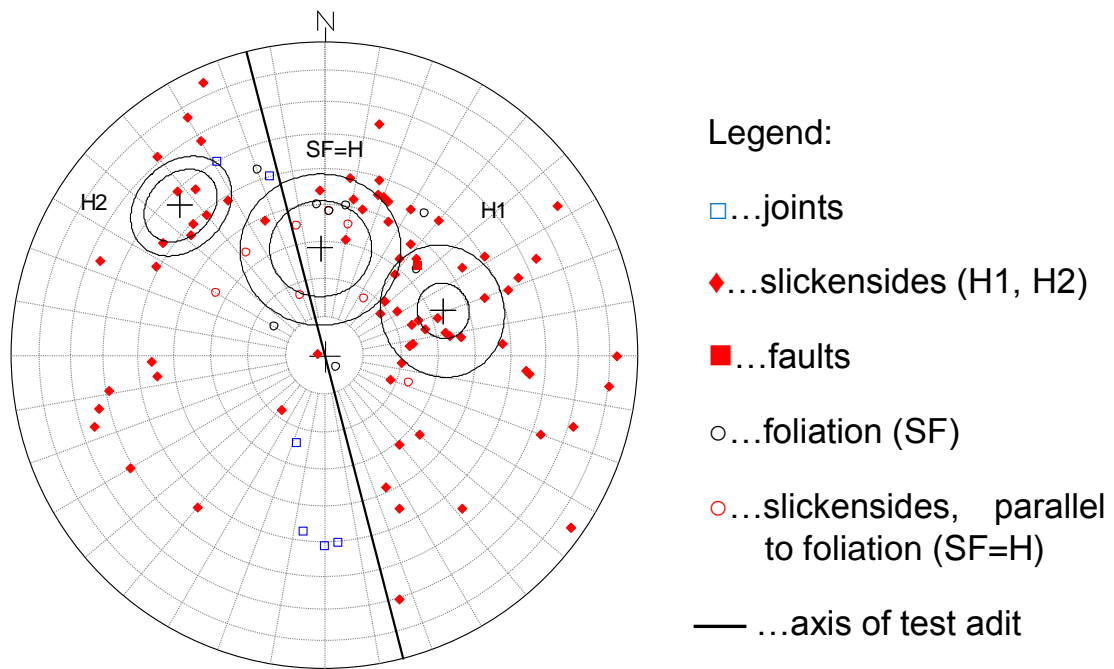


Figure 20: Stereoplot of pole points in the area of the test adit, TM-VS 5.70 m – TM-VS 25.14 m, tunnel advance from south-southeast to north-northwest.

The excavation behavior is significantly dominated by heterogeneous rock mass conditions and the numerous slickensides, which lead to a high potential for sliding blocks at the face and forming wedge-type intersections at the tunnel wall. Although the rock mass is mainly dry, occasionally dripping or slightly flowing water inflows were also observed.



Figure 21: Geological conditions at chainage TM-VS 25.14 m; fractured schistose gneiss with competent rock blocks (marked with dashed lines) and cataclastic shear bands.

### 4.1.1.2 Position of test cross sections

The double plate load tests were situated in four different test cross sections at chainage TM-VS 12.79 m (MS 1), TM-VS 15.39 m (MS 2), TM-VS 19.29 m (MS 3) and TM-VS 21.89 m (MS 4) (Figure 18). In order to avoid the tests influencing each other, the distance between the axes was set to at least 2.6 m (between MS 1 and MS 2, MS 2 and MS 3, and MS 3 and MS 4).

In order to evaluate the deformation properties accounting for the anisotropic conditions of the surrounding rock mass, the tests were performed in two loading directions in each test cross section. One measurement axis was parallel to the foliation of the rock mass (according to the documented geological conditions), while the second measurement axis was set perpendicular to the foliation (Figure 22). The measurement axis perpendicular to the foliation was denoted with “1”, the measurement axis parallel to the foliation was denoted with “2” (e.g. for test cross section 1 – perpendicular to foliation: MS 1.1; test cross section 1 – parallel to foliation: MS 1.2). The exact location of the distinct measurement axis, with regard to the orientation of the foliation was assigned by the geologist and with the help of 3D-stereo photos of the tunnel face.



Figure 22: Positioning of the measurement axis, adjusted to the foliation.

### 4.1.1.3 Test set-up

The unit for the double plate load tests basically consisted of the following parts:

- a) Middle part, consisting of four cylindrical steel tubes 168.3 x 16 mm, in available lengths of 125, 250, 500, 1000, 2000 and 3000 mm. This leads to a potential total length of 6000 mm. Grading of length can be done in steps of 125 mm.
- b) Abutment cones, consisting of four cylindrical shaped tubes 168.3 x 16 mm, with steel plates (20 and 30 mm, respectively) welded on the cones and additional stiffening plates.
- c) Press unit, featuring two single acting hydraulic cylinders (Type Enerpac RAC-1506) with a nominal load of 1589 kN and a stroke of 150 mm as well as two hydraulic cylinders (Type Enerpac CLSG-1506) with a nominal load of 1390 kN and a stroke of 150 mm.

The loading device, shown in Figure 23, was assembled with a total length of 4150 mm.



Figure 23: Assembled press unit.

### 4.1.1.4 Preliminary measures

During excavation works, recesses made of metal sheet rings, wrapped outside by mineral wool, were installed for the load plate abutment in the respective test cross sections. The recesses were required to provide a structural separation between shotcrete and abutment mortar, ensuring that there is no load transfer between shotcrete and abutment mortar. After completion of the excavation works, the load plates were installed. The manufacturing process was divided into following steps:

- a) Installation of four steel rods (M16, length = 120 cm) in the rock mass. The anchoring depth in the rock mass was between 20 cm and 30 cm. The steel rods in the boreholes were grouted with fast curing mortar (Figure 24).

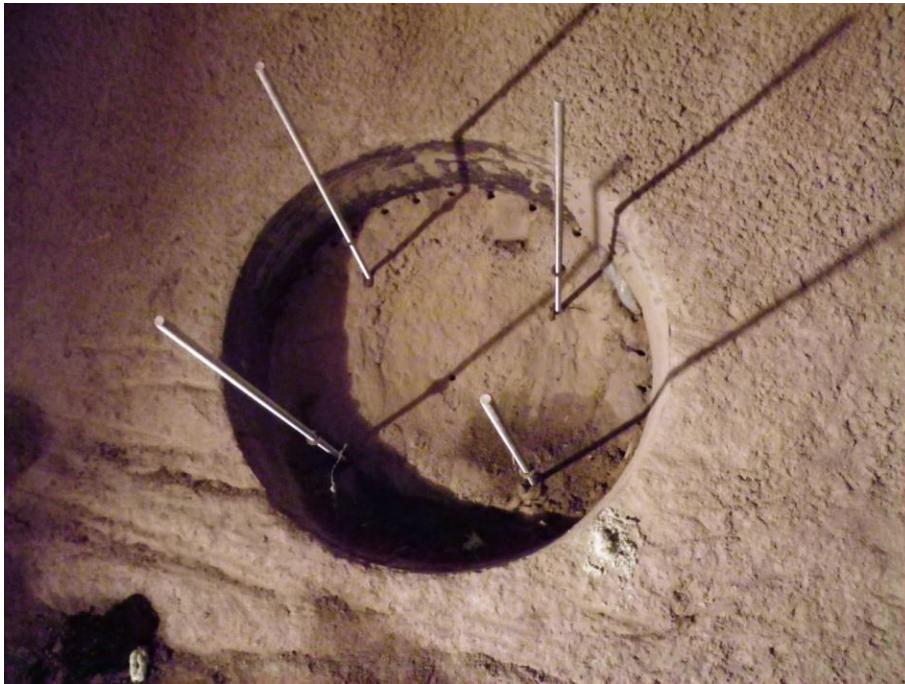


Figure 24: Installed steel rods for mounting the load plate.

- b) Placement of the load plates (steel plate  $d = 800$  mm,  $t = 8$  mm) on the steel rods (Figure 25). The load plates installed at the opposite side were correctly positioned and aligned by hexagon nuts and lock nuts. The required distance of 4150 mm between both load plates was controlled by a laser distance measurement device. Additionally the position was checked by a water level and plumb lines.





Figure 25: Mounted load plate on steel rods.

- c) Wooden plates, used as formwork, were placed at the load plates ( $d = 1000 \text{ mm}$ ,  $t = 27 \text{ mm}$ ) and fixed on the steel rods with hexagon nuts (Figure 26). The gaps between the metal sheet recesses and the wooden plates were sealed by polyurethane foam.



Figure 26: Load plates with mounted wooden plates as formwork (bottom left).

- d) The zone between rock mass and load plate was grouted with anchor mortar through the central pipe of the load plates (Figure 27).

- e) After curing of the anchor mortar, the wooden plates were replaced and the holes for the extensometers were drilled. After installation of the extensometers, they were grouted with anchor mortar to ensure a proper bond with the surrounding rock mass.



Figure 27: Grouted load plate and extensometers.

The manipulation of the loading unit was utilized by a hydraulic excavator and a telescopic loader. For the proper alignment of the press unit, winch hoists, mounted at the tunnel crown, were used (Figure 28). Moreover, the winch hoists were used for securing the loading device and to ensure working safety during test execution.



Figure 28: Set-up of the press unit by utilizing winch hoists.

### **4.1.1.5 Measurement of rock mass deformation**

The determination of the deformation of the rock mass was performed by magnetostrictive extensometers. The magnetic anchor parts of the extensometers were installed in a way that relative displacements both in the region influenced by the excavation, as well as in the “undisturbed” region could be measured (Figure 29). One extensometer was installed in the center of the load plates. Due to the anisotropic properties of the fault material, knowledge of the transfer of shear stresses due to point loads is of great interest. Hence, extensometers were also installed outside the load plate to gather information about the stress transfer by evaluating the spatial displacement development. The extensometers outside the load plate were installed at  $0^\circ$ ,  $120^\circ$  and  $240^\circ$  (viewing direction towards the load plate) (Figure 30). The drillings for the extensometer in the center were conducted in radial direction; the drillings for the extensometer outside the load plate were parallel to the one in the center. The central extensometer was equipped with six magnetic anchor parts, which were grouted in depths of 0.50 m, 1.00 m, 1.50 m, 2.15 m, 2.80 m and 3.40 m (measured from the load plate, see Figure 29). The extensometers outside the load plate were equipped with five magnetic anchor parts, which were grouted in depths of 0.50 m, 1.00 m, 1.50 m, 2.50 m and 3.40 m. The absolute displacements of the load plates were determined by utilizing wire-actuated transducers. One transducer was installed between the two load plates, in the axis of the loading direction. Two transducers were installed from the load plates to the “free” load plate at the bottom in the same testing cross section. This leads to a transducer-triangle, which allows the calculation of absolute displacements by utilizing geometric relationships.

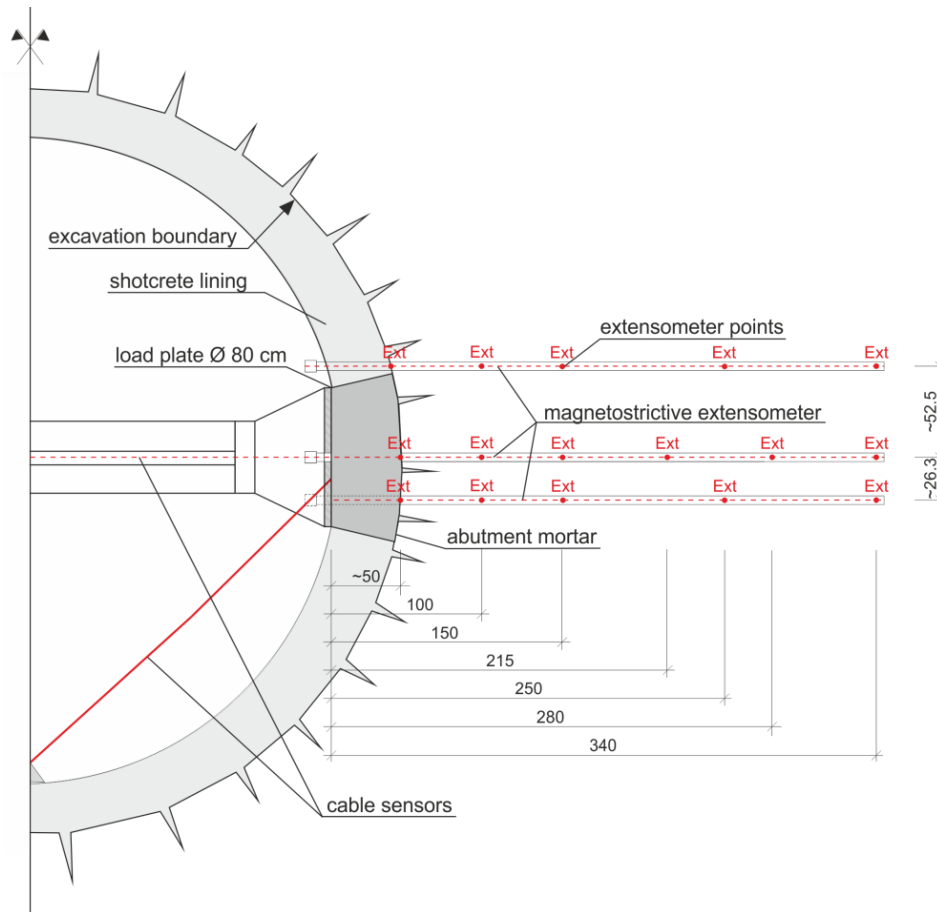


Figure 29: Schematic sketch of locations of extensometer points (magnetic anchor parts).

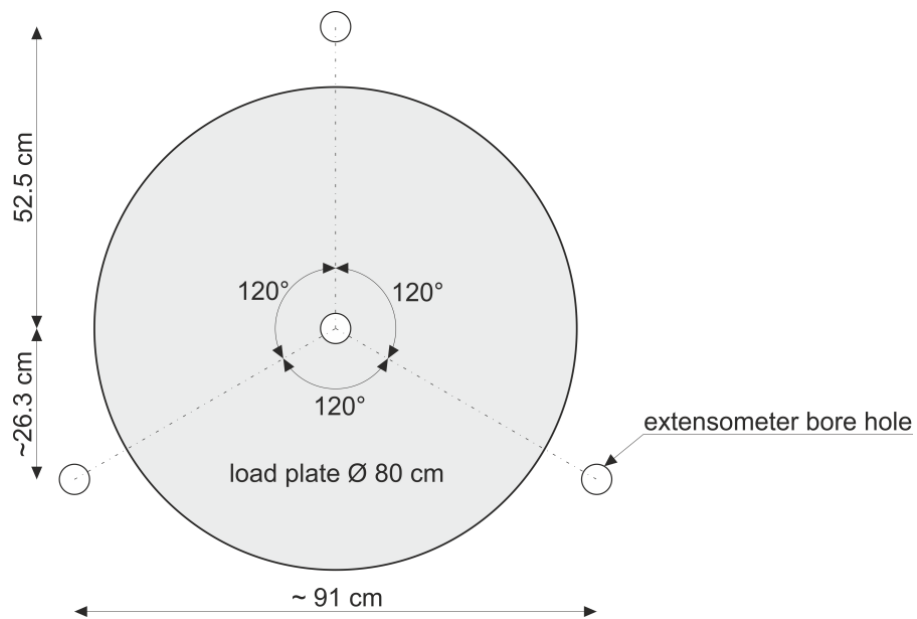


Figure 30: Top view load plate with extensometer boreholes.

### 4.1.1.6 Test execution

The rock mass was repeatedly loaded and unloaded, whereby the load was increased after each loading cycle. Every load step was kept constant until displacement rates became almost zero. The calculation of the maximum allowable load was determined according to ÖNORM B4435-2 (1999) and yielded an ultimate bearing capacity of 2315 kN. The initial design considered to decrease the maximum allowable load by a factor of 1.15 and to divide this “design load” into four load steps. Due to the stiff support of the test adit, no bearing failure was observed while reaching the maximum force of the loading device. Therefore, the loading scheme was adjusted constantly during test execution. Figure 31 and Figure 32 show the actually executed loading schemes. It is noted that for tests normal to the foliation (Figure 31) the first five loading-unloading cycles coincide for all four tests (black solid line), while after the fifth cycle they differ from each other. In the tests MS 1.1, MS 2.1 and MS 3.1 the extensometer probes were removed after four and five load steps, respectively. After that the load was increased up to the maximum load capacity of the hydraulic unit. In the tests MS 1.2, MS 2.2, MS 3.2, MS 4.1 and MS 4.2 the extensometer probes remained mounted during the whole test period and the load was increased in nine load steps until the maximum load capacity of the hydraulic unit was reached. The loading-unloading cycles given in Figure 32 for tests parallel to the foliation were fairly the same for MS 1.2, MS 2.2 and MS 3.2. MS 3.2 shows a slight deviation from MS 1.2 and MS 2.2 for the last cycle. MS 4.2 coincides with the accompanying three tests up to the sixth loading-unloading cycle. The value of loading increments was set to 60 bar, which equals a load of approximately 50 kN.

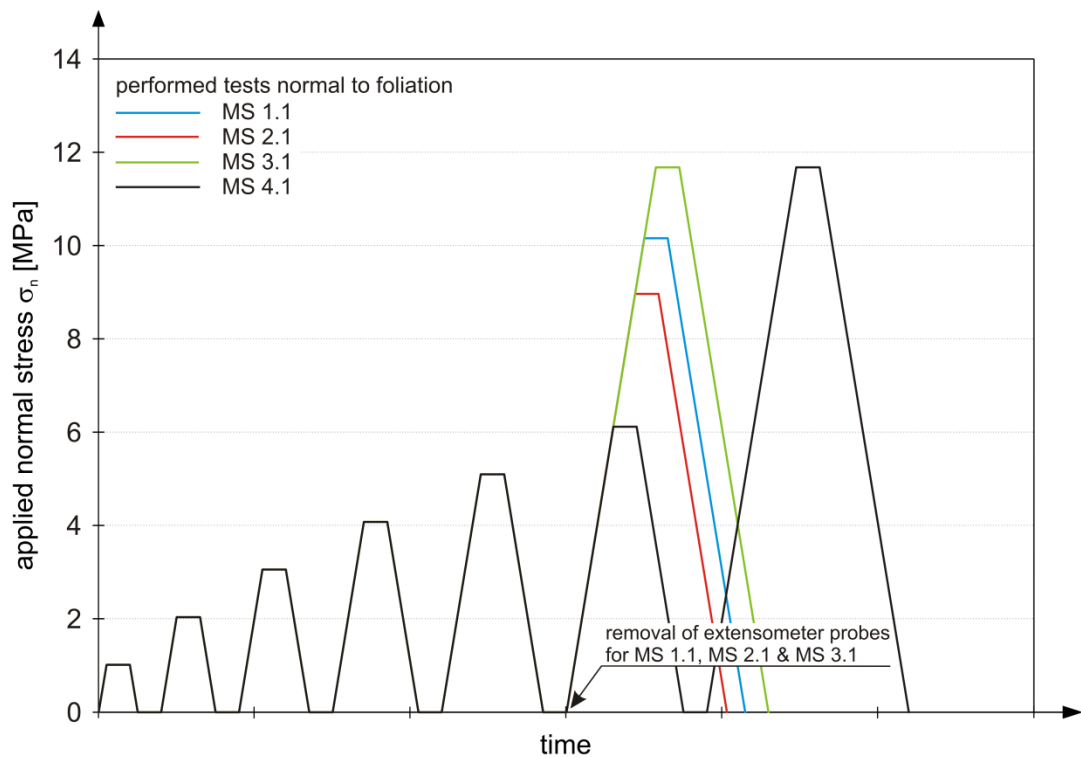


Figure 31: Stress vs. time diagram (performed loading schemes) for tests normal to foliation.

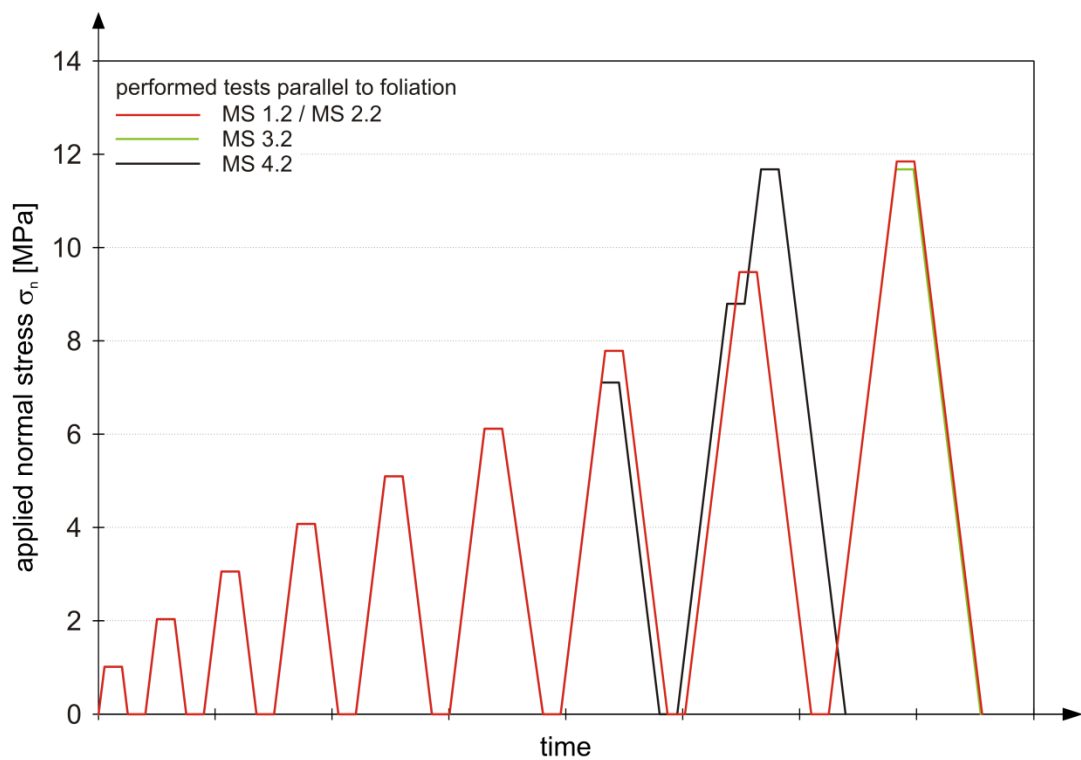


Figure 32: Stress vs. time diagram (performed loading schemes) for tests parallel to foliation.

### 4.1.1.7 Measurement data evaluation

The data evaluation was performed according to Ünal (1997) and DGEV (1985), both based on the theory of elastic-isotropic half space theory after Boussinesq. The approach, given by Ünal (1997), provides a valuable improvement of the evaluation procedure described in the ISRM suggested methods (ISRM 2007). Absolute displacements for both load plates were calculated from the measurement data, by simple trigonometric relationships. In a first step the starting points of each loading-unloading cycle were detected from the recorded load step data series. Stress-strain curves were determined for each extensometer point in the rock mass. Based on the stress-strain curves, the maximum and minimum normal stresses acting under the load plate and the appropriate strains were determined for each loading-unloading cycle (Figure 33).

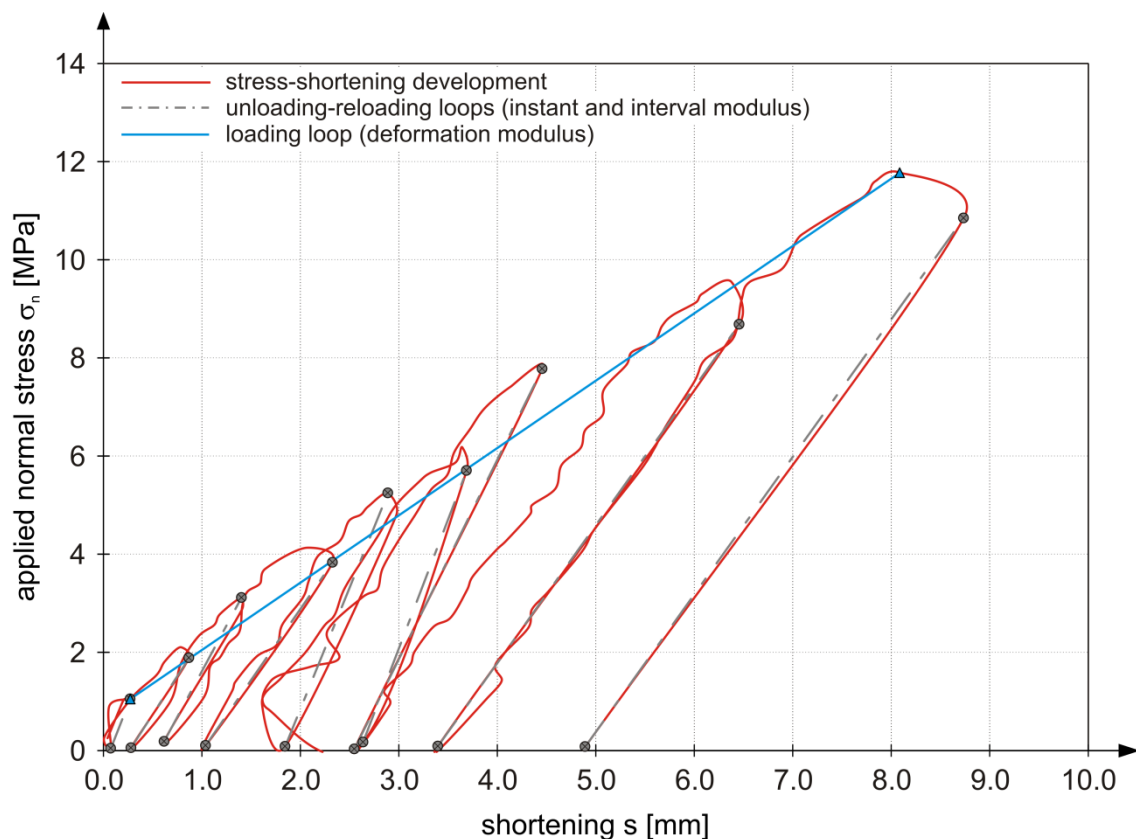


Figure 33: Example of stress vs. shortening diagram: minimum and maximum normal stresses under the load plate and associated shortening for loading-unloading loops.

### 4.1.1.8 Results

According to Ünal (1997) it is possible to determine an instant and an interval modulus of the rock mass. The instant modulus ( $E_{zi}$ , hereinafter called  $E_{inst}$ ) can be calculated for the rock surface or for any point inside the rock mass, corresponding to locations where displacements are measured (Equation (1)).

$$E_{z_i} = \Delta\sigma_m \cdot \frac{K_{z_i}}{\Delta s_i} \quad (1)$$

where:  $E_{zi} \dots$  instant modulus [MPa]  
 $\Delta\sigma_m \dots$  mean normal stress on the loaded surface [MPa]  
 $K_{zi} \dots$  coefficient accounting for the corresponding depth from the surface  $z_i$  [1/m]  
 $\Delta s_i \dots$  displacement in the direction of the applied load [m]

The coefficient  $K_{zi}$  is calculated by Equation (2).

$$K_{z_i} = \frac{r}{2} \cdot \left[ 2 \cdot (1 - \nu^2) \cdot \arcsin \frac{1}{\sqrt{z_i^2 + 1}} + (1 + \nu) \cdot \frac{z_i}{z_i^2 + 1} \right] \quad (2)$$

where:  $r \dots$  radius of the load plate [m]  
 $\nu \dots$  Poisson's ratio [-]  
 $z_i \dots$  depth of a point below the surface where displacements are measured [m]

Poisson's ratio,  $\nu$ , was set to 0.3, based on the results of triaxial compression tests conducted on samples taken in the test adit (3G Gruppe Geotechnik Graz ZT GmbH 2010). The interval modulus ( $E_{z_i-z_{i+1}}$ , hereinafter called  $E_{int}$ ) represents the modulus of deformation between two measuring points. By calculating  $K_z$  at any two depths (e.g.  $K_{z1}$  and  $K_{z2}$ ) and using the measured displacements  $s_1$  and  $s_2$  respectively, the instant modulus can be derived by Equation (3).

$$E_{z_i-z_{i+1}} = \Delta\sigma_m \cdot \frac{K_{z_i} - K_{z_{i+1}}}{\Delta s_i - \Delta s_{i+1}} \quad (3)$$

The instant modulus and the interval modulus were determined from the unloading-reloading cycles. The deformation modulus ( $E_{def}$ ) describes the deformability of the whole rock mass considered, and was determined from the loading cycle, according to DGEV (1985).



The deformation modulus is calculated by Equation (4).

$$E_{def} = \omega \cdot (1 - \nu^2) \cdot r \cdot \frac{\Delta\sigma_m}{\Delta s_i} \quad (4)$$

where:  $\omega$  ... dimensionless coefficient, accounting for the type of loading (stiff plate or flexible plate) and the location where displacements are measured (center or boundary of the plate) [-]

For the case of a stiff load-plate and displacement measurement in the center of the load-plate the coefficient  $\omega$  takes the value of  $\pi/2$ , according to the theory of elastic half-space.

A graphical representation of evaluated moduli is given in Figure 35 through Figure 42 for loading normal to foliation and Figure 43 through Figure 50 for loading direction parallel to foliation, respectively. The values therein are given as mean values, calculated from all performed load cycles. The red (measuring section top) and blue (measuring section bottom) rhombi therein are the values for the interval modulus, representing the moduli between two adjacent extensometer points, i.e. the value depicted in the interspace between “z0” and “z1” is the interval modulus between depth “z0” and “z1”. The arrows pointing to the left and right indicate the respective zone for which the interval modulus is evaluated. The red and blue squares depict the instant moduli, determined for each extensometer point inside the rock mass. The arrow pointing toward the right indicates the corresponding area for which the modulus is valid, i.e. starting from the square up to infinite distance. The value which is given at depth of measuring point “zero” represents the overall instant modulus for the whole rock mass considered. Additionally the values for the overall deformation moduli are depicted as red and blue dots.

The individual values for the depths of the extensometer points (z0 – z4) for each measuring section are given in Table 2. The depth is measured starting from the surface of the load plate. A compilation of evaluated moduli is summarized in tabular form in Appendix B on page A-3 for tests normal to the foliation (Table B-1) and page A-4 for tests parallel to the foliation (Table B-2), respectively.

The values for the overall instant modulus normal to the foliation range between 900 MPa and 5250 MPa (Figure 35 to Figure 42), while the overall instant modulus parallel to the foliation was determined to be between 1650 MPa and 4200 MPa (Figure 43 to Figure 50). Between chainage TM-VS 16.00 m and TM-VS 18.00 m, slightly more favorable rock mass conditions were encountered during excavation, most prominent at the upper part of the left sidewall. This is clearly confirmed by the occurrence of the highest overall instant moduli for tests MS 2.1 – top (4546 MPa, Figure 37) and MS 3.1 – top (5247 MPa, Figure 39).

The influence of local geological conditions can also be observed by evaluation of the displacements, which were measured in the test adit during excavation. Figure 34 shows the results of the evaluation of a chain inclinometer. A detailed description of the chain inclinometer, which was part of an accompanying in-situ test program performed in the Lavanttal fault zone, can be found in Pilgerstorfer et al. (2011). The inclinometer was installed in longitudinal direction (parallel to the tunnel axis) above the crown of the test adit, prior to the excavation. The decreasing tendency of vertical displacements between chainage TM-VS 16.00 m and TM-VS 18.00 m is clearly depicted, indicating higher stiffness of the surrounding rock mass.

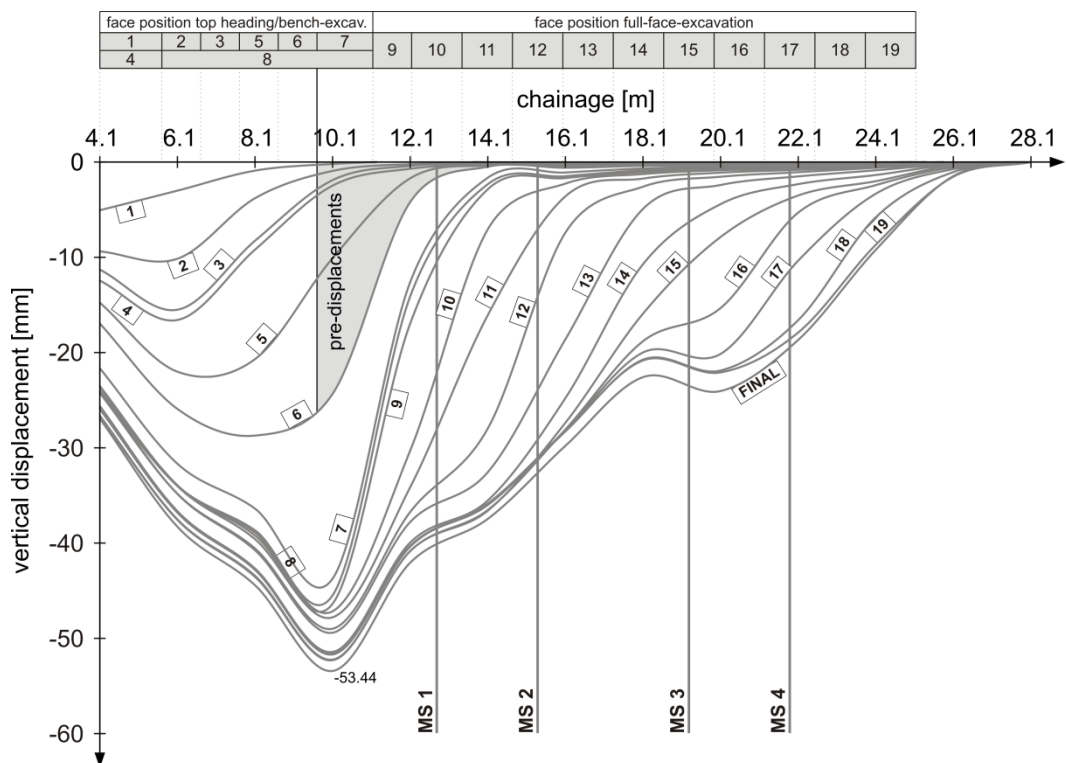


Figure 34: Results of the chain inclinometer, installed in the test adit – vertical displacements.

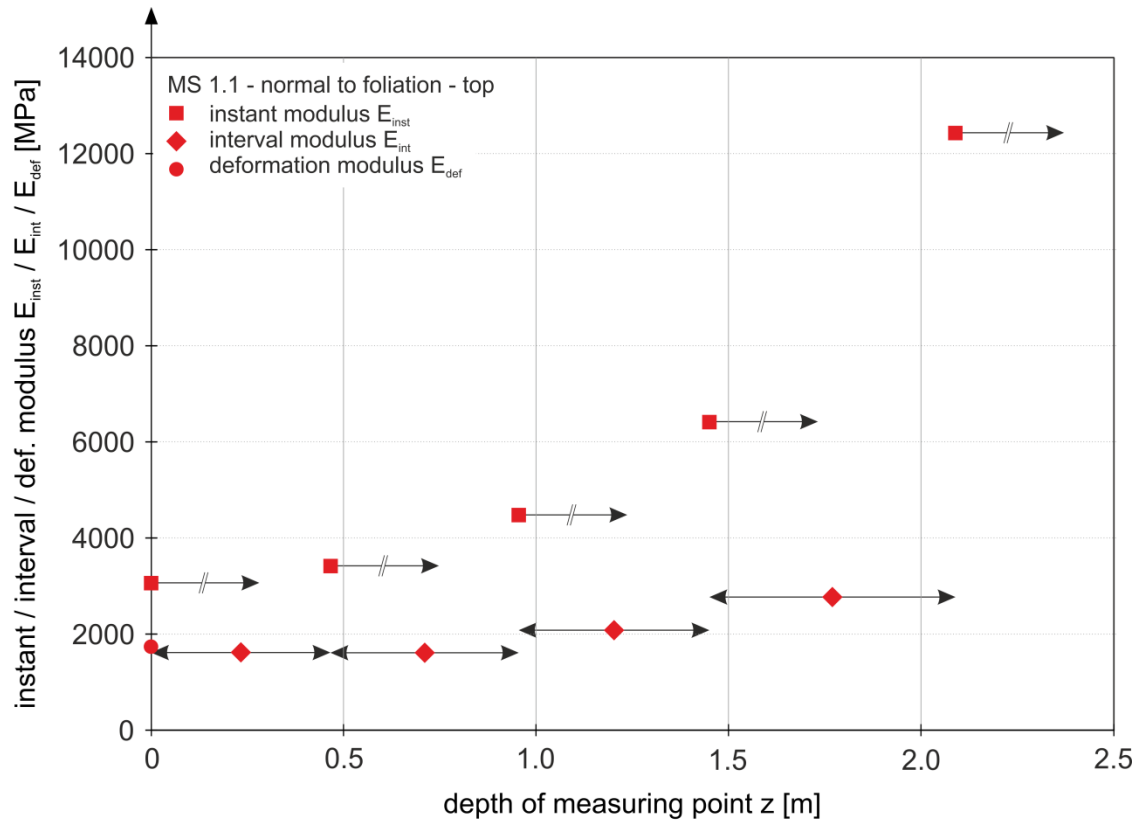


Figure 35: Evaluated moduli (instant, interval and deformation modulus) for MS 1.1 – normal to the foliation – *top*.

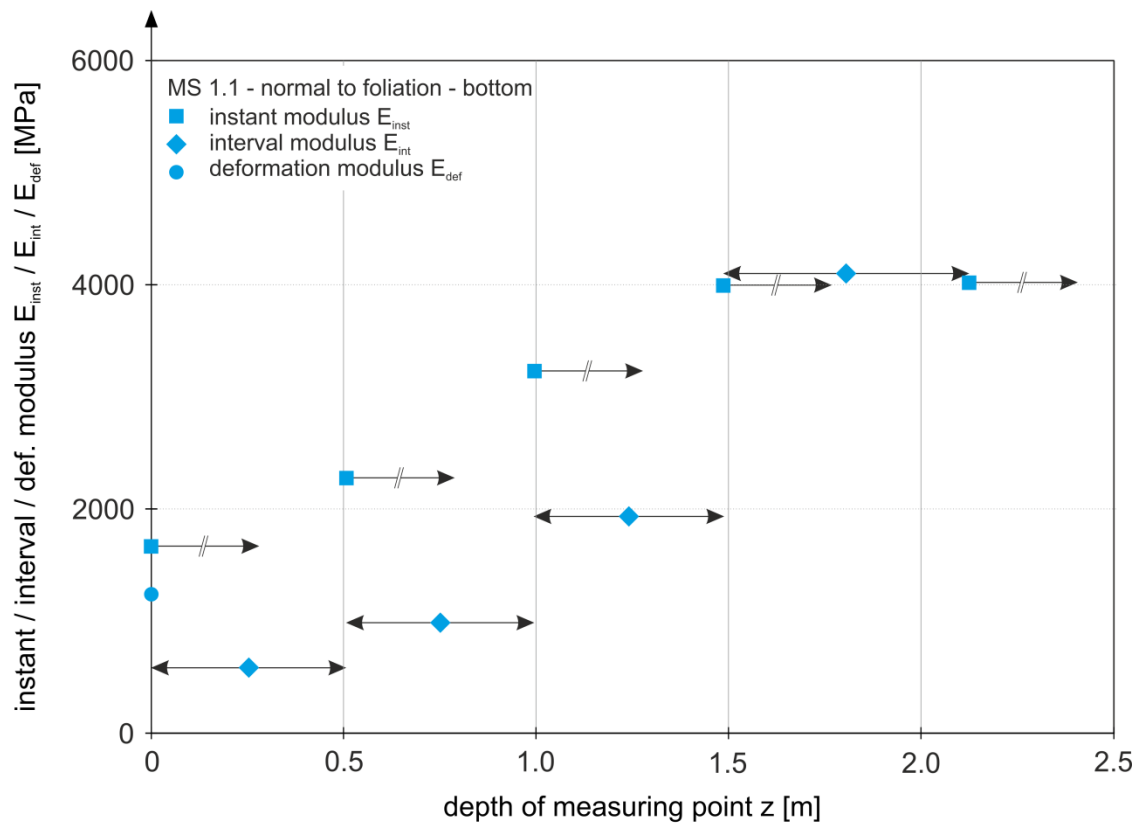


Figure 36: Evaluated moduli (instant, interval and deformation modulus) for MS 1.1 – normal to the foliation – *bottom*.

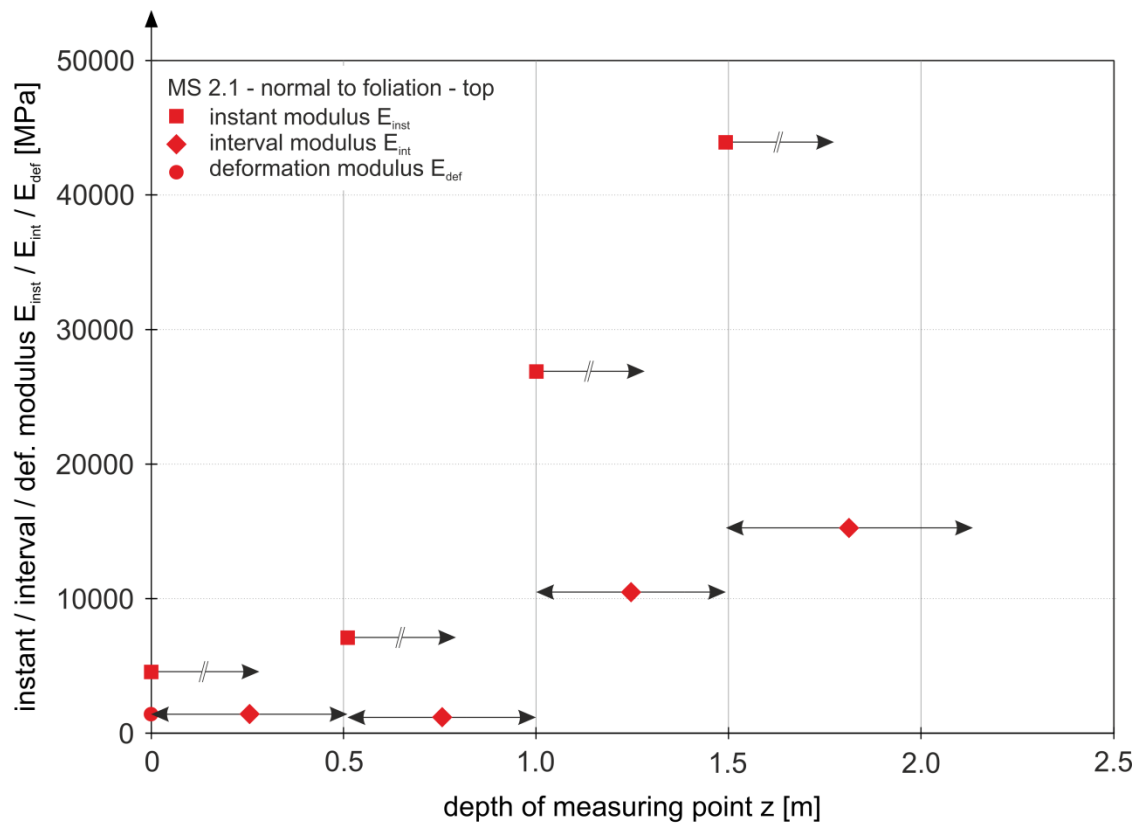


Figure 37: Evaluated moduli (instant, interval and deformation modulus) for MS 2.1 – normal to the foliation – *top*.

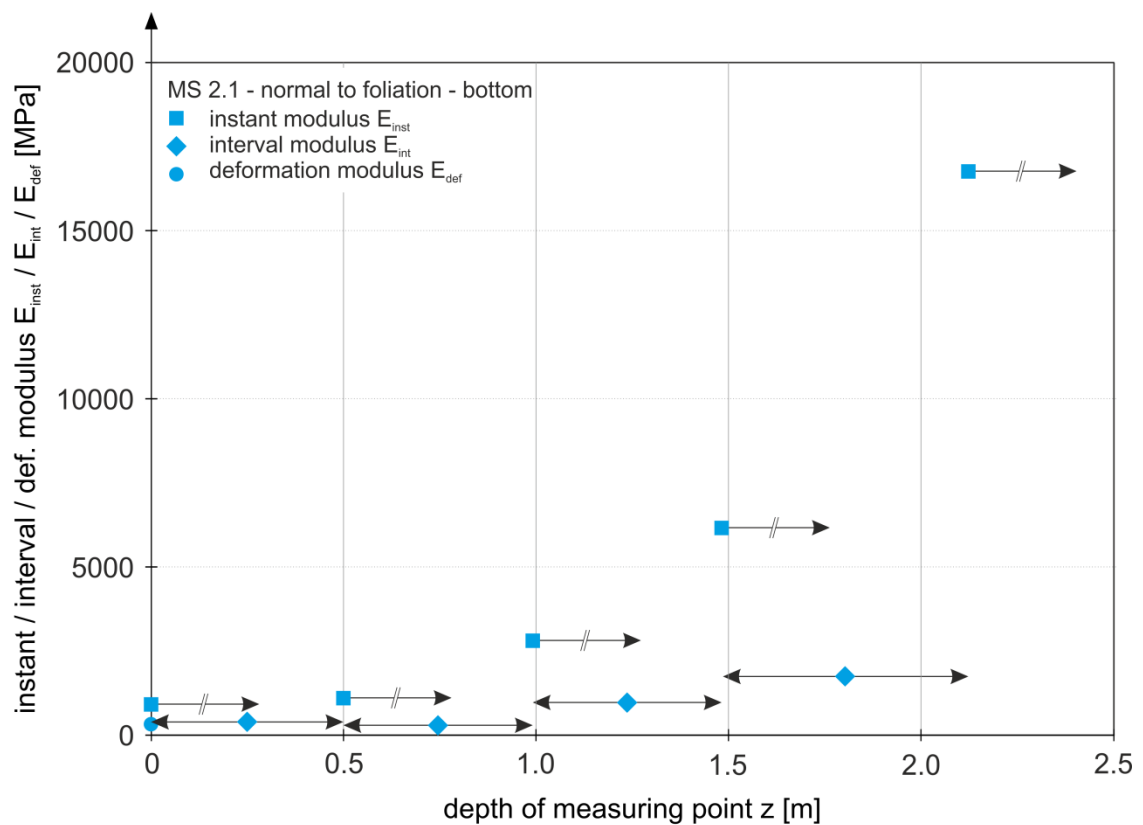


Figure 38: Evaluated moduli (instant, interval and deformation modulus) for MS 2.1 – normal to the foliation – *bottom*.

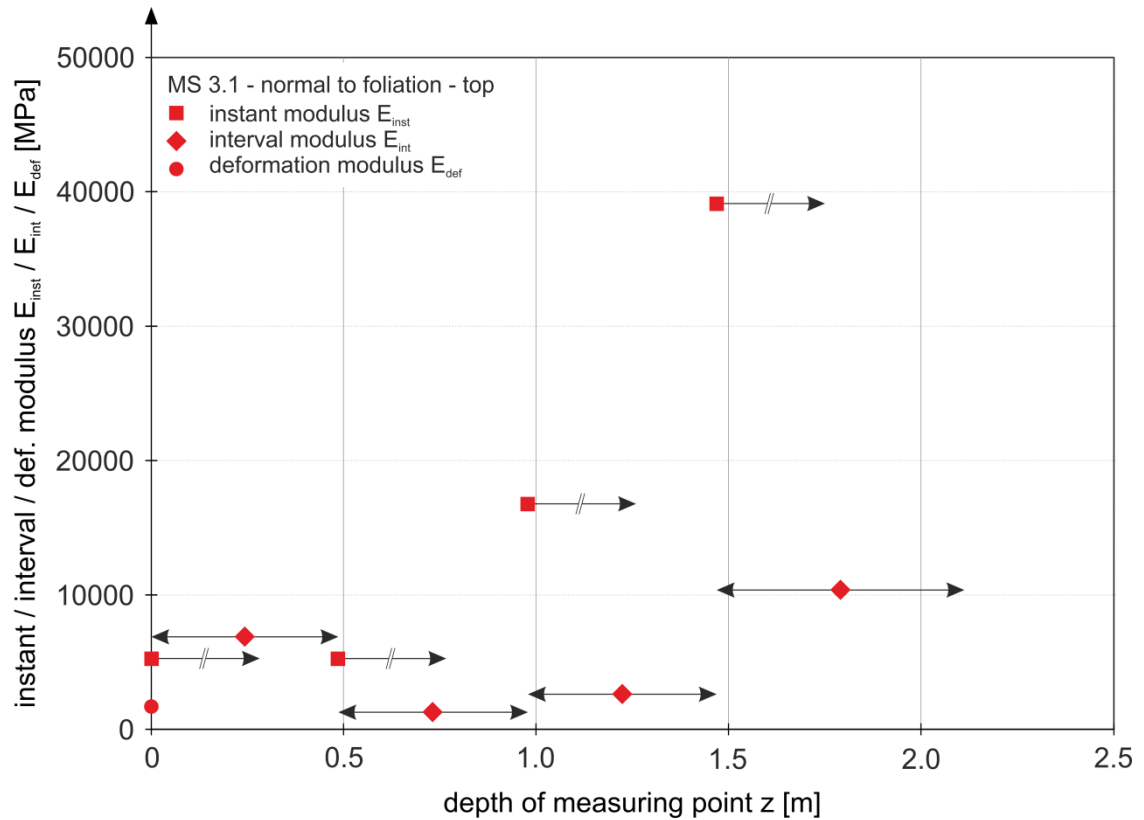


Figure 39: Evaluated moduli (instant, interval and deformation modulus) for MS 3.1 – normal to the foliation – *top*.

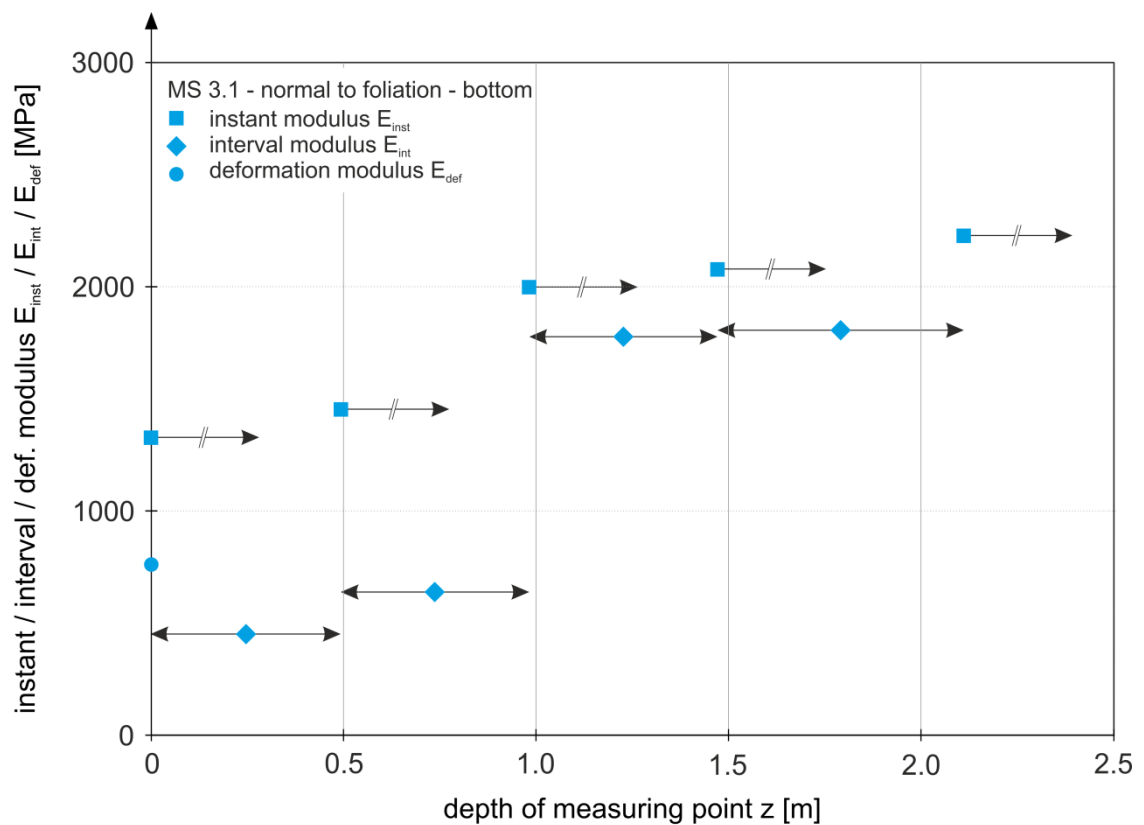


Figure 40: Evaluated moduli (instant, interval and deformation modulus) for MS 3.1 – normal to the foliation – *bottom*.

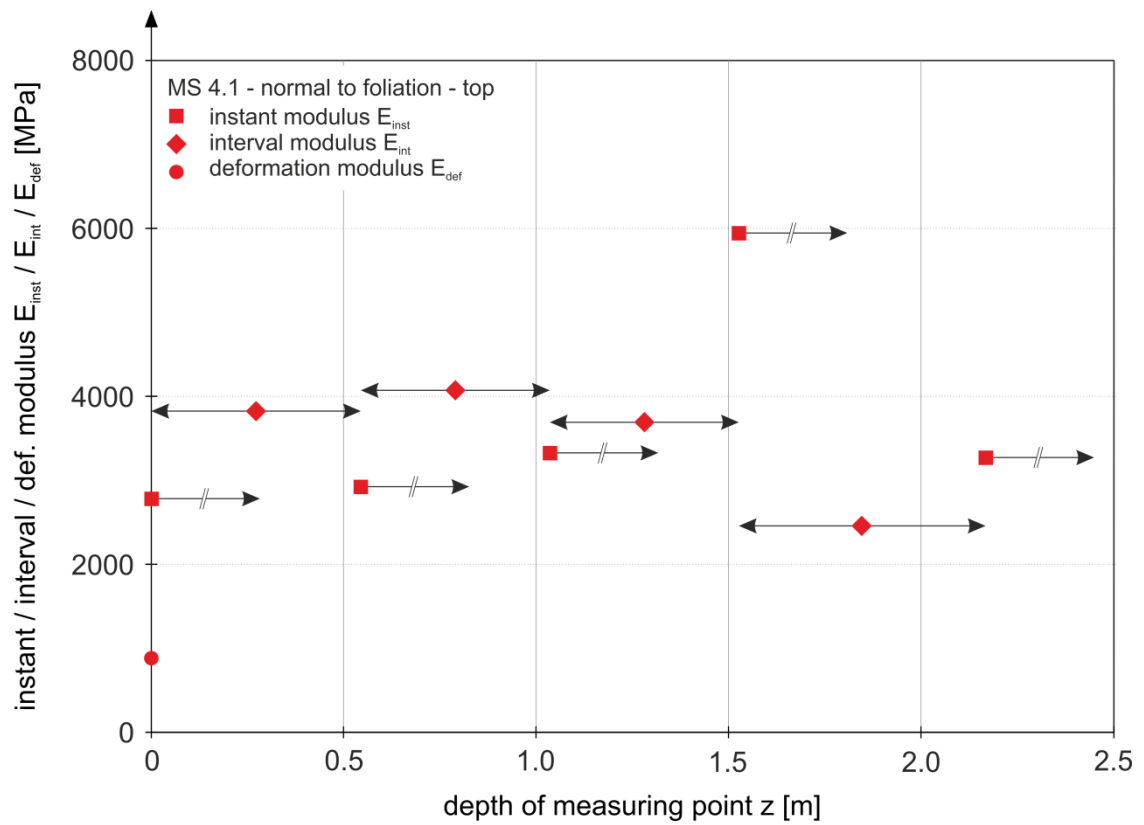


Figure 41: Evaluated moduli (instant, interval and deformation modulus) for MS 4.1 – normal to the foliation – *top*.

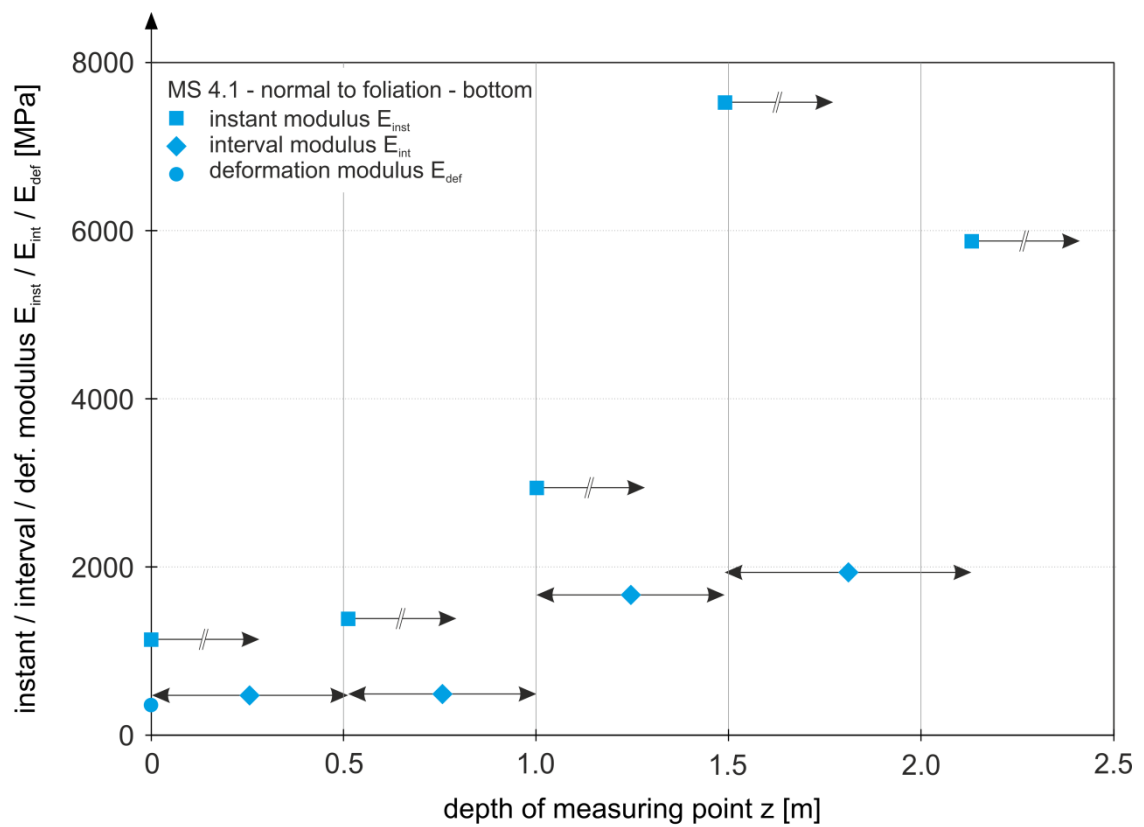


Figure 42: Evaluated moduli (instant, interval and deformation modulus) for MS 4.1 – normal to the foliation – *bottom*.

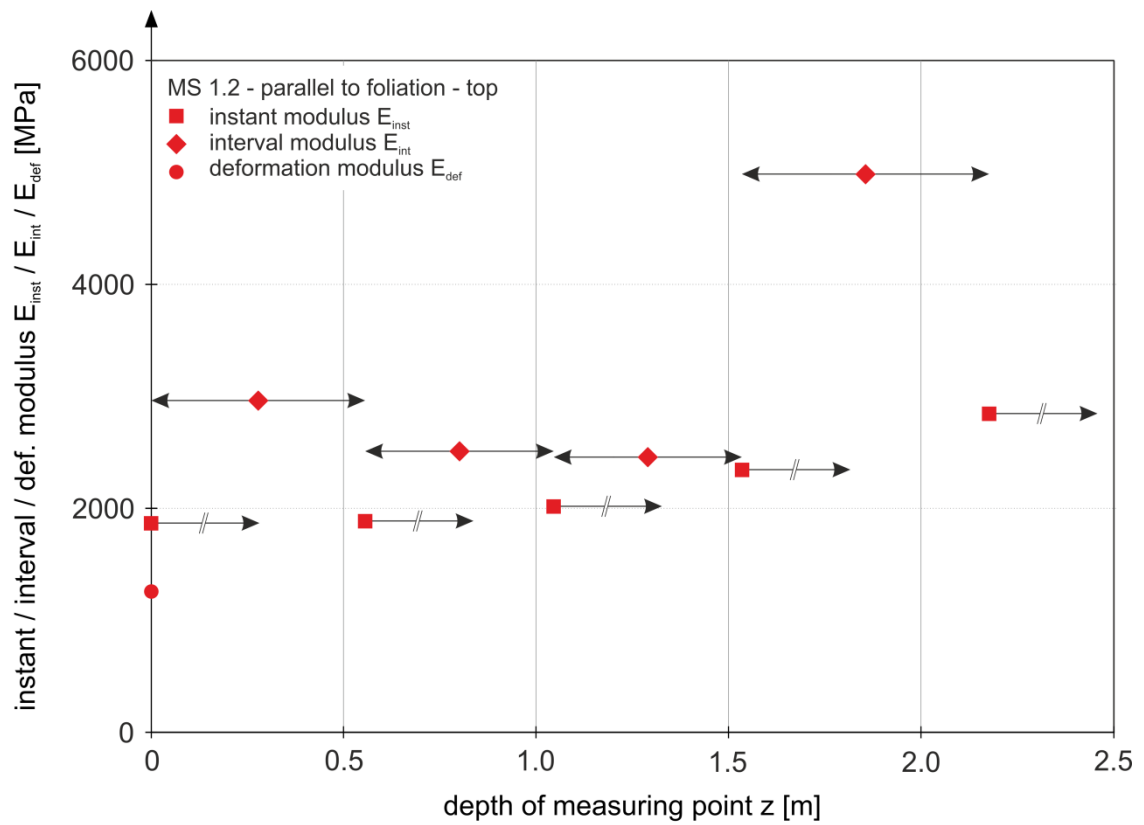


Figure 43: Evaluated moduli (instant, interval and deformation modulus) for MS 1.2 – parallel to the foliation – *top*.

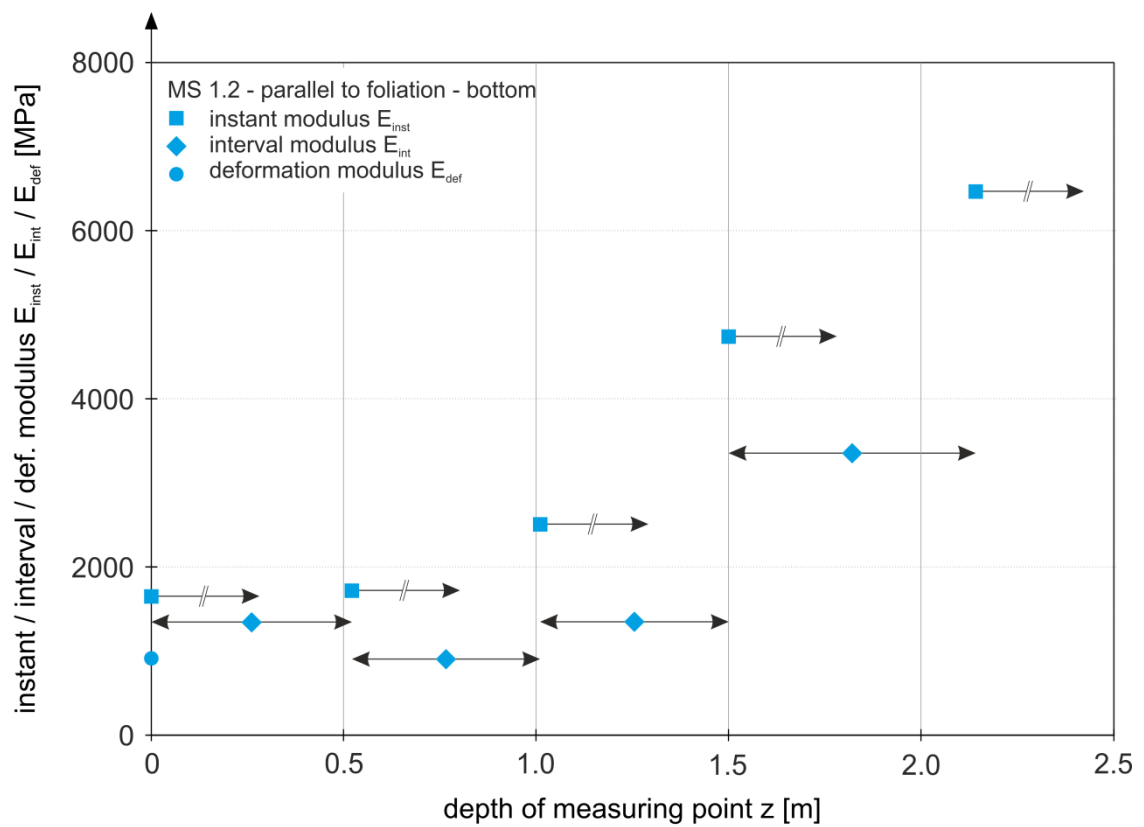


Figure 44: Evaluated moduli (instant, interval and deformation modulus) for MS 1.2 – parallel to the foliation – *bottom*.

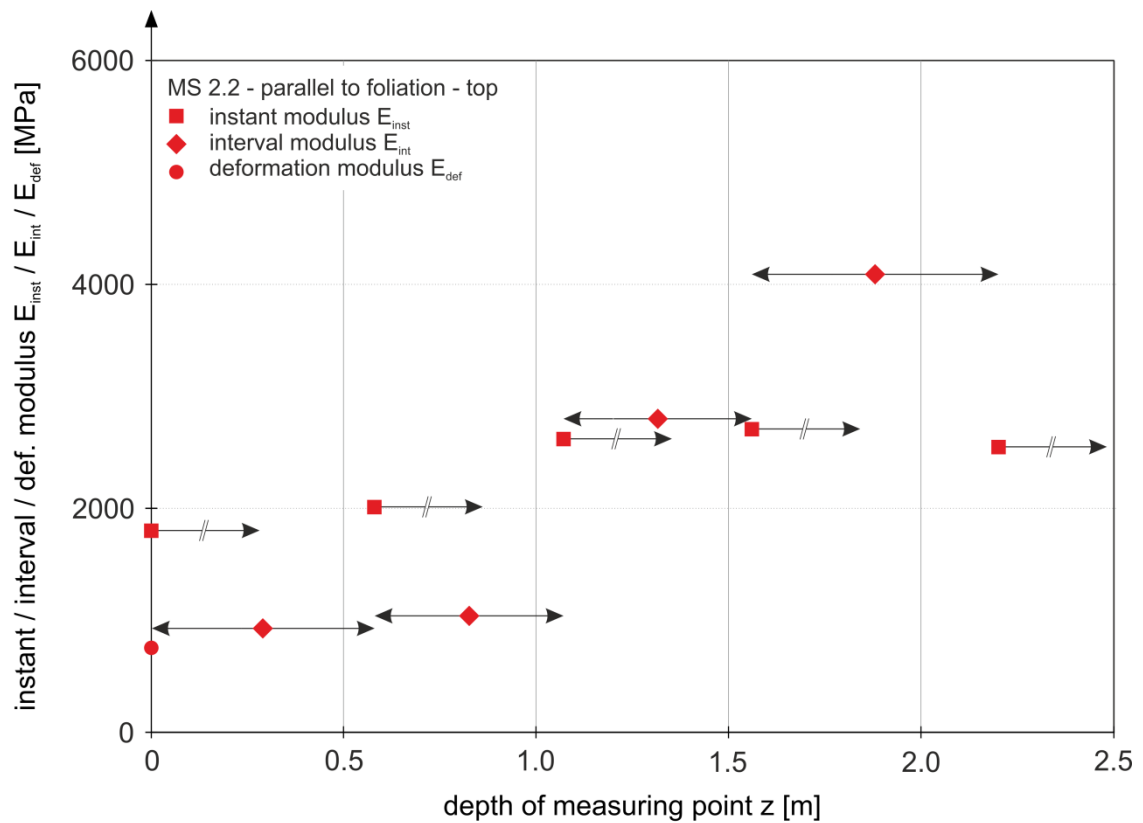


Figure 45: Evaluated moduli (instant, interval and deformation modulus) for MS 2.2 – parallel to the foliation – *top*.

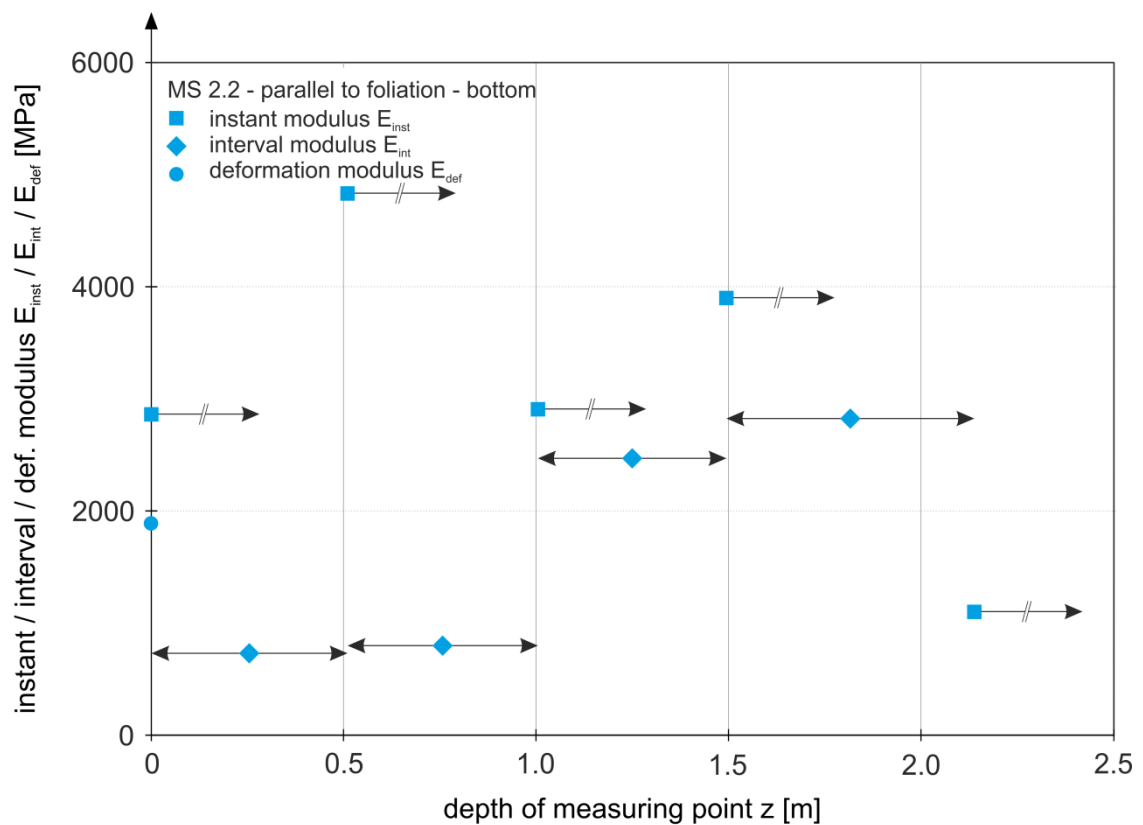


Figure 46: Evaluated moduli (instant, interval and deformation modulus) for MS 2.2 – parallel to the foliation – *bottom*.



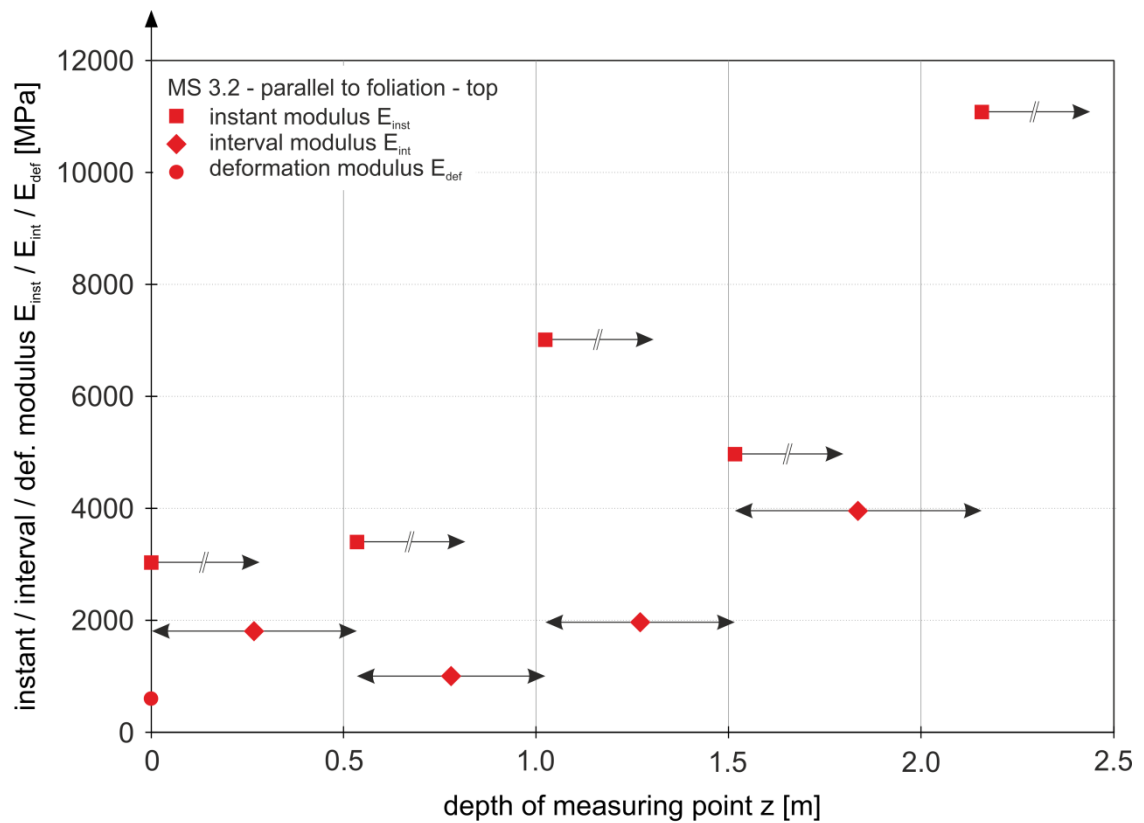


Figure 47: Evaluated moduli (instant, interval and deformation modulus) for MS 3.2 – parallel to the foliation – *top*.

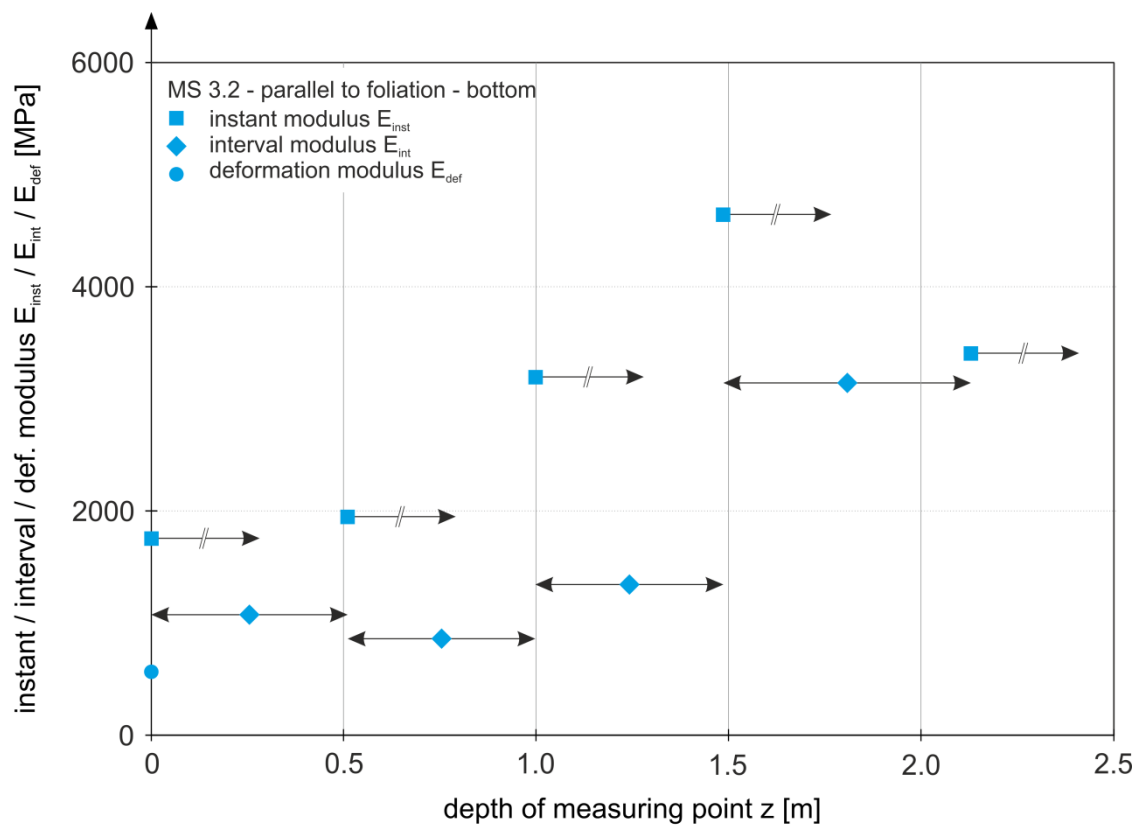


Figure 48: Evaluated moduli (instant, interval and deformation modulus) for MS 3.2 – parallel to the foliation – *bottom*.

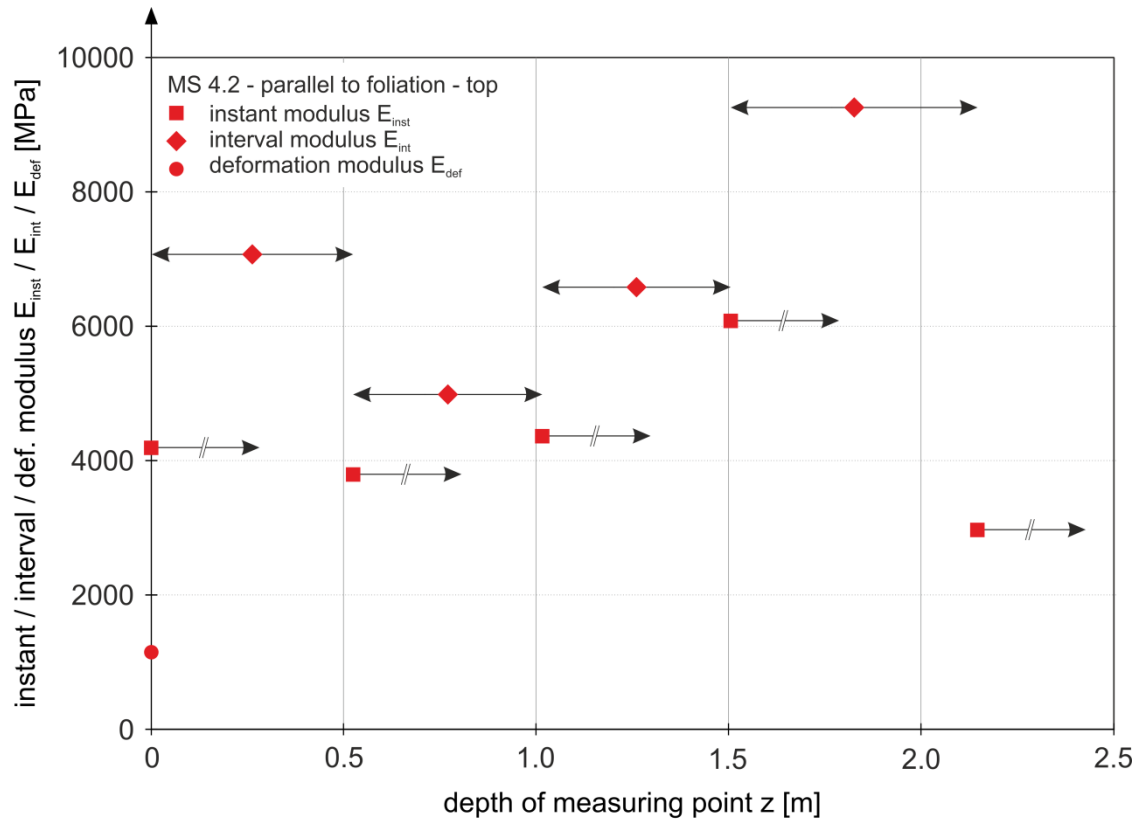


Figure 49: Evaluated moduli (instant, interval and deformation modulus) for MS 4.2 – parallel to the foliation – *top*.

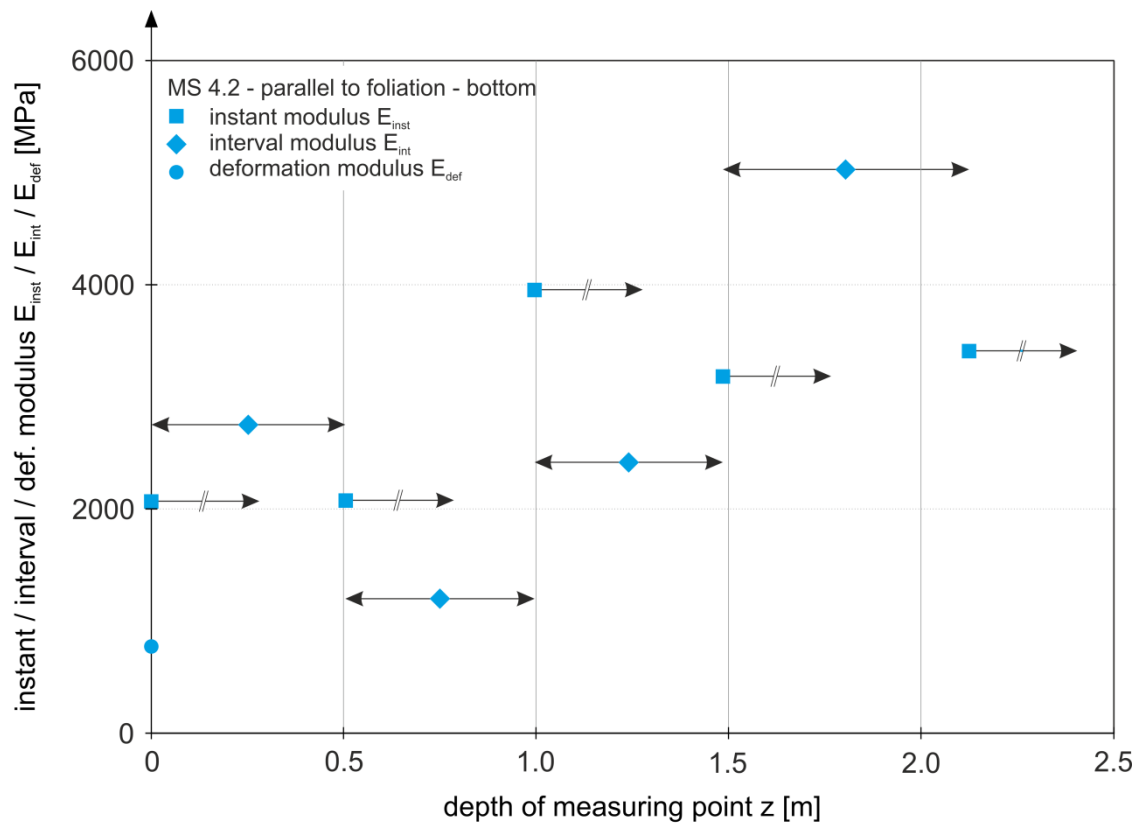


Figure 50: Evaluated moduli (instant, interval and deformation modulus) for MS 4.2 – parallel to the foliation – *bottom*.

The influence of the geological conditions on the deformability of the rock mass is clearly shown if the evaluated moduli are depicted as frequency distribution plots. Figure 51 shows the frequency distribution for the determined interval moduli at depth  $z_0$ . Depicted therein are the evaluated moduli for each loading-unloading cycle. Fitting a lognormal distribution to the values yields a modal value for moduli normal to foliation of about 1355 MPa, while the moduli parallel to foliation feature a modal value of approximately 1700 MPa. The determined higher values for the tests parallel to the foliation (by a factor of  $\sim 1.3$ ) can be deemed as plausible and have been expected. The anisotropy of the deformability is even more pronounced for the interval moduli, which is shown in Figure 52. A lognormal distribution for tests normal to the foliation yields a modal value of about 700 MPa. The statistical evaluation for the tests which were performed parallel to the foliation, exhibits a modal value of approximately 1300 MPa, which is about 1.9 times higher than the modal value for tests normal to the foliation.

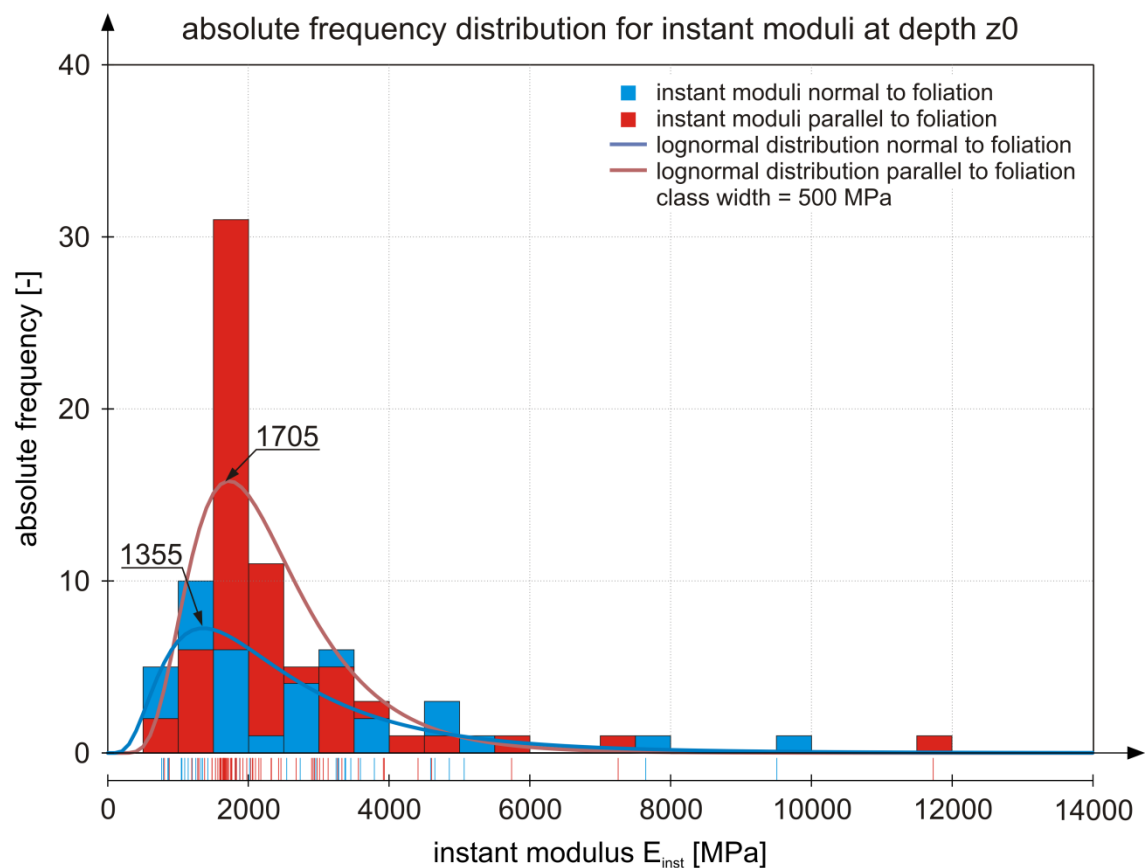


Figure 51: Frequency distribution plot for evaluated instant moduli at depth  $z_0$  normal and parallel to the foliation.

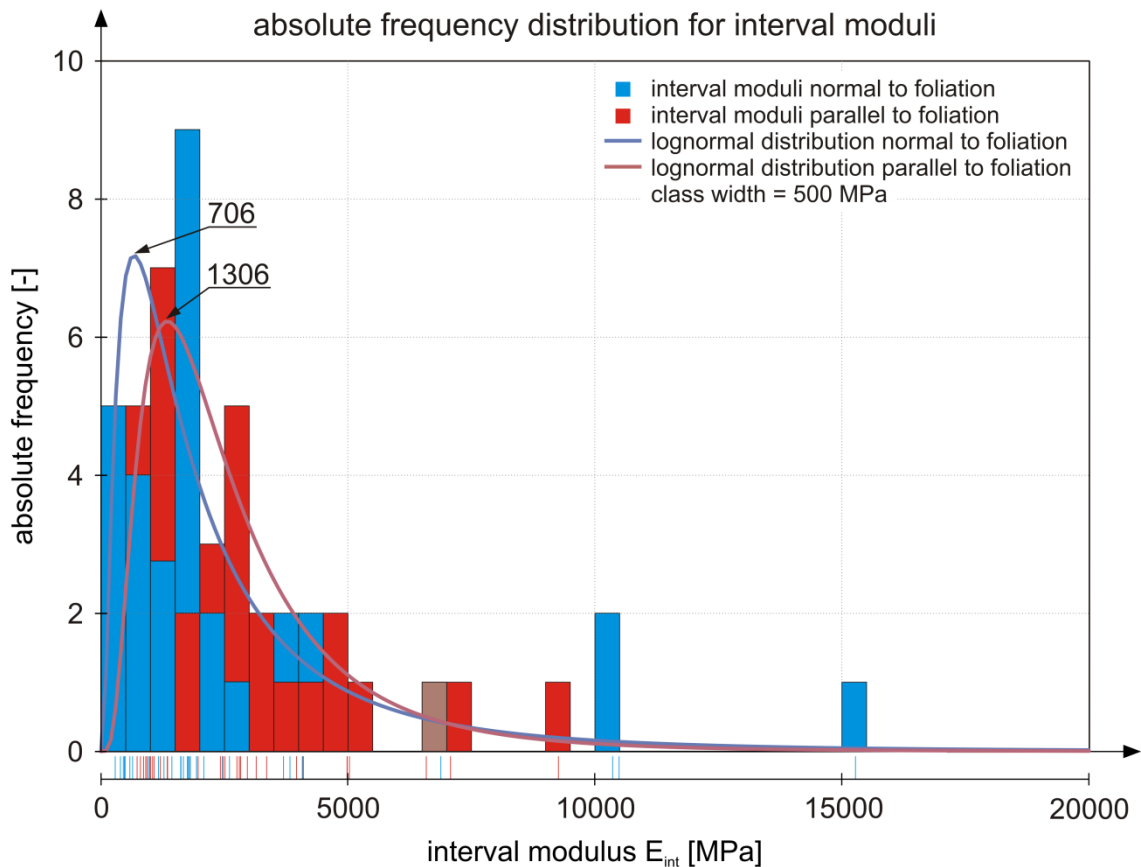


Figure 52: Frequency distribution plot for evaluated interval moduli normal and parallel to foliation.

After performing the plate load tests drill cores were taken at the measuring sections. The drillings were placed in the center of the load plate and were conducted in radial direction, according to the loading direction of the plate load tests. The evaluated moduli are qualitatively in good agreement with the encountered rock from the core drillings, which is exemplarily shown in Figure 53.

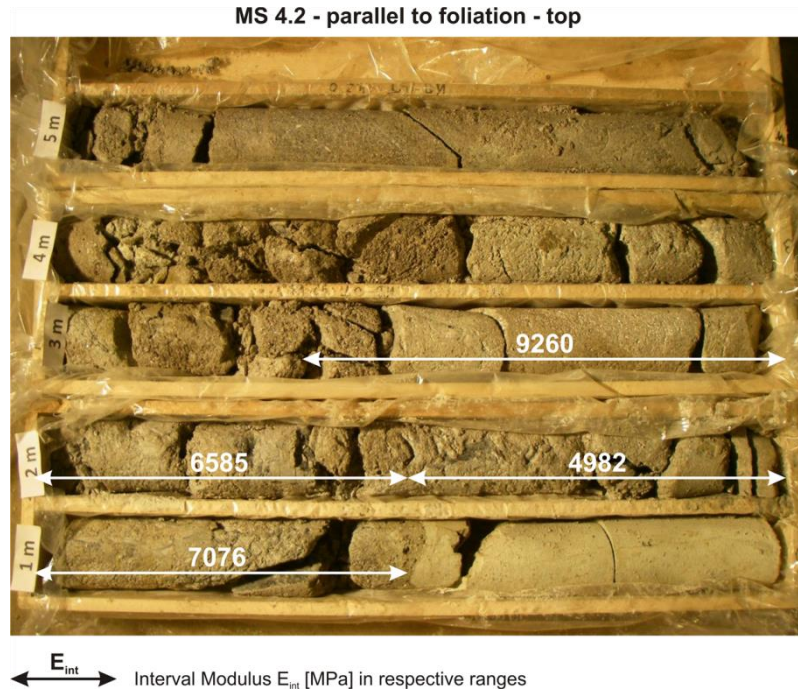


Figure 53: Core drilling taken in the test adit and allocation of determined interval moduli  $E_{int}$ , exemplarily shown for MS 4.2 – top.

Table 2: Compilation of depths of extensometer points for each measuring section.

		Depth [m]				
		z0	z1	z2	z3	z4
MS 1.1	top	0.000	0.466	0.955	1.450	2.089
	bottom	0.000	0.508	0.998	1.489	2.129
MS 1.2	top	0.000	0.557	1.047	1.536	2.179
	bottom	0.000	0.522	1.011	1.502	2.144
MS 2.1	top	0.000	0.511	1.002	1.494	2.135
	bottom	0.000	0.499	0.991	1.482	2.123
MS 2.2	top	0.000	0.581	1.073	1.562	2.203
	bottom	0.000	0.510	1.006	1.496	2.140
MS 3.1	top	0.000	0.485	0.978	1.469	2.113
	bottom	0.000	0.493	0.983	1.473	2.113
MS 3.2	top	0.000	0.535	1.025	1.518	2.158
	bottom	0.000	0.511	0.999	1.488	2.132
MS 4.1	top	0.000	0.545	1.037	1.528	2.170
	bottom	0.000	0.512	1.003	1.492	2.134
MS 4.2	top	0.000	0.526	1.017	1.507	2.149
	bottom	0.000	0.505	0.997	1.486	2.125

## **4.2 Laboratory tests**

Beside the in-situ tests conducted in the Lavanttal fault zone an extensive laboratory testing program on artificial bimrock material was performed. The goal was to investigate the stress-strain behavior of fault material under laboratory conditions, allowing a proper definition and discrimination of influencing factors. A new testing apparatus was developed, custom-tailored to account for peculiarities and special features of faulted rock.

### **4.2.1 Large oedometer tests on artificial block-in-matrix samples**

Current laboratory techniques for the determination of Young's moduli or constrained moduli are afflicted with restrictions: Typically in rock mechanics laboratories, the Young's modulus is determined on drill cores. For fault material, this test procedure is not applicable in many cases, due to the poor quality of the material, which leads to disintegration of drill cores. Standard oedometer tests, as characteristically used for soil testing are not adequate due to the small sample size and relatively low stress levels. Hence, those conditions do not reflect the stress conditions found at tunnel level. Standard oedometer tests do not allow obtaining reliable data about the stress dependency of moduli at high depths. In order to circumvent the shortcomings mentioned above, a large oedometer test apparatus was developed within the scope of this research.

Large oedometer tests were performed on artificial block-in-matrix rocks, in order to study the influence of block orientation and block proportion on the overall deformation properties. Another important point of interest was to study and gain knowledge about the stress dependency of moduli, which is particularly pronounced in weak rocks.

#### **4.2.1.1 Test apparatus**

The design of the large oedometer test apparatus (Figure 54) derives from the standard Cassagrande oedometer, paying respect to the state-of-the-art in all its aspects. The apparatus allows the measurement of the actual axial force imposed on the specimen, the vertical and lateral displacements, and the friction force between oedometer ring and specimen. A detailed description of the large oedometer test apparatus can be found in Wieser et al. (2012).



Figure 54: Large oedometer apparatus.

The apparatus consists of following components:

- I. Oedometer ring
- II. Base plate
- III. Two filter plates
- IV. Head plate

The large oedometer has an inner diameter of 300 mm, and a maximum height of 311 mm. The main dimensions are shown in Figure 55 and Figure 56. Dry and saturated specimen with a height between 60 mm and 100 mm for drained conditions (assembly with filter plates), and a height up to 200 mm for undrained conditions (assembly without filter plates) can be tested.

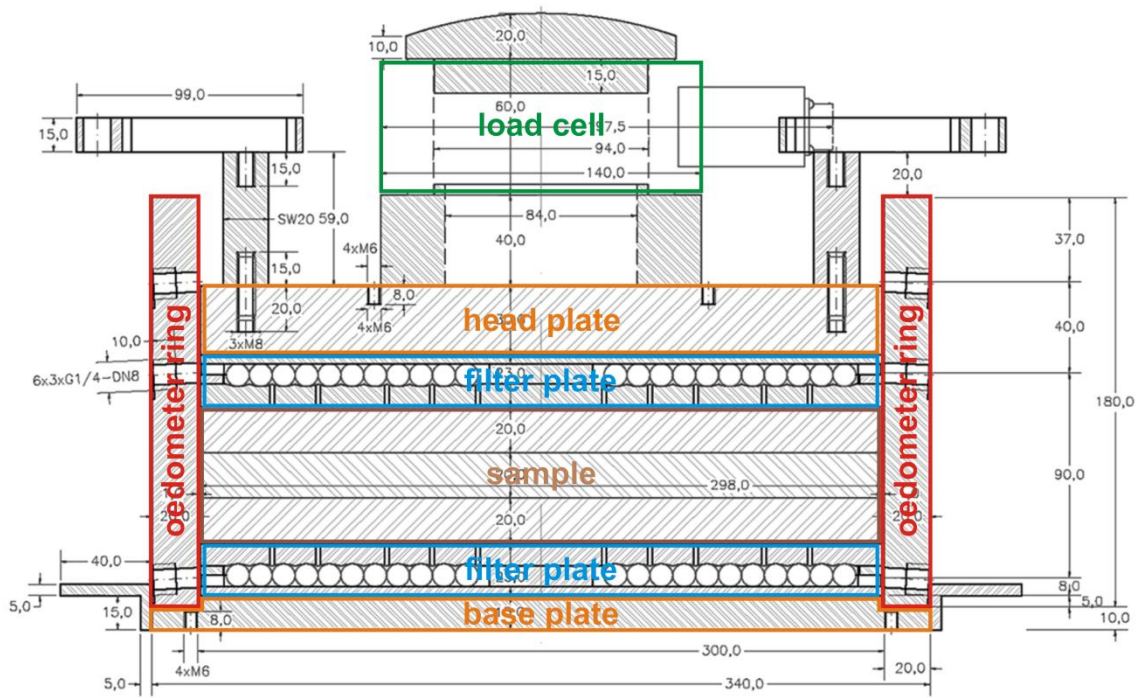


Figure 55: Large oedometer – cross section.

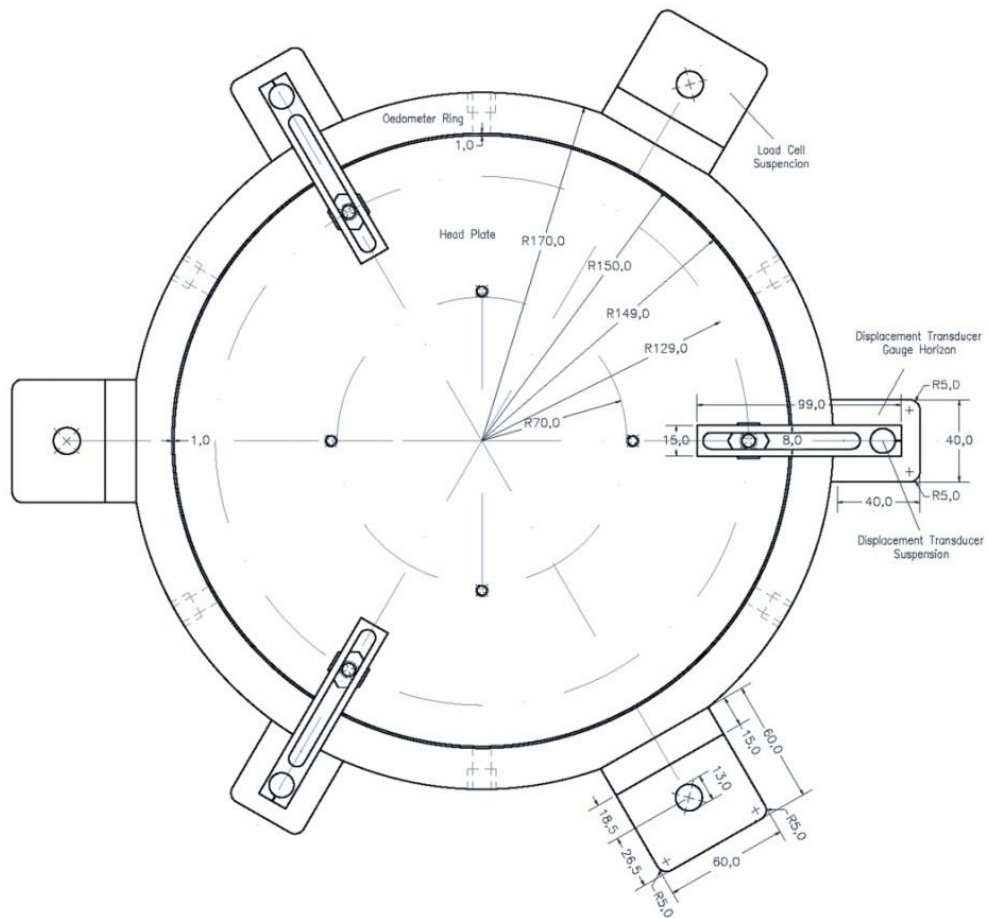


Figure 56: Large oedometer – plan view.



### 4.2.1.2 Sample preparation

For the matrix material a mixture of cement, finely crushed limestone and water was used. The used cement was Portland cement CEM II 32.5. The mixing proportion of aggregates features a ratio of 5 parts per weight finely crushed limestone, 1 part per weight cement and 1.8 parts per weight water. Several trial tests, featuring triaxial and uniaxial tests, were conducted to gain information about the strength properties of the matrix. The trial tests yielded a uniaxial compressive strength after seven days of approximately 2 – 3 MPa, a Young's modulus of 4000 MPa, and a Poisson's ratio of about 0.3.

The blocks were made of cement stone and feature an ellipsoidal shape, slightly tapered towards the block depth (Figure 57). The length is 87/98 mm (in z-direction), the width is 35/43 mm (in x-direction) and the depth is 14 mm (in y-direction). Portland cement type CEM II 42.5 was used and the water to cement ratio (W/C) was set to 0.4. The blocks were prefabricated in silicone casting molds. Triaxial trial tests were performed on the block material to determine the strength and deformation properties, yielding a uniaxial compressive strength of 37 MPa after seven days of curing time, a friction angle of 30° and a Young's modulus of about 16,000 MPa. Compared to the matrix material the strength ratio (strength of block material / strength of matrix material) amounts to the factor of ~ 15, and the deformability ratio is about 4 (Young's modulus of block material / Young's modulus of matrix material).

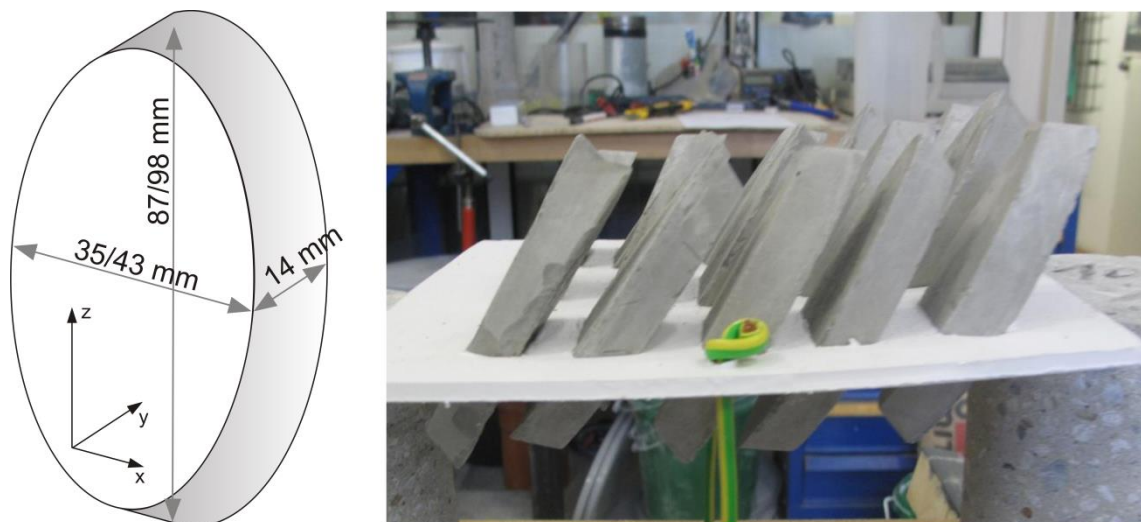


Figure 57: Sketch of block with dimensions (left) and fabricated blocks after stripping (right).

The artificial block-in-matrix samples were fabricated in custom-tailored shuttering. The formwork consisted of a wooden base plate, a tube made of multi-layered highly stable paper and cardboard sheeting. To achieve the shuttering maintaining its circular shape wooden slats were screwed to the base plate, holding the shuttering in place.

All specimens featured a diameter of 300 mm. The initial height was between 128 mm and 156 mm. Three different block arrangements in three different block proportions, as well as a pure matrix and pure block sample were tested. The specified block arrangements were (Figure 58, see Figure 57 for used block coordinate system):

- Blocks horizontally aligned (loading in y-direction of blocks)
- Blocks vertically aligned (loading in z-direction of blocks)
- Blocks twisted (loading in x-direction of blocks)

Figure 58 illustrates the block arrangement. For the sake of simplicity, the third arrangement will be called “twisted” assembly in the remainder of this work.

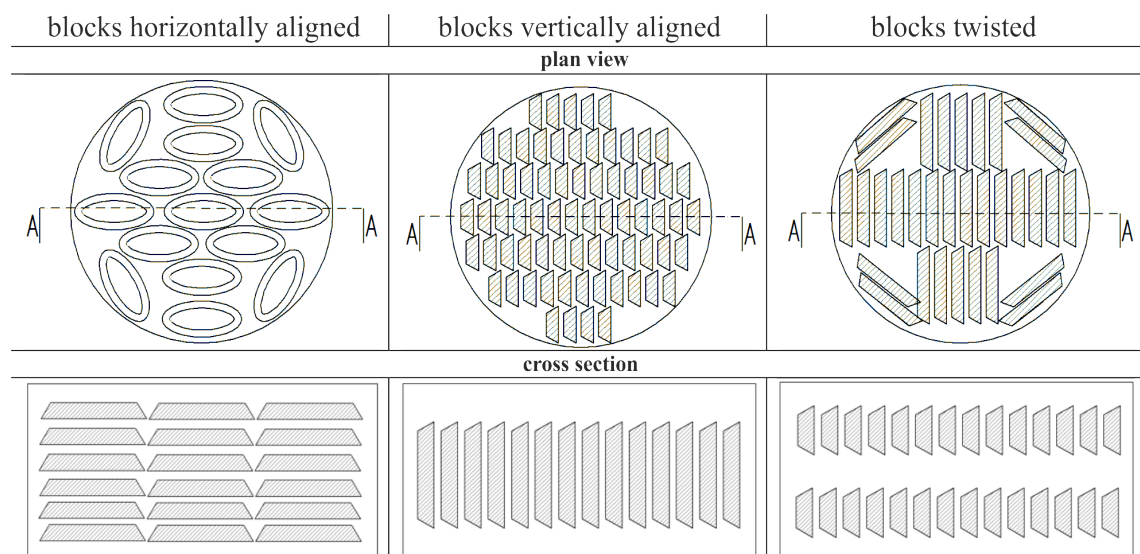


Figure 58: Different types of block alignment for large oedometer tests.

For sample preparation, the base of the formwork was filled with matrix material first. Secondly, the blocks were placed in the matrix in the intended block orientation and again covered with matrix material (Figure 59). This step was repeated layer by layer until the desired block proportion was reached. Attention was paid that the blocks were evenly distributed over the whole sample height. The blocks were fabricated at least one month ahead of sample preparation, hence featuring 28-day strength. The samples were left to cure for seven days at room temperature.



Figure 59: Sample preparation for large oedometer tests; blocks horizontally aligned (left), blocks vertically aligned (middle), blocks twisted (right).

Fourteen specimens, which differ in block proportion and block orientation, were fabricated and tested, as shown in Table 3.

Table 3: Performed oedometer tests.

sketch of block alignment (cross section)	block proportion	number of tested samples
	100% matrix	1
	100% block	1
	21%	1
	41%	1
	44%	1
	58%	1
	21%	1
	24%	1
	30%	1
	40%	1
	22%	1
	31%	1
	33%	1
	42%	1

### 4.2.1.3 Test set-up and instrumentation

A compression test machine with a maximum loading capacity of 3000 kN was utilized as loading device. The load is transmitted by a hydraulic loading actuator with a maximum stroke of 100 mm. The apparatus is controlled by software, allowing customized test procedures. The load transmitted by the compression test machine to the specimen is measured by a load cell with a nominal load of 2000 kN (type HBM C6B), situated on the head plate. The floating ring configuration was used for the tests, allowing the determination of friction forces between oedometer ring surface and specimen. The measurement of friction forces was accomplished by three load cells with a nominal load of 50 kN (type HBM C9B). The load cells are fixed to a suspension ring flap and loaded by a plunger, which is connected to the oedometer ring. For the determination of vertical displacements three inductive displacement transducers (type HBM WA-20) were used. They were fixed with suspension clamps on the head plate, and the measurement reference level is set on gauge horizons on the base plate. The reason for utilizing three displacement transducers was to account for potentially occurring differential displacements, due to the large sample diameter. Data acquisition was carried out by a measuring amplifier and a laptop computer.

### 4.2.1.4 Test procedure

The samples were repeatedly loaded and unloaded. Each loading and unloading cycle was kept constant until displacement rates became almost zero. After each loading-unloading loop the load was increased to a higher level, which was in most cases the double amount of the previous level. Table 4 gives an overview of the basic planned main load levels. A graphical representation of actually performed load levels is given in Figure 60 through Figure 63 for the different block arrangements as force versus time diagrams.

Table 4: Overview of applied load levels.

Load level	force (approximately)	remarks
load level 1	210 kN	Load was increased in three steps (70 kN – 140 kN – 210 kN) without unloading.
load level 2	500 kN	This load level applies a stress state which equals roughly the uniaxial compressive strength of the matrix.
load level 3	1000 kN	
load level 4	1500 kN	Applied at samples with high block proportion.

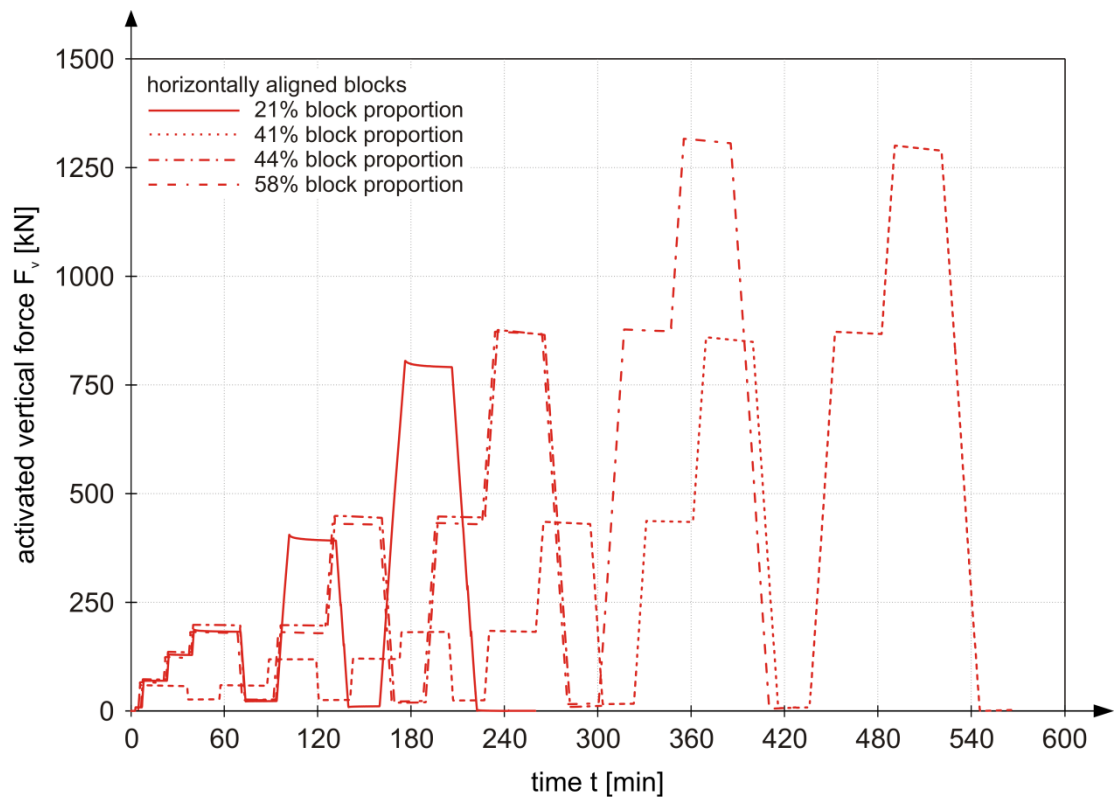


Figure 60: Force vs. time diagram (performed loading scheme) for samples with horizontally aligned blocks.

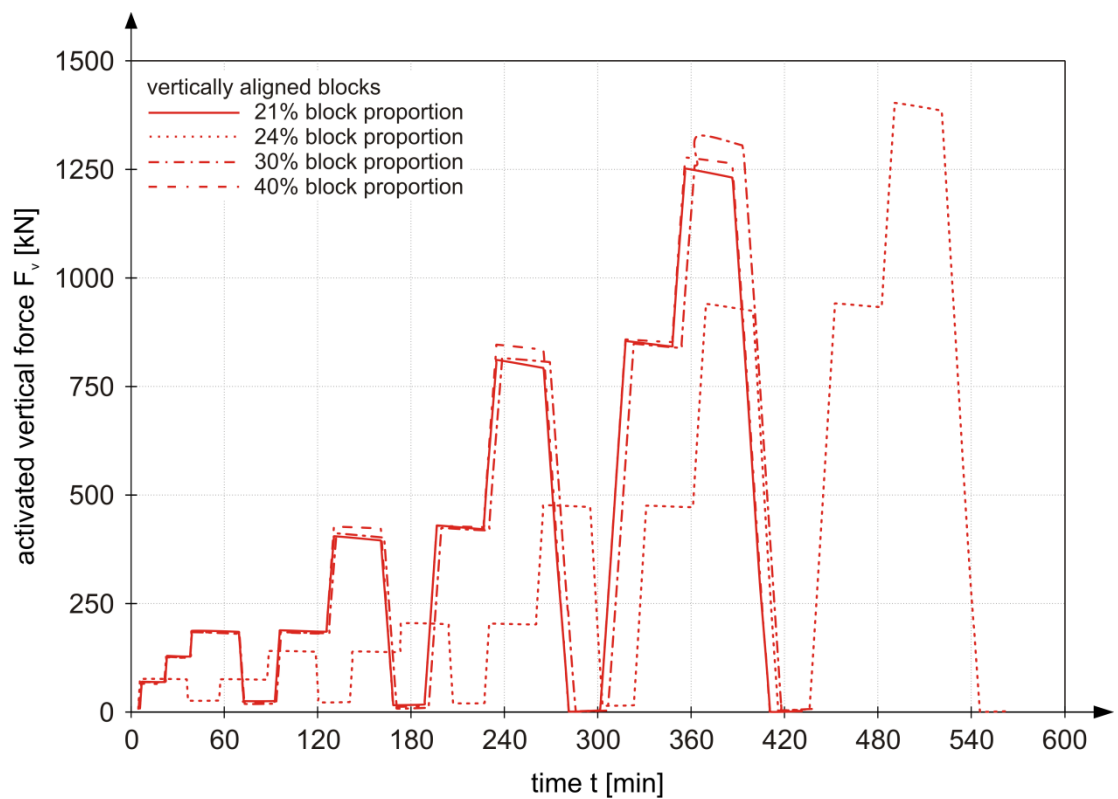


Figure 61: Force vs. time diagram (performed loading scheme) for samples with vertically aligned blocks.

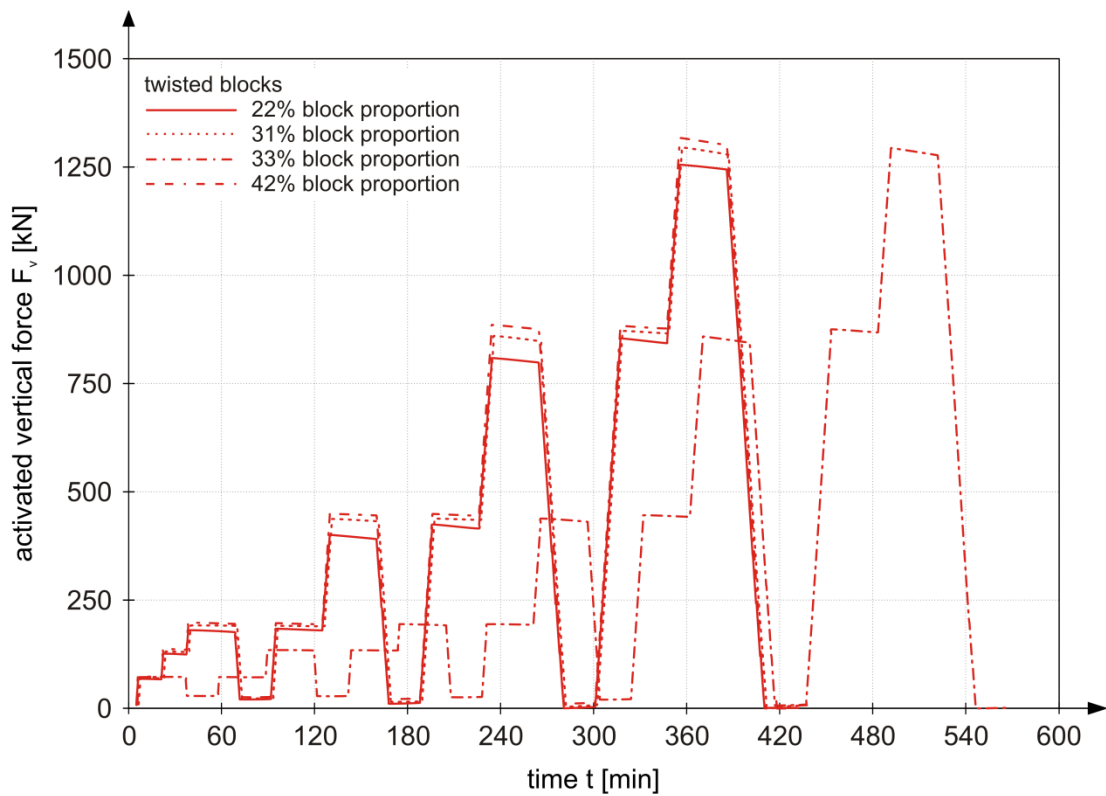


Figure 62: Force vs. time diagram (performed loading scheme) for samples with twisted blocks.

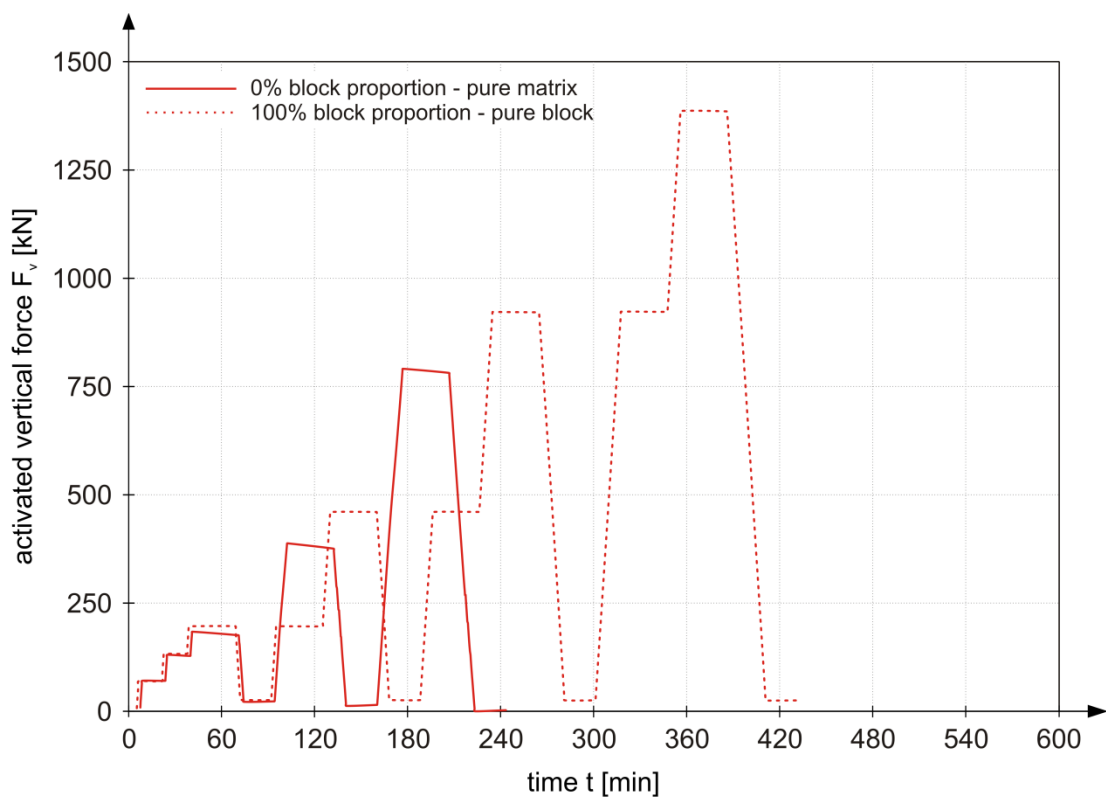


Figure 63: Force vs. time diagram (performed loading scheme) for pure matrix and pure block samples.

### 4.2.1.5 Data evaluation

The friction force between oedometer ring and sample, which is the sum of measured force of the three load cells bearing the oedometer ring, was subtracted from the measured axial force, yielding the effective axial force acting on the specimen.

After reaching the desired load level, the load was kept constant for a certain time period as mentioned in Chapter 4.2.1.4. During this period, vertical displacements increased due to time dependent creep and rearrangement processes in the sample. At the same time it was observed that the frictional forces increased which was evidenced in a constant increase of the measured load of the three load cells on which the oedometer ring rested. This implies that the sample tried to evade the vertical loading by lateral extension, hence increasing the frictional force between sample and oedometer ring. The effective load (which is further called activated vertical load or stress, respectively) is the difference between the measured axial force (from the load cell on the head plate) and the frictional force (sum of the small load cells bearing the oedometer ring). Hence, the effective load, acting on the sample, decreases with advancing time while keeping the axial load constant. This explains the decrease of activated vertical stress with increasing axial strain, which is depicted in the stress-strain – diagrams in Chapter 4.2.1.6.

For the determination of axial displacements the average of the three displacement transducers was calculated. Considering the initial sample height and the sample diameter, displacements are converted to axial strain and force is converted to axial stress. The starting points of each loading and unloading loop were identified and the activated axial stress and appropriate axial strain were determined. Stress-strain – diagrams were plotted and the constrained modulus ( $E_s$ ), also known as oedometer modulus, was obtained as secant modulus for each loading and unloading loop. Based on Hooke's law, Young's modulus was calculated using Equation (5):

$$E_s = E \cdot \frac{1 - \nu}{(1 + \nu) \cdot (1 - 2\nu)} \quad (5)$$

where:  $E_s$  ... oedometer modulus [MPa]  
 $E$  ... Young's modulus [MPa]  
 $\nu$  ... Poisson's ratio [-]

Poisson's ratio,  $\nu$ , was set to 0.30 for all tests, based on the results of triaxial tests on the matrix.

### 4.2.1.6 Results and discussion

A graphical representation of evaluated moduli is provided in Figure 64 through Figure 76. The lines therein indicate the sections where the moduli are determined. The moduli are evaluated as secant moduli. The solid lines represent the Young's moduli for the individual loading cycles, the dash-dotted lines indicate the unloading-moduli, while the dotted lines show the Young's moduli for the reloading loops. The results of the large oedometer tests are provided in a comprehensive manner in Appendix C (page A-5 to A-8) in Table C-1 for horizontally aligned blocks, Table C-2 for vertically aligned blocks, Table C-3 for twisted blocks, and Table C-4 for pure matrix and pure block samples, respectively.

The results of evaluated moduli for horizontally aligned blocks are depicted in Figure 64 to Figure 67. The unloading-moduli for horizontally aligned blocks feature about ten to approximately 30 times higher values than the loading-moduli. A slight hardening behavior can be observed in the unloading loops, being more pronounced for samples with higher block proportions. The ratios of unloading-moduli to reloading-moduli show values of about 1.3 to 2.0.

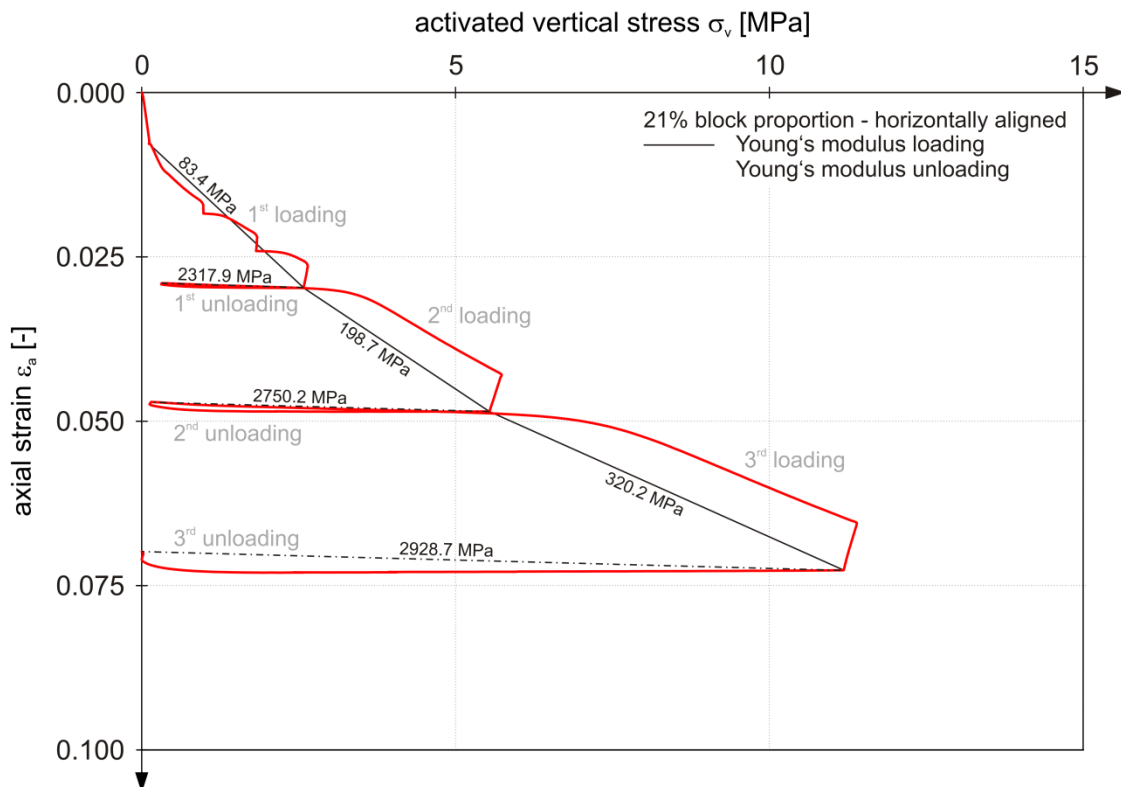


Figure 64: Evaluated moduli for 21% block proportion – horizontally aligned.



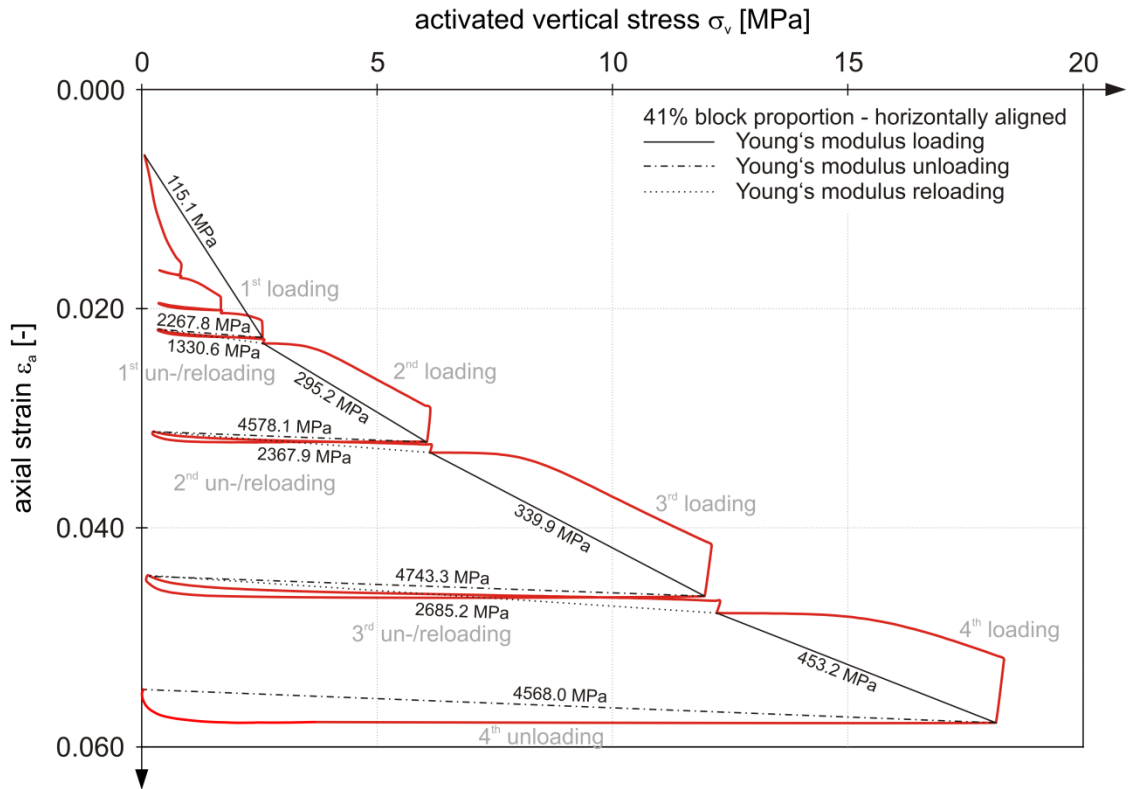


Figure 65: Evaluated moduli for 41% block proportion – horizontally aligned.

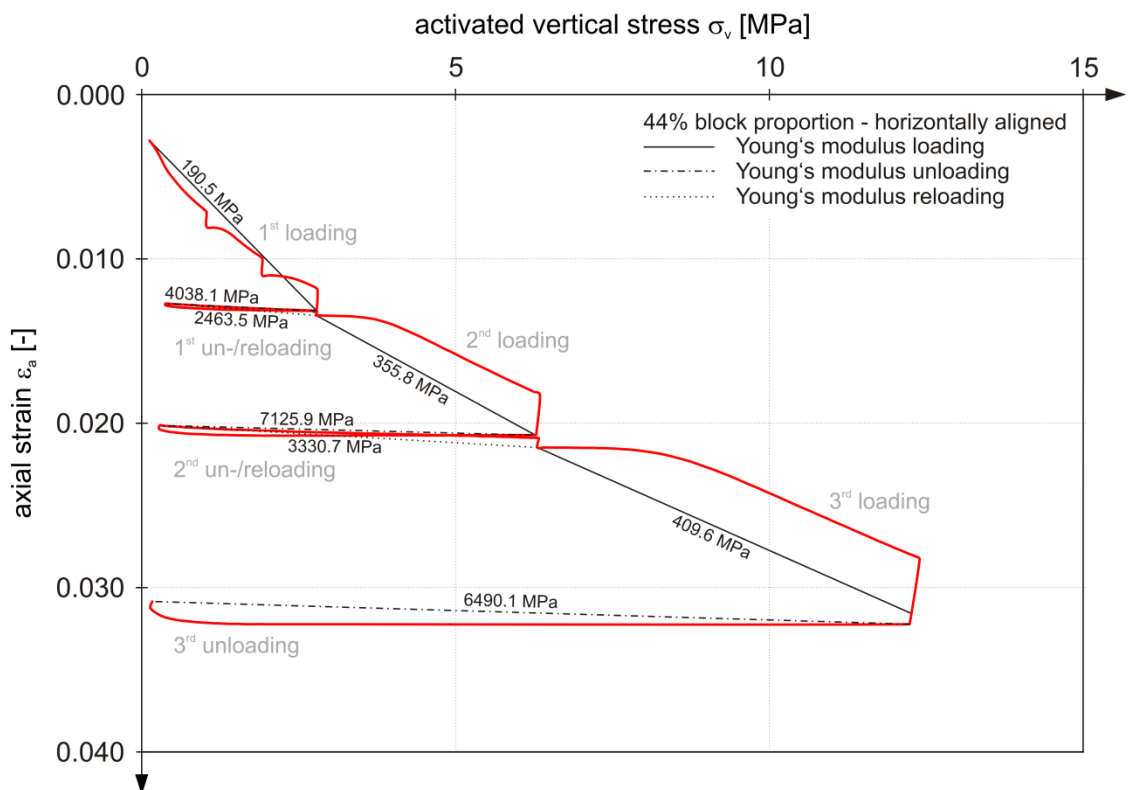


Figure 66: Evaluated moduli for 44% block proportion – horizontally aligned.

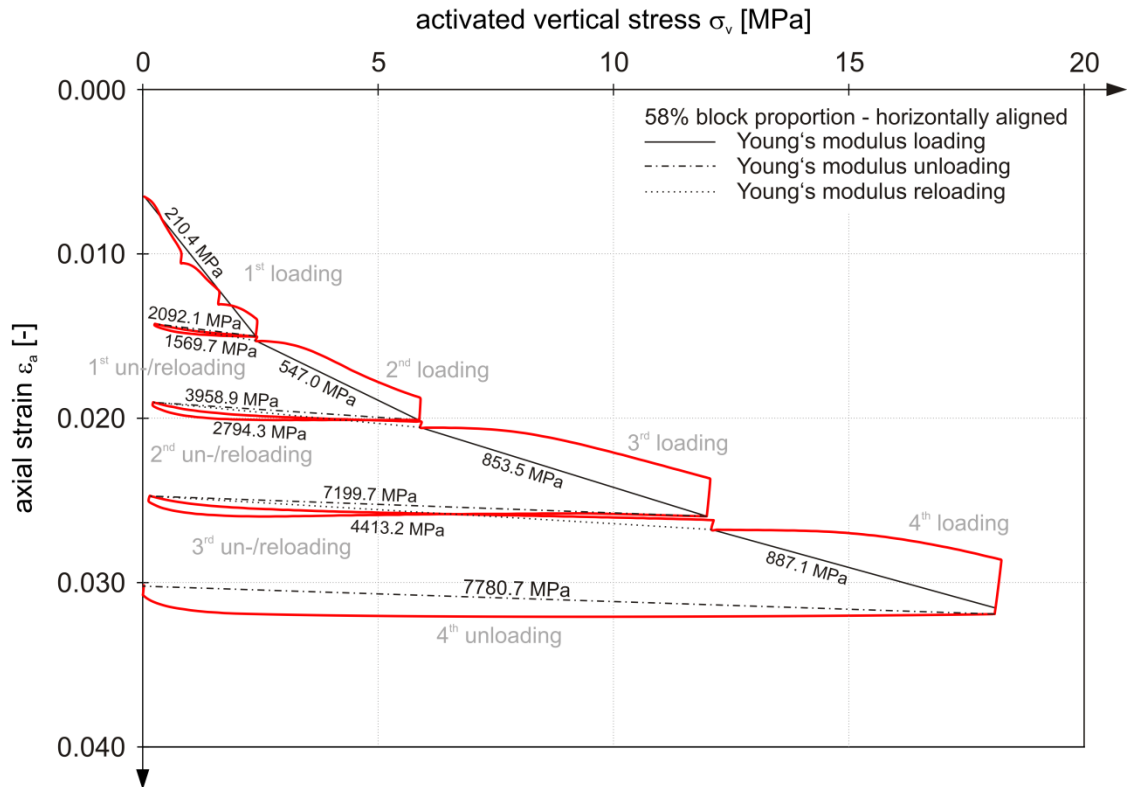


Figure 67: Evaluated moduli for 58% block proportion – horizontally aligned.

The samples with vertically aligned blocks (Figure 68 to Figure 71) show a much higher ratio of unloading-moduli to loading-moduli ( $\sim 20$  to  $50$ ), compared to the specimen with horizontally aligned blocks. On the other hand, the hardening behavior (increase of unloading-moduli with increasing stress level) is much less pronounced than in the horizontally aligned block arrangement. The ratio of unloading-moduli to reloading-moduli features approximately the same values as the samples with horizontally aligned blocks.

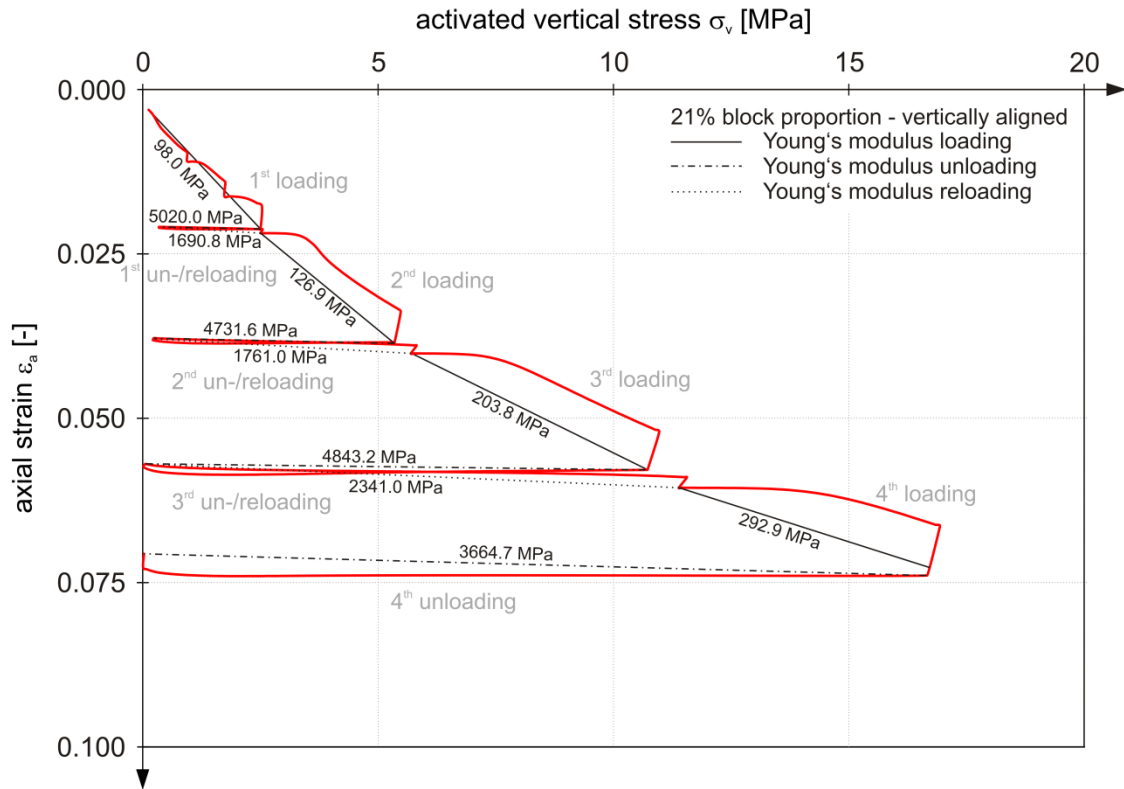


Figure 68: Evaluated moduli for 21% block proportion – vertically aligned.

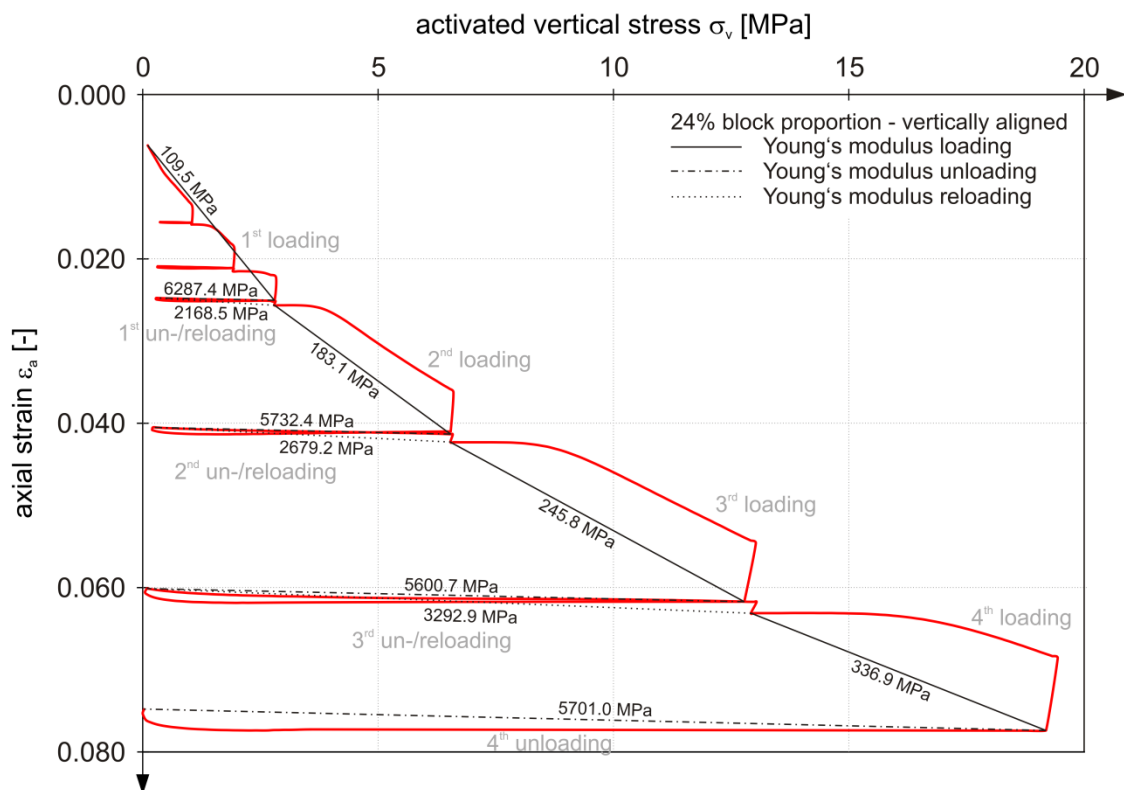


Figure 69: Evaluated moduli for 24% block proportion – vertically aligned.

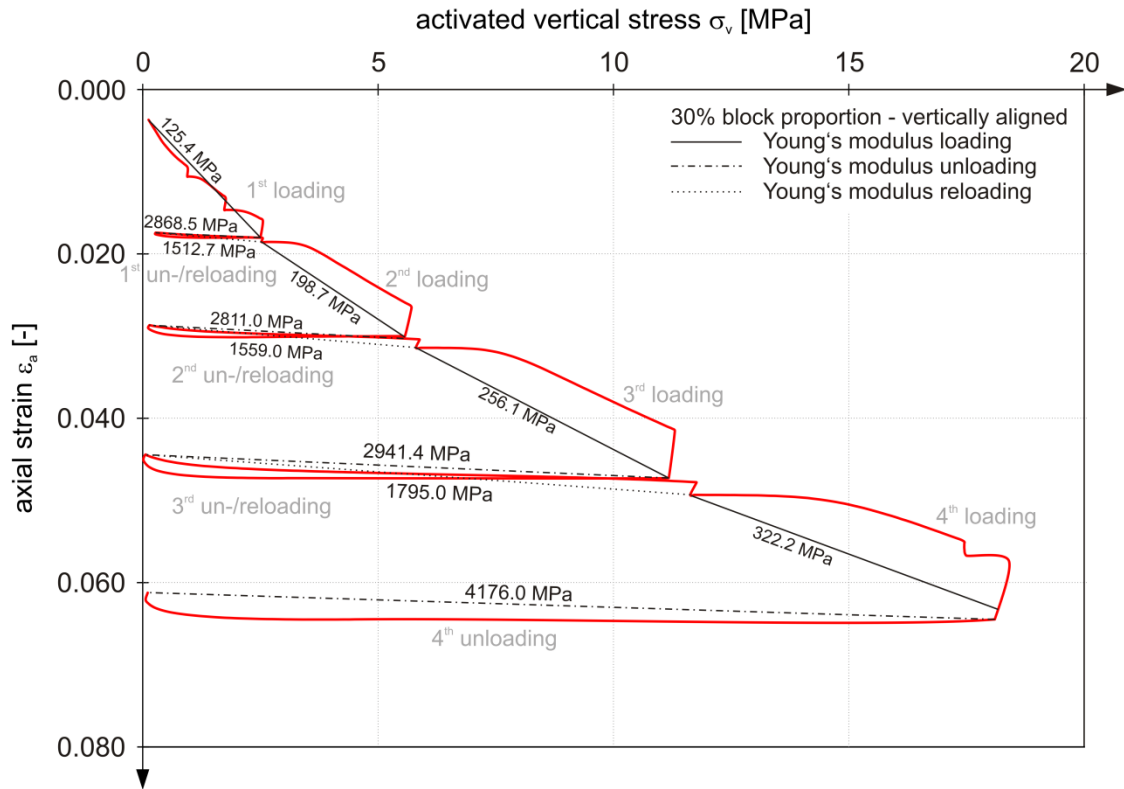


Figure 70: Evaluated moduli for 30% block proportion – vertically aligned.

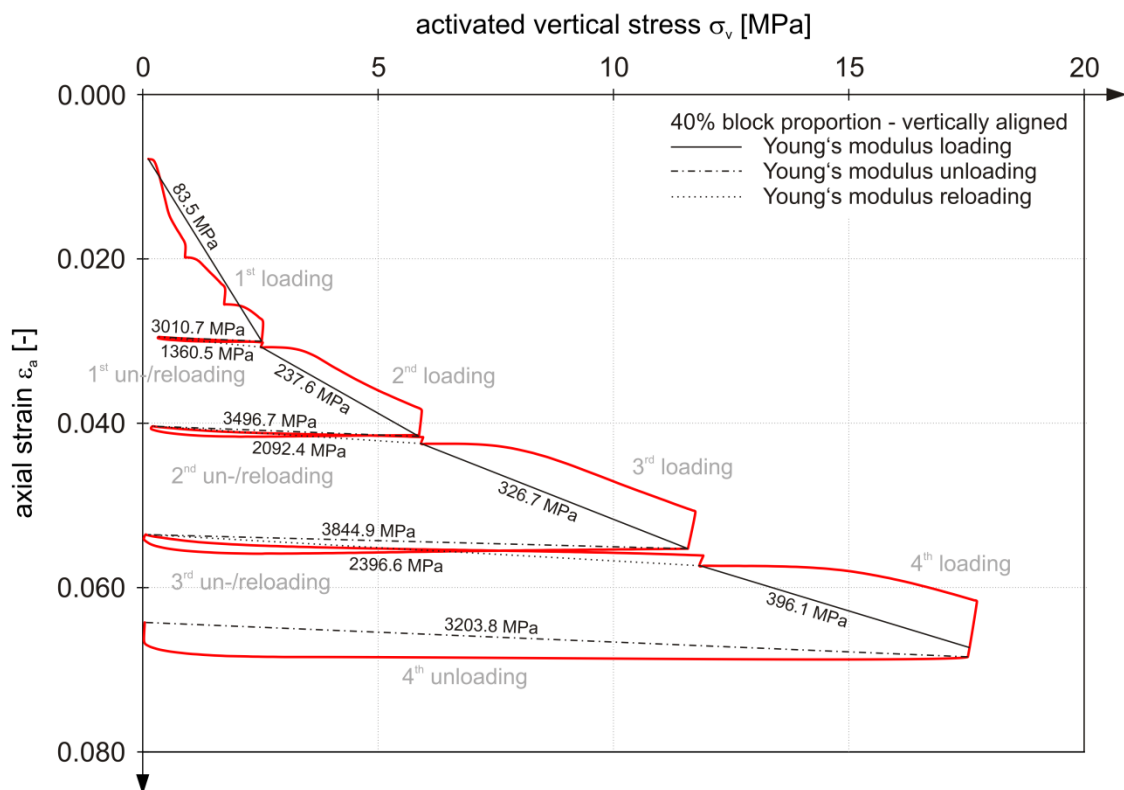


Figure 71: Evaluated moduli for 40% block proportion – vertically aligned.

The ratios of unloading-moduli to loading-moduli for the twisted block arrangement (Figure 72 to Figure 75) feature factors of about 15 to 30, being in the range between the horizontally and vertically aligned block specimen. Again, the hardening behavior is less pronounced, and is only observed for higher block proportions. The ratio between unloading- and reloading-moduli yielded factors of approximately two. The values for the loading-moduli are lower than those of the horizontally aligned block samples.

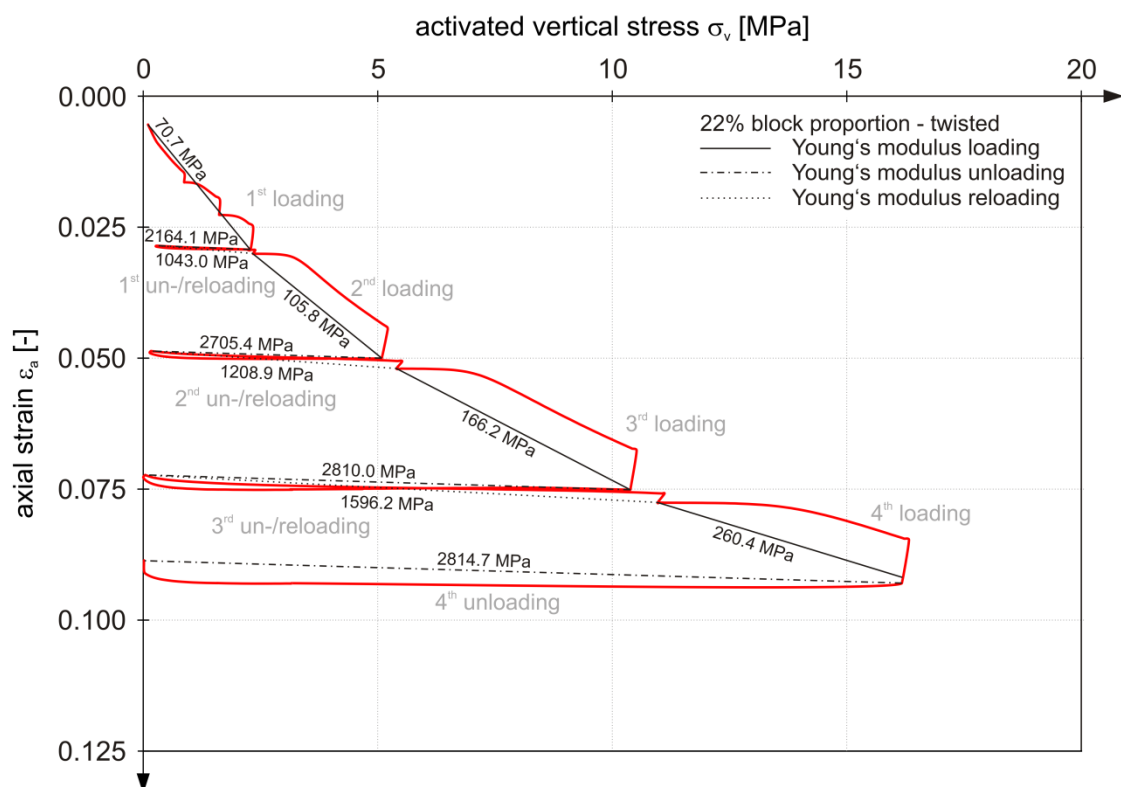


Figure 72: Evaluated moduli for 22% block proportion – twisted.

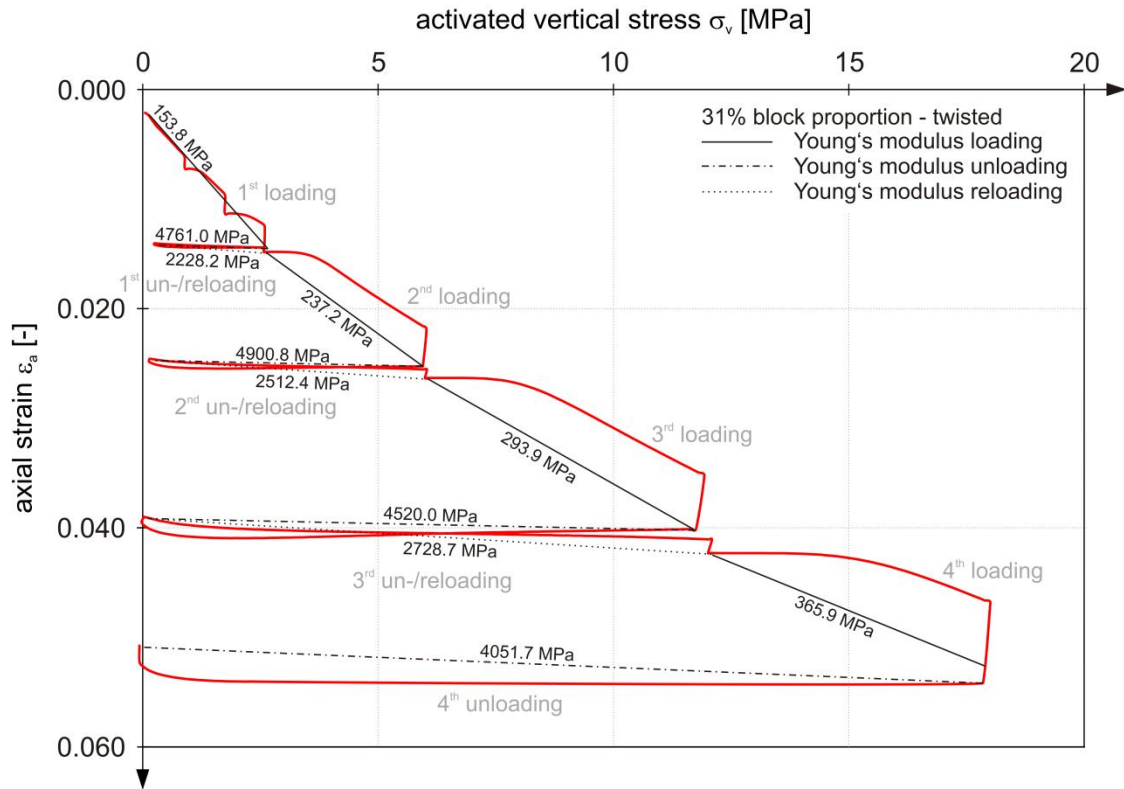


Figure 73: Evaluated moduli for 31% block proportion – twisted.

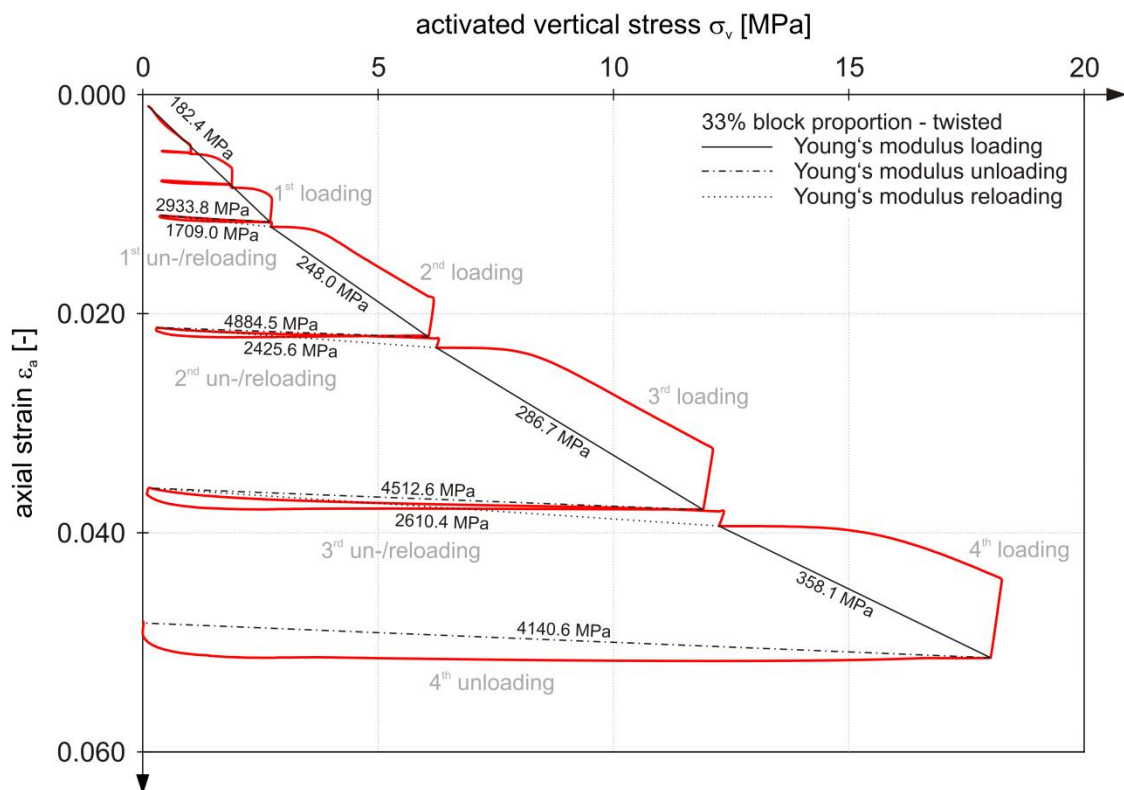


Figure 74: Evaluated moduli for 33% block proportion – twisted.

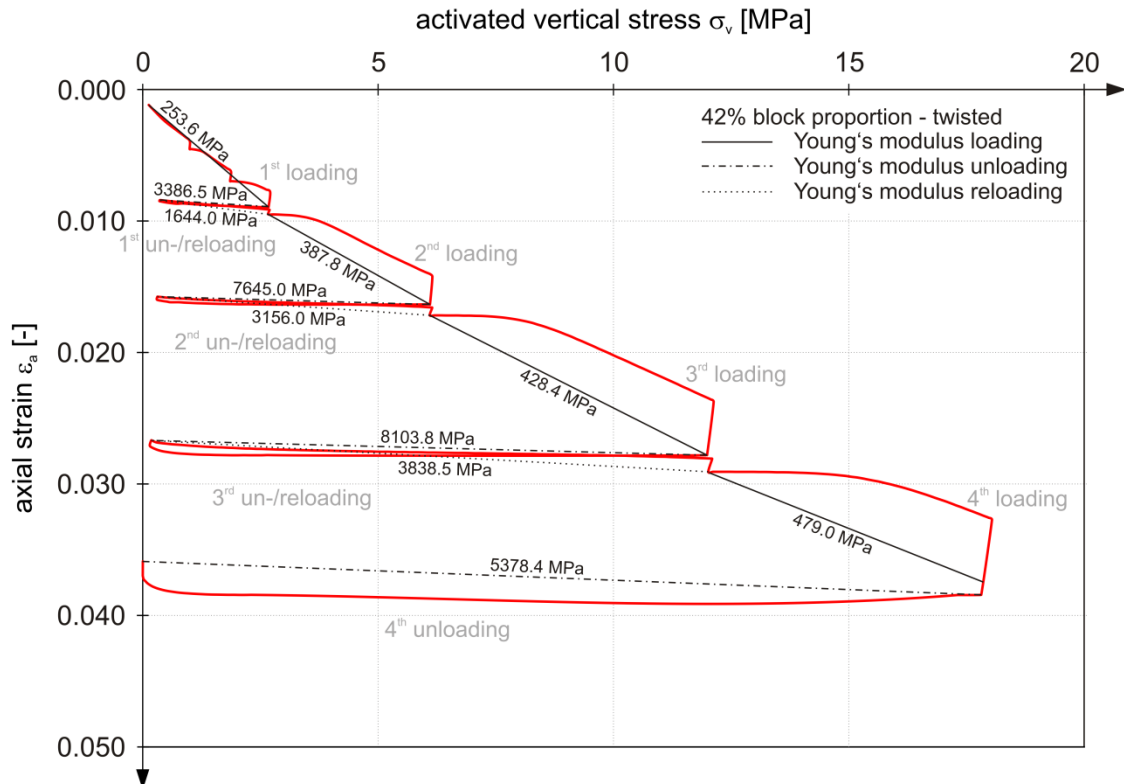


Figure 75: Evaluated moduli for 42% block proportion – twisted.

Figure 76 and Figure 77 depict the values for the pure matrix and the pure block sample. The ratio of both loading- and unloading-moduli between block and matrix is between eight (for low stress levels) and 60 (for high stress levels). Hence it can be concluded that the stress dependency of moduli is much more pronounced for the pure block material. However, it cannot be stated that it is a general behavior, that stiffer materials feature a much higher stress dependency of deformability. It is the case that the stress dependency and its occurrence is much more a question of the current degree of porosity of a material, which is governed by the applied stress level. Furthermore, imposing stress levels exceeding the strength yields plastic deformations. Hence evaluation of deformation moduli consists of elastic and plastic strains, which decrease the appearance of stress dependent deformation behavior.

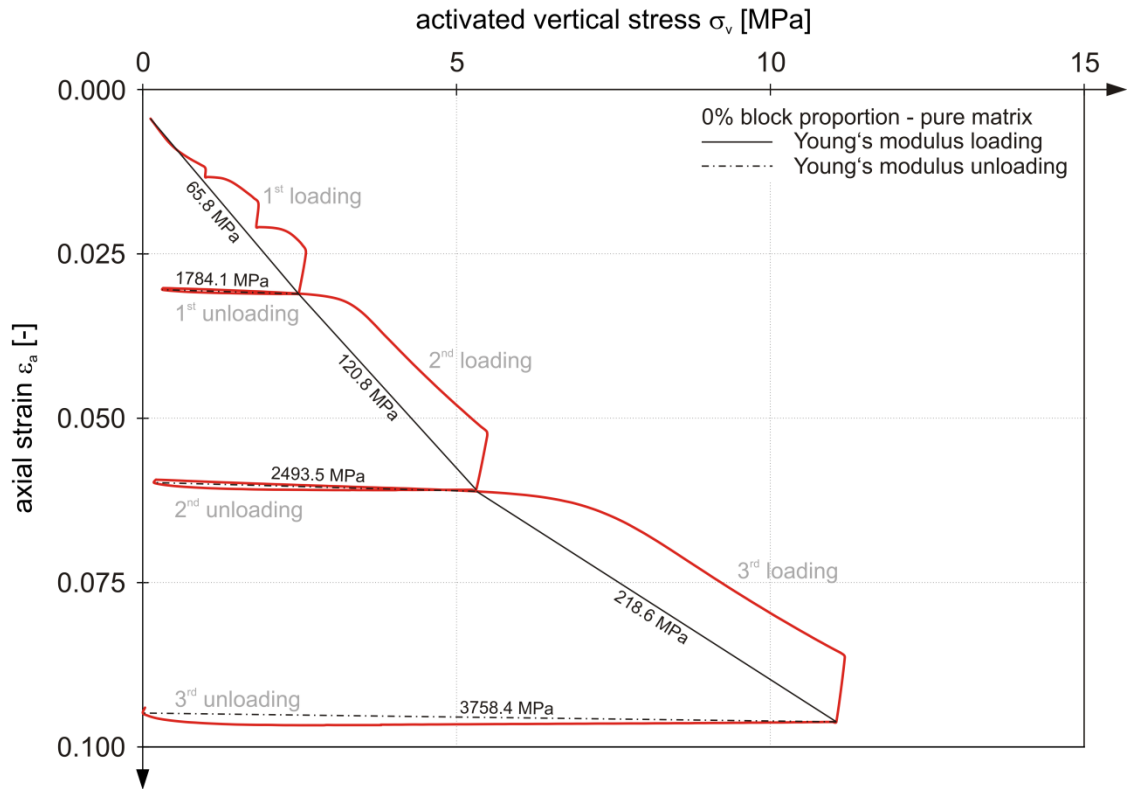


Figure 76: Evaluated moduli for 0% block proportion – pure matrix.

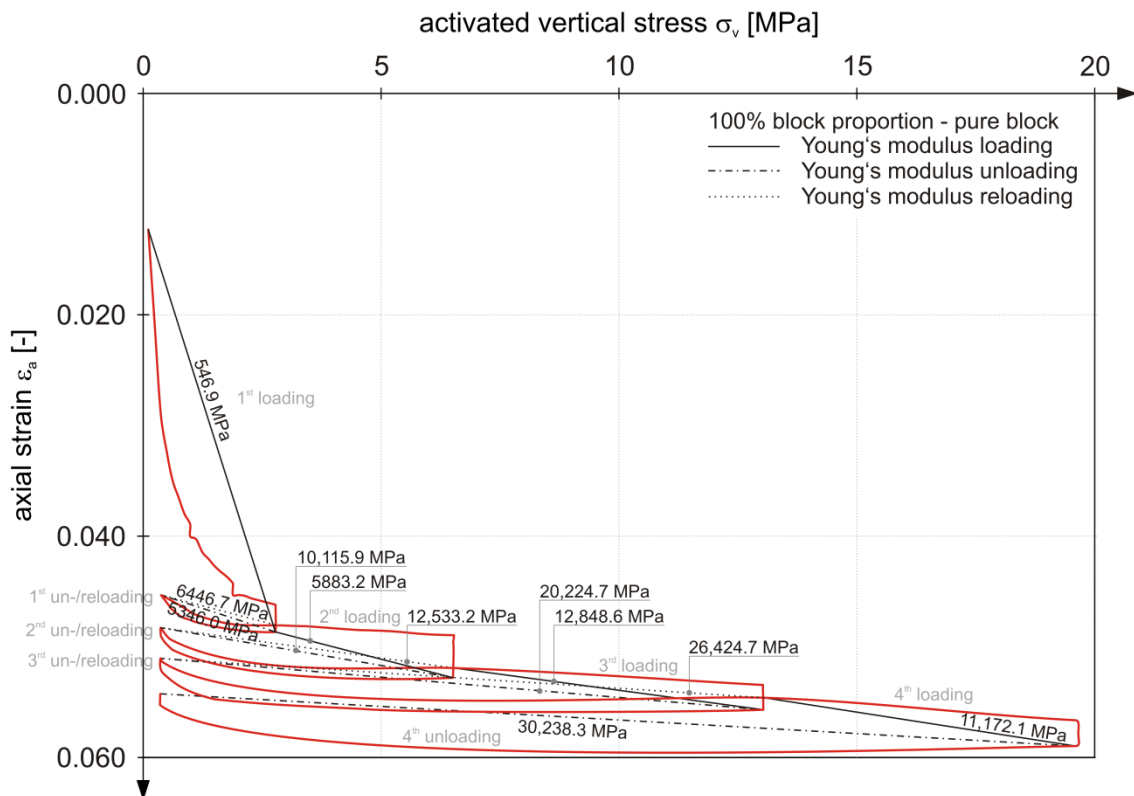


Figure 77: Evaluated moduli for 100% block proportion – pure block.



A quite clear picture is given if the individual data points of evaluated moduli are plotted in a Young's modulus versus axial stress diagram, allowing the observation of stress dependent deformation behavior. The results are depicted for each block arrangement in a separate diagram, given in Figure 78 (horizontally aligned blocks), Figure 79 (vertically aligned blocks) and Figure 80 (twisted blocks), respectively. In order to determine an empirical relationship governing the development of the deformation behavior with increasing stress level, a mathematical relationship fitting the discrete data points was required. It was found that the exponential function given in Equation (6) is able to yield an almost perfect fit:

$$y = \kappa \cdot e^{\eta/x}, \quad (6)$$

where the data points are given as  $(x,y)$  tuples and  $\kappa$  and  $\eta$  are function parameters, describing the shape of the exponential function. Introducing the Young's modulus  $E$  and the axial stress  $\sigma_v$ , Equation (6) rewrites to Equation (7):

$$E = \kappa \cdot e^{\eta/\sigma_v} \quad (7)$$

A closer inspection of the function parameters  $\kappa$  and  $\eta$ , showed that they depend on the volumetric block proportion. Moreover, it turned out that  $\kappa$  and  $\eta$  nearly feature a linear dependency on the block proportion. This was achieved by slight modifications of the best-fit curves for each block proportion sample, however, still yielding regression coefficients above 0.9. This approach was deemed to be valid, since one is dealing with a "given" material featuring a natural scatter in its properties. The function parameters  $\kappa$  and  $\eta$  and their dependence on the volumetric block proportion for the different block arrangements are shown in Table 5. The great advantage of this approach lies in its simplicity: Just the knowledge of the volumetric block proportion is needed as input, in order to calculate the development of the overall stiffness for a desired stress range.

Table 5: Function parameters  $\kappa$  and  $\eta$  for different block arrangements.

function parameter	Block arrangement		
	horizontally aligned	vertically aligned	twisted
$\kappa$	for $VBP < 50$	$\kappa = 8 \cdot VBP + 175$	$\kappa = 11 \cdot VBP + 58$
	$\kappa = 4.8 \cdot VBP + 370$		
	for $VBP \geq 50$		
	$\kappa = 0.000032 \cdot VBP^{4.28}$		
$\eta$	$\eta = 0.032 \cdot VBP - 5.4$	$\eta = 0.038 \cdot VBP - 6.0$	$\eta = 0.15 \cdot VBP - 8.3$

VBP ... volumetric block proportion in [%]

If one compares Figure 78, Figure 79 and Figure 80 it can be clearly seen that the samples with horizontally aligned blocks feature values for the Young's modulus which are about the double amount of the vertically aligned or twisted block samples. Moreover, for the vertically aligned and twisted block arrangement a linear increase of stiffness with increasing block proportion can be observed, while for the horizontally aligned block assembly this is only the case for block proportion up to 42%. Above 42% block proportion stiffness is disproportionately increasing. Considering the bounding conditions, which are present in layered arrangement of different materials, provides an explanation for the influence of block proportion and block orientation on the deformation behavior. The layered assembly (horizontally aligned blocks) represents a uniform stress state, while the vertical arrangement (vertically aligned blocks, twisted blocks) features uniform strain conditions. The overall modulus for the uniform stress state condition ("series") is given by Equation (8).

$$\frac{1}{E} = \frac{VBP}{E_B} + \frac{(1-VBP)}{E_M} \quad (8)$$

where:  $VBP$  ... volumetric block proportion (from 0 – 1)  
 $E$  ... overall modulus [MPa]  
 $E_B$  ... block modulus [MPa]  
 $E_M$  ... matrix modulus [MPa]

The overall modulus for the uniform strain condition (“parallel”) reads as follows (Equation (9)):

$$E = E_B \cdot VBP + E_M \cdot (1 - VBP) \quad (9)$$

where:  $VBP$  ... volumetric block proportion (from 0 – 1)  
 $E$  ... overall modulus [MPa]  
 $E_B$  ... block modulus [MPa]  
 $E_M$  ... matrix modulus [MPa]

If one has a closer look at Equation (8) and Equation (9), it can be seen that the series case yields a lower bound of moduli, while the parallel case represents the upper bound below which modulus values of mixtures of two different stiffnesses should fall. In the present case, a different picture is given. However, the reason for this lies at hand: For the horizontally aligned block assembly Equation (8) is valid and applicable, since each layer of blocks is fully filled with blocks (up to the degree which is allowed by the block geometry), hence representing a uniform stress state. However, in the vertically aligned and twisted block arrangement a uniform strain state is not ensured, since the blocks in the block layers are not continuously aligned from the bottom to the top of the sample, but the blocks are more or less “floating” in the matrix. If such a sample is axially loaded large strain contrasts at the boundary between the stiff blocks and the weak matrix occur, which forces the blocks to be “pushed” into the matrix. Hence the stiff block inclusions yield a relatively low contribution to the overall stiffness of the sample.

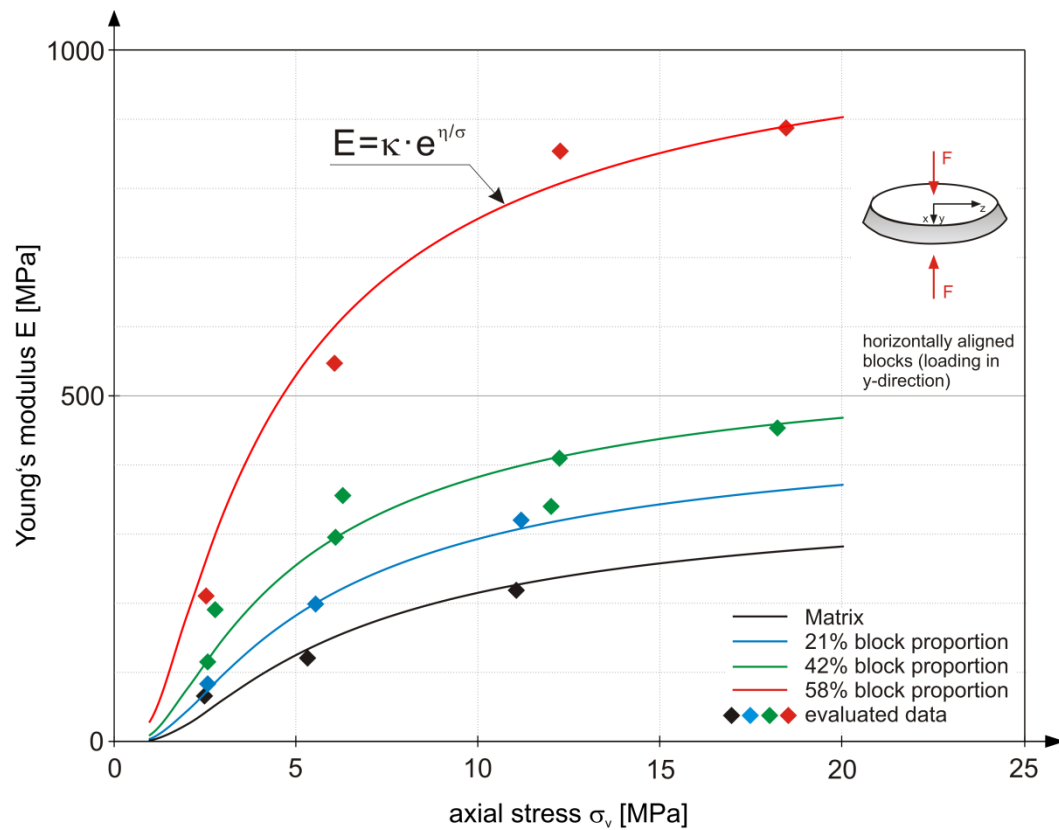


Figure 78: Evaluated Young's moduli vs. axial stress and fitting function for horizontally aligned block arrangement.

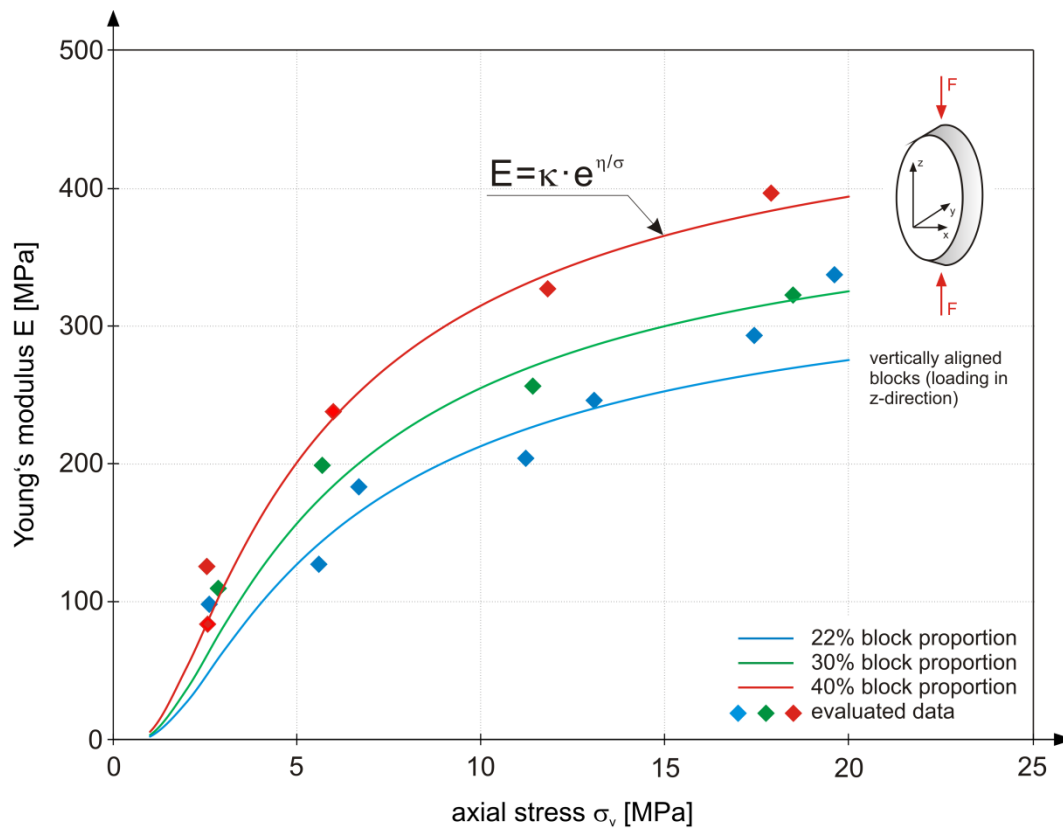


Figure 79: Evaluated Young's moduli vs. axial stress and fitting function for vertically aligned block arrangement.

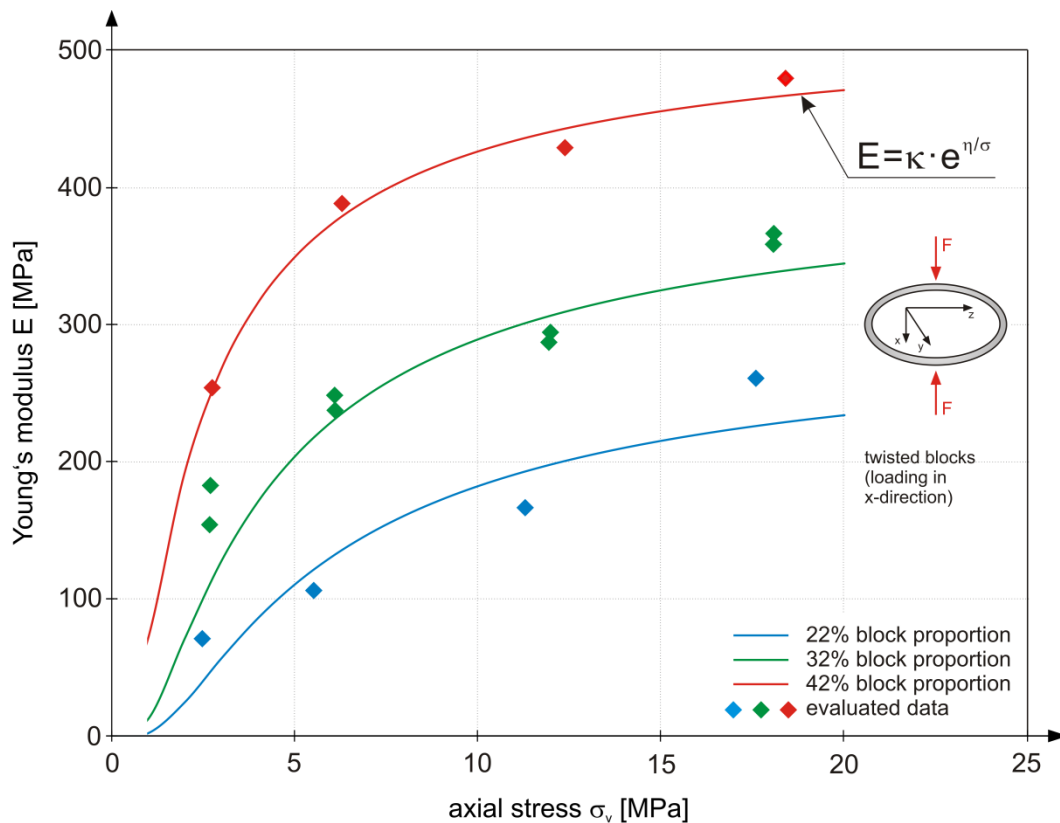


Figure 80: Evaluated Young's moduli vs. axial stress and fitting function for twisted block arrangement.

### 4.3 Influence of geological structures on deformation properties of fault material

The results of double plate load tests conducted in the Lavanttal fault zone provided information about the influence of geological structures on the deformation properties. As expected, the values for Young's moduli parallel to the foliation are slightly higher than those normal to foliation. Considering the instant moduli it was found that moduli parallel to the foliation are about 1.3 times higher than those normal to the foliation. For the interval moduli a factor of approximately 1.9 between moduli normal and parallel to the foliation was determined. The influence of local geological conditions (despite the fabric of the rock mass) and properties are also clearly depicted in the results. The more favorable rock mass conditions, encountered between chainage TM-VS 16.00 m and TM-VS 18.00 m, are reflected in the results of the tests conducted in the associated test adit section. Tests MS 2.1 – top (normal to foliation, chainage 15.39 m) and MS 3.1 – top (normal to foliation, chainage 19.29 m) yielded the highest values for the instant moduli.

#### 4.4 Summary of influence of block proportion and block orientation on deformation properties of bimrocks

The results of large oedometer tests on artificial bimrocks showed that stiffness is basically increasing with increasing block proportion. However, certain peculiarities were identified:

- a) In general, the samples with horizontally aligned blocks yield the highest values for the overall stiffness, which are approximately the double amount, compared to the vertically aligned and twisted block arrangement specimens.
- b) Horizontally aligned block arrangements feature an unproportional increase of stiffness with increasing block proportion. The samples with block proportions below approximately 40% show a linear increase in stiffness, while samples with block proportions above 40% exhibit a disproportional increase in overall stiffness. The disproportional factor for the tested 58% block proportion samples yields values which are about 5.5 to 6.5 times higher than the linear increase between the tested 21% and 42% block proportion samples.
- c) For vertically aligned and twisted block specimens, an almost perfect linear increase of stiffness with increasing block proportion was observed. However, the linear increasing factor is higher for samples with twisted blocks than for the vertically aligned block arrangement. The samples with block proportion of about 30% feature almost the same values, both for the vertically aligned and twisted block arrangement. For high block proportions (~ 40%) the twisted block arrangement exhibits higher values for the stiffness, while for low block proportions (~ 20%) a lower magnitude of stiffness, compared to the vertically aligned block arrangement is observed.  
It turned out that the stress dependency of deformability is more pronounced for samples with vertically aligned blocks than for twisted blocks. This is indicated by a markedly decreasing curve gradient above a vertical stress level of about 5 MPa in the twisted block arrangement.
- d) Regarding the ratios between unloading- and loading-moduli and unloading- and reloading-moduli following values were determined (Table 6):

Table 6: Evaluated values for the ratios between unloading- and loading-moduli, and the ratios between unloading- and reloading-moduli.

block arrangement	ratio unloading-/loading-moduli	ratio unloading-/reloading-moduli
horizontally aligned blocks	10 – 30	1.3 – 2.0
vertically aligned blocks	20 – 50	1.3 – 2.0
twisted block arrangement	15 – 30	2.0
pure matrix samples	17 – 27	n/a
pure block samples	1.5 – 10	0.77 – 0.83

- e) Assessment of the model test results also provided an approach for the estimation of the overall modulus of bimrocks for the uniform stress state and uniform strain conditions if the block modulus, matrix modulus and volumetric block proportion are known.

## 5 Strength properties of fault rocks

For the design of underground engineering works, the strength of rock material is one of the elementary input parameters. However, as mentioned in the previous chapters, the determination of mechanical parameters such as cohesion or friction angle is often extraordinarily challenging. In this work, an extensive laboratory program was performed to gain knowledge about the stress-strain relationship of artificial block-in-matrix rocks and to determine and investigate the factors influencing the strength of fault-like material. The development of an exhaustive database, gained by laboratory studies allows a proper characterization and dissociation of encountered stress-strain behavior types, providing the basis for a qualitative constitutive model for block-in-matrix rocks.

### 5.1 Direct shear tests on artificial block-in-matrix samples

To study the basic mechanical properties of fault material an extensive laboratory program was conducted on artificial block-in-matrix rocks.

There are a few works available dealing with laboratory tests on bimrocks, as mentioned in Chapter 2. Most of them deal with uniaxial or triaxial tests. However, with triaxial tests large strains are difficult to achieve and the investigation of the failure surface is rarely possible. However, when dealing with tunnels or deep open pit mines in difficult ground conditions, one often has to expect relatively large displacements, due to the low strength and deformation properties. Therefore, it was decided to examine the mechanical behavior of artificial bimrocks in direct shear tests, which allows the application of large strains and examination of the failure surface.

#### 5.1.1 Sample preparation

The mixture for the matrix material was basically the same as for the large oedometer samples, which is described in Chapter 4.2.1.2. However, for the sake of a comfortable readability, the matrix properties are given here in detail. Special requirements which should be met by the matrix properties were specified. The goals were:

- I. A relatively short curing time, to ensure prefabrication of samples within a tight timetable, and
- II. limited, controllable strength and deformation properties in order to ensure high contrast between matrix and block properties.



Various materials like gypsum, clay, silt, and crushed rock of different lithologies were considered and tested, and multiple had to be discarded. After performing several tests, including uniaxial and triaxial compression tests and visual inspection of curing behavior (onset of cracking due to shrinkage), it turned out that a mixture of finely crushed limestone, cement and water meets the intended properties best. A crushed rock/cement ratio of 5:1 was used while the water/cement ratio was set to 1.8, allowing good workability. This obvious high ratio is required due to the fact that the mixture contains almost no coarse aggregates. The properties of the matrix material, determined by uniaxial compressive strength tests and triaxial tests, are a UCS of approximately 2 MPa and a Young's modulus of 4000 MPa after seven days curing time, respectively. The strength development for the matrix material, gained by UCS tests is depicted in Figure 81. The results of triaxial tests are shown in Table 7.

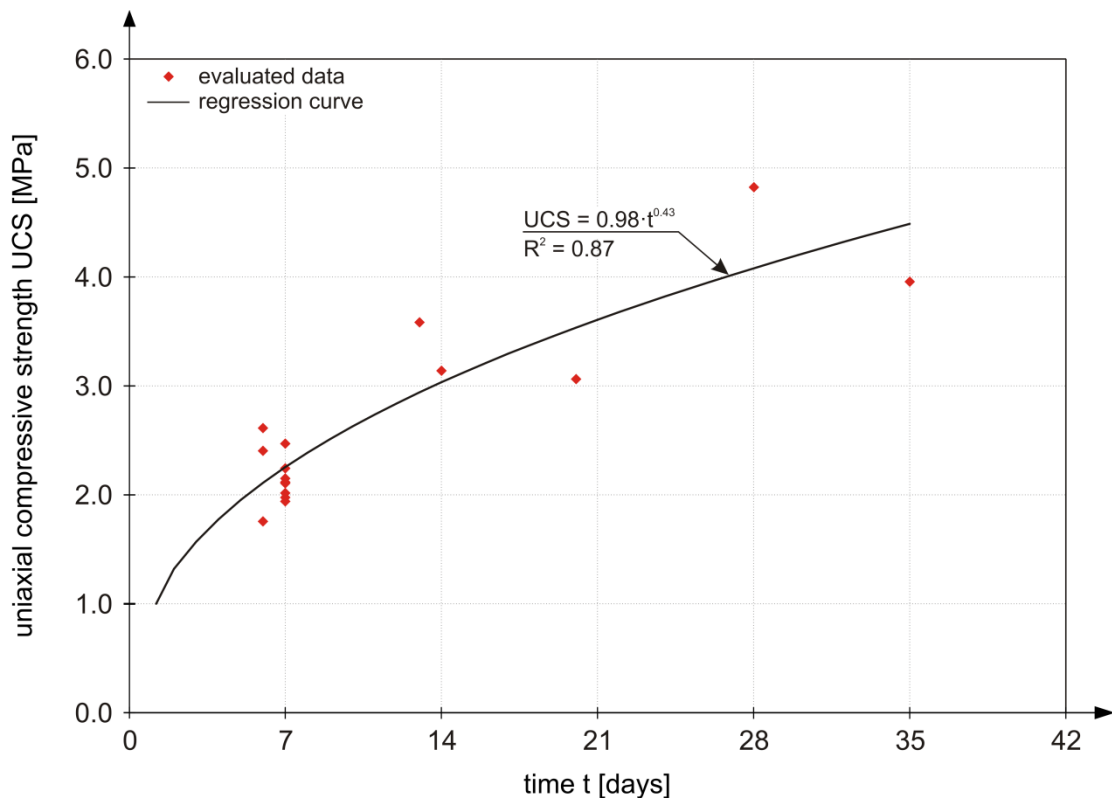


Figure 81: Strength development for the matrix material, determined by uniaxial compressive strength tests.

The blocks were made of cement-stone and feature a lenticular, ellipsoidal shape, slightly tapered in y-direction (Figure 57, Table 8 bottom). The length is 87/98 mm (z-direction), the width is 35/43 mm (x-direction) and the thickness is 14 mm (y-direction), respectively. A Portland cement type CEM II 42.5 was used and the water/cement ratio was set to 0.4. The blocks were prefabricated in silicone molds and were left to cure for at least 28 days. Triaxial tests were performed on the block material to determine the strength and deformation properties, yielding a uniaxial compressive strength of 37 MPa after seven days

curing time, a friction angle of  $30^\circ$  and a Young's modulus of about 16,000 MPa. The 7-day strength ratio between matrix material and block material is about 15, and the 7-day stiffness ratio amounts to the factor 4.

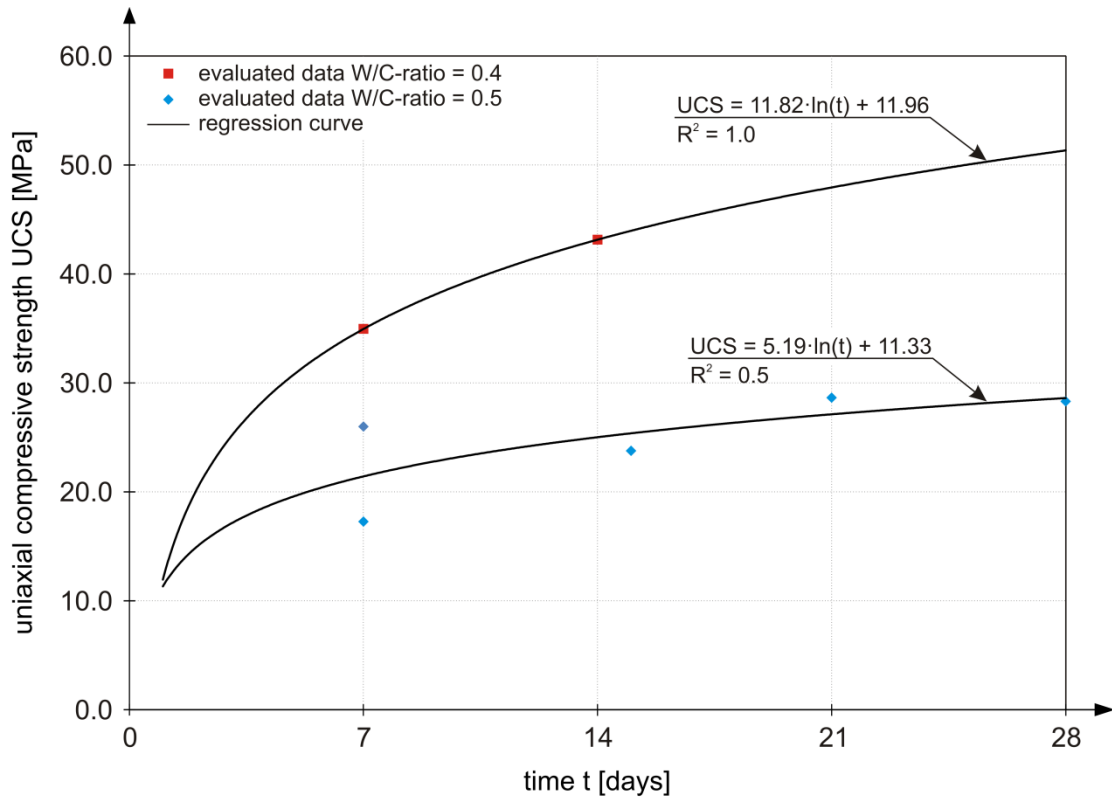


Figure 82: Strength development for the block material, determined by uniaxial compressive strength tests (W/C: Water/Cement).

Table 7: Results of triaxial tests on matrix- and block-material.

days	Matrix			Block		
	UCS [MPa]	E [MPa]	$E_{def}$ [MPa]	UCS [MPa]	E [MPa]	$E_{def}$ [MPa]
7	2.02	4130	2580	36.92	16,220	14,800
14	3.21	5720	4120	45.65	14,530	11,190
28	3.74	7480	6650	50.22	11,290	9960

where:  $UCS$  ... uniaxial compressive strength  
 $E$  ... Young's modulus  
 $E_{def}$  ... deformation modulus

The samples were prefabricated in two quadratic steel shear boxes. The boxes have a height of 180 mm and a length/width of 200 mm. The gap between the boxes is 20 mm, which was sealed with polystyrene bars during sample preparation. First the lower box was filled with matrix material. After a curing time of about one hour, allowing the matrix to stiffen a little, the blocks were placed in the matrix in the intended orientation and block proportion (Figure 83). Thereby it was ensured that the plane of symmetry of the blocks (governed by the block orientation) corresponds with the center plane of the shear surface. With the help of stencils, made of laminated cardboard, it was ensured that the blocks remained in the desired position (Figure 84). After the matrix had stiffened up to a level that blocks would stay in place and would not be rotated or pushed into the matrix, the upper box was filled with matrix material. The samples were left to cure for seven days.



Figure 83: Assembly of the shear boxes, lower box filled with matrix material and blocks attached; exemplarily shown for 25% block proportion/30° block orientation (left) and 50% block proportion/90° block orientation (right).

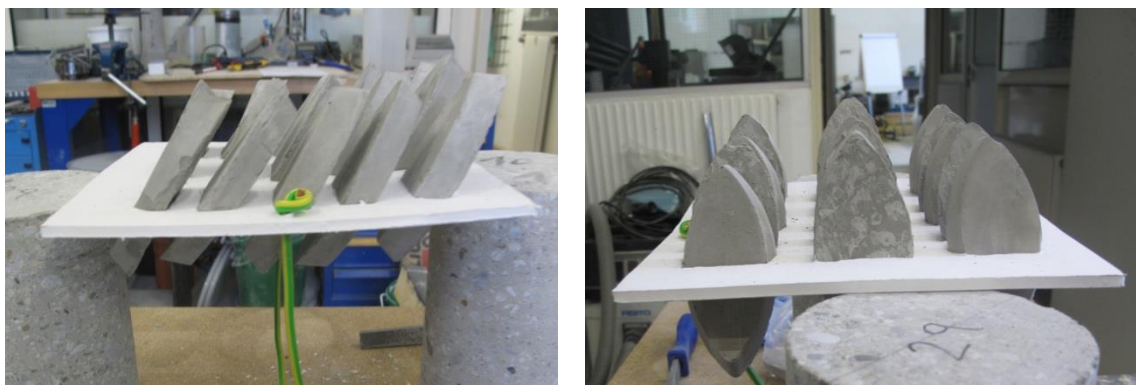


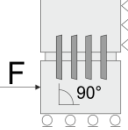
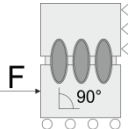
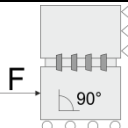
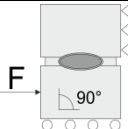
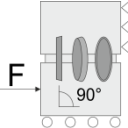
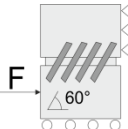
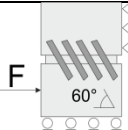
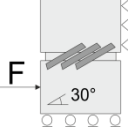
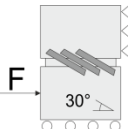
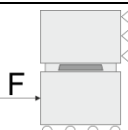
Figure 84: Blocks arranged in intended block orientation with the help of stencils, ready to be placed in the matrix.

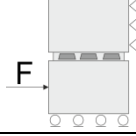
### 5.1.2 Test program

It was tried to cover a broad range of possible block orientations with regard to the shear direction. Specimen with four different block orientations, each with

three different block proportions were fabricated, along with pure matrix and pure block samples (Table 8). In order to account for the natural scatter of strength properties and the variability in sample preparation quality three tests of each block orientation/block proportion combination were performed.

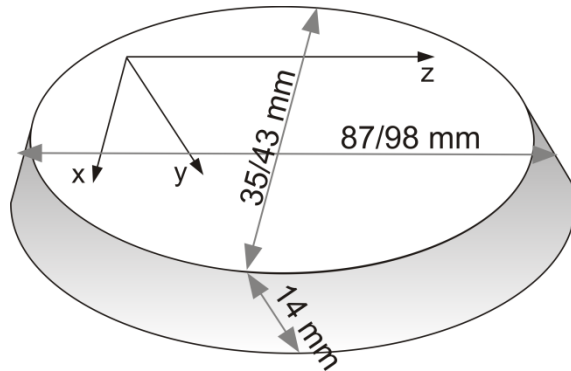
Table 8: Compilation of performed direct shear tests.

Orientation	Block proportion	Symbol	No. of tests	Sketch
n/a	0% - pure matrix	n/a	3	n/a
90°	25%	→     $\sigma$ in z-dir.	3	
	50%	→     $\sigma$ in z-dir.	3	
	75%	→     $\sigma$ in z-dir.	3	
90°	25%	→     par. $\sigma$ in z-dir.	1	
	50%	→     par. $\sigma$ in z-dir.	1	
	75%	→     par. $\sigma$ in z-dir.	1	
90°	50%	→     $\sigma$ in x-dir.	1	
90°	50%	→     par. $\sigma$ in x-dir.	1	
90°	50%	random, $\sigma$ in z-dir.	1	
60°	25%	→ ///	3	
	50%	→ ///	3	
	75%	→ ///	2	
60°	50%	→ \\\	1	
	75%	→ \\\	1	
30°	25%	→ ///	2	
	50%	→ ///	2	
	75%	→ ///	2	
30°	25%	→ \\\	1	
	50%	→ \\\	1	
	75%	→ \\\	1	
0°	25%	→ ---- long.	2	
	50%	→ ---- long.	2	
	75%	→ ---- long.	2	

0°	25%	→ ---- trans.	1	
	50%	→ ---- trans.	1	
	75%	→ ---- trans.	1	
n/a	100% pure block	n/a	3	n/a

**legend:**

- shear direction  
 ||| blocks vertically aligned, shear in y-direction of block  
 ||| par. blocks vertically aligned, shear in x-direction of block  
 /// blocks inclined in pos. y-direction (inclined against shear direction)  
 \\ blocks inclined in neg. y-direction (inclined in shear direction)  
 ---- long. blocks horizontally aligned, shear in z-direction  
 ---- trans. blocks horizontally aligned, shear in x-direction



Additional tests were performed on samples with only one block embedded in matrix material, which are shown in Table 9. Testing of “one-block” samples allows eliminating the effect of blocks influencing each other during the shearing process. Since the geometry and thus the cross sectional area of the block was “fixed”, the shear area had to be adjusted in order to fabricate samples with different block proportions. The maximum block proportion which could be tested was 40%. Above 40% block proportion, the area of the matrix was too small in order to ensure that the block was properly surrounded by matrix material on the one hand, and on the other hand the initial normal dead load of the shear device, which is about 2 kN, would have exceeded the matrix strength, resulting in an initial failure of the sample right at the beginning of the testing process.

Table 9: Performed direct shear tests on samples with one block embedded in matrix.

Block proportion	Orientation	Symbol	No. of tests
10%	90°	→	3
20%	90°	→	3
30%	90°	→	3
40%	90°	→	3

**legend:**

→ shear direction  
 ||| blocks vertically aligned, shear in y-direction of block

Besides the actual test program several trial tests on artificial block-in-matrix rocks were performed utilizing different test procedures. In order to determine the influence and effect on the test results, identical samples with the same block proportion and block orientation were fabricated and tested both under constant normal load and constant normal stiffness conditions (Table 10).

Table 10: Trial tests for studying the influence of different test procedures.

Block proportion	Orientation	Symbol	Type of test	No. of tests
0%	pure matrix	n.a.	CNL	1
0%	pure matrix	n.a.	CNS	1
25%	30°	→ ///	CNL	1
25%	30°	→ ///	CNS	1
50%	60°	→ ///	CNL	1
50%	60°	→ ///	CNS	1

**legend:**

→ shear direction  
 /// blocks inclined in pos. y-direction (inclined against shear direction)  
 CNL constant normal load conditions  
 CNS constant normal stiffness conditions

### 5.1.3 Test set-up

The test apparatus is a digitally controlled servo-hydraulic system (Figure 85). This servo-hydraulic, automatic control system allows performing tests under constant normal load (CNL) and constant normal stiffness (CNS) conditions, including test specific loading and control procedures. Using linear variable differential transducers (LVDTs) and load cell sensors as feedback command

allows the simulation of normal stiffness in CNS tests. The maximum normal load capacity is 500 kN, while the maximum shear force is +250 kN / -160 kN. Four vertical and two horizontal LVDTs allow an accurate measurement of shear and normal displacements. By evaluation of the vertical LVDTs the rotation of the shear box (pitch and roll) can be determined, occasionally occurring yaw is captured by the horizontal LVDTs. Two load cells allow the measurement of the shear and normal load.

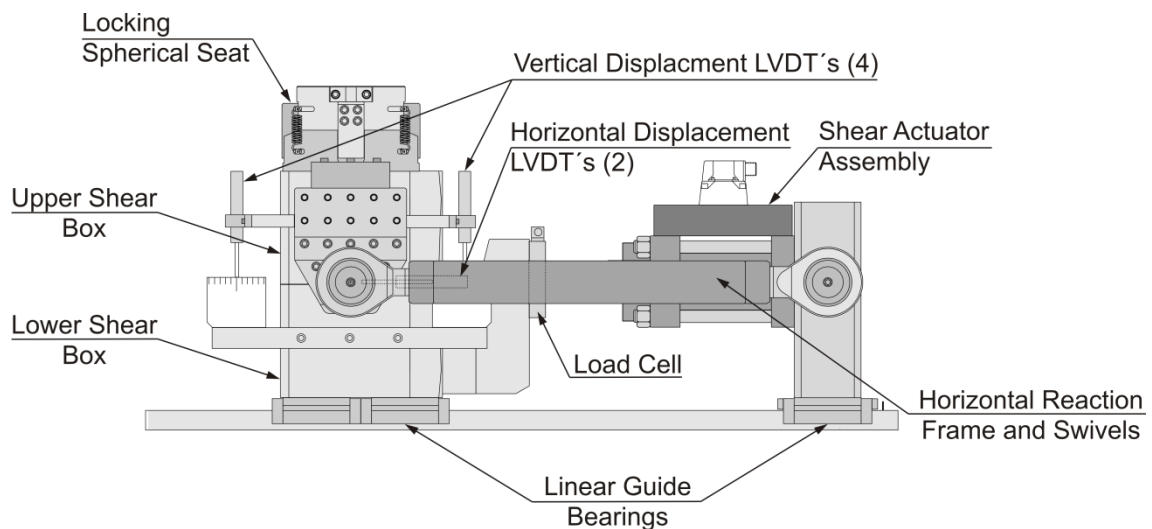


Figure 85: Digitally controlled servo hydraulic shear testing system.

### 5.1.4 Test procedure

The majority of the tests were performed under constant normal stiffness (CNS) conditions. For evaluation of CNS shear tests, the external normal stiffness and the internal normal stiffness of the shear test sample have to be considered. The external normal stiffness, which is kept constant during shearing, represents a boundary condition describing the deformability of the surrounding rock mass.

For the shear tests on artificial block-in-matrix rocks, the external stiffness was set to infinite. This was deemed to be appropriate due to the fact that if we consider a fault zone, bounded by host rock, the stiffness contrast between both rock zones is very pronounced. The internal normal stiffness of the shear test sample is governed by the current normal stress, the material parameters and the shear box assembly.

In order to determine the internal normal stiffness of the samples, normal loading loops were performed prior to the exposure of shear load. Each normal loading loop was performed with two different loop stages, consisting of a loading-unloading-reloading – loop. Applying the conceptual normal stiffness model after Saeb and Amadei (1992), allows a proper separation of dilation and friction contribution and investigation of their effect on the strength envelope, which is described in detail in Chapter 5.1.5. After performing the normal loading loops

the initial normal stress was applied and shearing was initiated at a constant horizontal displacement rate of 0.5 mm/min. The maximum shear displacement was 25 mm, unless a sample reached the residual state much earlier.

### 5.1.5 Data evaluation

#### *Accounting for boundary conditions*

In the context of direct shear tests the boundary conditions are referred to as the perpendicular confinement of the joint, hence they are related to the normal stiffness. A condition where the normal stiffness does not vary with shear displacement is defined as constant normal stiffness (CNS). Accounting for the boundary conditions in direct shear tests is essential, since normal displacements naturally occur during shearing. Therefore, the normal stiffness influences the normal stress and hence affects the dilation and peak shear strength.

The normal stiffness behavior can be described by a combination of the external stiffness  ${}^e k_n$  and the internal stiffness  ${}^i k_n$ . The external stiffness considers boundary conditions like the deformability of the surrounding rock mass. The internal stiffness considers the behavior within the sample. In terms of jointed rock mass, it considers the effects of joint closure and aperture and the elastic deformation of asperities. As a conceptual mechanical model a multi spring model (Figure 86) can be used to describe the total normal stiffness  $K_{tot}$ .

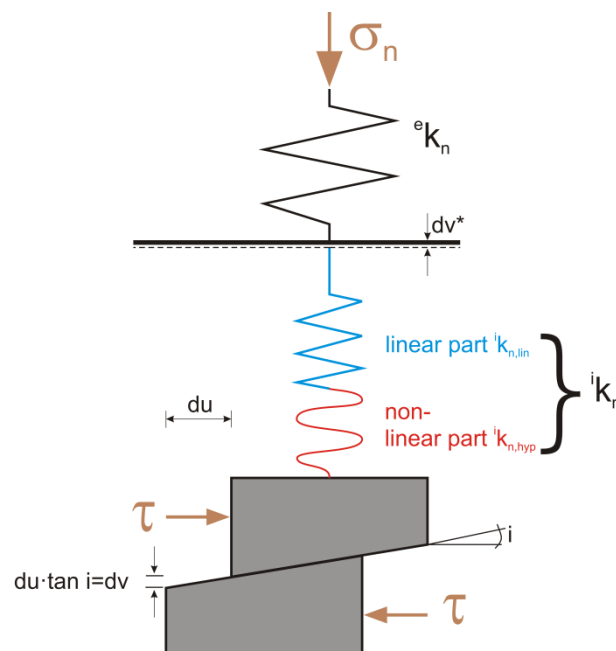


Figure 86: Multi-spring model for normal stiffness evaluation (modified after Pötsch 2011).

The normal stiffness concept was originally derived and applied for simulating the shear behavior of joints under CNS conditions. Within the scope of this laboratory program on artificial bimrocks intact samples were tested. However,



for the determination of the internal stiffness, and thus allowing a proper separation of dilational and frictional contribution to shear strength and resistance, this conceptual model is not constrained in its applicability.

Bandis (1990) showed that the normal displacement behavior of a joint under normal stress features a non-linear relationship, following a combination of a linear and hyperbolic law. The linear and the hyperbolic parts are given in Equation (10) and Equation (11), respectively.

$${}^i k_{n,lin} = \frac{\sigma_n}{v} \quad (10)$$

where:  ${}^i k_{n,lin}$  ... linear part of the internal normal stiffness  
 $\sigma_n$  ... applied normal stress  
 $v$  ... associated normal displacement

$${}^i k_{n,hyp} = k_{ni} \cdot \left( \frac{k_{ni} \cdot v_m + \sigma_n}{k_{ni} \cdot v_m} \right)^2 \quad (11)$$

where:  ${}^i k_{n,hyp}$  ... hyperbolic part of the internal normal stiffness  
 $k_{ni}$  ... initial normal stiffness  
 $v_m$  ... maximal joint closure  
 $\sigma_n$  ... applied normal stress

The normal loading loops, which were performed prior to the exposure of shear load, were carried out at two different loop stages, each stage consisting of a loading-unloading-reloading – loop. Figure 87 shows exemplarily the load-displacement behavior of an artificial bimrock sample.

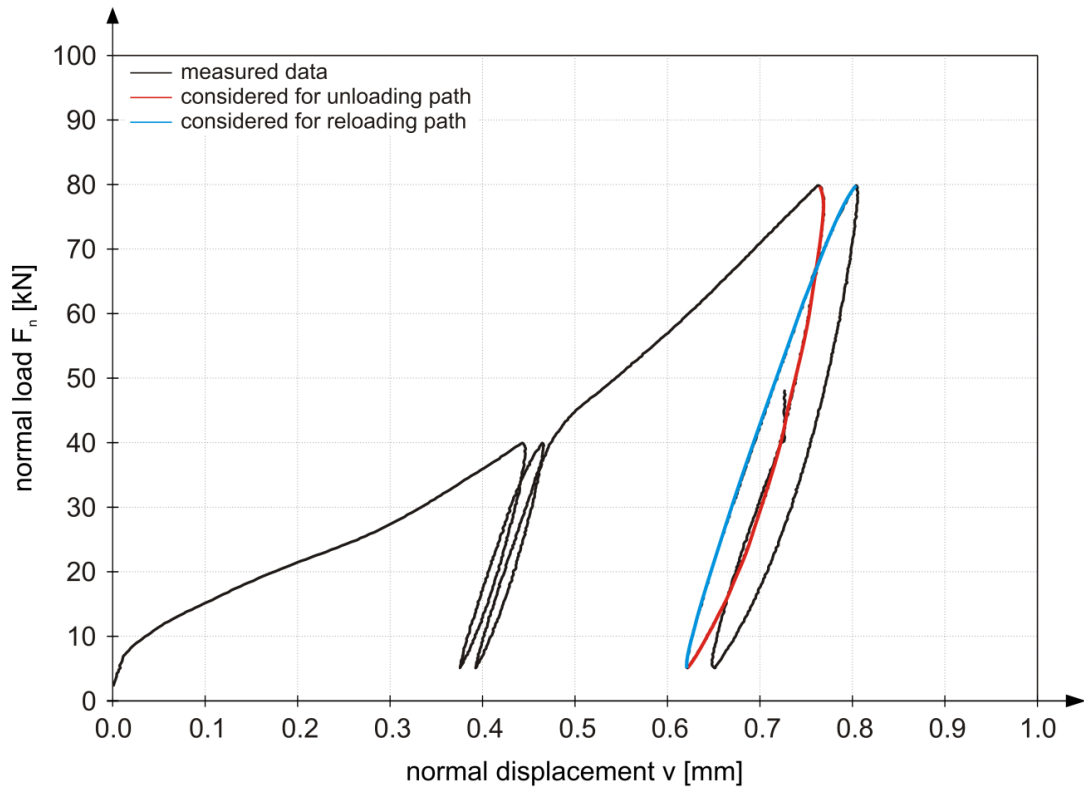


Figure 87: Exemplary illustration of performed normal loading loops.

It can be seen from Equation (11) that the hyperbolic part of the internal normal stiffness depends on the current normal stress  $\sigma_n$  and the maximum joint closure  $v_m$ . However, since intact samples were tested and hence no joint closure could be determined, the measured data were fitted with the functional approximation by combining the linear and hyperbolic relationship (Figure 88).

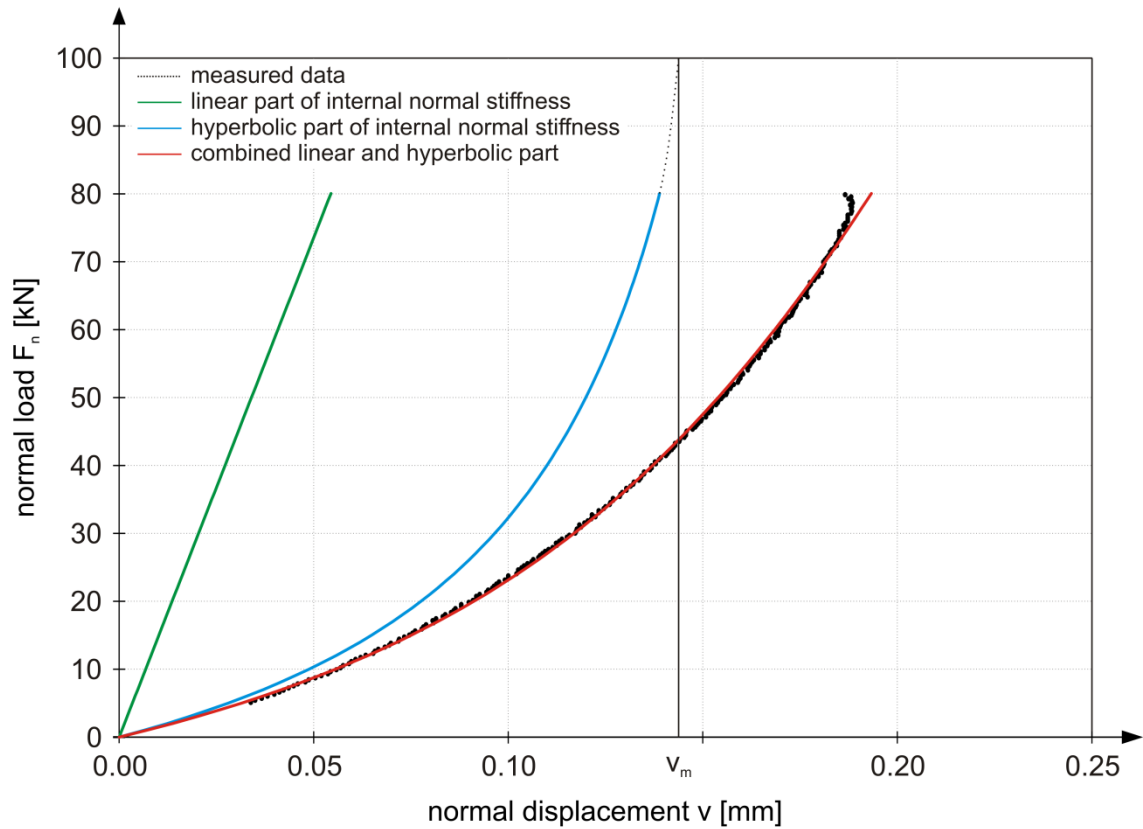


Figure 88: Typical normal load-displacement behavior of the artificial samples – approximation of  ${}^i k_{n,lin}$  and  ${}^i k_{n,hyp}$  to the measured normal response.

The total normal stiffness  $K_{tot}$  for CNS tests is a combination of the external normal stiffness, the linear part and the non-linear part of the internal normal stiffness (Equation (12)):

$$K_{tot} = \frac{{}^e k_n \cdot {}^i k_{n,lin} \cdot {}^i k_{n,hyp}}{{}^e k_n \cdot {}^i k_{n,lin} + {}^e k_n \cdot {}^i k_{n,hyp} + {}^i k_{n,lin} \cdot {}^i k_{n,hyp}} \quad (12)$$

where:  $K_{tot}$  ... total normal stiffness  
 ${}^i k_{n,hyp}$  ... hyperbolic part of the internal normal stiffness  
 ${}^i k_{n,lin}$  ... linear part of the internal normal stiffness  
 ${}^e k_n$  ... external normal stiffness

If the external normal stiffness is set to infinity (no vertical displacement allowed), which was the case for all performed CNS direct shear tests, the total normal stiffness  $K_{tot}$  rewrites to (Equation (13)):

$$K_{tot} = \frac{{}^i k_{n,lin} \cdot {}^i k_{n,hyp}}{{}^i k_{n,lin} + {}^i k_{n,hyp}} \quad (13)$$

The effective dilation angle  $i$  is now determined by Equation (14):

$$\tan i = \frac{d\sigma_n}{K_{tot} \cdot du} \quad (14)$$

The first part of Patton's law (Patton 1966), in which the effective or apparent friction angle  $\varphi$  is the sum of the basic friction angle  $\varphi_b$  and the dilation angle  $i$ , is applied (Equation (15)). Knowing the dilation angle  $i$  allows the calculation of the basic friction angle  $\varphi_b$ .

$$\tau = \sigma_n \cdot \tan(\varphi_b + i) \quad (15)$$

### ***Intact strength and shear resistance***

Direct shear tests are usually conducted on rock joints, hence a classical evaluation of such tests focuses on determination of shear behavior of two separated surfaces with certain properties like joint roughness, etc. Since intact samples were tested, special attention had to be paid to a proper data evaluation. Primarily the knowledge about the intact rock strength is of interest. When dealing with underground structures constructed in weak rock mass, large strains often have to be expected due to the poor material quality. Excessive deformation processes in tunneling, which were reported by several authors (e.g. Schubert 1993, Kovari et al. 2005), show radial strains of above 10%. Due to the high strength and stiffness contrasts between block and matrix and the contrary behavior of high ductility for matrix and high brittleness for blocks it can be assumed that such material can sustain high strains until failure. Exposing high strains on such material primarily forces the blocks to constantly realign in the weak matrix and hence preventing themselves from failure. Shear bands will usually form through the matrix. However, yet the blocks improve the overall strength, since they enforce an increased shear band tortuosity due to their dowel effect.

In direct shear tests, the shear surface is predetermined preventing the development of a "natural" failure surface. Therefore, special attention was paid to determine the intact strength of the block-in-matrix material at a stage prior to the failure of the matrix or the blocks. The critical strain threshold was determined through analysis of the pure matrix and pure block samples. Failure of the sample took place when a sudden drop of shear strength in the shear strength versus shear displacement – diagram was observed. The associated shear displacement at pronounced shear strength decrease was defined as the limit between the evaluation of intact strength and residual strength. All pure matrix and pure block samples exhibited failure between 1 mm and 2 mm of shear

displacement, hence it was decided to set the threshold value below which the sample can be deemed as intact to 1.5 mm. For evaluation purposes, a lower bound for shear displacement had to be introduced in order to cut off the initial part at the start of the shearing process. At the beginning of the shearing process in a CNS test the initial normal stress remains rather constant and only shear stress increases until the sample tends to dilate. Evaluating a friction angle or cohesion in this initial phase would lead to erroneous results. The majority of samples showed that the initial phase ended after 0.1 mm to 0.3 mm. Therefore, the lower bound of shear displacement was set to 0.5 mm. For samples featuring a delayed onset of dilation the lower bound was adopted, according to their examined behavior.

The evaluation method is principally based on a cohesion-weakening – frictional strengthening (CWFS) model, which signifies that the mobilized strength components (cohesive, frictional and dilational) are strain dependent. Equation (16) expresses the adapted Mohr-Coulomb failure criterion in the CWFS model.

$$\tau = c(\varepsilon) + \sigma_n(\varepsilon) \cdot \tan(\varphi_b + i) \quad (16)$$

In a first step the corresponding stress path between 0.5 mm and 1.5 mm of shear displacement was determined. Fitting a straight line to the stress path in the region of interest and intersecting it with the vertical shear stress axis  $\tau$  allows the determination of the initial value for the cohesion, as shown in Figure 89. The amount of mobilized cohesion was subtracted from every discrete value for  $\tau$  (Equation (17)).

$$d\tau_{i,corr} = d\tau_i - c_{ini} \quad (17)$$

A proper determination of (de-) mobilization of cohesion, dilation and friction over the shear displacement and their exact sequencing is not a trivial task. It is stated by several investigators (e.g. Hajiabdolmajid et al. 2002, Schofield, 1998) that there is no permanent cohesion in rocks, at least at relatively low confinement, where the cohesive strength component is gradually lost when the rock mass is strained beyond its peak strength. The mechanical processes involved therein are well known and understood, although mainly in a qualitative way. The only way to date for a proper separation of mobilization and demobilization of cohesion and a simultaneous or subsequent mobilization of friction and dilation is to perform laboratory or in-situ tests, followed by numerical back analysis. In such numerical back analysis the individual strength components and their appearance are adjusted until a good agreement between laboratory tests and numerical simulation is achieved. However, it is quite obvious that having several independent variables (to a certain degree) would

result in different combinations of values leading to the same outcome. For the evaluation of the shear tests, a simple and straightforward approach was chosen. It can be assumed that cohesion gradually decreases from its initial value  $c_{ini}$  until the sample fails and after the sample is completely separated no cohesion is present. For the sake of simplicity and due to the lack of better knowledge of the exact development of cohesion demobilization in detail, it is assumed that cohesion suddenly drops to zero after the sample starts to dilate (increase of  $\sigma_n$ ).

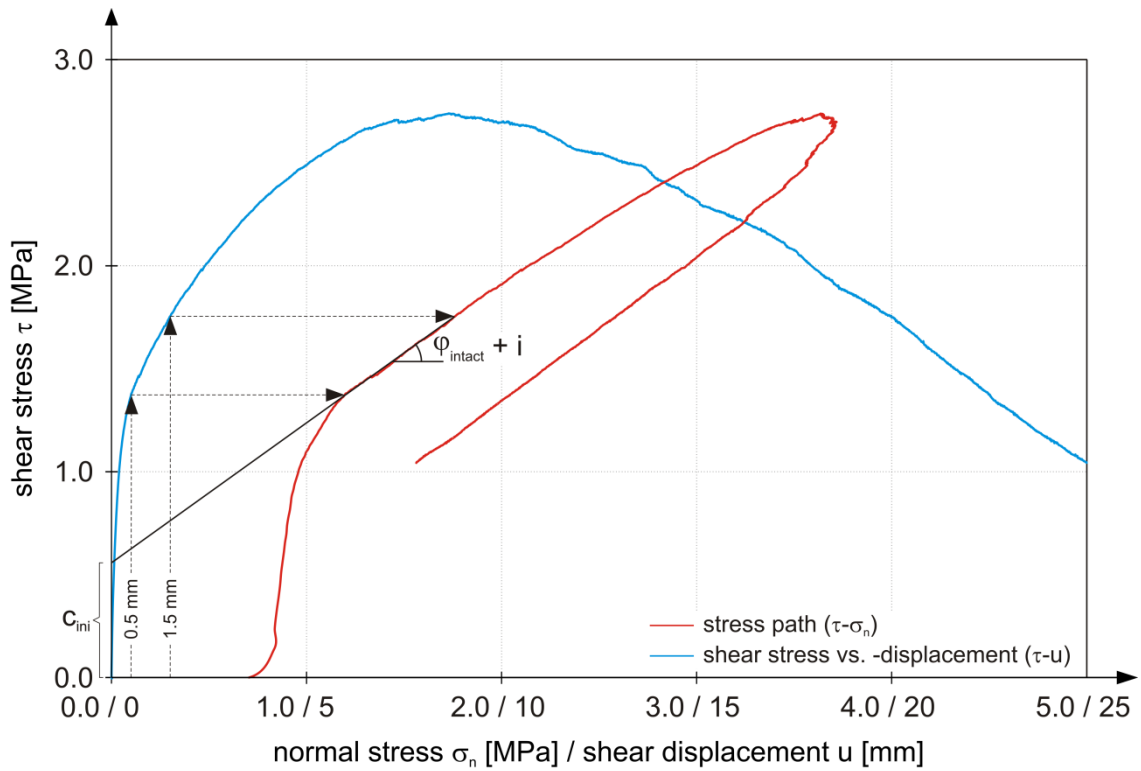


Figure 89: Graphical description of chosen evaluation method for determination of intact parameters for  $c$ ,  $\varphi$  and  $i$ .

The determination of the total normal stiffness  $K_{tot}$  by evaluation of the stress – normal displacement behavior, which is explained above, allows the calculation of the mobilized dilation angle  $i$  and the mobilized friction angle  $\varphi$  (Equation (18) and Equation (19)).

$$\varphi_{b,i} + i_i = \arctan\left(\frac{d\tau_{i,corr}}{d\sigma_{n,i}}\right) \quad (18)$$

$$\tan i_i = \frac{d\sigma_{n,i}}{K_{tot} \cdot du_i} \quad (19)$$

During the course of evaluation process it became obvious that describing the behavior of bimrocks by three parameters  $c$ ,  $\varphi$  and  $i$  would lead to suitable results only in a few cases. The mechanical processes inherent are too complex to be

expressed in a few parameters. Although the classical Mohr-Coulomb failure criterion is widely accepted and used due to its simplicity, it has certainly its limitations when it comes to complex mechanical behavior.

In order to fully capture the mechanical behavior of bimrocks and the peculiarities of different block orientations and block proportions on the overall properties one has to consider the entire stress path and stress-displacement development. Therefore, the results section will focus on a comprehensive description of the individual stress paths and stress-displacement plots, highlighting the characteristics and features of different block proportions and block orientations. The development of a new constitutive law was beyond the scope of this dissertation, however, the overall mechanical behavior of bimrocks is given in a descriptive, qualitative way.

## 5.2 Results and discussion

### 5.2.1 Shear behavior types

After evaluating all tests performed, it turned out that the stress-displacement behavior and the associated stress paths can be classified into six different main behavior types. A compilation of identified shear behavior types is given in Table 11.

Table 11: Compilation of the observed shear behavior types.

Shear behavior type	characteristic for	
	Block proportion	Block orientation
A	0% - pure matrix 100% - pure block	n.a.
B	25%	0°
B*	25%	30°
C	50% 75%	0°
D	50% 75%	30°
E	25% 50% 75%	60°
F	25% 50% 75%	90°

Type A, which is shown in Figure 90 and valid for the pure matrix and pure block samples, is characterized by a distinct drop of shear stress after relatively low shear displacement accompanied by a relatively low increase of normal stress. After reaching the peak shear strength, the shear resistance gradually decreases to 40% and reduces further with ongoing shear displacement to about 20% of the peak value.

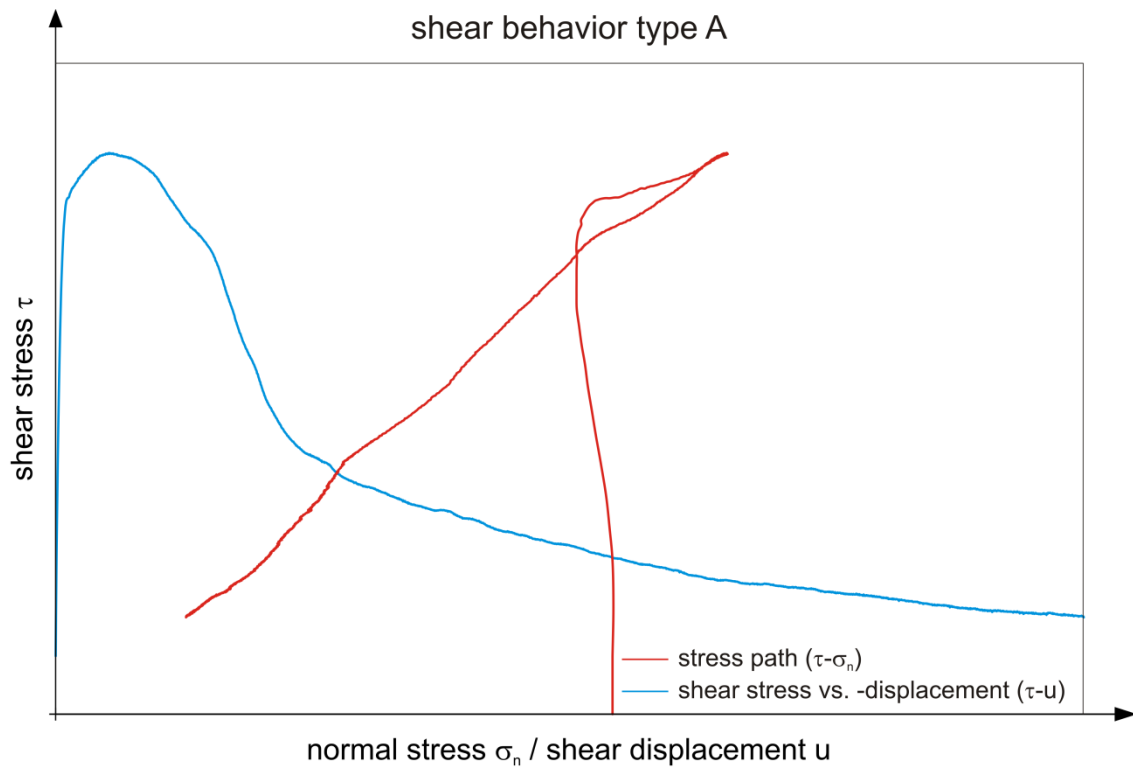


Figure 90: Stress-displacement development and stress path plot for shear behavior type A.



The shear behavior of low block proportions (25%), in combination with flat lying blocks ( $0^\circ$  block orientation – Type B) and slightly inclined blocks ( $30^\circ$  block orientation – Type B\*) is depicted in Figure 91. These samples also feature a relatively sudden decrease in shear resistance after low shear displacement, but the residual shear strength remains at about 50% of the peak shear strength. The reason for this can be found in the improved strength in the predefined shear area, due to the flat lying blocks. Failure of the blocks can be observed in the descending direction of the stress path, indicated by sudden drops of shear stress. The dotted lines in Figure 91 are valid for slightly inclined blocks (type B\*). The behavior is principally the same in a qualitative way; however, the peak shear strength is considerably higher. The stress-displacement plot shows a more ductile behavior, represented by a less pronounced drop of shear stress and a plateau after reaching the amount of maximum shear strength. After approximately 30% of the maximum shear displacement ( $\sim 7 - 10$  mm) the shear stress gradually decreases.

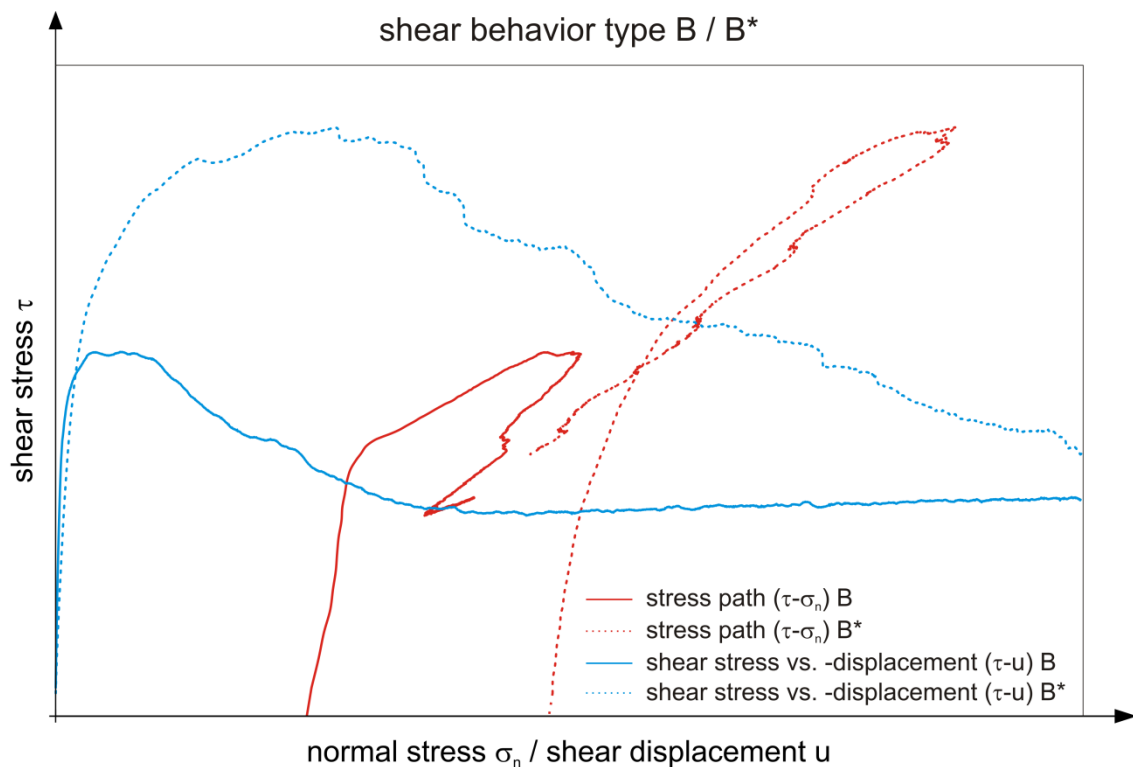


Figure 91: Stress-displacement development and stress path plot for shear behavior type B and type B\*.

Shear behavior type C is characterized by a peak shear stress after relatively low shear displacement, which basically indicates the same behavior as for type A and B/B\* (Figure 92). However, after a slight drop of shear stress the amount of shear resistance stays fairly constant for some millimeters of shear displacement and even slightly increases with proceeding shear displacement. This behavior was observed for flat lying blocks ( $0^\circ$  block orientation) in combination with high block proportions of 50% and 75%, respectively. In these particular cases the shear zone is filled with blocks to a large extent, hence the behavior is mainly dominated by the blocks. The shear surface usually develops not as a horizontal plane in the middle of the gap between the two shear boxes but tends to form from the top surface of the lower shear box at the rear to the bottom side of the upper shear box at the front. Therefore, the failure plane has to develop in a strongly acute angle through the blocks, resulting in higher shear strength compared to type A and B/B\*. Moreover, due to the fact that the shear surface zone is highly occupied by blocks, the blocks have the potential only to a minor degree to be pushed into the matrix during the shearing process. After low shear displacement the blocks tend to touch each other.

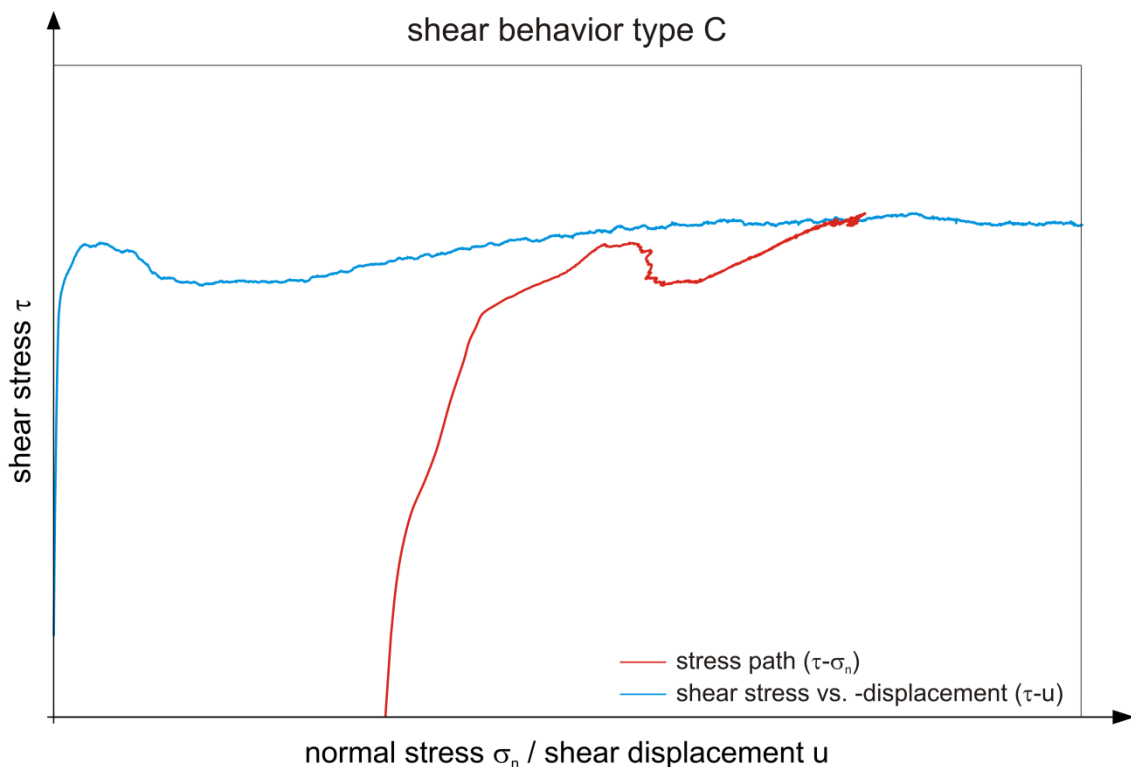


Figure 92: Stress-displacement development and stress path plot for shear behavior type C.

Contrary to the previously explained types A to C, type D features no pronounced peak shear stress at relatively low shear displacement, as shown in Figure 93. After the sample starts to dilate a steady increase of normal stress  $\sigma_n$  and shear stress  $\tau$  is observed. After approximately 10 mm of shear displacement the shear stress shows a horizontal plateau, which is caused by failure of blocks or, more likely, a sudden loss of contact strength between the blocks and the matrix. After about  $2/3^{\text{rd}}$  of the total shear displacement, shear stress steadily increases and reaches its maximum value at the maximum shear displacement, which features approximately the double amount of the initial shear stress value when the sample starts to dilate. Type D is typical for  $30^\circ$  block orientation, in combination with block proportions of 50% and 75%, respectively. Even more pronounced for type D than for type C is the fact that the developing shear surface is forced to proceed through the longitudinal plane of the blocks, due to the  $30^\circ$  block orientation.

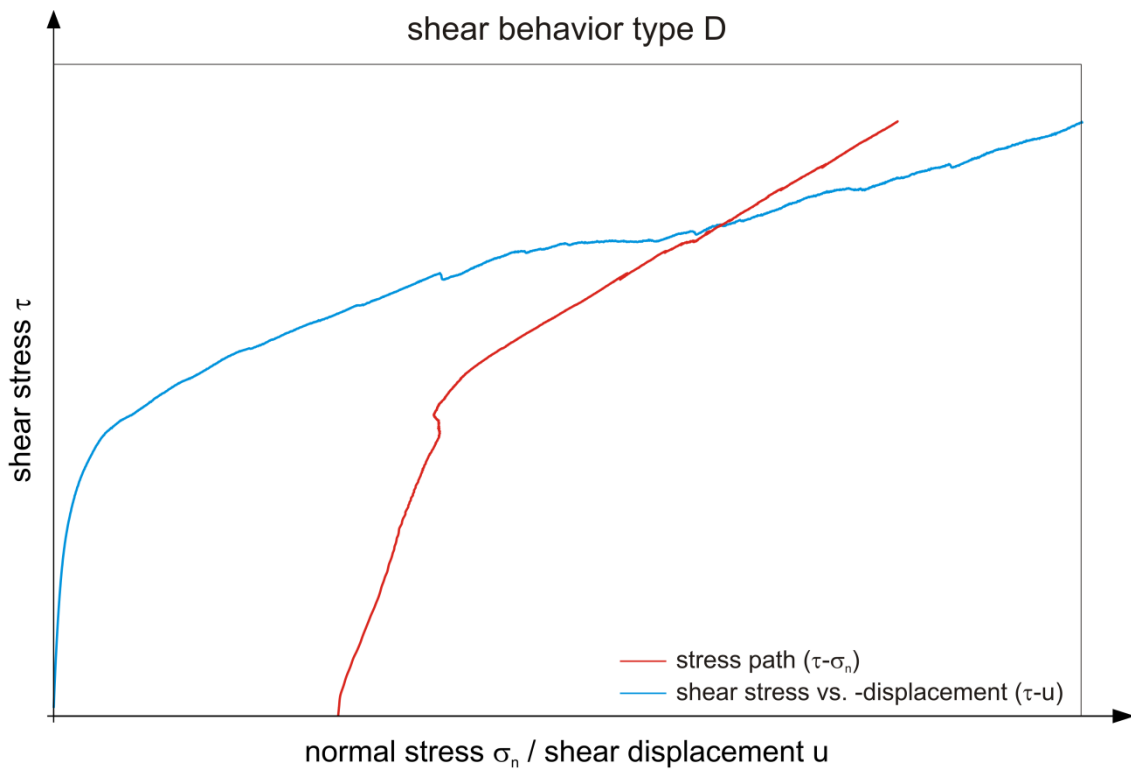


Figure 93: Stress-displacement development and stress path plot for shear behavior type D.

Type E (Figure 94) is characterized by a steady increase of shear stress and normal stress after the sample starts to dilate. The peak shear strength is reached at a relatively high shear displacement magnitude. After approximately 15 mm to 20 mm of shear displacement shear resistance tends to decline, indicated by a decrease of shear stress. Worth to mention is the fact that with advancing shear displacement the shear stress increment is gradually decreasing to zero when reaching the peak shear strength. This behavior is also evident in the normal stress vs. shear stress plot, indicated by a convex development of the stress path after the beginning of increasing normal stress. In the sense of a classical Mohr-Coulomb failure criterion, this would imply a constant reduction of frictional resistance. Type E is representative for  $60^\circ$  block orientation and all varieties of tested block proportions. A small difference between low and medium or high block proportions can be observed in the stress-displacement behavior, where the decrease of shear resistance after the peak shear strength is more pronounced for the low block proportion samples.

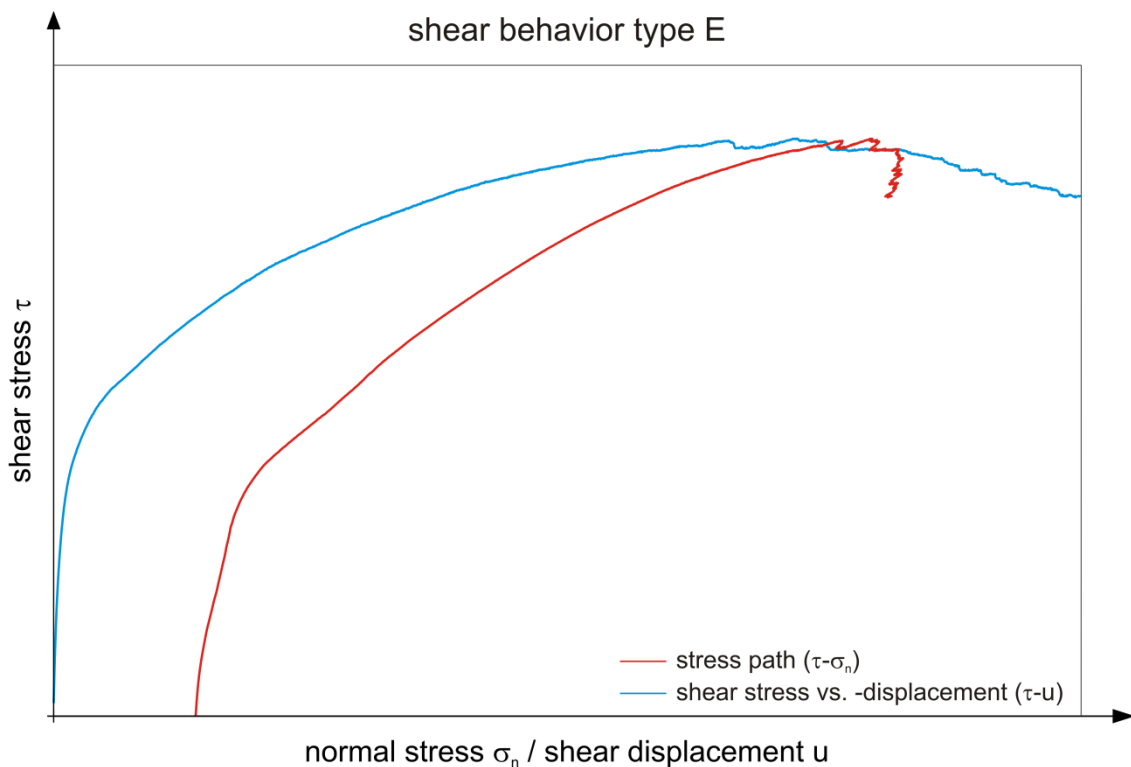


Figure 94: Stress-displacement development and stress path plot for shear behavior type E.

Shear behavior type F (Figure 95) features an almost perfectly linear increase of normal stress  $\sigma_n$  and shear stress  $\tau$ . In contrast to shear type E, the frictional resistance is not decreasing and remains fairly constant. Type F is characterized by achieving the maximum shear strength at a lower shear displacement magnitude, compared to type E. In the post peak region, a constant decrease of shear stress in combination with decreasing normal stress is observed. This behavior type is typical for the  $90^\circ$  block orientations for all block proportions between 25% and 75%.

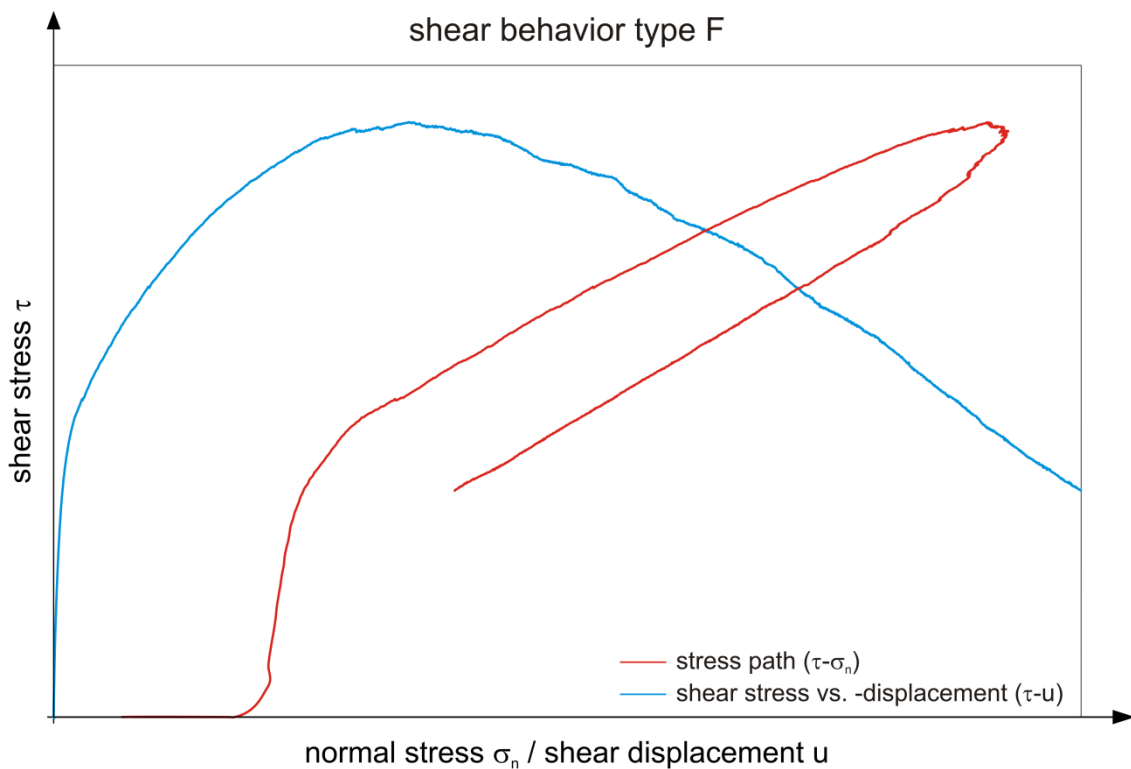


Figure 95: Stress-displacement development and stress path plot for shear behavior type F.

## 5.2.2 Influence of block proportion and block orientation on peak shear strength

In this section, the peak shear strength and the associated shear displacement for different block orientations and block proportions are depicted.

The results of the samples with 90° block orientation depict a conclusive picture (Figure 96). The peak shear strength increases with increasing block proportion. The associated shear displacements are only marginally influenced by block proportion and remain fairly the same. A closer inspection of the shear surface after the test shows that the blocks exhibit brittle failure, which results in very smooth cracks (Figure 97). A relatively planar shear surface develops. With increasing shear displacement the blocks experience further crushing and damaging, yielding small finely-grained block particles which provide only a minor contribution to shear resistance increase.

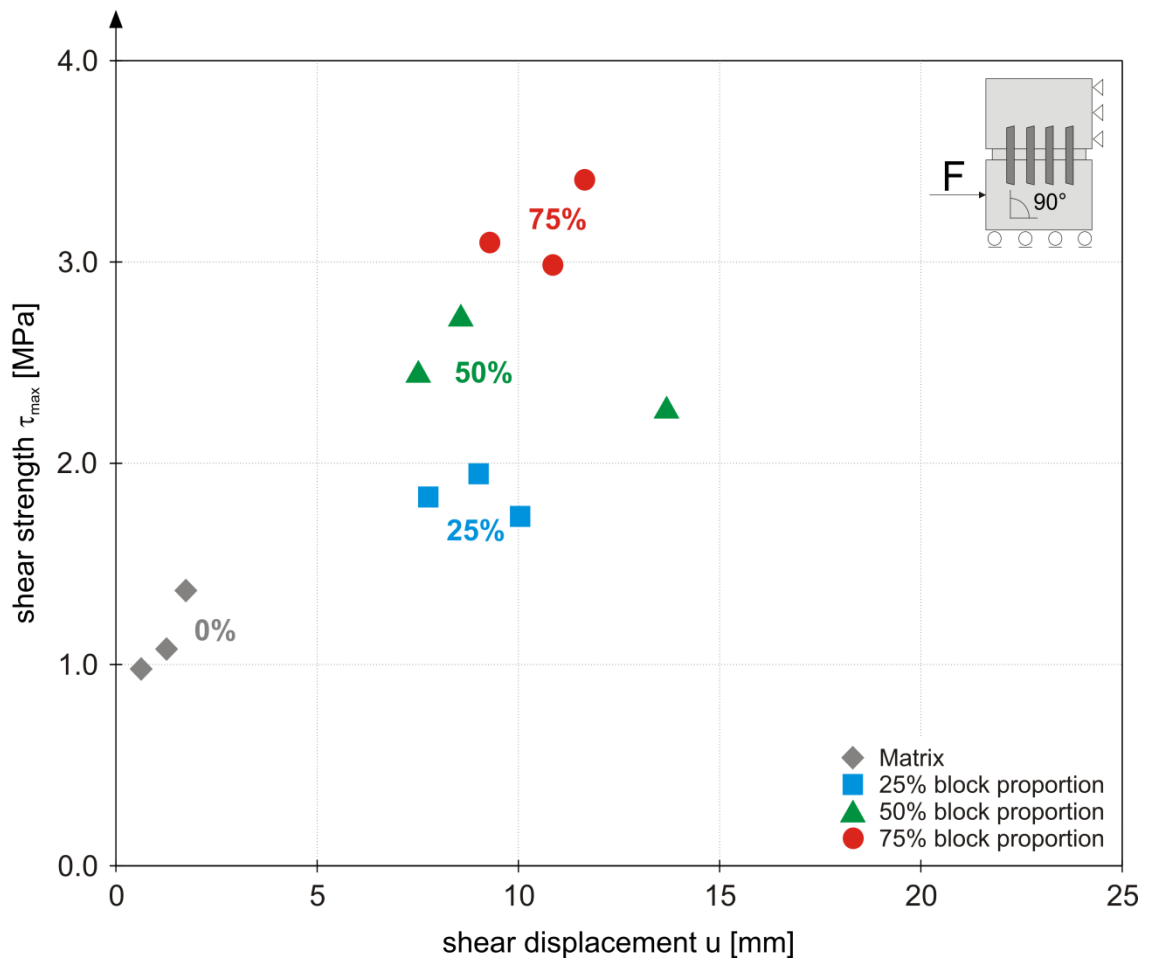


Figure 96: Peak shear strength versus shear displacement for 90° block orientation.

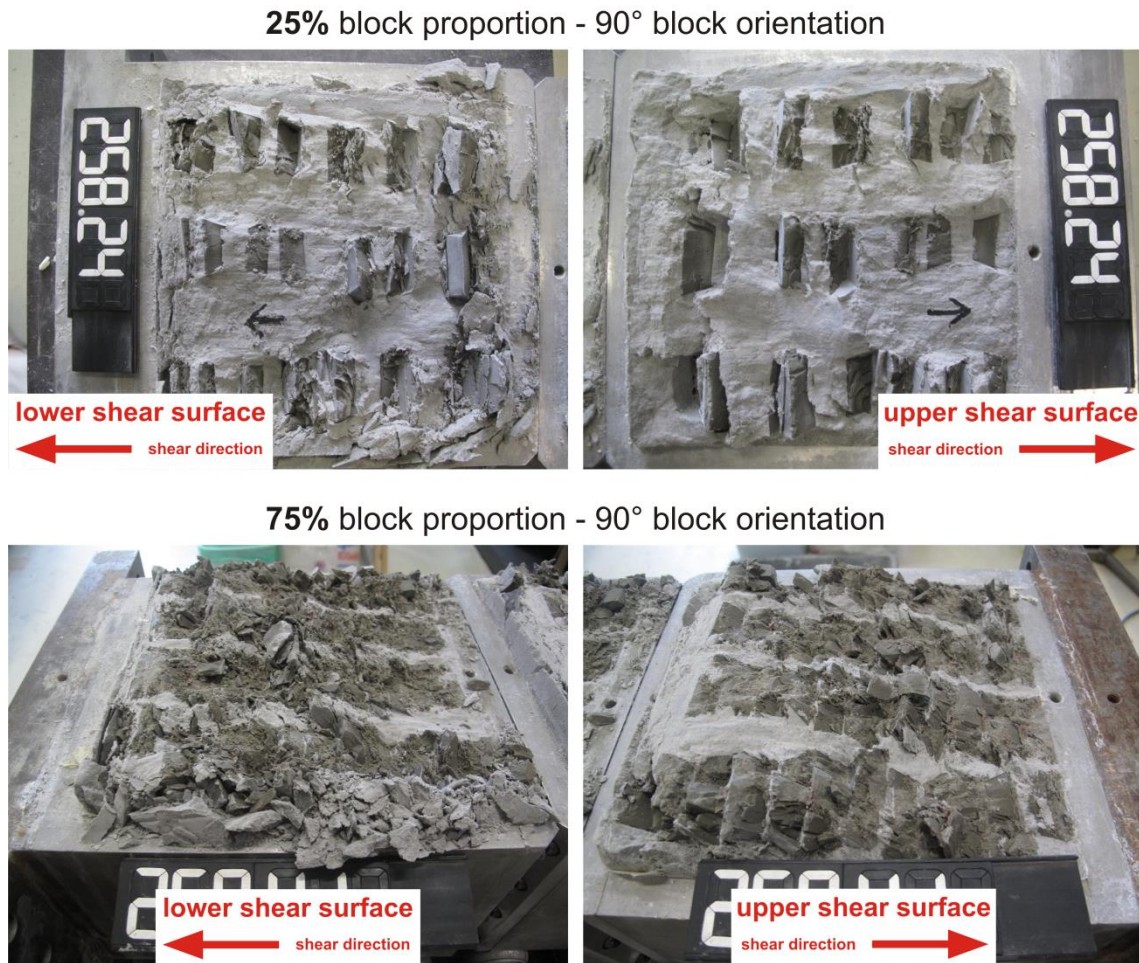


Figure 97: Shear surfaces after the test for 90° block orientation and 25% (top) and 75% block proportion (bottom).

A contrary picture is given for the 60° block orientation samples (Figure 98). The increase in shear strength is less pronounced than in the 90° block orientation samples. However, the specimen with blocks inclined against shear direction feature a much more ductile behavior, expressed in higher associated shear displacements at maximum shear strength. The highest amount of shear strength is observed for 50% block proportion, while for higher block proportions a decrease of peak shear strength appears. This behavior might be deemed as somewhat implausible at first glance. However, having a closer look on the shear surfaces after the test for the 50% and 75% block proportion samples (see Figure 99) this finding can be explained. At the beginning of the shear process the 60° block orientation samples exhibit slight sliding along blocks. With further shear displacement blocks are damaged and crushed, resulting in a pronounced shear surface roughness which steadily increases with advancing shear displacement. This behavior of increased shear surface is more pronounced for the 50% block proportion samples due to the fact that there is still sufficient amount of matrix between the blocks, allowing the blocks to rotate and to be pushed into the matrix to a certain degree. This increases the crushing process and hence the amount of increased roughness. For the 75% block proportion samples, blocks are mainly

aligned side by side with only a minor degree of matrix between the blocks. Hence rotational effects are restrained, which results in a more brittle failure of blocks (Figure 99 lower right side) and less pronounced shear surface roughness, yielding a lower value for the peak shear strength. The tests with 75% block proportion, inclined against shear direction, show an offset in shear displacement at peak shear strength. The sample with 75% block proportion, reaching its peak shear strength at approximately 16 mm of shear displacement, shows a slight decrease of shear resistance between 16 mm and 25 mm. On the other hand, the second sample with 75% block proportion, inclined against shear direction, features a continuous increase of shear stress and reaches the maximum shear strength at 25 mm of shear displacement. However, both samples exhibit basically the same behavior, which is explained in detail in Chapter 5.2.3.

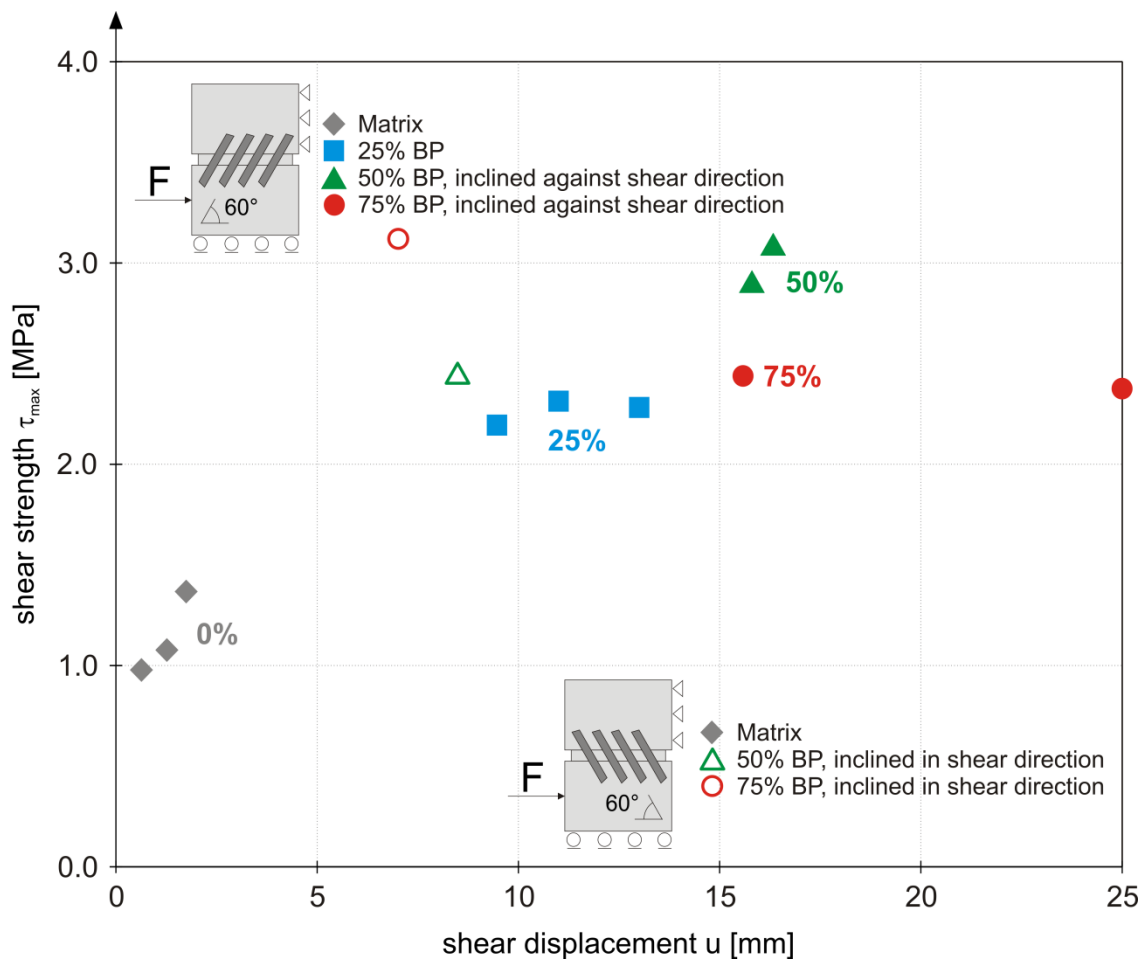


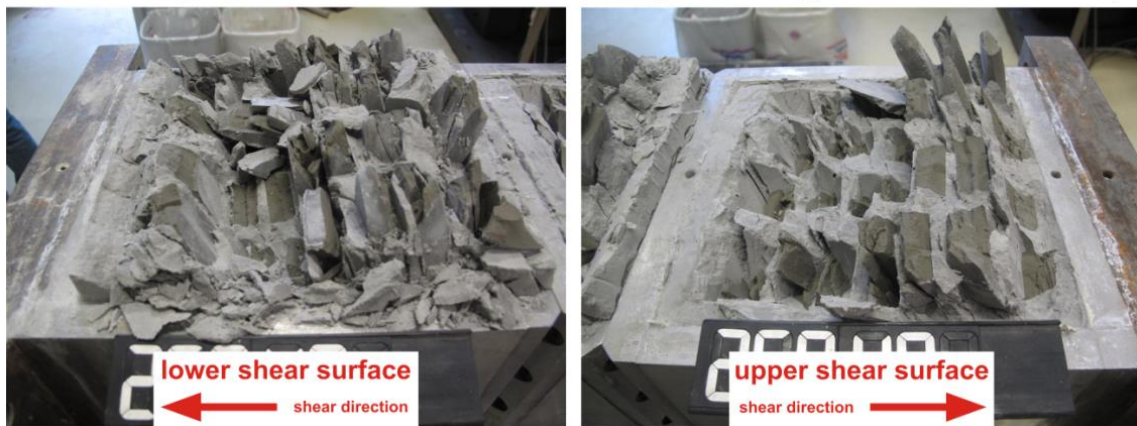
Figure 98: Peak shear strength versus shear displacement for 60° block orientation.

Considering the arrangement with blocks inclined in shear direction (not colored labels in Figure 98), it appears that these results do not fit well into the picture of the observed results for blocks inclined against shear direction. The 50% block proportion arrangement samples with blocks inclined in shear direction feature a lower value of maximum shear strength, while the 75% block proportion sample yields quite higher peak shear strength, compared to the specimen with blocks



inclined against shear direction. However, one must be aware that samples with blocks inclined in shear direction exhibit a completely different failure behavior. In this arrangement the blocks experience solely tensional stresses during shearing, due to the geometric conditions. Once the blocks have failed in tension, which yields smooth failure planes of the blocks, the ability to increase the shear surface roughness is given to a minor degree only.

**50% block proportion - 60° block orientation (inclined **against** shear direction)**



**75% block proportion - 60° block orientation (inclined **against** shear direction)**

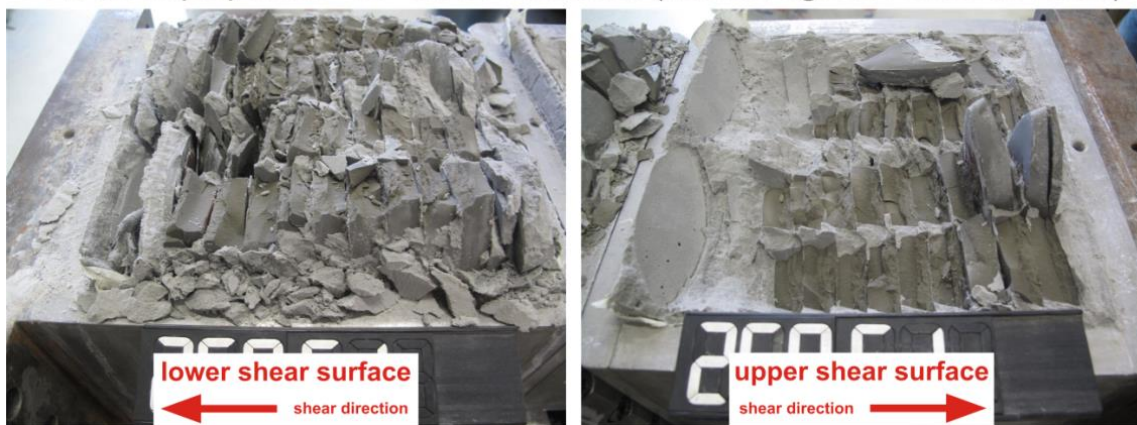


Figure 99: Shear surfaces after the test for 60° block orientation and 50% (top) and 75% block proportion (bottom), blocks inclined against shear direction.

Pure sliding along the smooth block failure surfaces takes place with increasing shear displacement and crushing of blocks is observed at a small scale only. This yields very fine-grained block particles in the shear surface which constitute negligible contribution to shear resistance (Figure 100).

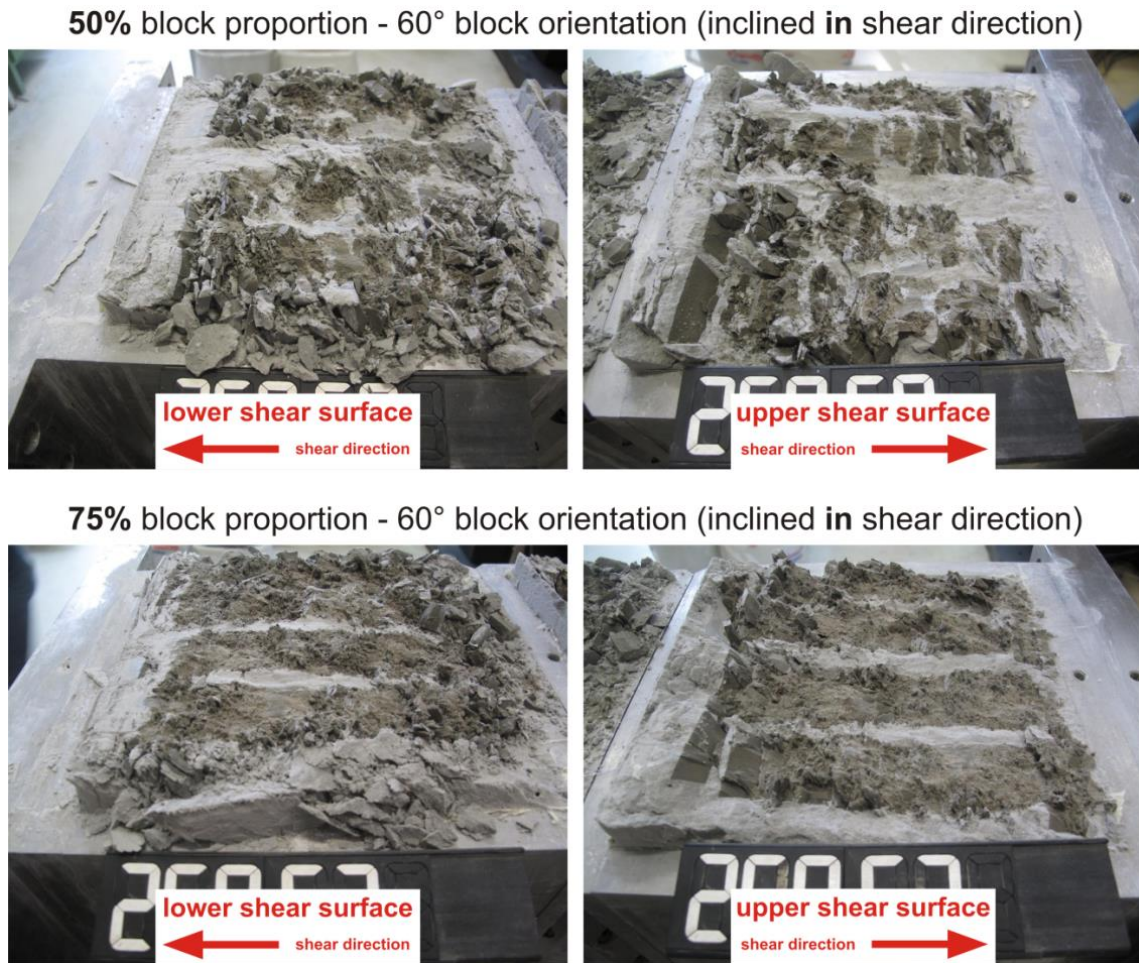


Figure 100: Shear surfaces after the test for 60° block orientation and 50% (top) and 75% block proportion (bottom), blocks inclined in shear direction.

Compared to the 90° and 60° block orientation samples, specimen with 30° block orientation provide some differences (Figure 101). For 25% block proportion, inclined against shear direction, a much more brittle behavior can be observed, accompanied by lower peak shear strength. Also the 50% block proportion samples feature lower maximum shear strength, compared to samples with 60° and 90° orientation at same block proportion. It can be seen that the 50% block proportion samples, inclined against shear direction, show a scattered result. One sample reaches the maximum shear strength at approximately 4 mm of shear displacement, while the second tested sample exhibits the peak shear strength at 25 mm shear displacement. Samples with 30° block orientation and 50% block proportion were ascribed to shear behavior type D, which features a steady increase of shear stress until the maximum shear displacement. However, sample one (maximum shear strength at 4 mm of shear displacement) shows a pronounced horizontal plateau of shear stress with no further increase in shear strength with increasing shear displacement, while for the second sample shear stress is continuously increasing, although only with a low gradient. Therefore, both 50% block proportion samples exhibit basically the same behavior.

The 75% block proportion specimen stand out with relatively high peak shear strength at maximum shear displacement, representing a very ductile behavior. The results for samples with blocks inclined in shear direction depict a coherent picture for all block proportions tested. Maximum shear strength is reached after relatively low shear displacement (brittle behavior), and the samples feature almost linearly increasing shear strength with increasing block proportion.

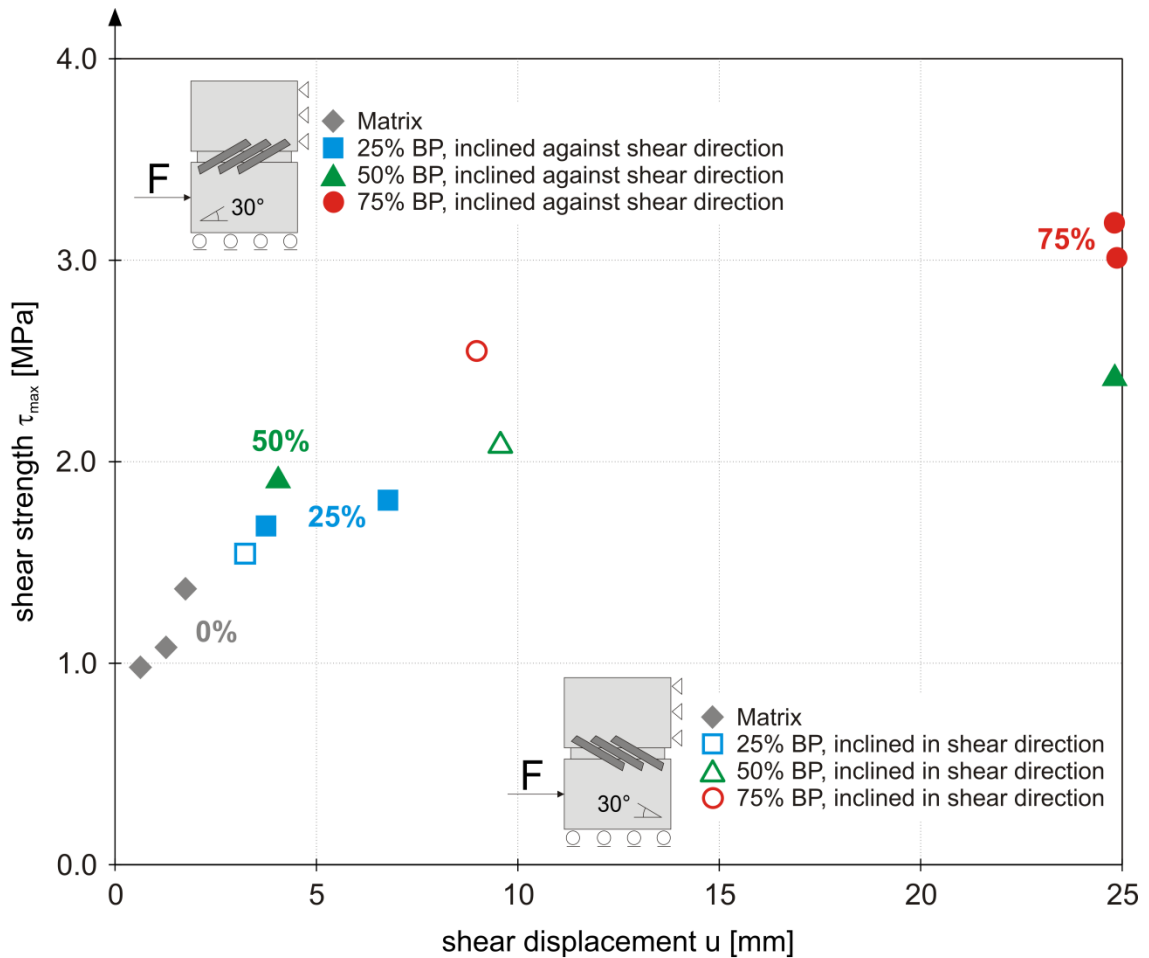


Figure 101: Peak shear strength versus shear displacement for 30° block orientation.

A closer examination of the shear surfaces after the test backs the above mentioned results (Figure 102). For samples with blocks inclined against shear direction, pure sliding along blocks with almost no damage of blocks takes place, which results in an undulating shear surface at large scale but still very smooth surfaces at small scale. This yields high values for dilatancy but constitutes only insignificant contribution to shear resistance.

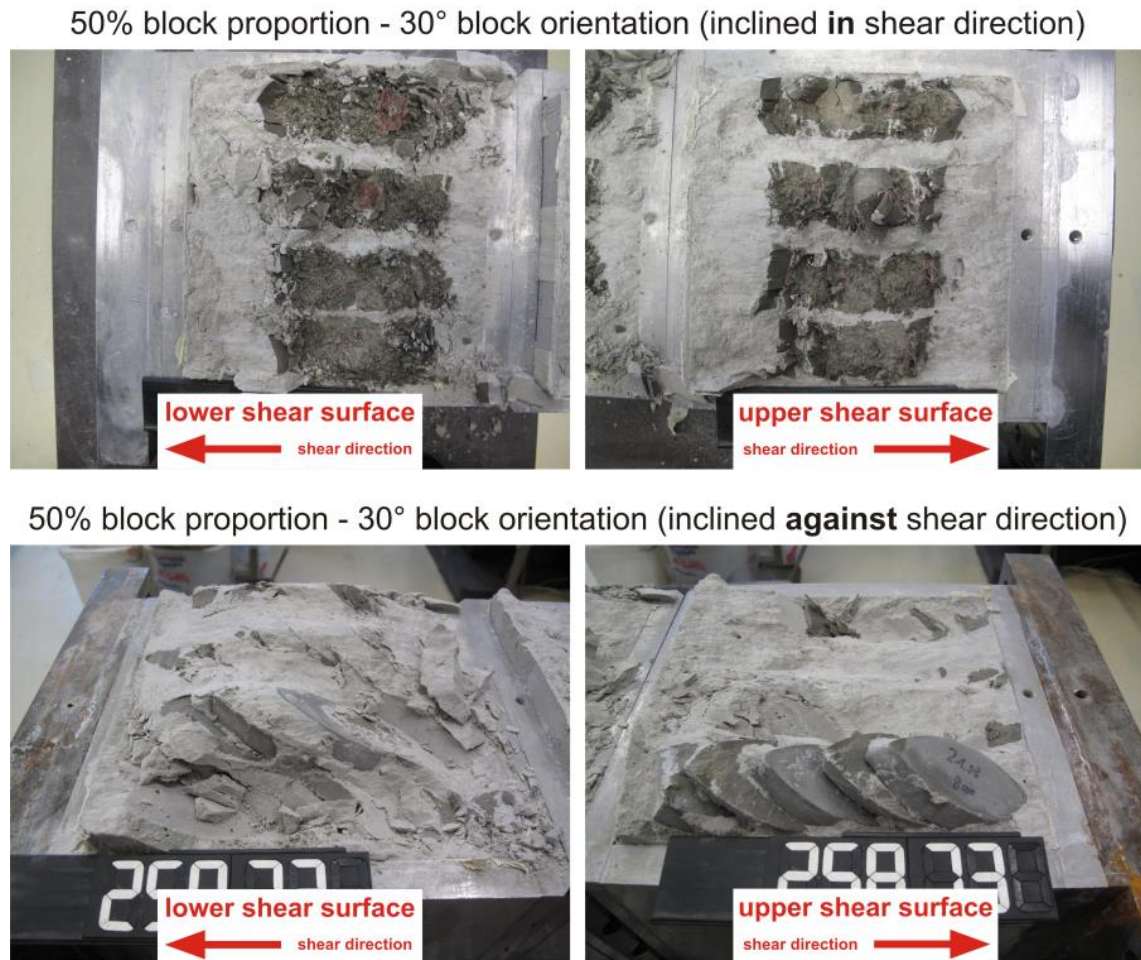


Figure 102: Shear surfaces after the test for 30° block orientation and 50% block proportion, blocks inclined in shear direction (top) and inclined against shear direction (bottom).

The normalized shear strength versus the block proportion is depicted in Figure 103 through Figure 105. In this context, “normalized” means that the discrete values of peak shear strength are divided by the mean value of maximum shear strength of all tests performed on pure matrix material. The results depict a conclusive picture. If one considers samples with 90° block orientation it can be seen that the shear strength almost linearly increases with increasing block proportion (Figure 103). Fitting a best fit straight line to the mean value of each block proportion yields a gradient for the line, given in Equation (20).

$$\tau_{\max, \text{norm}}^{90^\circ} = 1.0 + 0.0236 \cdot BP \quad (20)$$

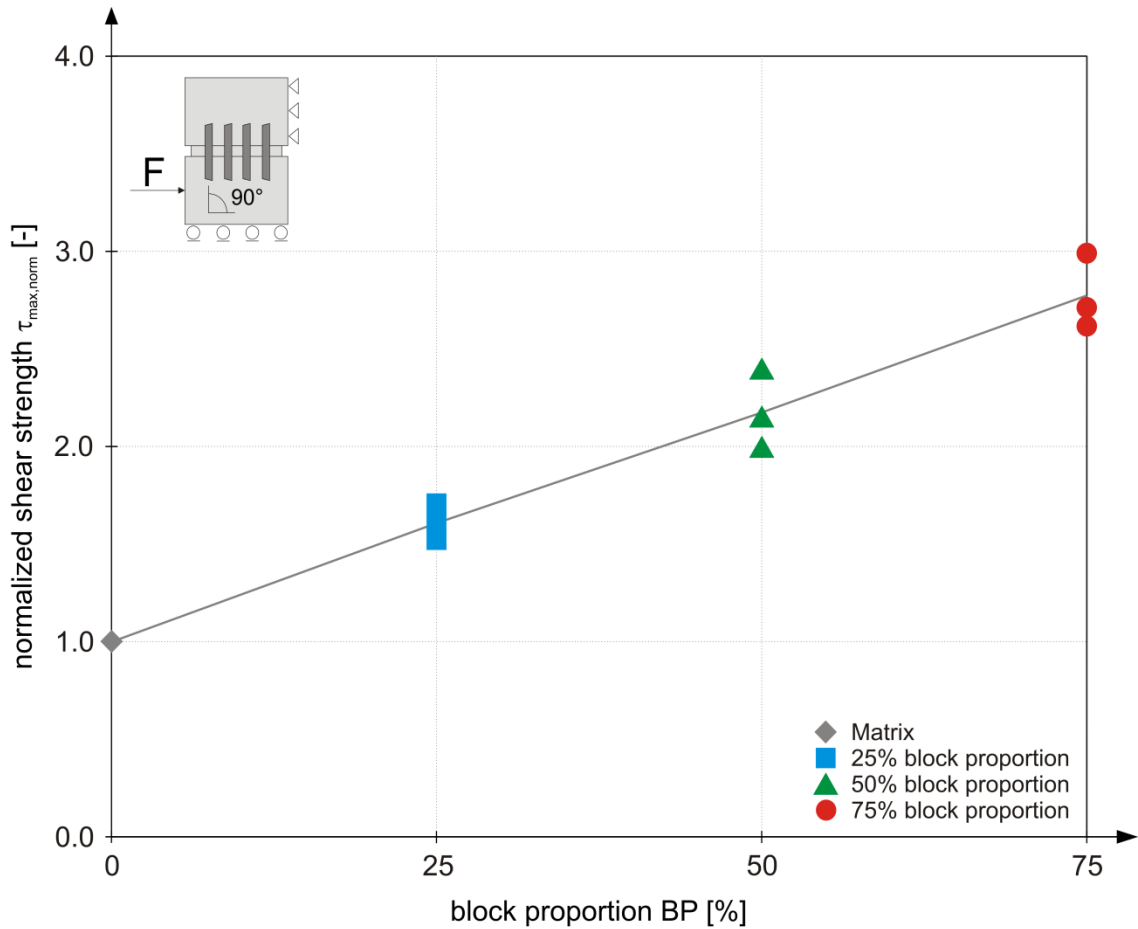


Figure 103: Peak shear strength (normalized by matrix strength) versus block proportion for 90° block orientation.

Up to 50% block proportion the samples with 60° block orientation, inclined against shear direction yielded the highest contribution to shear strength, while a decrease of shear strength for 75% block proportion was observed (Figure 104). The reason for this finding was explained earlier in this section. The samples with blocks inclined in shear direction exhibit a perfectly linear trend. Fitting a straight line to the mean values yields Equation (21) for blocks inclined against shear direction.

$$\begin{aligned} \tau_{max, norm}^{60^{\circ} \backslash \backslash} &= 1.0 + 0.0339 \cdot BP; & \text{for } BP \leq 50 \\ \tau_{max, norm}^{60^{\circ} \backslash \backslash} &= 3.67 - 0.0207 \cdot BP; & \text{for } BP > 50 \end{aligned} \quad (21)$$

The increase of peak shear strength with increasing block proportion for samples with blocks inclined in shear direction is given in Equation (22):

$$\tau_{max, norm}^{60^{\circ} \backslash \backslash} = 1.0 + 0.0231 \cdot BP \quad (22)$$

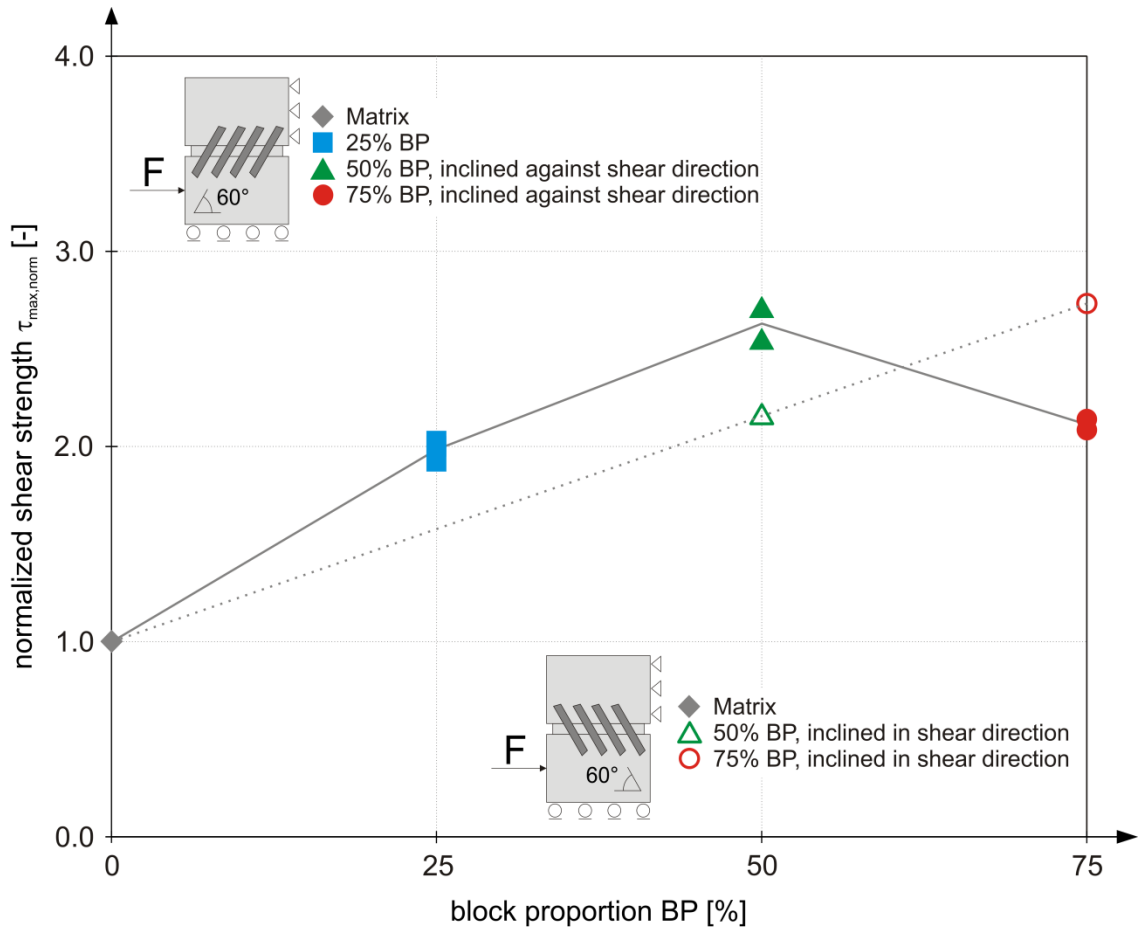


Figure 104: Peak shear strength (normalized by matrix strength) versus block proportion for 60° block orientation.

The samples with 30° block orientation (Figure 105), where blocks are inclined against shear direction, feature a linear increase with increasing block proportion, which is more pronounced for block proportions above 50%. A straight line was fitted to the discrete data points, somewhat omitting the slightly more pronounced increase in shear strength above 50% block proportion. However, for the sake of straightforward practical purposes and due to the natural scatter of laboratory test results, this approach was deemed as valid. Blocks, which are inclined in shear direction, show an almost perfectly linear increase with increasing block content.

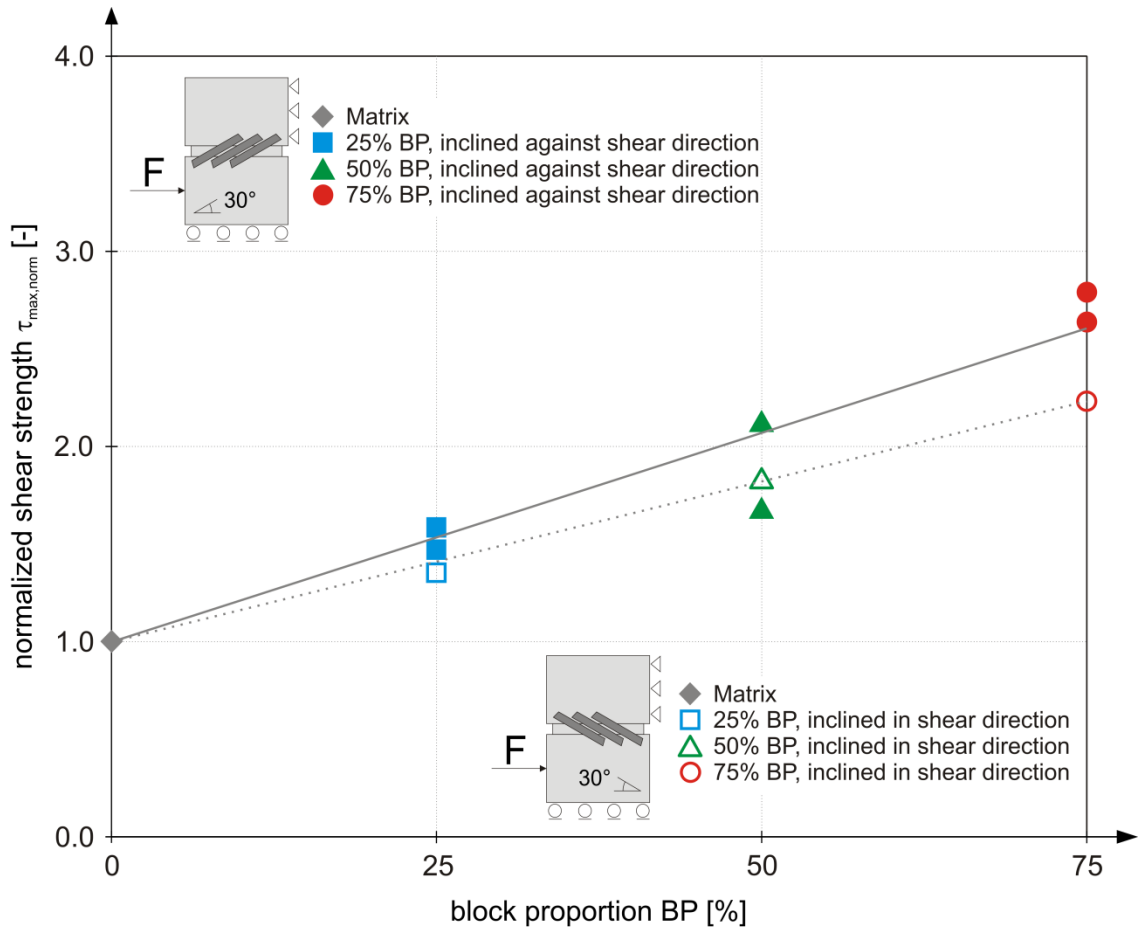


Figure 105: Peak shear strength (normalized by matrix strength) versus block proportion for 30° block orientation.

The increase in peak shear strength for samples with blocks inclined against shear direction follows Equation (23).

$$\tau_{max, norm}^{30^{\circ}///} = 1.0 + 0.0214 \cdot BP \quad (23)$$

Specimen with blocks inclined in shear direction show an increase of peak shear strength of the form (Equation (24)):

$$\tau_{max, norm}^{30^{\circ}\\\\} = 1.0 + 0.0164 \cdot BP \quad (24)$$

The change in shear strength with block proportion for all three tested variations in block orientation (30°, 60° and 90° block orientation) is given in Table 12 at a glance. If one has a closer look on the equations, summarized in Table 11, it becomes evident, that samples with 30° block orientation, inclined against shear direction, samples with 60° block orientation, inclined in shear direction, as well as samples with 90° block orientation feature almost the same amount of increase of shear strength with increasing block proportion.

The increase factors are in the range between 2.1% and 2.4% of shear strength increase per percent of block proportion increase. Samples with 30° block orientation, with blocks inclined in shear direction provide a lower bound of shear strength increase with increasing block proportion. Samples with 60° block orientation, inclined against shear direction exhibit the highest contribution to shear strength increase with increasing block proportion.

By knowing the shear strength of the matrix, in combination with the block proportion, the relationships, shown in Table 12, provide a rough guide to estimate the peak shear strength of a bimrock material.

Table 12: Compilation of factors for the change of peak shear strength with block proportion.

(normalized) peak shear strength	Block orientation		
	30° block orientation	60° block orientation	90° block orientation
$\tau_{max, norm}$	Blocks inclined <i>against</i> shear direction		1.0 + 0.0236 · BP
	1.0 + 0.0214 · BP	for BP ≤ 50	
		1.0 + 0.0339 · BP	
		for BP > 50	
		3.67 – 0.0207 · BP	
Blocks inclined <i>in</i> shear direction			
1.0 + 0.0164 · BP	1.0 + 0.0231 · BP		

BP ... block proportion in [%]



### 5.2.3 Influence of block proportion and block orientation on the stress path and stress-displacement behavior

The samples with  $60^\circ$  block orientation, which were assigned to shear behavior type E, feature a steady increase of shear stress and normal stress after the sample starts to dilate (Figure 106). However, a peculiarity of the  $60^\circ$  block orientation arrangement is that the amount of incremental increase in shear stress constantly decreases with increasing shear displacement. After reaching the peak shear strength a non-pronounced or even non-existent post peak region is present for blocks inclined against shear direction. For samples with blocks inclined in shear direction a much more pronounced increase of shear stress with less pronounced increase of normal stress, resulting in much higher shear resistance, is observed. In addition, a distinct post peak region is present. These findings are clearly depicted in the shear stress versus shear displacement plots (Figure 107). For the samples with blocks inclined against shear direction the peak shear strength is reached after very high shear displacement. The reason for this is found in the continuous damage of blocks with advancing shear displacement and hence a persistent increase in shear resistance. However, during the shearing process the broken block particles are further damaged and crushed, yielding more and more finely-grained particles. The fine block particles still contribute to shear resistance, although the incremental increase of shear resistance is continuously decreased.

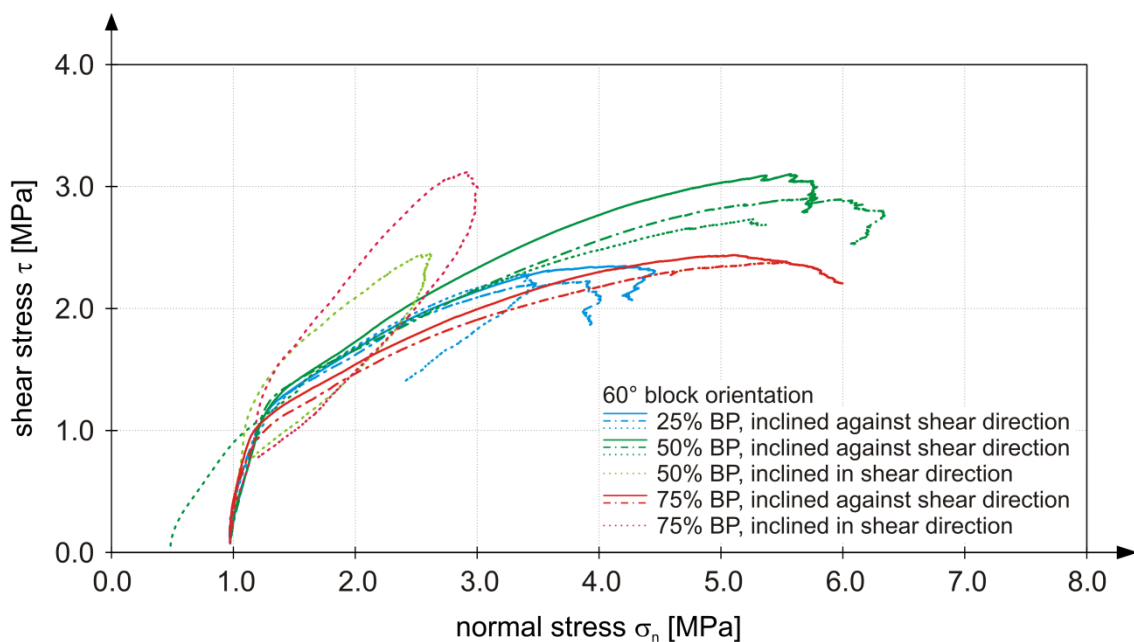


Figure 106: Stress paths for  $60^\circ$  block orientation and different block proportions.

A contrary picture is given for blocks which are inclined in shear direction. As already explained above, the blocks exhibit mostly tensional stress, hence providing relatively high shear resistance at the beginning of the shearing process. Once the blocks have failed in tension the smooth crack surfaces of the blocks provide no considerable contribution to shear resistance. Only small block particles are formed with increasing shear displacement. Hence a pronounced decrease in shear resistance is observed.

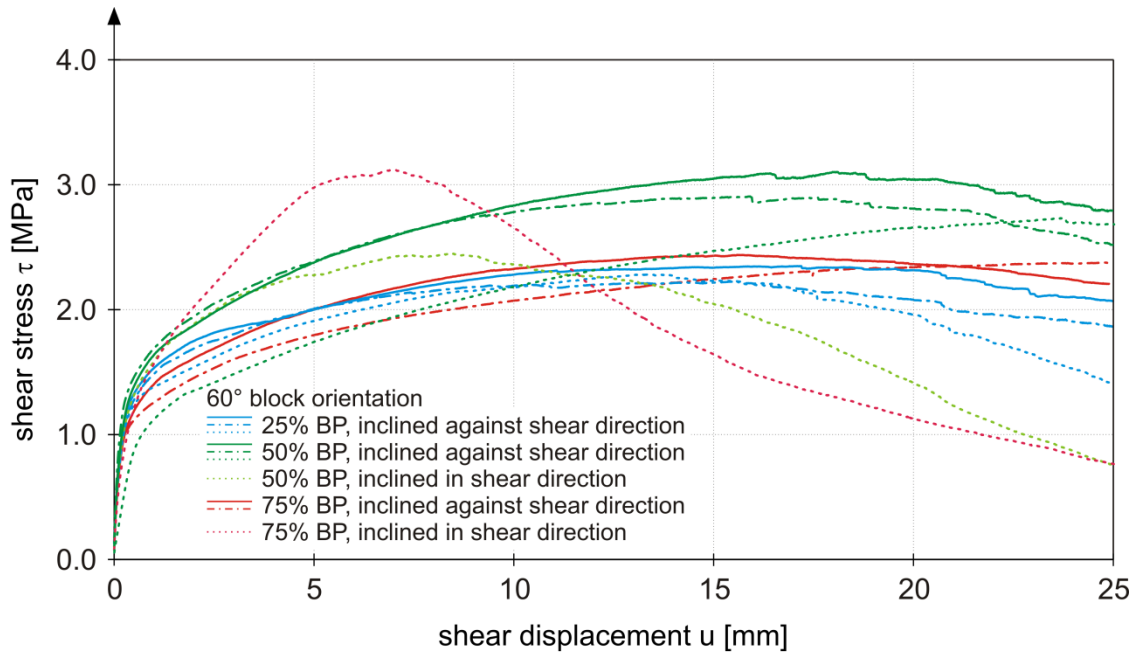


Figure 107: Shear stress versus shear displacement plot for 60° blocks orientation and different block proportions.

The samples with 90° block orientation show qualitatively a similar behavior as the 60° block orientation samples (Figure 108 and Figure 109). However, the increase of shear stress and hence the shear resistance after the onset of dilation is much more pronounced than for the 60° oriented blocks, resulting in lower amount of normal stress at peak shear strength. Also a distinct post peak region is observed. The maximum shear strength is reached after approximately the half of the maximum shear displacement. The shear stress – shear displacement plots qualitatively feature the same development for all tested block proportions, hence an influence of block proportion, as it is the case for the 60° block orientation samples, is not present.

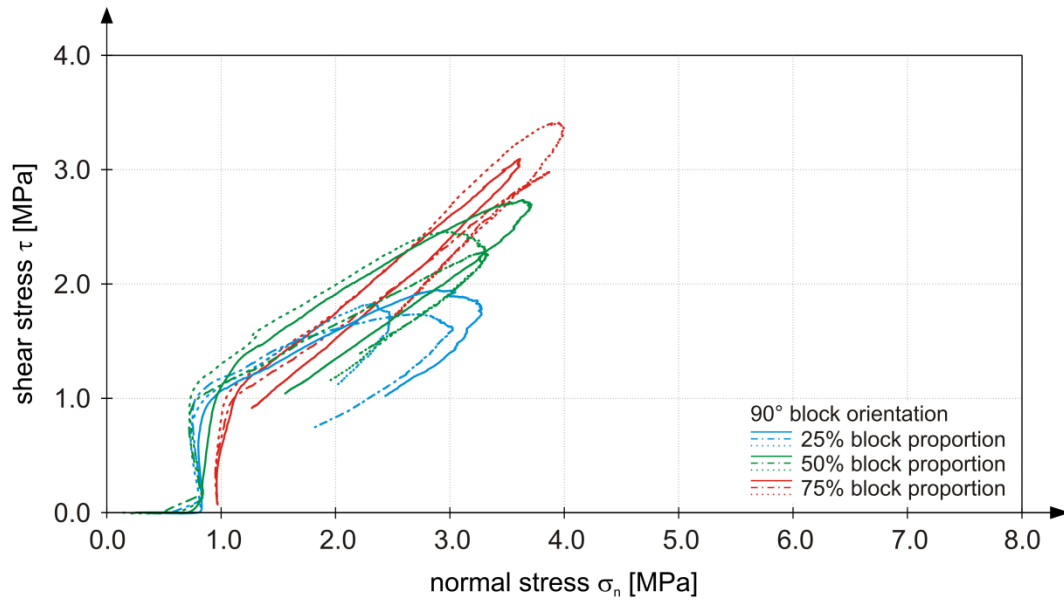


Figure 108: Stress paths for 90° block orientation and different block proportions.

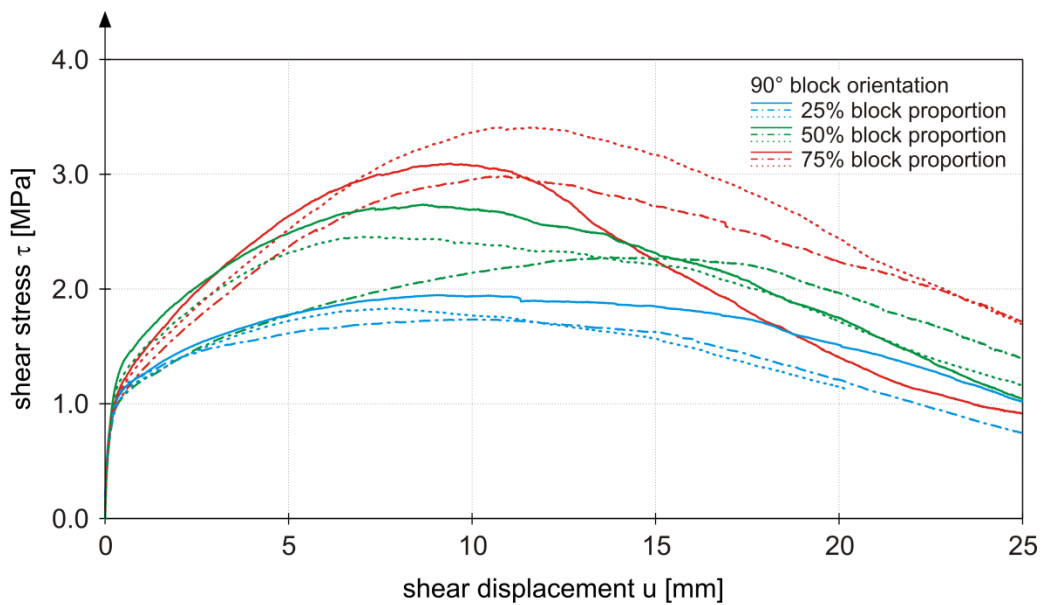


Figure 109: Shear stress versus shear displacement plot for 90° blocks orientation and different block proportions.

Considering the accumulated shear energy over the shear displacement allows a proper evaluation and investigation of the effect of block inclination with regard to the shear direction (blocks inclined in or against shear direction). The accumulated shear energy,  $W$ , is defined in Equation (25).

$$W_{(u)} = \int_0^u \tau_{(u)} \cdot du \quad (25)$$

The shear energy development was calculated for each tested sample. For the sake of allowing a proper comparison between the results, they were normalized

by the accumulated shear energy development of the matrix sample (representing a horizontal line at “ $W_{\text{norm}}=1$ ” in Figure 110 and Figure 111). The normalized shear energy developments are depicted in Figure 110 for  $30^\circ$  block orientation and Figure 111 for  $60^\circ$  block orientation samples, respectively. The solid lines therein represent samples with blocks inclined against shear direction, while the dash-dotted lines are valid for samples with blocks inclined in shear direction. It becomes evident that samples with blocks inclined against shear direction feature a pronounced ductile behavior, which is represented by a steady, mostly linear increase of shear energy development over the shear displacement. A contrary picture shows for samples with blocks being inclined in shear direction. A much more brittle behavior is observed, featuring a peak shear strength value after relatively low shear displacement, followed by a continuous decrease of shear resistance over the remaining shear displacement. This particular feature holds true for all tested samples, hence this behavior is not influenced by block proportion.

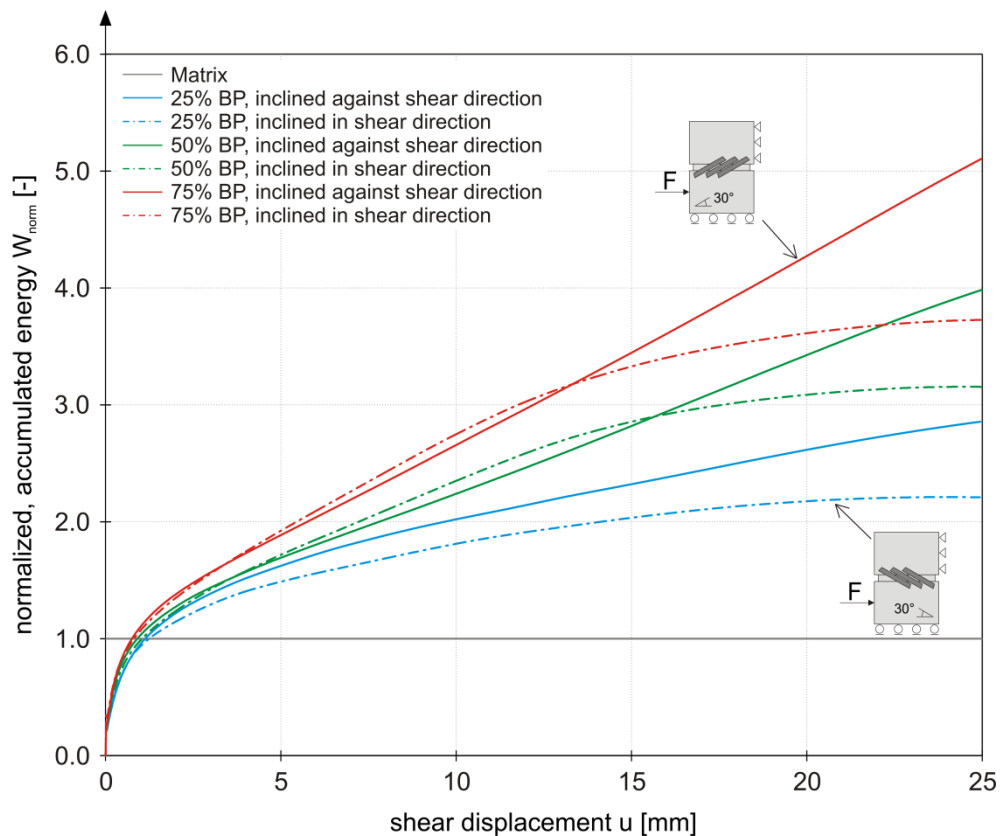


Figure 110: Normalized accumulated shear energy versus shear displacement for  $30^\circ$  block orientation.

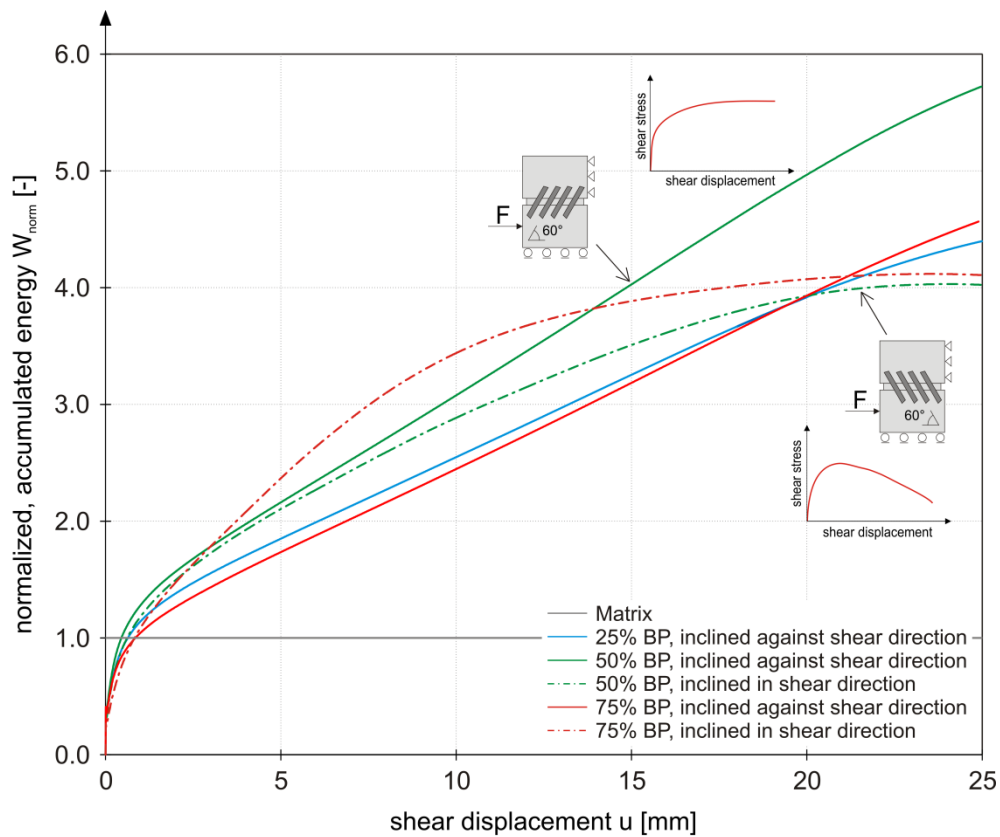


Figure 111: Normalized accumulated shear energy versus shear displacement for  $60^\circ$  block orientation.

## 5.2.4 Influence of local block arrangement on the stress path and stress-displacement behavior

Within a certain (global) block orientation, the (local) arrangement of blocks, with regard to the shear direction, in combination with different block proportions was varied and tested. This variation was restricted to the global  $90^\circ$  block orientation. A variation for the  $30^\circ$  and  $60^\circ$  block orientation within this context would have led to excessive and highly unmanageable specimen preparation effort due to unchangeable geometric constraints.

For the first two types of block arrangement, which were investigated and are explained here, the blocks are vertically aligned ( $90^\circ$  block orientation, normal stress in z-direction of the blocks). The blocks are arranged in a way that for type I the blocks are exposed to shearing in y-direction of the block and for type II the shear direction coincides with the blocks' x-axis (Figure 112). The upper half of Figure 112 shows the aligned blocks during sample preparation, while the sketch in the lower half depicts the orientation of shear stress  $\tau$  and normal stress  $\sigma_n$ .

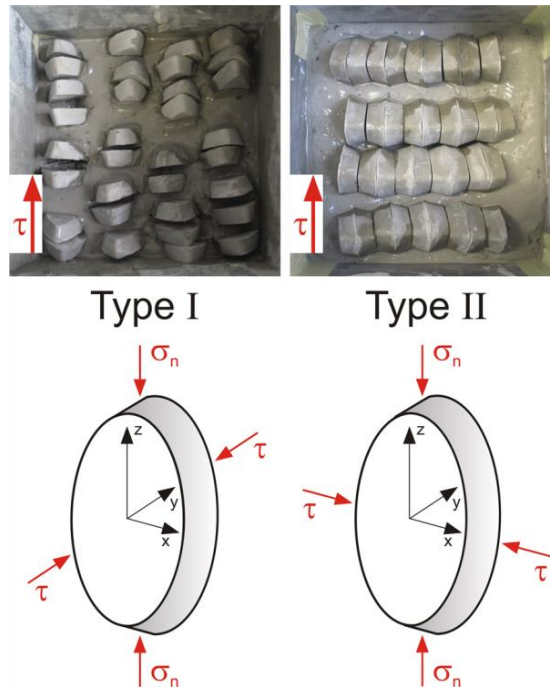


Figure 112: Graphical explanation of global 90° block orientation and local block arrangement type I and type II.

The stress paths are shown in Figure 113. The solid lines illustrate block arrangement type I, while the dotted lines stand for block arrangement type II. The development of the individual stress paths for different block proportions and the two types of local block arrangement appears qualitatively similar. However, samples with block arrangement type II provide much higher shear resistance after the samples start to dilate, expressed by a higher curve gradient and higher amount of peak shear strength. This behavior was basically as expected. The samples with block arrangement type II exhibit a slightly more ductile behavior, expressed by higher shear displacement magnitudes at peak shear strength (Figure 114). Therefore, block arrangement type II could be ascribed to shear behavior type F, while block arrangement type I was assigned to shear behavior type E (see Chapter 5.2.1 for explanation).

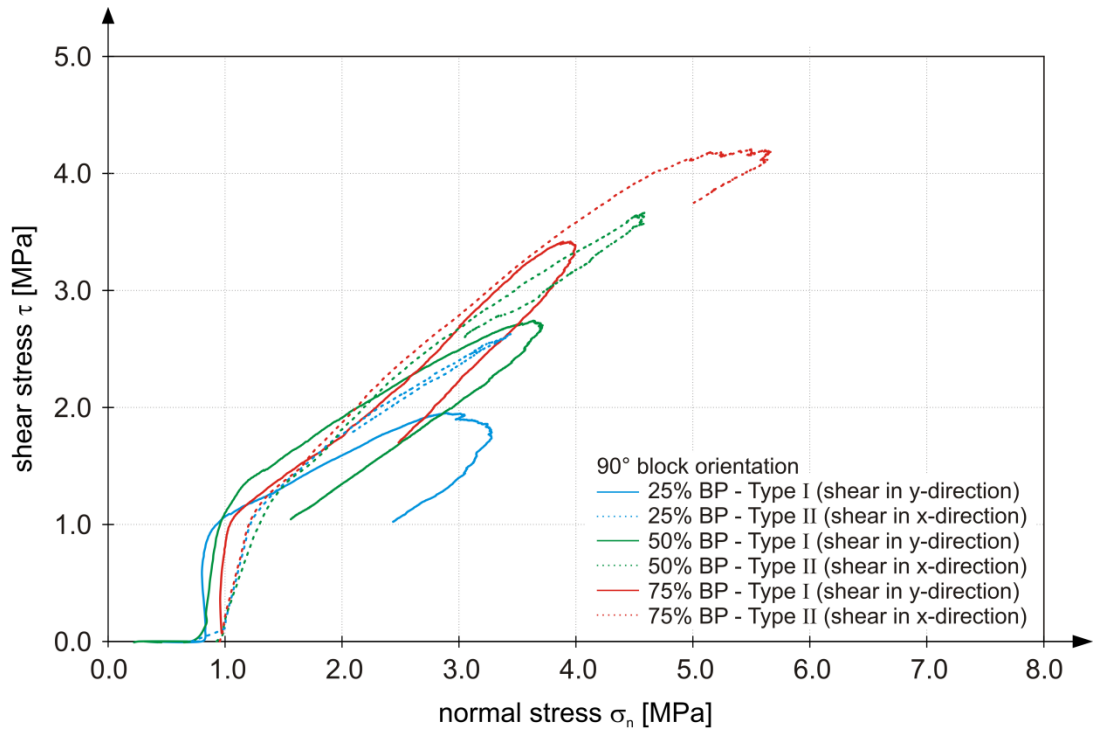


Figure 113: Stress paths for global 90° block orientation and local type I and type II block arrangement.

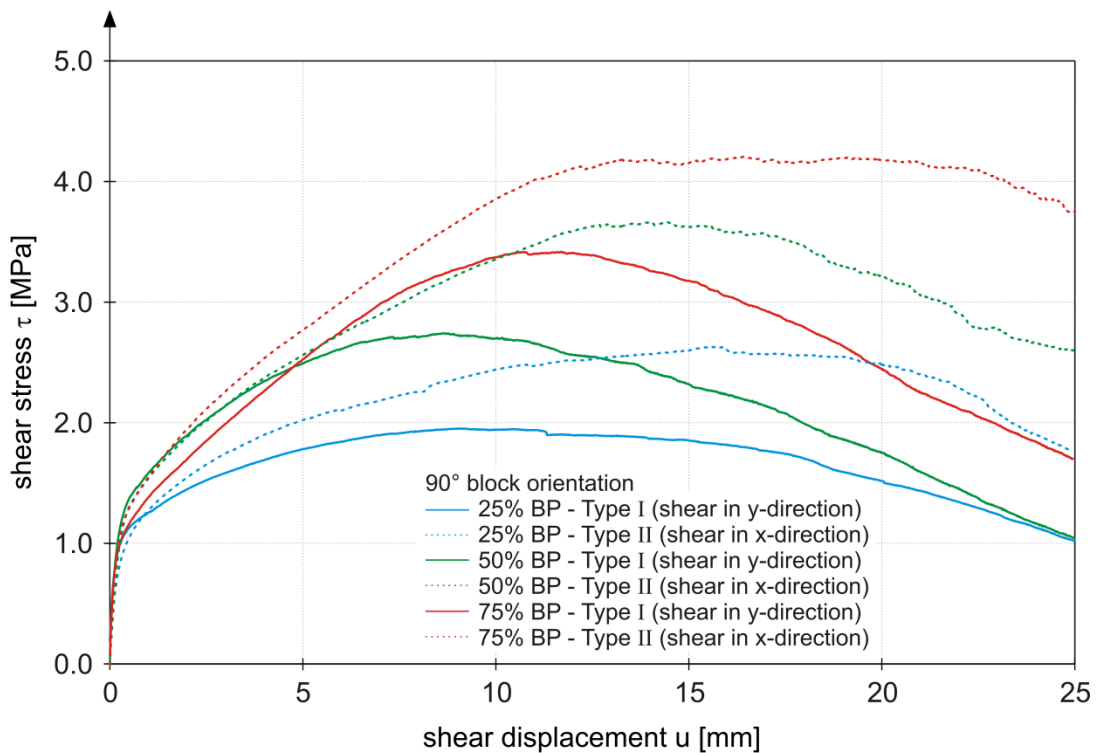


Figure 114: Shear stress versus shear displacement for global 90° block orientation and local type I and type II block arrangement.

Considering a relatively simple mechanical model allows an explanation for this finding. If we assume the blocks acting as beams, supported by the matrix and exposed to shear force, one can apply a mechanical analogy to moment of resistance, where blocks in arrangement type I are bent along their weak axis, while type II blocks are loaded along their strong axis. The moment of resistance,  $W$ , for a rectangular section is given by Equation (26).

$$W = \frac{b \cdot h^2}{6} \quad (26)$$

For the sake of simplicity, the ellipsoidal shape of the blocks is converted to a rectangular section, having the same length (z-axis of block) as the blocks and a height (x-axis of block) adjusted to receive an area equivalent to the original block area (in x-z – plane). The moments of inertia for both type I and type II arrangement calculate to (Equation (27)):

$$\begin{aligned} W_{\text{type I}} &= \frac{x \cdot y^2}{6} = \frac{28.5 \cdot 15^2}{6} = 1068.8 \text{ [mm}^3\text{]} \\ W_{\text{type II}} &= \frac{y \cdot x^2}{6} = \frac{15 \cdot 28.5^2}{6} = 2030.6 \text{ [mm}^3\text{]} \end{aligned} \quad (27)$$

The ratio of the moments of inertia between type II (strong axis) and type I (weak axis) is (Equation (28)):

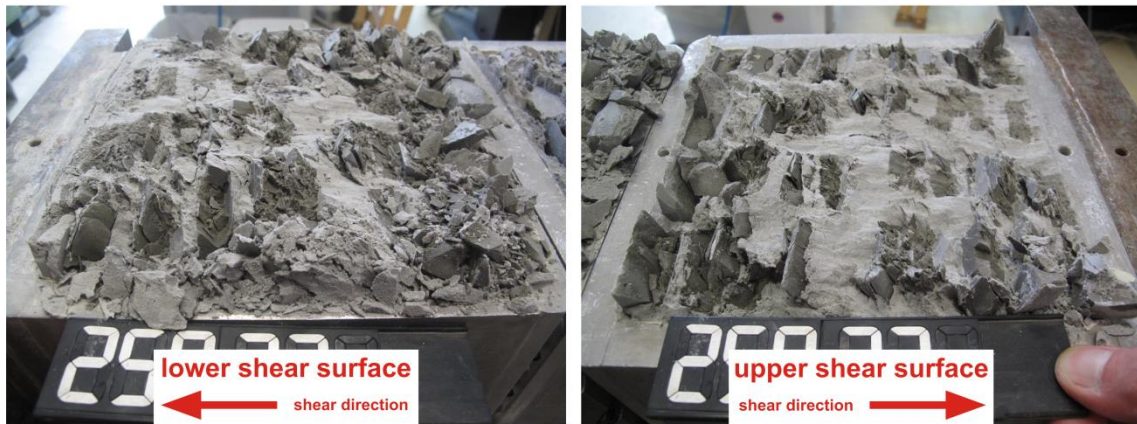
$$\psi = \frac{W_{\text{type II}}}{W_{\text{type I}}} = \frac{2030.6}{1068.8} = 1.9 \text{ [-]} \quad (28)$$

If one disregards all other mechanical effects involved, omitting the influence of the matrix, etc., this would imply that block arrangement type II should feature about 1.9 times higher values for peak shear strength than block arrangement type I. However, the mechanical processes are certainly much more complex. If we consider the shear surfaces after the test for both block arrangement type I and type II, respectively, a completely different shear surface development becomes evident (Figure 115). Block arrangement type I features relative smooth cracking of blocks. With increasing shear displacement additional damaging of blocks at small scale takes place, increasing the shear surface roughness to a certain degree. On the other hand block arrangement type II provides a fairly divergent picture. It turned out that the blocks are partially pulled out of the matrix due to the ellipsoidal shape of the blocks and a more favorable block arrangement than in the type I case. Pulling out of blocks pronounced in the front section of the shear box. The blocks themselves exhibit mostly smooth cracking, especially in the central part of the shear surface. In the rear part the blocks are more damaged and crushed, yielding finely-crushed block particles. The peculiarities of the shear surfaces are also reflected in the shear stress-shear



displacement plots (Figure 114). Specimen with block arrangement type II show peak shear strength at higher shear displacement, compared to the results of samples with block arrangement type I. The decrease of shear resistance after maximum shear stress is also less pronounced in type II arrangements, due to the much higher shear surface roughness and waviness, featuring a zigzag-shaped surface (Figure 115 bottom).

**50% block proportion - 90° block orientation - block arrangement type I**



**75% block proportion - 90° block orientation - block arrangement type II**

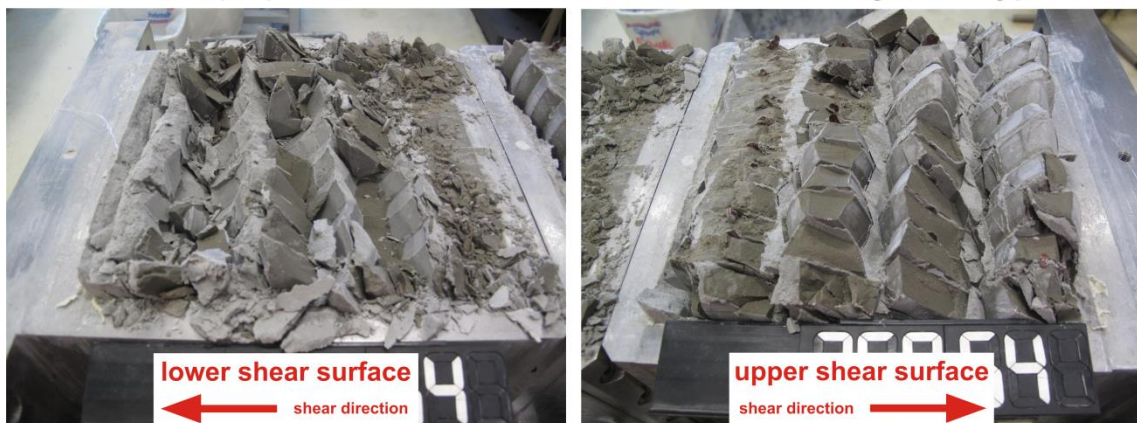


Figure 115: Shear surfaces after the test for 90° block orientation and block arrangement type I (50% block proportion, top), and block arrangement type II (75% block proportion, bottom).

In order to study the geometric influence of the shape of the blocks on the shear behavior several tests were performed on samples which cover mainly all possible block arrangements, within a certain global block orientation. The tests were conducted on specimen having the same block proportion of 50% and the same global block orientation of 90°. Figure 116 shows the five different types of local block arrangement. The upper half therein depicts the samples during preparation (top view on the lower shear box), while the lower sketches explain the orientations of shear stress  $\tau$  and normal stress  $\sigma_n$  with respect to the block coordinate system.

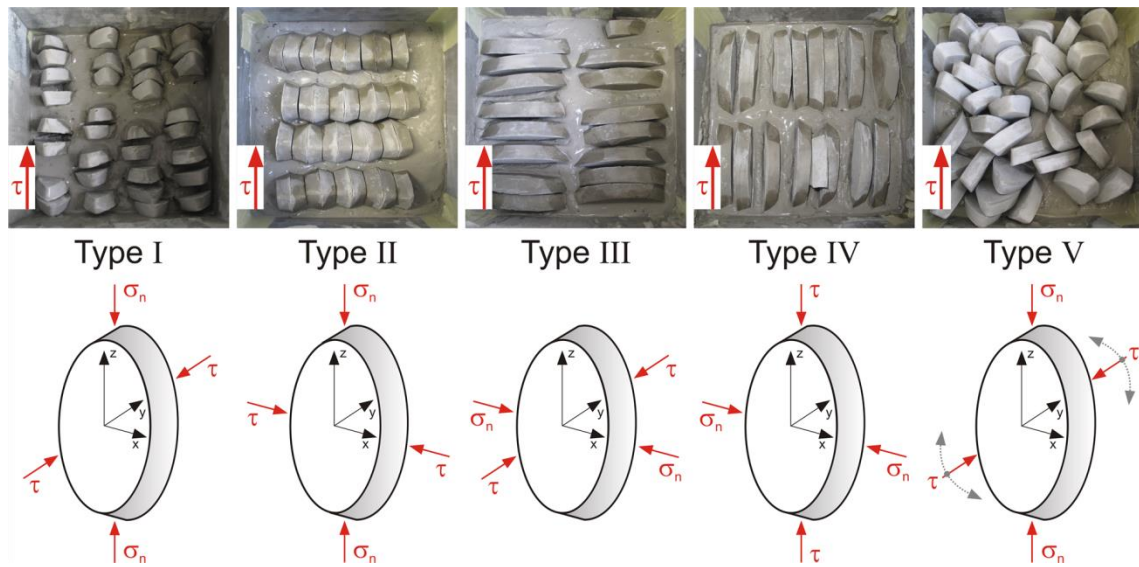


Figure 116: Graphical explanation of global 90° block orientation (50% block proportion) and local block arrangement type I to type V.

The stress paths of the five block arrangement types are depicted in Figure 117. The shear stress – normal stress behavior is basically the same for types I to III and V, type IV shows a pronounced increase of shear stress with increasing normal stress (high shear resistance), but does not possess a post peak area. Comparing groups with the same normal stress direction (type I and II, type III and IV) it is evident that type II and type IV provide higher peak shear strength than their counterparts type I and III. However, the difference in maximum shear strength is much more pronounced between type I and II, than for type III and IV. A reason for this may be found in the type of matrix embedding. For type I and II (normal stress acting in z-direction of the block), major parts of the blocks are located outside the predetermined shear zone, and therefore, they are only marginally influenced by the shear process. On the other hand in type III and IV arrangements, the blocks are mainly situated directly in the shear zone. Hence the entire block is exposed to a complex stress situation which results in diminishing influence of the block arrangement itself. Considering type V (normal stress in z-direction, blocks randomly arranged with regard to shear stress) one would expect that the peak shear stress would fall between the values of those provided by type I and II. However, type V shows a lower peak shear stress than type I, but the shear resistance until maximum shear stress is partly higher than that of the type I sample. The shear stress development versus shear displacement is depicted in Figure 118. Block arrangement type I, II and V exhibit basically the same behavior, which could be assigned to type E and F of the basic shear behavior types, given at the beginning of Chapter 5.2.1. Maximum shear stress is reached after approximately 8 mm for type I, while type II shows a more ductile behavior, resulting in a higher shear displacement value at peak shear strength (approximately 14 mm). Type V is situated between type I and II. Considering the post peak behavior, type V possesses the highest shear resistance, given by a lower decrease of shear stress, compared to type I and II. Type III provides a

distinct plateau where shear stress remains fairly constant over a shear displacement range between 7 mm and 13 mm. After reaching the peak shear strength a decrease of shear resistance is only marginally present. Type IV could be ascribed to shear behavior type D, for which an almost continuous increase in shear stress over the entire shear displacement is observed.

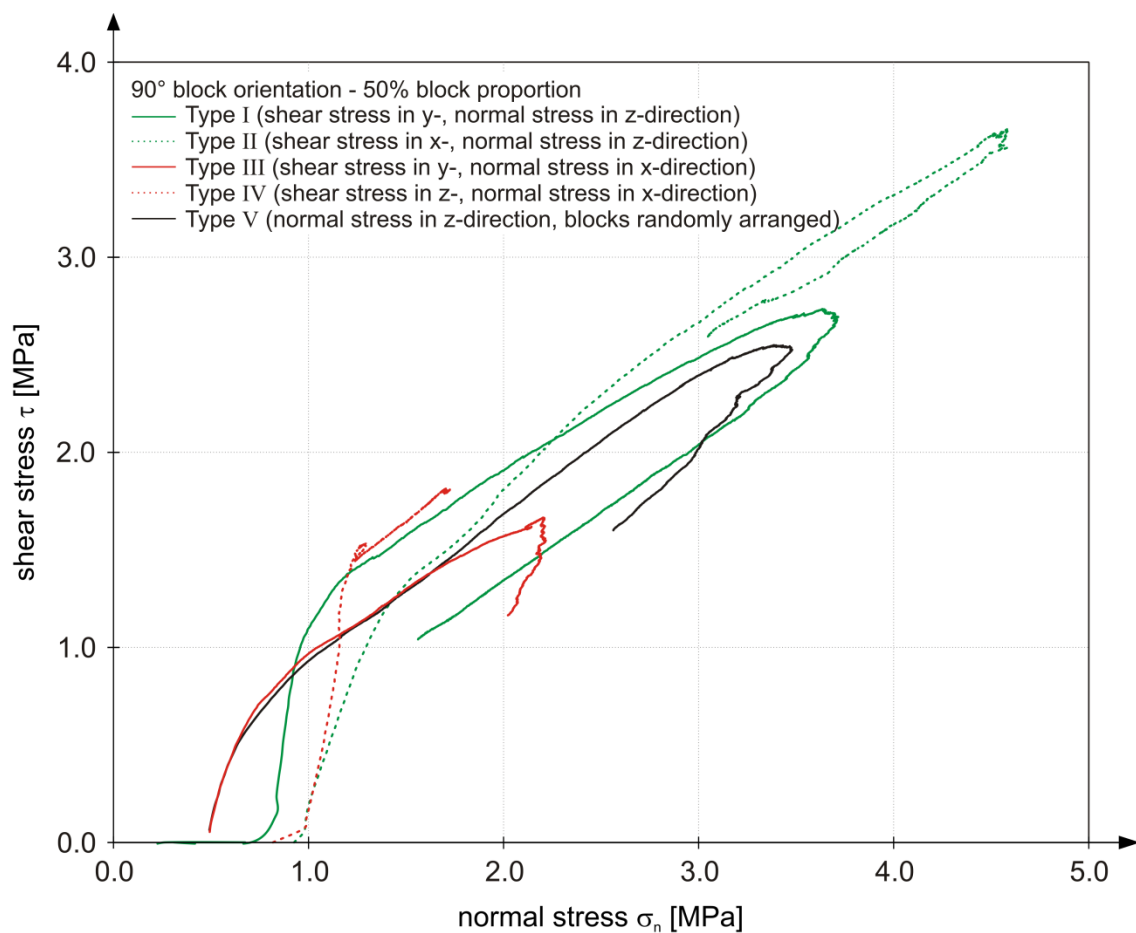


Figure 117: Stress paths for global 90° block orientation and 50% block proportion and local type I to type V block arrangement.

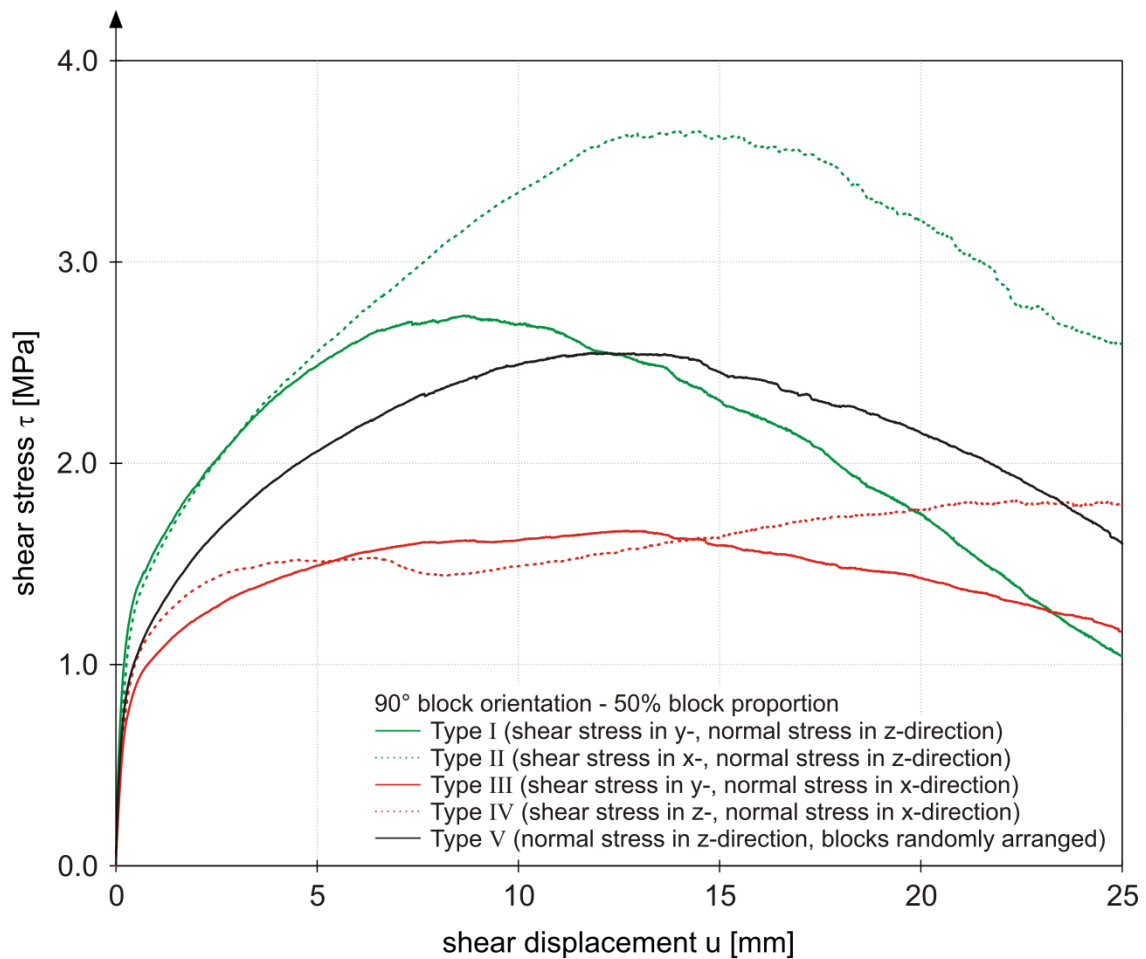


Figure 118: Shear stress versus shear displacement for global 90° block orientation and 50% block proportion and local type I to type V block arrangement.

### 5.2.5 Engineering properties of intact bimrocks

Engineering parameters like friction angle, cohesion and dilation angle of intact bimrock were evaluated and are presented in this section. The parameters were analyzed for block orientations which allowed a reasonable and proper evaluation according to the evaluation process described in Chapter 5.1.5. This was particularly the case for the samples with block orientations of 60° and 90°. The results of 0° and 30° block orientation specimen yielded stress paths which could not be described with a simple Mohr-Coulomb failure criterion. A parameter evaluation would have led to absolutely erroneous and misleading results. As mentioned in Chapter 5.1.5 and highlighted in Chapter 5.2, the mechanical behavior and processes involved in bimrocks are far too complex and manifold to be reasonably described by simple stress-strain relationships like a Mohr-Coulomb failure criterion. Therefore, the values stated here should not be understood as “de facto” values, allowing a proper structural design, but should stress the difficulties and deficiencies which arise when certain characteristics of mechanical behavior are lost by describing it with an imperfect set of parameters.

Figure 119 depicts the values for the “intact” friction angle for samples with  $90^\circ$  block orientation. When taking into account the mean values an almost linear increase of friction with increasing block proportion can be observed. This behavior was expected and can be deemed as plausible. The determined increase of friction with increasing block proportion is basically in good agreement with the findings of previous studies (Figure 14 in Chapter 2.2). However, the factor of frictional increase, evaluated in this research, is lower, compared to other studies. Lindquist (1994) and Wen-Jie et al. (2011), for example, determined a magnitude of increase of friction angle of about  $0.33^\circ$  per percent of block proportion increase (Figure 14), while this study yielded a factor of frictional increase of about  $0.12^\circ$  per percent of block proportion (Figure 119).

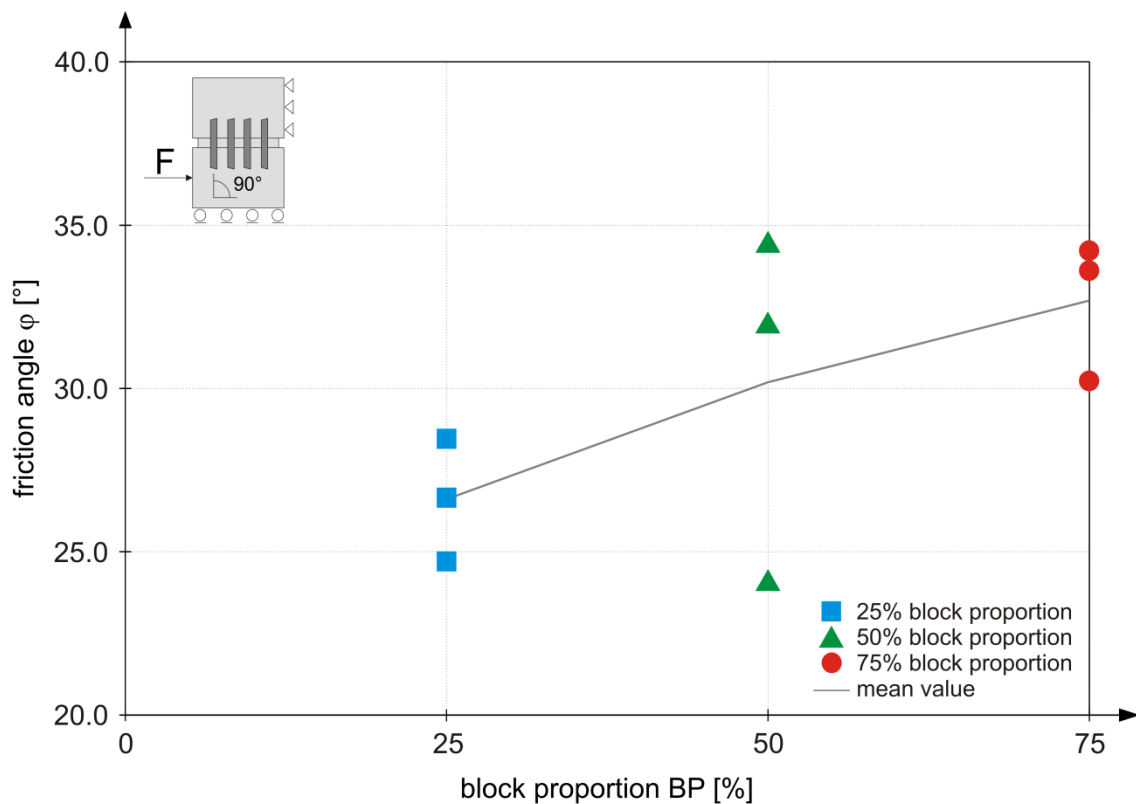


Figure 119: “Intact” friction angle  $\varphi$  for  $90^\circ$  block orientation and different block proportions.

A contrary picture is given for the development of cohesion over block proportion (Figure 120). Increasing the block proportion from 25% to 50% yields almost no change in cohesion, while for block proportions above 50% a pronounced decrease in cohesion is observed. Cohesion drops down to about half the amount of the 25% and 50% block proportion samples. This finding basically reflects the observed behavior of cohesion loss determined by Lindquist (1994). Considering the dilation angle  $i$  for the  $90^\circ$  block orientation samples it can be seen that between 25% and 50% block proportion an increase in dilation of about  $1.5^\circ$  is present (Figure 121). However, a further increase of block proportion slightly decreases dilation. A reason for this behavior might be that in the 75%

block proportion assembly the blocks are aligned next to each other, with almost no matrix between the blocks. This enhances the brittleness, since the blocks have only very limited ability to rotate in the matrix.

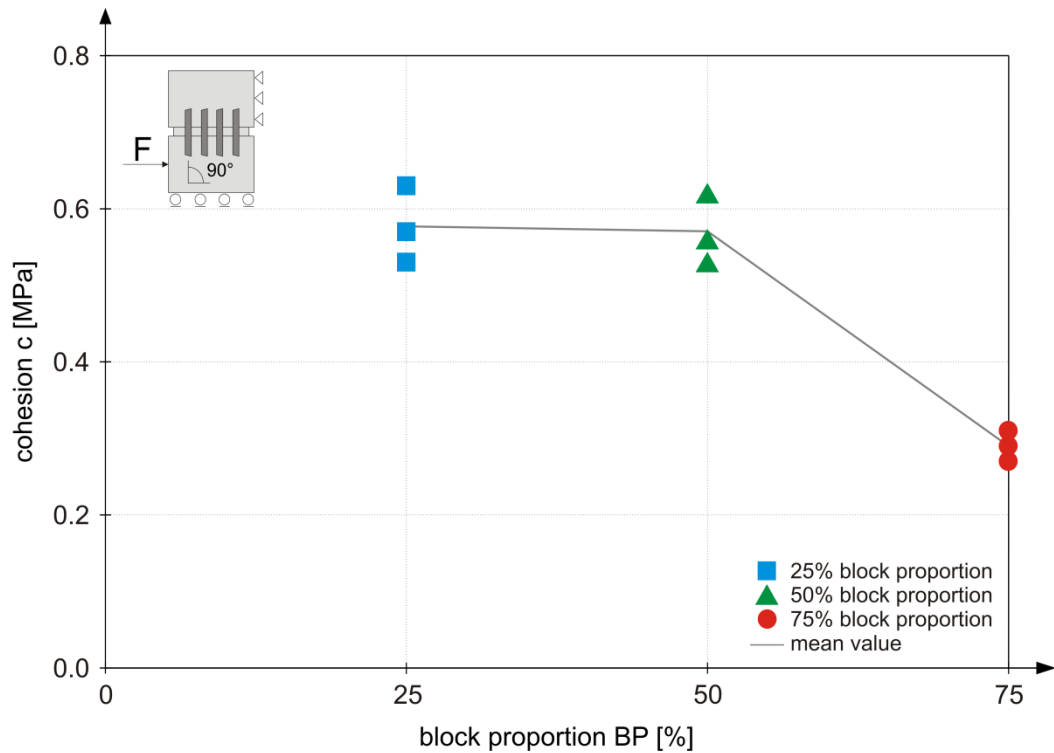


Figure 120: “Intact” cohesion  $c$  for 90° block orientation and different block proportions.

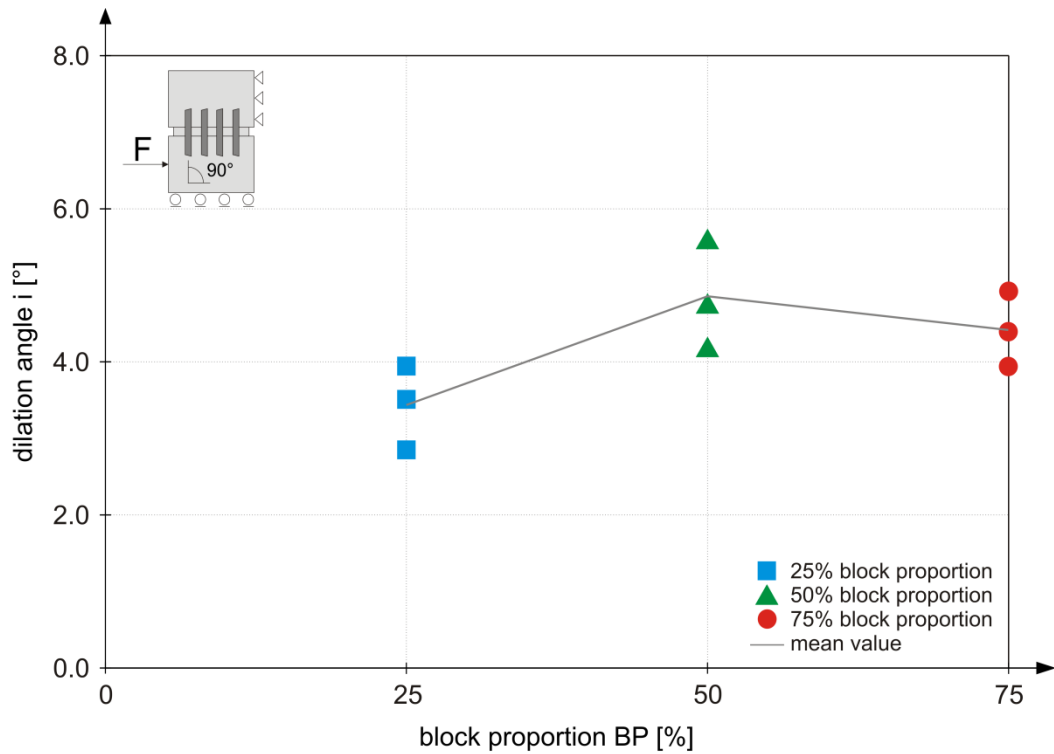


Figure 121: “Intact” dilation angle  $i$  for 90° block orientation and different block proportions.

The results of intact friction angle  $\varphi$  for  $60^\circ$  block orientation samples are summarized in Figure 122. A contrary picture is given for the development of friction angle over block proportion compared to the  $90^\circ$  block orientation samples. Although the results are somewhat scattered, a decrease in friction with increasing block proportion can be observed. For 25% and 50% block proportion one outlier each can be identified. A closer investigation of the associated stress paths unveils reasons for these somewhat peculiar results. The 25% block proportion sample features a rather steep inclination of the stress path between 0.5 mm and 1.5 mm shear displacement, which decreases with further shear displacement. On the contrary, the 50% block proportion specimen shows a slight kink in the stress path after a certain shear displacement and a pronounced increase in shear resistance with increasing shear displacement (Figure 106). This peculiarity emphasizes the difficulties which arise when attempts are made to describe a complex behavior with just one parameter, since important features are concealed or even get lost. Considering the entire stress path it is obvious that the 50% block proportion samples feature considerable higher shear strength and resistance. Taking into account the mean value for each tested set of block proportions, it appears that cohesion  $c$  remains fairly constant with increasing block proportion. However, the values are highly scattered, especially for the 50% block proportion samples (Figure 123). The value for cohesion is mainly determined by the onset of dilation (increase of shear and normal stress). Although the fabrication of samples was carried out carefully and meticulously, a small deviation between the samples can have a huge impact on such subtleties like onset of dilation and hence would lead to scattered results. Taking such figures as “face values” would often be misleading and risky.

The dilation angle  $i$  is only marginally influenced by block proportion and shows a slight increase with increasing block proportion (Figure 124).

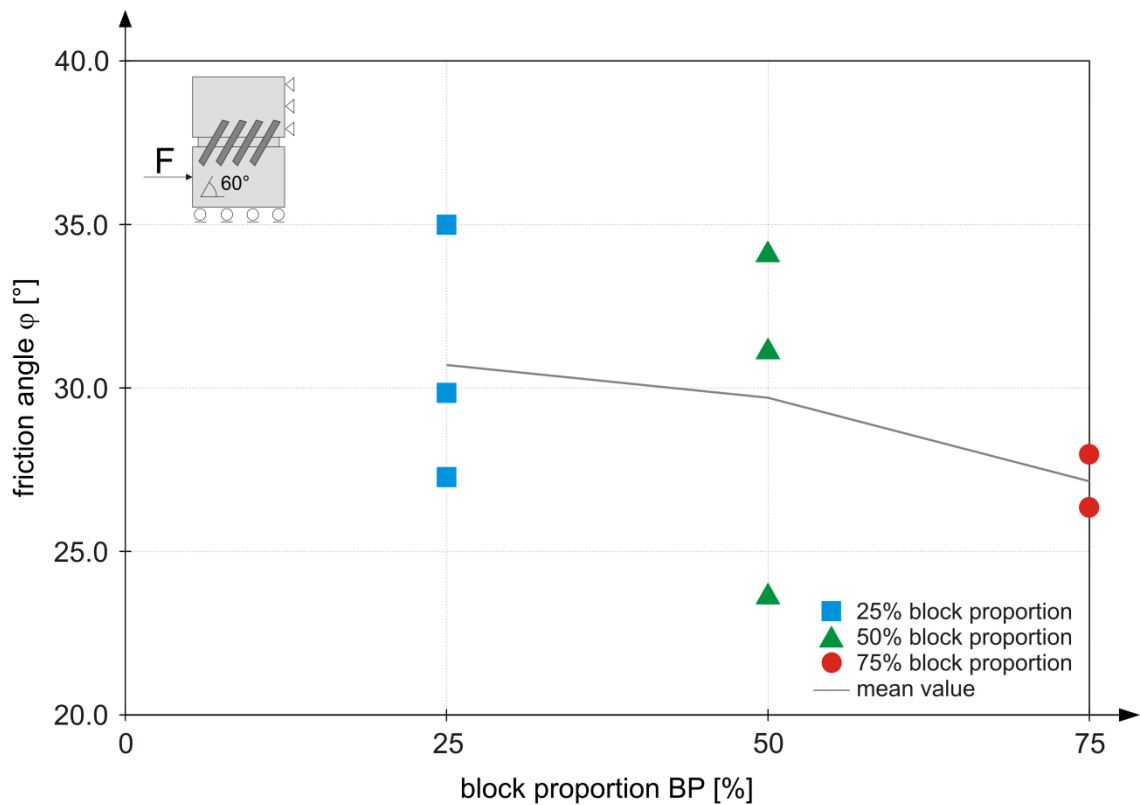


Figure 122: "Intact" friction angle  $\varphi$  for 60° block orientation and different block proportions.

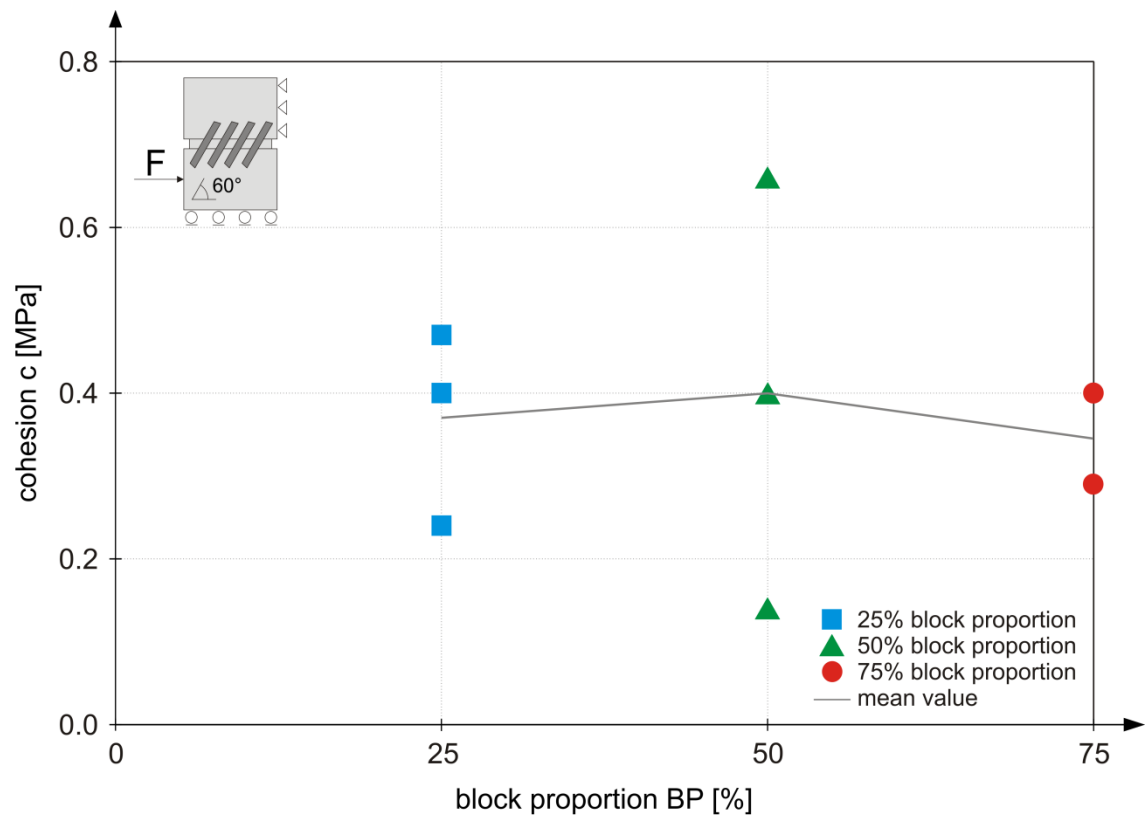


Figure 123: "Intact" cohesion  $c$  for 60° block orientation and different block proportions.



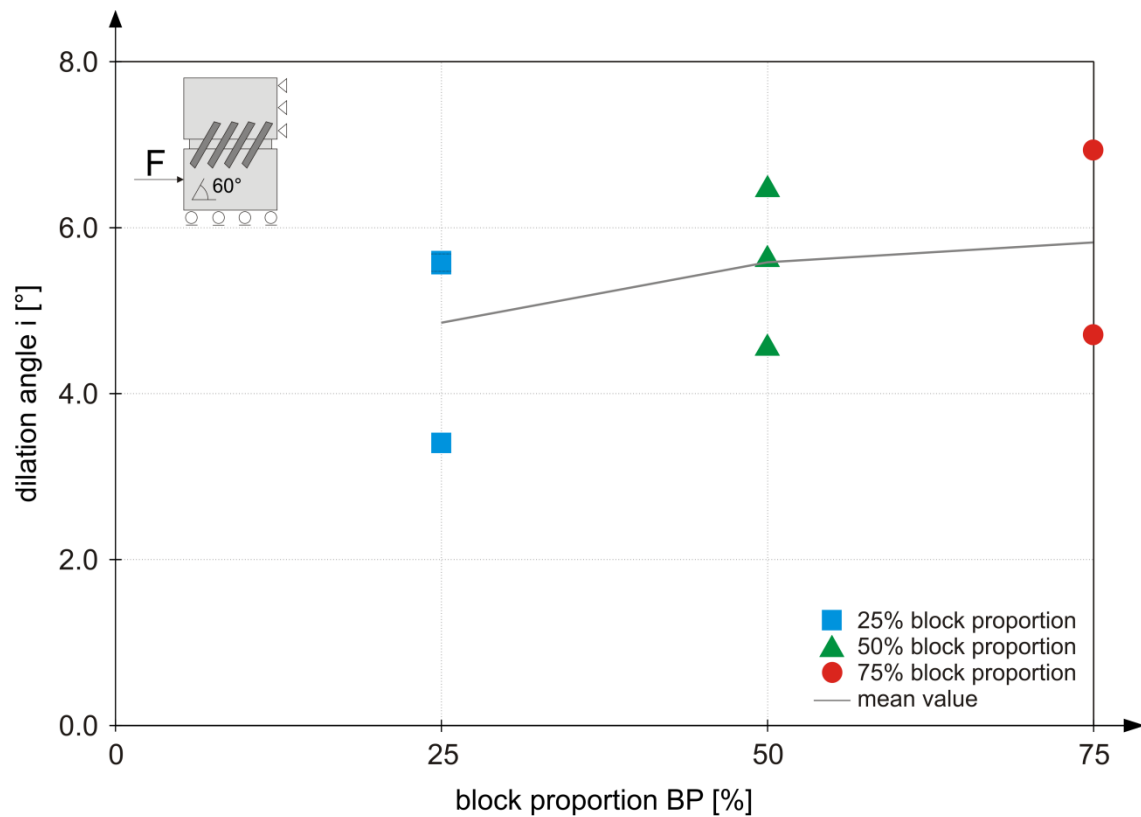


Figure 124: “Intact” dilation angle  $i$  for 60° block orientation and different block proportions.

## 5.2.6 Investigation of shear strength of “1”-block bimrocks

In this study, several tests were also performed on samples containing just one block. The reason for doing so was to avoid the blocks influencing each other during the shearing process and hence to omit the accompanied effects on the overall behavior. The aim was to study the influence on strength of one strong inclusion in a weaker surrounding by narrowing or avoiding any potential side effects and hence gaining insight into the mechanical principles involved.

Since the geometry of the blocks was “fixed”, the shear surface area of the samples had to be adjusted, in order to allow different block proportions to be tested. The “1”-block test series was carried out just for 90° block orientation (normal stress in z-direction, shear stress in y-direction of block, see Figure 112, type II) and block proportions of 10%, 20%, 30% and 40%, due to geometric constraints given by the test apparatus. The variation of block proportion was accomplished by calculating the required shear surface area based on the cross section of the block. Once knowing the shear surface area, recesses featuring the same width/height ratio as the blocks were fabricated and placed in the shear box. The gap between the shear box boundary and the recess was filled with fast curing mortar, while the inner part was filled with matrix material and one block was placed in the center of the shear surface area. The tests were carried out

under single-stage constant normal load conditions (CNL). Three tests of each block proportion configuration were performed.

The decrease of shear surface area with increasing block proportion caused some difficulties for the 30% and 40% block proportion samples. Due to the small area the dead load of the shear device, which is about 2 kN, provided very high initial normal stresses acting on the sample. Furthermore an instantaneous tilting of the upper shear box after removing the retaining bolts was likely to occur for high block proportions. The tests with 10% and 20% block proportions yielded very promising results. However, the results for 30% and 40% block proportions have to be treated with caution. Test number 3 (Test #3 in Figure 127) for 30% block proportion showed an excessive tilting and rotation during the increase of shear stress, resulting in lower peak shear strength. Hence test number 3 does not fit with the other two tests, performed on lower initial normal stress and therefore will not be considered for determination of the Mohr-Coulomb failure line. For the 40% block proportion sample test number 2 (Test #2 in Figure 128) exhibited an abortive failure immediately after applying the initial normal stress and starting the shearing process.

Figure 125 to Figure 128 depict the stress paths of the three performed tests of each test series. Since artificial fabricated samples were tested, the peak shear strength values do not perfectly follow a straight failure line. The Mohr-Coulomb failure line was fitted to the maximum shear stress values, using the least squares method.

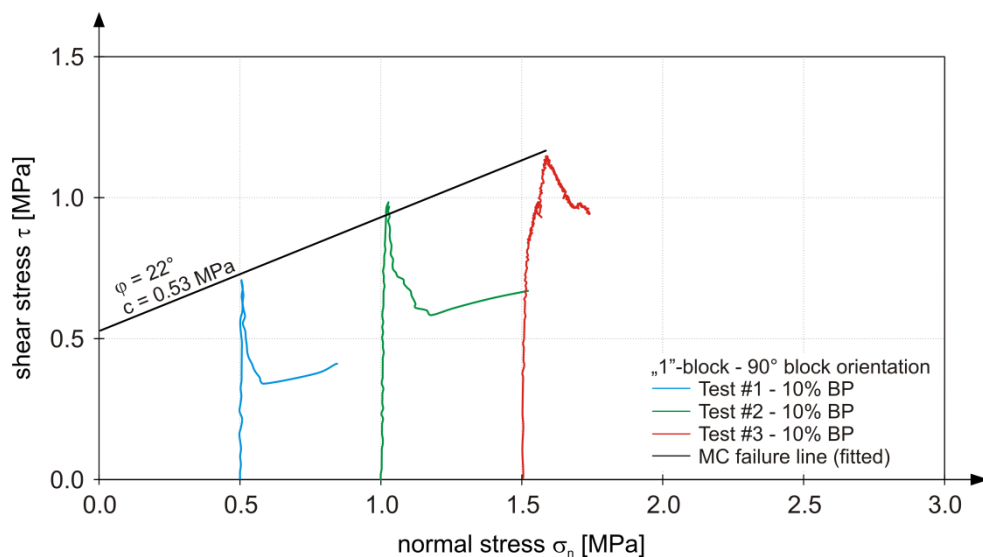


Figure 125: Stress paths for “1”-block samples with 10% block proportion.

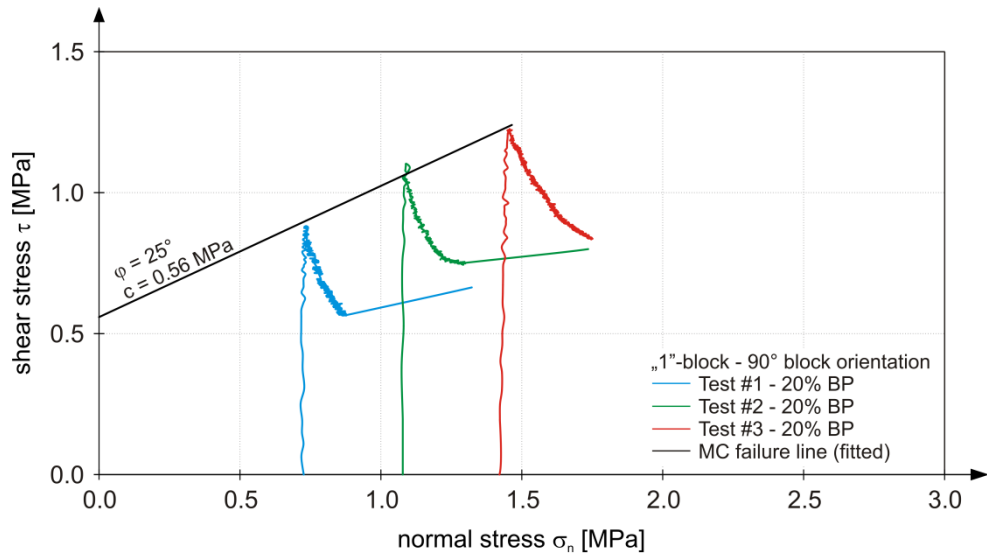


Figure 126: Stress paths for “1”-block samples with 20% block proportion.

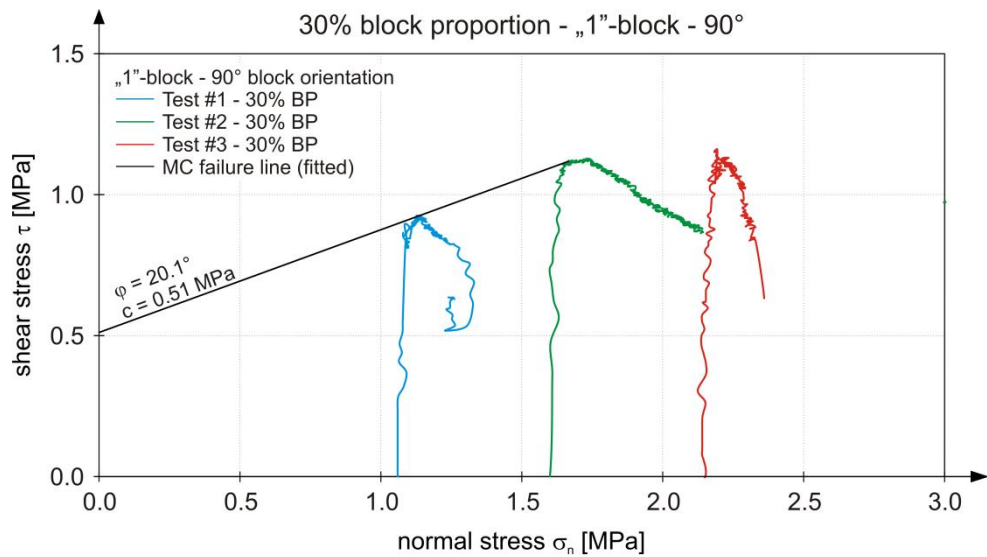


Figure 127: Stress paths for “1”-block samples with 30% block proportion.

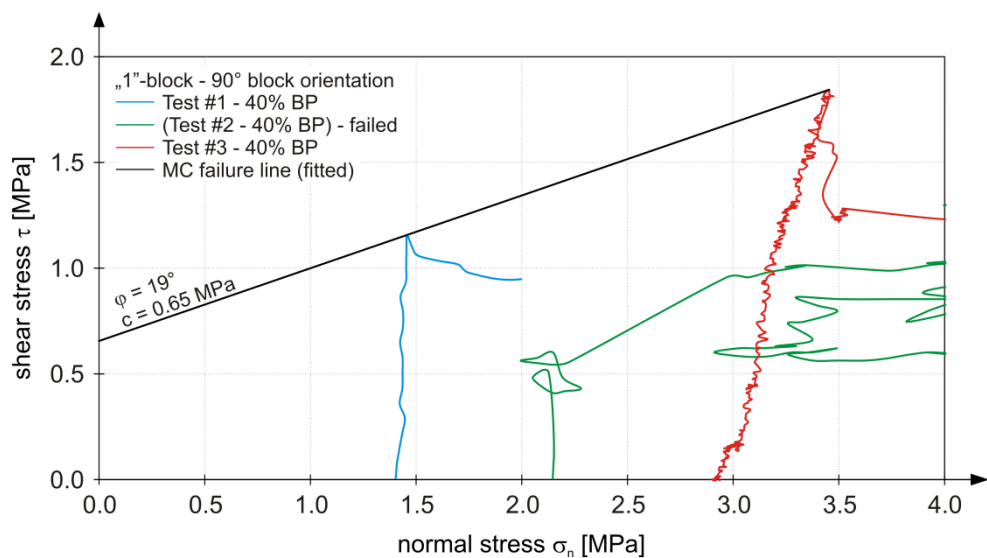


Figure 128: Stress paths for “1”-block samples with 40% block proportion.

The evaluated values for friction angle  $\varphi$  and cohesion  $c$  are depicted in Figure 129 and Figure 130, respectively, and summarized in Table 13. If one considers the results for 10% and 20% block proportion an increase of friction can be observed, which appears plausible and is as expected. The 30% and 40% samples yielded lower values for the friction angle. However, these results must be interpreted with caution, due to the difficulties mentioned above. For the cohesion also an increase with increasing block proportion can be observed.

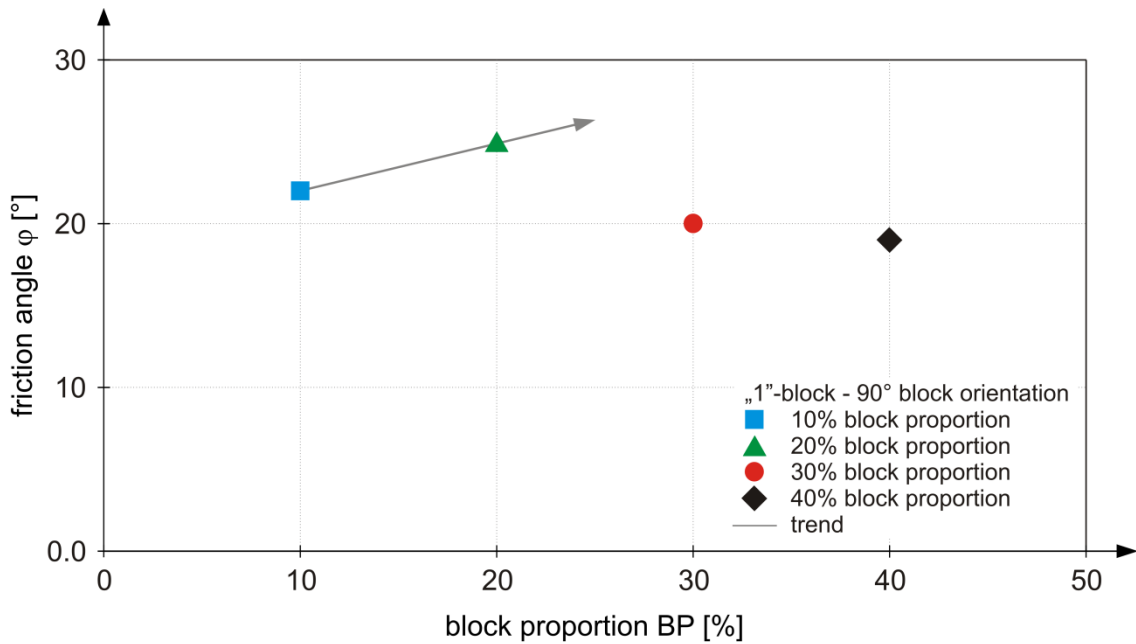


Figure 129: Evaluated friction angle  $\varphi$  versus block proportion for “1”-block samples.

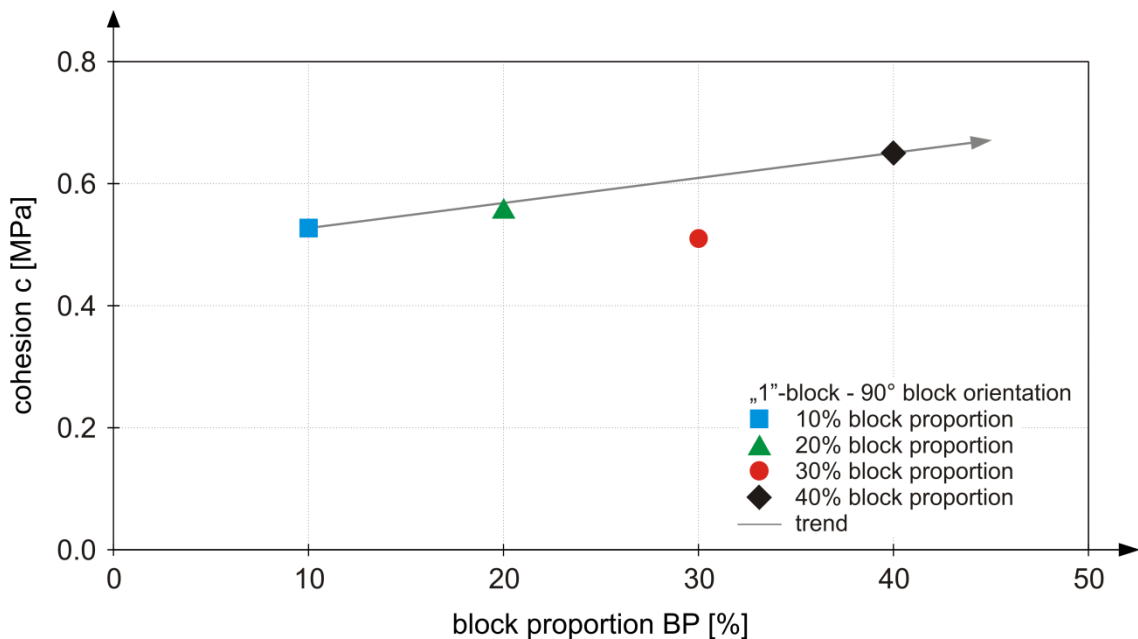


Figure 130: Evaluated cohesion  $c$  versus block proportion for “1”-block samples.

Table 13: Evaluated values for cohesion  $c$  and friction angle  $\varphi$  for “1”-block samples.

“1”-block	Block proportion			
	10%	20%	30%	40%
cohesion $c$ [MPa]	0.53	0.56	0.51	0.65
friction angle $\varphi$ [°]	22	25	20.1	19

The increase of friction with increasing block proportion is given in Equation (29):

$$\varphi_{\text{“1”-block}} = 19 + 0.3 \cdot BP \quad (29)$$

The increase of cohesion with increasing block proportion for “1”-block samples follows Equation (30):

$$c_{\text{“1”-block}} = 0.49 + 0.0041 \cdot BP \quad (30)$$

One must be aware that the relationships between the increase of friction and cohesion and block proportion are only valid for the range of tested block proportions. Considering the formula for the development of friction over block proportion it becomes evident that friction would certainly be overestimated for high block proportions. Therefore, it might be reasonably assumed, that there is an upper threshold block proportion, above which the friction angle is only marginally affected by the presence of blocks, like it was stated in several previous studies (Irfan and Tang 1993, Lindquist 1994, Wen-Jie et al. 2011).

The results for the increase of friction with increasing block proportion are basically in good agreement with the findings of previous studies. Both Lindquist (1994), who conducted triaxial tests on artificial bimrocks, and Wen-Jie et al. (2011), who performed in-situ shear tests, determined a magnitude of frictional increase of about  $0.33^\circ$  per percent block proportion increase (Figure 14 in Chapter 2.2). Coli et al. (2011), who conducted in-situ direct shear tests on bimrocks, evaluated a factor of increase of friction angle with increasing block proportion of  $0.7^\circ/\% \text{ BP}$ .

On the other hand, the equation for the increase of cohesion is basically in good agreement with the results of the pure matrix and pure block samples, conducted with the standard size configuration. The pure block samples yielded values for cohesion of about 1.0 MPa, while Equation (30) would provide an amount of cohesion of 0.9 MPa.

### **5.3 Summary of the influence of block proportion on strength properties of bimrocks**

The major findings determined and evaluated in Chapter 5 regarding the influence of block proportion on the strength properties of bimrocks are summarized in this section. It was found that shear strength almost linearly increases with increasing block proportion. The increase of shear strength is most pronounced for blocks with 60° block orientation. The 30° block orientation arrangements provide the lower bound of increasing shear strength with increasing block proportion, while the 90° block orientation samples show a magnitude of strength increase, which falls between 30° block orientation specimens with blocks both inclined in and against shear direction and the 60° block orientation specimens with blocks inclined against shear direction. Samples with 60° block orientation containing blocks inclined in shear direction show almost the same amount of shear strength increase as the 90° block orientation samples. Some peculiarities of certain block orientations were also identified. The 30° block orientation samples show a more pronounced increase in shear strength above 50% block proportion. A contrary picture is shown for 60° block orientation samples with block inclined against shear direction where a decrease of shear strength above 50% block proportion is observed.

Regarding the intact properties, it was found that for 90° block orientation friction of samples basically increases with increasing block proportion, while cohesion remains constant or decreases with increasing block proportion. The same behavior of cohesion decrease was observed for 60° block orientation samples, while for that arrangement also a decrease of friction with increasing block proportion was observed. In both cases (60° and 90° block orientations) dilation exhibits an increasing trend with increasing block proportion.

The tested “1”-block samples show basically the same behavior as the standard bimrock samples. An increase of friction with increasing block proportion was observed, while cohesion shows a decreasing trend with increasing block proportion.

### **5.4 Summary of the influence of block orientation on strength properties of bimrocks**

The influence of block orientation is provided in this section at a glance. As a basic behavior, both for the 30° and 60° block orientation samples, it was observed that samples with blocks inclined against shearing direction show higher magnitudes of peak shear strength than specimens with blocks inclined in shear direction. The samples with 60° block orientation provide the highest contribution to shear strength for all block proportions, except for very high block proportions of 75% for samples with blocks inclined against shear

direction. The samples with  $60^\circ$  block orientation show a very ductile behavior, expressed in an almost constant increase in shear resistance up to relatively high shear displacement magnitudes. The highest amount of shear resistance increase was observed for samples with  $90^\circ$  block orientation, accompanied by a more brittle behavior than the  $60^\circ$  block orientation samples. Peak shear strength is reached after about half of the maximum shear displacement and a pronounced post-peak behavior can be observed. The  $30^\circ$  block orientation samples show a very brittle behavior for low block proportions of 25%, while the samples with 50% and 75% block proportion feature a ductile behavior, expressed in a steady, almost linear increase in shear resistance until the maximum shear displacement is reached. In those cases no post-peak region is present. The  $30^\circ$  block orientation samples show the lowest contribution to shear strength, except for samples with blocks inclined against shear direction and high block proportions of 75%. These samples feature markedly higher shear strength values than samples with  $60^\circ$  block orientation and blocks inclined in shear direction. Regarding the local block arrangement, it was observed that shearing the blocks about their strong axis provides about 1.3 times higher values for maximum shear strength than shearing about the weak axis. This increase is more pronounced for local block arrangements, where the major axis of the block coincides with the normal stress direction, highlighting the effect of block geometry on the shear behavior.

## 6 Conclusions

Fault zones are complex structures, featuring highly heterogeneous rock mass conditions, and they form the most challenging stretches during tunneling.

The present research provides insight into the overall mechanical properties and studies the basic mechanical behavior of bimrocks.

The in-situ plate load tests, performed in the Lavanttal fault zone provided valuable information about the anisotropic deformation properties. Furthermore the magnitude of the Young's modulus was assessed and defined in a suitable range. The gained knowledge has led to a reliable and improved prognosis of the system behavior and considerable risk decrease for the intended TBM advances in fault zones, especially through the Lavanttal fault system.

A large oedometer test was developed in the course of the research, custom-tailored to meet the peculiarities of fault material. The large oedometer tests performed on artificial block-in-matrix rocks exhibited the influence of block orientation and block proportion on the overall deformability. The stress-dependency of deformation behavior was discussed in detail. The developed empirical relationships, based on the volumetric block proportion, the block orientation and the matrix' deformability, allow a straightforward assessment of the overall deformability of bimrocks.

The extensive laboratory program for the determination and investigation of shear behavior of artificial bimrocks facilitated a deeper insight in the mechanical behavior and promoted knowledge of understanding the mechanical processes involved. A high-sophisticated method for the evaluation of direct shear tests was applied, allowing a proper determination of engineering properties. However, the evaluation process stressed the shortcoming of describing highly complex mechanical behavior only by a few parameters. The peculiarities of different block proportions and block orientations and their influence on the stress path and the stress-displacement behavior are highlighted and discussed in detail. The findings yielded a qualitative characterization of a constitutive model for bimrocks.

However, several issues which were not discussed in this thesis render the need for further research. Following unresolved issues were identified, providing a basis for further studies:

1. The large oedometer tests were carried out at a constant stiffness ratio between block and matrix. Further research should focus on performing tests with varying stiffness ratios between matrix and blocks, in order to enhance and extend the relationships for the overall deformability of bimrocks provided in this thesis.



2. All direct shear tests were performed with the same block geometry. The investigation of the influence of different block geometries by laboratory tests is still open. An attempt should be made to discover the effect of altered block geometries (variation of length/width ratios, testing of compact/slender block shapes) on the mechanical behavior. It can be assumed that the influence of block geometry on the deformability is less pronounced than on the strength. However, a sound quantification of the impact of block geometry on the overall deformability dictates further treatment.
3. Variations in strength between matrix and block were not accounted for in this work. Future research should elaborate on strength contrasts between matrix and block and investigate their influence on the overall mechanical behavior. The development of threshold values demarcating the influence of strength contrasts between weak matrix and strong blocks would constitute an appreciated contribution to the mechanical behavior of fault material.
4. As mentioned above the direct shear tests on bimrocks yielded a qualitative description of the constitutive mechanical relationships. The application of a mathematical description for the stress-strain behavior of bimrocks allows the development of a constitutive model. The constitutive law should be applied in numerical simulations in order to supplement and validate the results and findings of the laboratory tests. 3D numerical parametric studies with different fault zone orientations (macro scale) and block proportions and block orientations (micro scale) would allow an assessment of the influence on the displacement development and hence facilitating the determination of the ground pressure acting on the tunnel support and of the impact on the system behavior.

An absolute quantification of the overall rock mass parameters of fault material is still a challenging task. However, the present research facilitates the assessment of the anticipated rock mass behavior. Applying the observational approach in tunneling allows the determination of expected rock mass behavior and the identification of displacement normal behavior. The once determined normal behavior for a certain geological condition in a fault zone (e.g. block proportion and block orientation with regard to the tunnel axis), enables the assessment of the probable rock mass behavior for different fault zone conditions, encountered in the further course of tunnel advance. The gained knowledge, provided in this thesis, allows estimation whether a predicted fault zone orientation and their local geological peculiarities exhibit a more favorable rock mass behavior or not. The work, therefore, contributes to a knowledge based expert system through its findings, assisting in predicting the ground- and system-behavior and supports the evaluation and interpretation of displacement monitoring data.

The imperative role of a proper investigation and ground characterization cannot be overstressed. Since the ground characterization provides the basis for the ground model, which consequently is the basis for excavation and support design, a sound and accurate geomechanical characterization, particularly for fault zones is of crucial importance. Inadequate admissions and deficiencies, perpetrated in the early stages of a project, will inevitably lead to a persistent higher level of risk and uncertainties in all subsequent project phases.

The author is convinced that in-situ and laboratory testing, when coupled with appropriate evaluation methods capturing all sources of the gathered data, yields a vast amount of reliable and valuable information for the geomechanical characterization and design of underground structures. It is stressed that in-situ and laboratory testing cannot be replaced by mere numerical tools, no matter how advanced they may be.

## 7 References

- 3G Gruppe Geotechnik Graz ZT GmbH (2008)  
Charakterisierung von tektonischen Störungszonen im Kristallinabschnitt des Koralmtunnels. Internal project communication for the Koralm tunnel project.
- 3G Gruppe Geotechnik Graz ZT GmbH (2010)  
Ergänzendes Erkundungsprogramm für die Hauptstörung des Lavanttaler Störungssystems – Versuchsstollen Endbericht. Internal project communication for the Koralm tunnel project.
- ASTM D 7012-10 (2010)  
Standard Test Method for Compressive Strength and Elastic Moduli of Intact Rock Core Specimens under Varying States of Stress and Temperatures. American Society for Testing and Materials: West Conshohocken.
- Austrian Society for Geomechanics (2010)  
Guideline for the Geotechnical Design of Underground Structures with Conventional Excavation. translated from 2<sup>nd</sup> revised edition. Salzburg.
- Bandis, S.C. (1990)  
Mechanical properties of rock joints. In *Proc. Int. Symp. On Rock Joints*. Barton & Stephansson (eds.), 4-6 June 1990, Leon, Norway, pp. 125-140.
- Barbero, M., Bonini, M. & Borri-Brunetto, M. (2007)  
Numerical modelling of the mechanical behaviour of bimrock. In *Proc. 11<sup>th</sup> Congress of the International Society for Rock Mechanics*. Ribeiro e Sousa, Olalla & Grossmann (eds.), pp. 377–380, Taylor & Francis Group: London.
- Brosch, F.J., Kurz, W. & Klima, K. (2006)  
Definition and Characterization of Faults and Fault Rocks. *Felsbau* 24, No. 5, pp. 13-20, Verlag Glück Auf: Essen.
- Bürgi, C. (2000)  
*Cataclastic fault rocks in underground excavations – a geological characterisation*. Ph.D. Dissertation, EPF-Lausanne, Switzerland.
- Coli, N., Berry, P. & Boldini, D. (2011)  
In situ non-conventional shear tests for the mechanical characterisation of a bimrock. *Int. J. Rock Mech. & Min. Sci.* Vol. 48, pp. 95-102, Elsevier: Amsterdam.
- Coli, N., Boldini, D. & Bandini, A. (2012)  
Modeling of complex geological rock mixtures under triaxial testing conditions. In *Proc. Eurock 2012 – Rock Engineering & Technology for Sustainable Underground Construction*. 28-30 May 2012, Stockholm, Sweden.

- Coli, M. & Tanzini, M. (2013)  
Characterization of the “Chaotic Complex” (Northern Apennines, Italy). In *Proc. Eurock 2013 – Rock Mechanics for Resources, Energy and Environment*. Kwasniewski & Lydzba (eds.), 21-26 September 2013, Wrocław, Poland, pp. 111-116, Taylor & Francis Group: London.
- DGEG (1985)  
Empfehlung Nr. 6 des Arbeitskreises 19 – Versuchstechnik Fels – der Deutschen Gesellschaft für Geotechnik e.V. Doppel-Lastplattenversuche in Fels. *Bautechnik* Vol. 62, No. 3, pp. 102-106, Wilhelm Ernst & Sohn: Berlin.
- DGGT (2004)  
Neufassung der Empfehlung Nr. 1 des Arbeitskreises „Versuchstechnik Fels“ der Deutschen Gesellschaft für Geotechnik e.V.: Einaxiale Druckversuche an zylindrischen Gesteinsprüfkörpern. Mutschler, T. (ed.), *Bautechnik* Vol. 81, No. 10, pp. 825-834, Wilhelm Ernst & Sohn: Berlin.
- Fasching, F. & Vanek, R. (2011)  
Engineering geological characterisation of fault rocks and fault zones. *Geomechanics and Tunnelling* Vol. 4, No. 3, pp. 181-194, Wilhelm Ernst & Sohn: Berlin.
- Goodman, R.E. & Ahlgren, C.S. (2000)  
Evaluating Safety of Concrete Gravity Dam on Weak Rock: *Scott Dam. J. Geotech. Geoenviron. Eng.* Vol. 126, No. 5, pp. 429-442.
- Goricki, A., Rachaniotis, N., Hoek, E., Marinos, P., Tsotsos, S. & Schubert, W. (2006)  
Support Decision Criteria for Tunnels in Fault Zones. *Felsbau* 24, No. 5, pp. 51-57, Verlag Glück Auf: Essen.
- Habimana, J., Labiouse, V. & Descoedres, F. (2002)  
Geomechanical characterisation of cataclastic rocks: experience from the Cleuson-Dixence project. *Int. J. Rock Mech & Min. Sci.* Vol. 39, pp. 677-693, Elsevier: Amsterdam.
- Hajiabdolmajid, V., Kaiser, P.K. & Martin, C.D. (2002)  
Modelling brittle failure of rock. *Int. J. Rock Mech. & Min. Sci.* Vol. 39, No. 6, pp. 731-741, Elsevier: Amsterdam.
- Hirsch, T.J. (1962)  
Modulus of Elasticity of concrete affected by elastic moduli of cement paste matrix and aggregate. *Journal of the American Concrete Institute* Vol. 59, Issue 3, pp. 427-452.

- Hoek, E., Carranza-Torres, C. & Corkum, B. (2002)  
Hoek-Brown failure criterion – 2002 edition. In: *Proc. 5<sup>th</sup> North American Rock Mechanics Symposium – Mining and tunneling innovation and opportunity*. Hammar, R., Bawden, W., Curran, J. & Telesnicki, M. (eds.), 07-10 Juli 2002, Toronto, Canada, pp. 267-273, University of Toronto Press: Toronto.
- Irfan, T.Y. & Tang, K.Y. (1993)  
Effects of the coarse fractions on the shear strength of colluvium. Geo-Report No. 23, Geotechnical Engineering Office, Civil Engineering Department, Hong Kong.
- ISRM (2007)  
The complete ISRM suggested methods for rock characterization, testing and monitoring: 1974-2006. R. Ulusay and J.A. Hudson (eds.), Suggested Methods Prepared by the Commission on Testing Methods, International Society for Rock Mechanics, Compilation Arranged by the ISRM Turkish National Group, Kozan Ofset, Ankara, Turkey.
- Laznicka, P. (1988)  
Breccias and Coarse Fragmentites: Petrology, Environments, Ores. *Developments in Economic Geology*, Vol. 25, Elsevier: Amsterdam.
- Kahraman, S. & Alber, M. (2006)  
Estimating unconfined compressive strength and elastic modulus of a fault breccia mixture of weak blocks and strong matrix. *Int. J. Rock Mech. & Min. Sci.* Vol. 43, pp. 1277-1287, Elsevier: Amsterdam.
- Kovari, K., Ehrbar, H. & Theiler, A. (2005)  
Druckhafte Strecken im TZM Nord: Projekt und bisherige Erfahrungen. In *Proc. Symp. Geologie Alptransit Zürich – Geologie und Geotechnik der Basistunnel am Gotthard und am Lötschberg*. Löw, S. (ed.), 26-28 September 2005, pp. 239-252, vdf Hochschulverlag an der ETH Zürich.
- Lindquist, E.S. (1994)  
*The strength and deformation properties of melange*. Ph.D. Dissertation, Dept. of Civil Engineering, University of California at Berkeley, USA, Publ. UMI, Inc., Ann Arbor: Michigan.
- Lindquist, E.S. & Goodman, R.E. (1994)  
Strength and deformation properties of a physical model melange. In *Rock Mechanics*, Nelson & Laubach (eds.), pp. 843-850, Balkema: Rotterdam.
- Marinos, V., Marinos, P. & Hoek, E. (2005)  
The geological strength index: applications and limitations. *Bull. Eng. Geol. Environ.* 64, pp. 55-65.

- Medley, E.W. (1994)  
*The engineering characterization of melanges and similar block-in-matrix rocks (bimrocks)*. Ph.D. Dissertation, Dept. of Civil Engineering, University of California at Berkeley, USA, Publ. UMI, Inc. Ann Arbor: Michigan.
- Medley, E.W. (1999)  
Systematic Characterization of Melange Bimrocks and Other Chaotic Soil/Rock Mixtures. *Felsbau* 17, No. 3, pp. 152-162, Verlag Glück Auf: Essen.
- Medley, E.W. (2001)  
Orderly Characterization of Chaotic Franciscan Melanges. *Felsbau* 19, No. 4, pp. 20-33, Verlag Glück Auf: Essen.
- ÖBB-Infrastruktur AG (2013)  
Project information about the Koralmbahn Graz – Klagenfurt [online]. Available at: [http://www.oebb.at/infrastruktur/de/5\\_0\\_fuer\\_Generationen/5\\_4\\_Wir\\_bauen\\_fuer\\_Generationen/5\\_4\\_1\\_Schieneninfrastruktur/Suedstrecke/Koralmbahn/index.jsp](http://www.oebb.at/infrastruktur/de/5_0_fuer_Generationen/5_4_Wir_bauen_fuer_Generationen/5_4_1_Schieneninfrastruktur/Suedstrecke/Koralmbahn/index.jsp) [Accessed: 13 December 2013].
- ÖNORM B4435-2 (1999)  
Erd- und Grundbau: Flächengründungen – EUROCODE-nahe Berechnung der Tragfähigkeit. Österreichisches Normungsinstitut, Fachnormenausschuss 023-Grundbau, Wien.
- Pan, Y.W., Hsieh, M.H. & Liao, J.J. (2008)  
Mechanical Properties of Virtual Block-in-matrix Colluvium. In *Proc. 42<sup>nd</sup> US Rock Mechanics Symposium*, 29 June-2 July 2008, San Francisco.
- Patton, F.D. (1966)  
Multiple modes of shear failure in rock. In *Proc. 1<sup>st</sup> Congr. Int. Soc. Rock Mech.*, Vol. 1, Lisboa, pp. 509-513.
- Pilgerstorfer, T., Radoncic, N., Moritz, B. & Goricki, A. (2011)  
Evaluation and interpretation of monitoring data in the test adit EKT Paierdorf. *Geomechanics and Tunnelling* Vol. 4, No. 5, pp. 423-434, Wilhelm Ernst & Sohn: Berlin.
- Pötsch, M. (2011)  
*The analysis of rotational and sliding modes of failure for slopes, foundations, and underground structures in blocky, hard rock*. Ph.D. Dissertation, Institute for Rock Mechanics and Tunnelling, Graz University of Technology, Austria.
- Raymond, L.A. (1984)  
Classification of mélanges. In: *Melanges: Their nature, origin and significance*. Raymond, L.A. (ed.), Geological Society of America, Boulder, Colorado, Special Publication 228, pp. 7-20.

- Riedmüller, G., Brosch, F.-J., Klima, K. & Medley, E.W. (2001)  
Engineering Geological Characterization of Brittle Faults and Classification of Fault Rocks. *Felsbau* 19, No. 4, pp. 13-18, Verlag Glück Auf: Essen.
- Saeb, S. & Amadei, B. (1992)  
Modelling Rock Joints under Shear and Normal Loading. *Int. J. Rock Mech. Min. Sci. & Geomech. Abstr.* Vol. 29, No. 3, pp. 267-278, Elsevier: Amsterdam.
- Savely, J.P. (1990)  
Comparison of shear strength of conglomerates using a Caterpillar D9 ripper and comparison with alternative methods. *Int. Journ. of Mining and Geol. Eng.* Vol. 8, pp. 203-225.
- Scholfield, A.N. (1998)  
Don't use the C word – Mohr-Coulomb error correction. *Ground Engineering*, pp. 29-32.
- Schubert, W. (1993)  
Erfahrungen bei der Durchörterung einer Großstörung im Inntaltunnel. *Felsbau* 11, No. 6, pp. 287-290, Verlag Glück Auf: Essen.
- Sibson, R.J. (1977)  
Fault rocks and fault mechanisms. *J. Geol. Soc.* 133, pp. 191-213.
- Sönmez, H., Gokceoglu, C., Tuncay, E., Medley, E.W. & Nefeslioglu, H.A. (2004)  
Relationships between Volumetric Block Proportions and Overall UCS of a Volcanic Bimrock. *Felsbau* 22, No. 5, pp. 27-34, Verlag Glück Auf: Essen.
- Sönmez, H., Altinsoy, H., Gokceoglu, C. & Medley, E.W. (2006)  
Considerations in Developing an Empirical Strength Criterion for Bimrocks. In *Proc. Asian Rock Mechanics Symposium (ARMS)*, 6-10 November, Singapore.
- Stock, A.F., Hannant, D.J. & Williams, R.I.T. (1979)  
The effect of aggregate concentration upon the strength and modulus of elasticity of concrete. *Magazine of Concrete Research* Vol. 31, Issue 109, pp. 225-234.
- Ünal, E. (1997)  
Determination of in situ Deformation Modulus: New Approaches for Plate-Load Tests. *Int. J. Rock Mech. Min. Sci.* Vol. 34, No. 6, pp. 897-915, Elsevier: Amsterdam.
- Waters, A.C. & Campbell, C.D. (1935)  
Mylonites from the San Andreas Fault zone, *Am. J. Sci.* 29, pp. 473-503.
- Wen-Jie, X., Qiang, X. & Rui-Lin, H. (2011)  
Study on the shear strength of soil-rock mixture by large scale direct shear test. *Int. J. Rock Mech. & Min. Sci.* Vol. 48, pp. 1235-1247, Elsevier: Amsterdam.

Wieser, P. (2011)

*Design of a Large Oedometer for the Determination of Stress Dependent Moduli on Fault Rocks.* Master Thesis, Institute for Rock Mechanics and Tunnelling, Graz University of Technology, Austria.



# Appendix

## Appendix A Performed loading schemes for the plate load tests

Chainage	Test No.	Loading scheme (values in [MPa])
TM-VS 12.79 m	MS 1.1	0 – 1.02 – 0 – 2.04 – 0 – 3.06 – 0 – 4.08 – 0 – 5.10 – 0 – removal of ext. probes – 10.16
	MS 1.2	0 – 1.02 – 0 – 2.04 – 0 – 3.06 – 0 – 4.08 – 0 – 5.10 – 0 – 6.12 – 0 – 7.79 – 0 – 9.48 – 0 – 11.85
TM-VS 15.39 m	MS 2.1	0 – 1.02 – 0 – 2.04 – 0 – 3.06 – 0 – 4.08 – 0 – 5.10 – 0 – removal of ext. probes – 8.97
	MS 2.2	0 – 1.02 – 0 – 2.04 – 0 – 3.06 – 0 – 4.08 – 0 – 5.10 – 0 – 6.12 – 0 – 7.79 – 0 – 9.48 – 0 – 11.68
TM-VS 19.29 m	MS 3.1	0 – 1.02 – 0 – 2.04 – 0 – 3.06 – 0 – 4.08 – 0 – 5.10 – 0 – removal of ext. probes. – 11.68
	MS 3.2	0 – 1.02 – 0 – 2.04 – 0 – 3.06 – 0 – 4.08 – 0 – 5.10 – 0 – 6.12 – 0 – 7.79 – 0 – 9.48 – 0 – 11.68
TM-VS 21.89 m	MS 4.1	0 – 1.02 – 0 – 2.04 – 0 – 3.06 – 0 – 4.08 – 0 – 5.10 – 0 – 6.12 – 0 – 11.68
	MS 4.2	0 – 1.02 – 0 – 2.04 – 0 – 3.06 – 0 – 4.08 – 0 – 5.10 – 0 – 6.12 – 0 – 7.11 – 0 – 8.80 – 11.68

## Appendix B Evaluated interval- and instant-moduli for the plate load tests

Table B-1: Evaluated interval- and instant-moduli for measuring sections normal to the foliation.

loading <i>normal</i> to foliation		Depth				
		z0	z1	z2	z3	z4
MS 1.1	Interval modulus		1619	1612	2080	2769
	Instant modulus	3061	3417	4478	6411	12,430
	Deform. modulus	1738				
	Interval modulus		584	985	1932	4098
	Instant modulus	1664	2276	3227	3992	4018
	Deform. modulus	1239				
MS 2.1	Interval modulus		1435	1162	10,490	15,275
	Instant modulus	4546	7096	26,930	43,989	n/a
	Deform. modulus	1412				
	Interval modulus		393	287	963	1747
	Instant modulus	912	1098	2808	6160	16,765
	Deform. modulus	326				
MS 3.1	Interval modulus		6880	1274	2601	10,358
	Instant modulus	5247	5247	16,777	39,124	121,062
	Deform. modulus	1692				
	Interval modulus		451	639	1780	1810
	Instant modulus	1328	1454	2001	2081	2231
	Deform. modulus	761				
MS 4.1	Interval modulus		3825	4075	3695	2460
	Instant modulus	2783	2923	3328	5949	3271
	Deform. modulus	882				
	Interval modulus		473	488	1668	1935
	Instant modulus	1136	1383	2943	7532	5878
	Deform. modulus	358				

values in [MPa]

Table B-2: Evaluated interval- and instant-moduli for measuring sections parallel to the foliation.

loading <i>parallel</i> to foliation		Depth					
		z0	z1	z2	z3	z4	
MS 1.2	top	Interval modulus	2962	2509	2458	4985	
		Instant modulus	1866	1887	2019	2346	2848
		Deform. modulus	1257				
	bottom	Interval modulus	1342	905	1348	3353	
		Instant modulus	1649	1716	2506	4747	6473
		Deform. modulus	913				
MS 2.2	top	Interval modulus	931	1044	2800	4091	
		Instant modulus	1800	2015	2622	2707	2550
		Deform. modulus	754				
	bottom	Interval modulus	730	798	2470	2825	
		Instant modulus	2862	4837	2910	3902	1100
		Deform. modulus	1889				
MS 3.2	top	Interval modulus	1807	1005	1966	3958	
		Instant modulus	3031	3399	7021	4975	11,079
		Deform. modulus	602				
	bottom	Interval modulus	1073	861	1342	3141	
		Instant modulus	1752	1948	3195	4645	3407
		Deform. modulus	565				
MS 4.2	top	Interval modulus	7076	4982	6585	9260	
		Instant modulus	4189	3791	4368	6087	2966
		Deform. modulus	1147				
	bottom	Interval modulus	2751	1198	2416	5029	
		Instant modulus	2066	2074	3958	3183	n/a
		Deform. modulus	773				

values in [MPa]

## Appendix C Evaluated moduli for the large oedometer tests

Table C-1: Evaluated moduli for samples with horizontally aligned blocks.

Blocks horizontally aligned	Block proportion							
	21%		41%		44%		58%	
	$E_s$ [MPa]	E [MPa]	$E_s$ [MPa]	E [MPa]	$E_s$ [MPa]	E [MPa]	$E_s$ [MPa]	E [MPa]
1 <sup>st</sup> loading	112.2	83.4	154.9	115.1	256.5	190.5	283.2	210.4
2 <sup>nd</sup> loading	267.4	198.7	397.4	295.2	478.9	355.8	736.3	547.0
3 <sup>rd</sup> loading	431.1	320.2	457.6	339.9	551.4	409.6	1148.9	853.5
4 <sup>th</sup> loading	----	----	610.0	453.2	----	----	1194.2	887.1
1 <sup>st</sup> unloading	3120.2	2317.9	3052.8	2267.8	5435.9	4038.1	2816.2	2092.1
1 <sup>st</sup> reloading	----	----	1791.1	1330.6	3316.2	2463.5	2113.0	1569.7
2 <sup>nd</sup> unloading	3702.2	2750.2	6162.9	4578.1	9592.6	7125.9	5329.3	3958.9
2 <sup>nd</sup> reloading	----	----	3187.5	2367.9	4483.6	3330.7	3761.6	2794.3
3 <sup>rd</sup> unloading	3942.4	2928.7	6385.3	4743.3	8736.6	6490.1	9691.9	7199.7
3 <sup>rd</sup> reloading	----	----	3614.7	2685.2	----	----	5940.9	4413.2
4 <sup>th</sup> unloading	----	----	6149.3	4568.0	----	----	10474	7780.7

Table C-2: Evaluated moduli for samples with vertically aligned blocks.

Blocks vertically aligned	Block proportion							
	21%		24%		30%		40%	
	$E_s$ [MPa]	E [MPa]	$E_s$ [MPa]	E [MPa]	$E_s$ [MPa]	E [MPa]	$E_s$ [MPa]	E [MPa]
1 <sup>st</sup> loading	132.0	98.0	147.4	109.5	168.9	125.4	112.4	83.5
2 <sup>nd</sup> loading	170.8	126.9	246.5	183.1	267.4	198.7	319.9	237.6
3 <sup>rd</sup> loading	274.3	203.8	330.8	245.8	344.7	256.1	439.8	326.7
4 <sup>th</sup> loading	394.3	292.9	453.6	336.9	433.7	322.2	533.2	396.1
1 <sup>st</sup> unloading	6757.6	5020.0	8463.8	6287.4	3861.5	2868.5	4052.8	3010.7
1 <sup>st</sup> reloading	2276.1	1690.8	2919.1	2168.5	2036.4	1512.7	1831.4	1360.5
2 <sup>nd</sup> unloading	6369.5	4731.6	7716.7	5732.4	3784.0	2811.0	4707.0	3496.7
2 <sup>nd</sup> reloading	2370.6	1761.0	3606.7	2679.2	2098.7	1559.0	2816.7	2092.4
3 <sup>rd</sup> unloading	6519.7	4843.2	7539.5	5600.7	3959.6	2941.4	5175.8	3844.9
3 <sup>rd</sup> reloading	3151.4	2341.0	4432.8	3292.9	2416.3	1795.0	3226.2	2396.6
4 <sup>th</sup> unloading	4933.3	3664.7	7674.4	5701.0	5622.7	4176.9	4312.8	3203.8

Table C-3: Evaluated moduli for twisted blocks.

Blocks twisted	Block proportion							
	22%		31%		33%		42%	
	$E_s$ [MPa]	E [MPa]	$E_s$ [MPa]	E [MPa]	$E_s$ [MPa]	E [MPa]	$E_s$ [MPa]	E [MPa]
1 <sup>st</sup> loading	95.1	70.7	207.0	153.8	245.6	182.4	341.4	253.6
2 <sup>nd</sup> loading	142.5	105.8	319.3	237.2	333.9	248.0	522.1	387.8
3 <sup>rd</sup> loading	223.7	166.2	395.7	293.9	386.0	286.7	576.6	428.4
4 <sup>th</sup> loading	350.5	260.4	492.6	365.9	482.1	358.1	644.8	479.0
1 <sup>st</sup> unloading	2913.2	2164.1	6409.0	4761.0	3949.3	2933.8	4558.8	3386.5
1 <sup>st</sup> reloading	1404.0	1043.0	2999.5	2228.2	2300.5	1709.0	2213.1	1644.0
2 <sup>nd</sup> unloading	3641.9	2705.4	6597.2	4900.8	6575.3	4884.5	10,291	7645.0
2 <sup>nd</sup> reloading	1627.4	1208.9	3382.1	2512.4	3265.3	2425.6	4248.5	3156.0
3 <sup>rd</sup> unloading	3782.7	2810.0	6084.7	4520.0	6074.7	4512.6	10,909	8103.8
3 <sup>rd</sup> reloading	2148.8	1596.2	3673.2	2728.7	3513.9	2610.4	5167.2	3838.5
4 <sup>th</sup> unloading	3789.0	2814.7	5454.2	4051.7	5573.9	4140.6	7240.2	5378.4

Table C-4: Evaluated moduli for pure matrix and pure block samples.

	Block proportion			
	0% - pure matrix		100% - pure block	
	$E_s$ [MPa]	$E$ [MPa]	$E_s$ [MPa]	$E$ [MPa]
1 <sup>st</sup> loading	88.5	65.8	736.2	546.9
2 <sup>nd</sup> loading	162.6	120.8	7919.7	5883.2
3 <sup>rd</sup> loading	294.2	218.6	17,296.2	12,848.6
4 <sup>th</sup> loading	----	----	15,039.3	11,172.1
1 <sup>st</sup> unloading	2401.6	1784.1	7196.5	5346.0
1 <sup>st</sup> reloading	----	----	8678.3	6446.7
2 <sup>nd</sup> unloading	3356.6	2493.5	13,617.6	10,115.9
2 <sup>nd</sup> reloading	----	----	16,871.7	12,533.2
3 <sup>rd</sup> unloading	5059.4	3758.4	27,225.6	20,224.7
3 <sup>rd</sup> reloading	----	----	35,571.7	26,424.7
4 <sup>th</sup> unloading	----	----	40,705.5	30,238.3

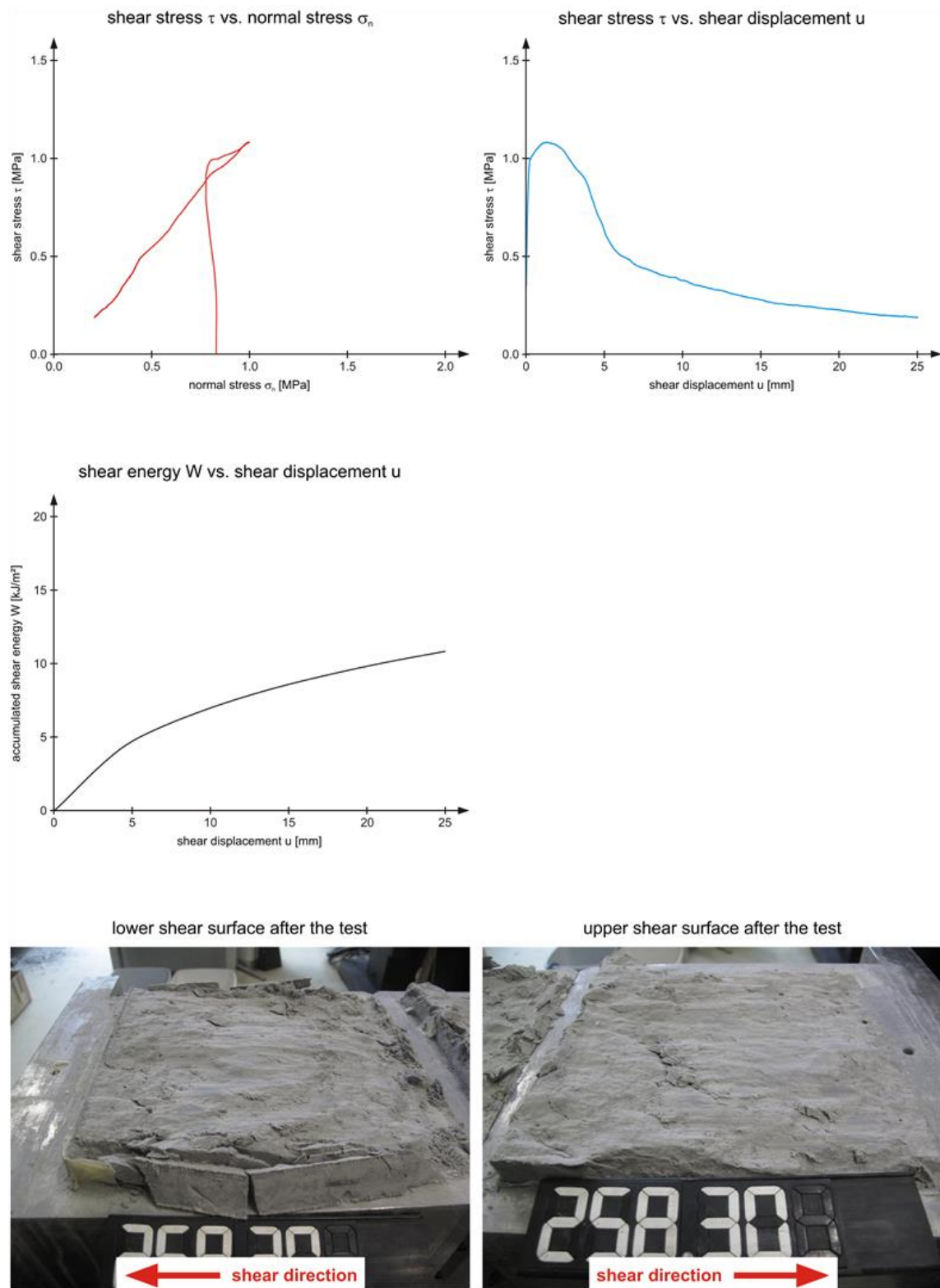


## **Appendix D    Compilation of test results for direct shear tests on artificial bimrocks**

This chapter contains the results of the performed direct shear tests on artificial bimrocks. The results are depicted in the same manner for each test. The sub-headline in brackets shows the symbol for the block arrangement, as indicated in Table 8. The upper left graph shows the stress path in a shear stress vs. normal stress diagram. For those samples, for which the engineering intact properties were evaluated, the Mohr-Coulomb failure line is provided in this figure, together with the range in which the failure line was evaluated, indicated by hair cross symbols (in most cases the range was between 0.5 mm and 1.5 mm of shear displacement). The upper right chart provides the shear stress vs. shear displacement plot. The left figure in the middle shows the evaluated shear energy  $W$  (accumulated shear energy vs. shear displacement). A chart on the right in the center is provided for the tests for which intact properties were evaluated. Depicted therein is the development of the measured, apparent sum of friction and dilation angles over the shear displacement, as well as the back-calculated development of the friction angle and the dilation angle over shear displacement. The two images at the bottom show the failure surfaces after the test. The lower shear surface is shown on the lower left side, while the upper shear surface is depicted on the lower right side.

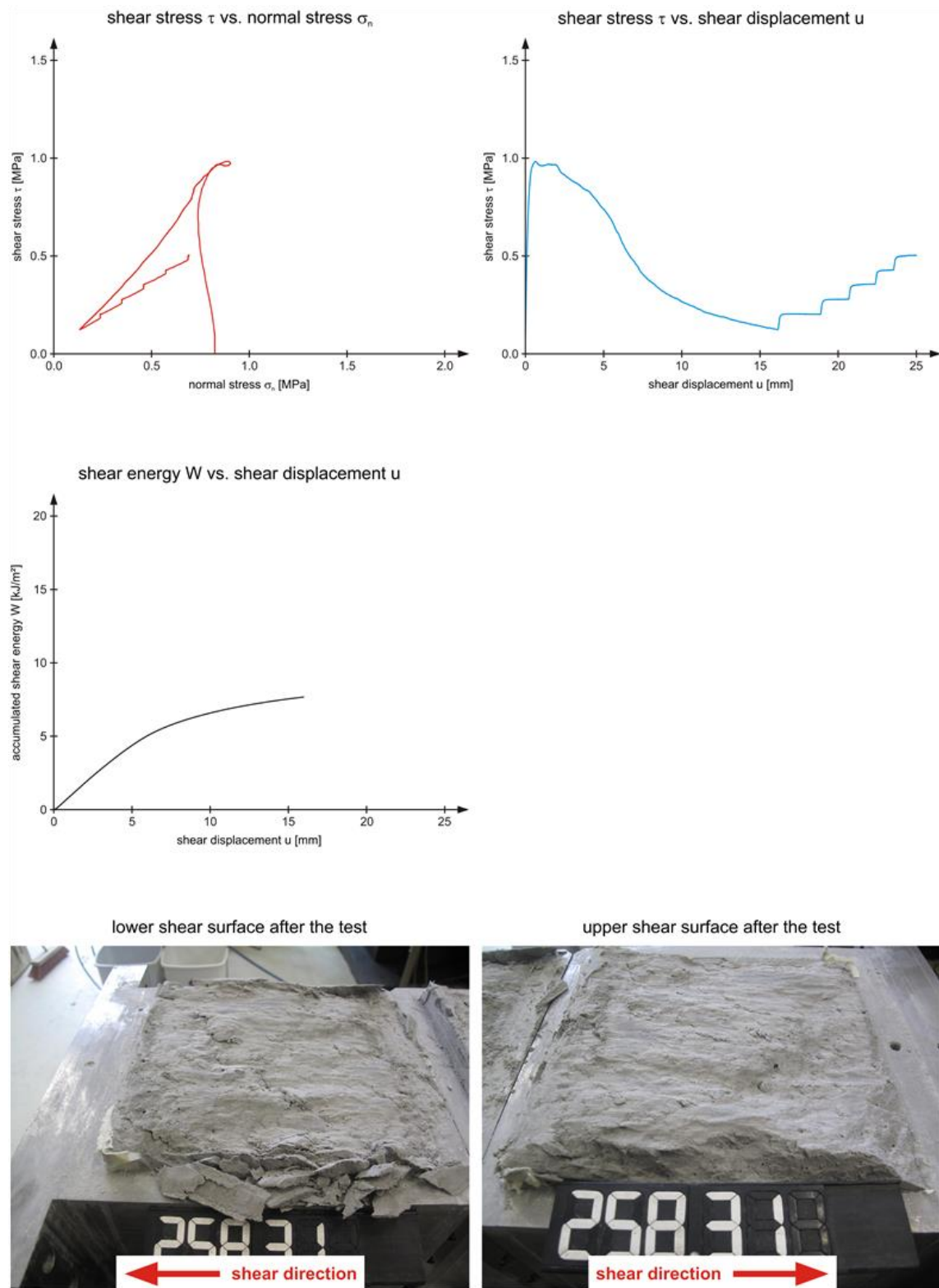
0% block proportion – pure matrix – test no. 1

(n/a)



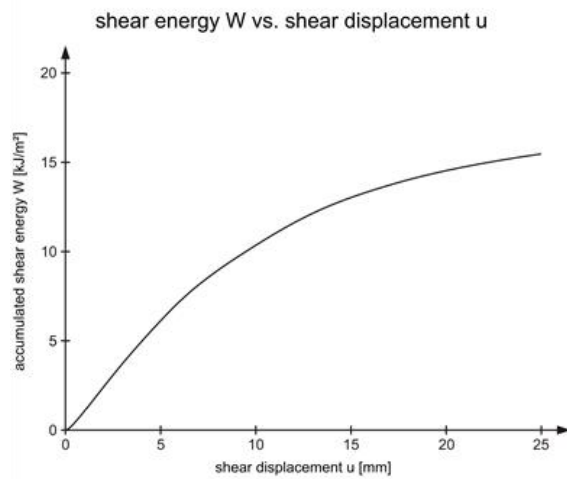
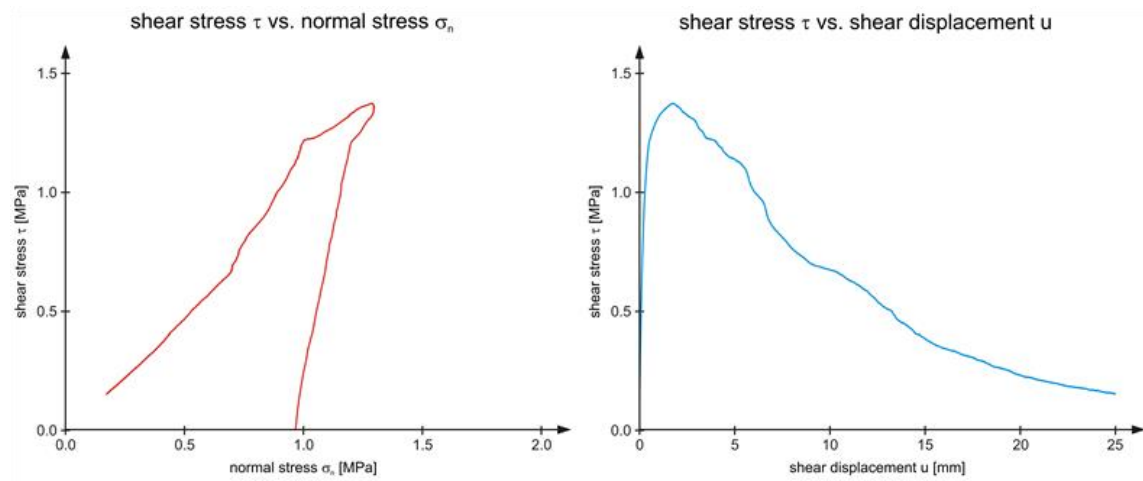
0% block proportion – pure matrix – test no. 2

(n/a)



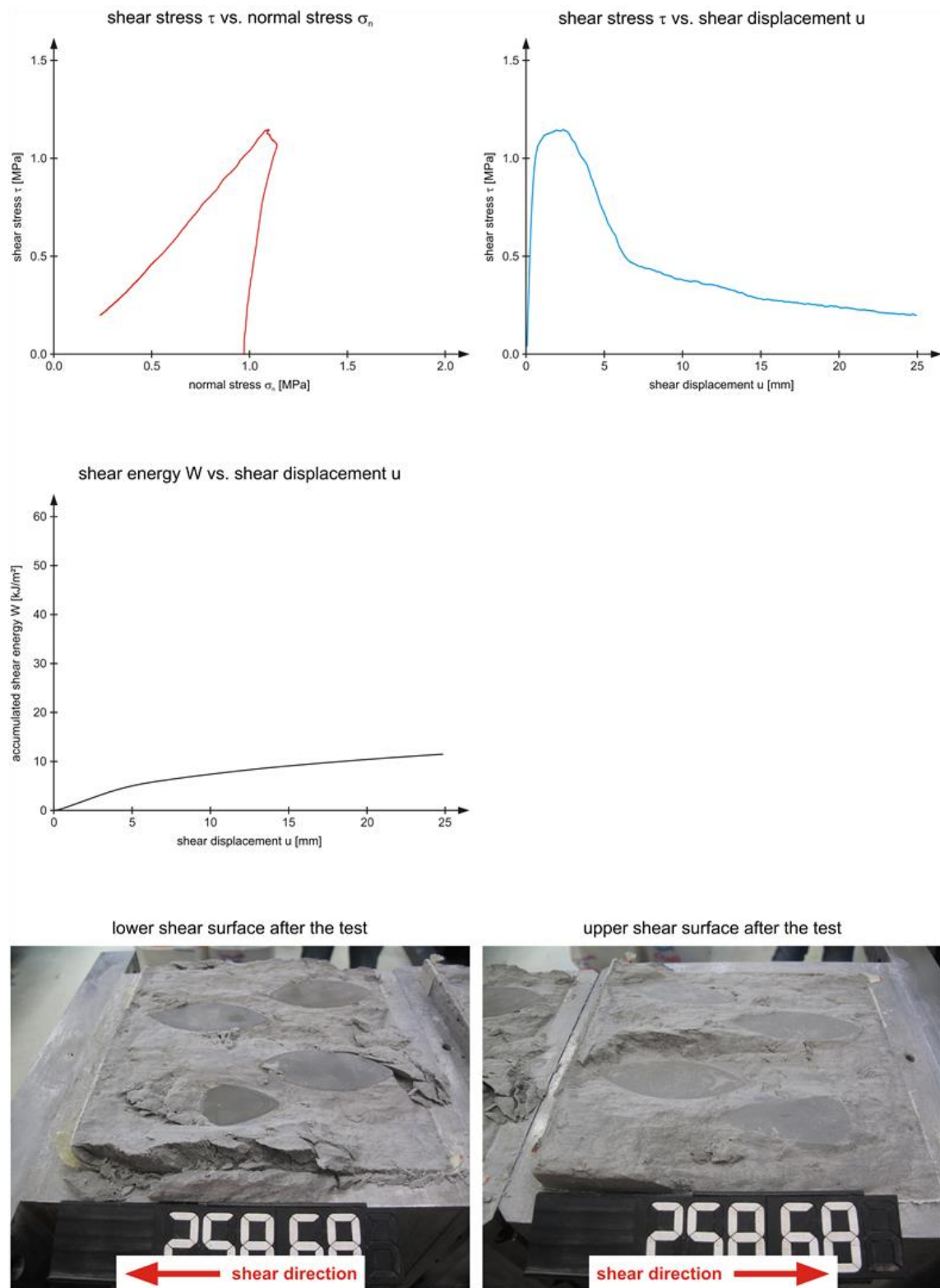
0% block proportion – pure matrix – test no. 3

(n/a)



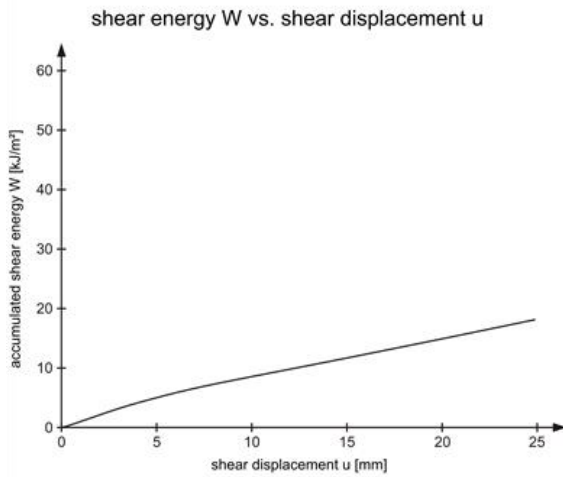
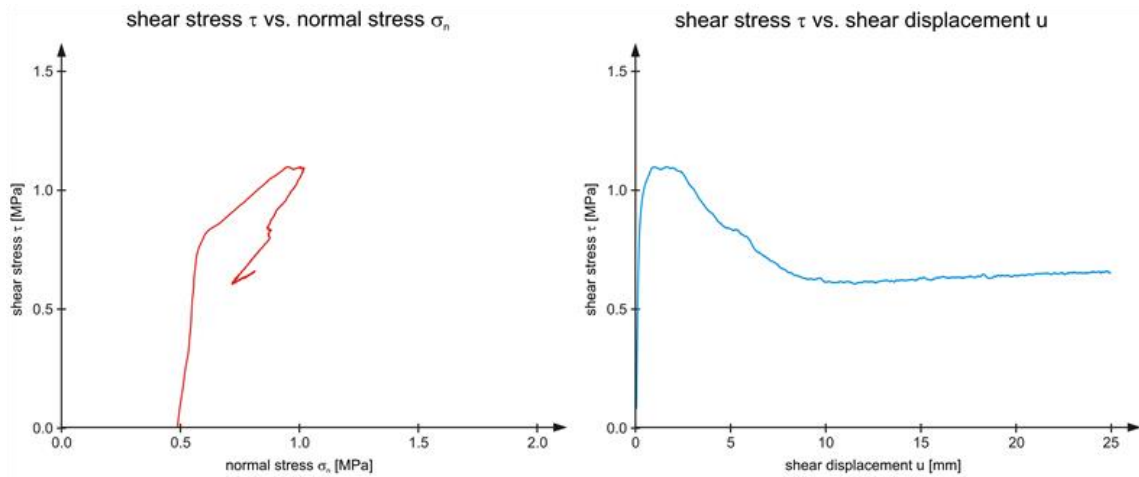
25% block proportion – 0° block orientation – shear in z-direction – test no. 1

(→ ---- long.)



25% block proportion – 0° block orientation – shear in z-direction – test no. 2

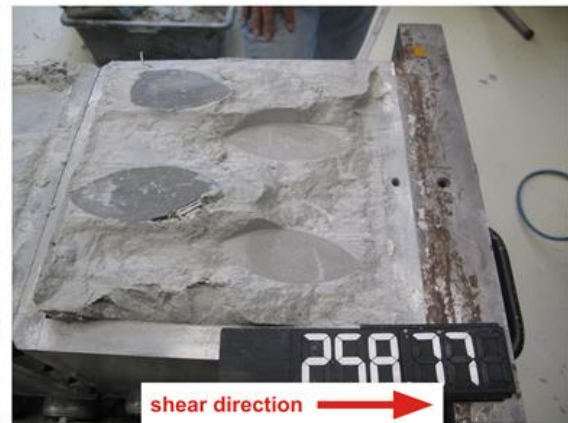
(→ ---- long.)



lower shear surface after the test

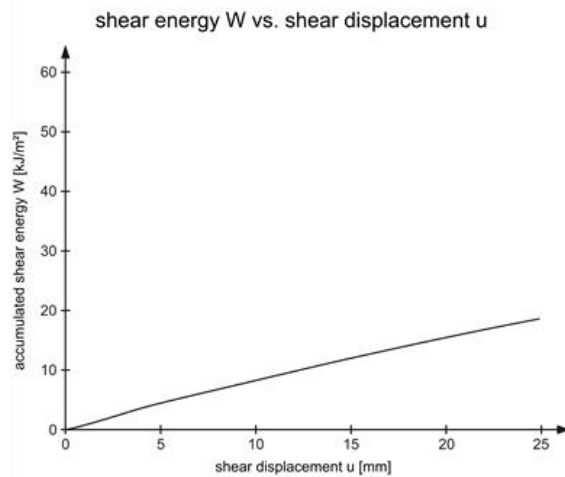
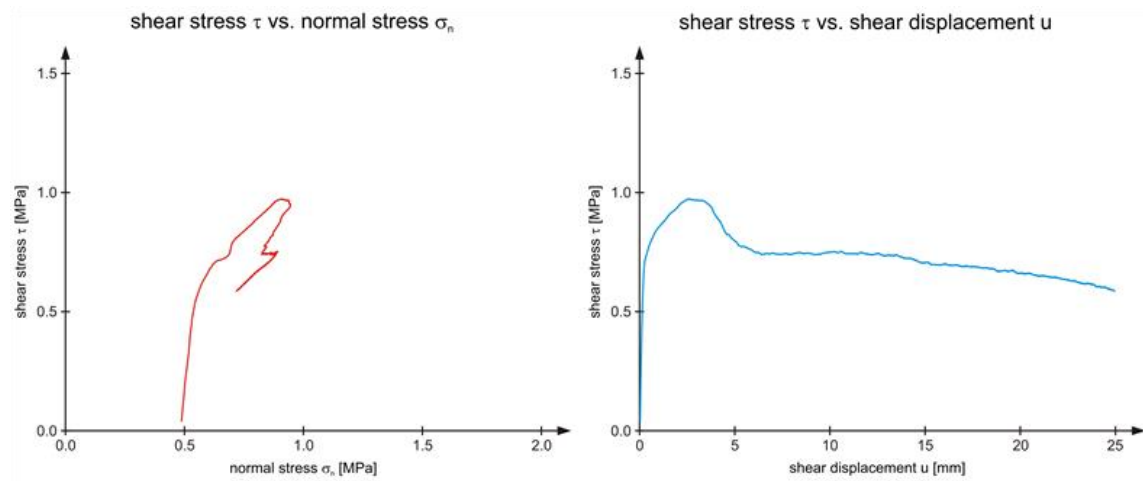


upper shear surface after the test

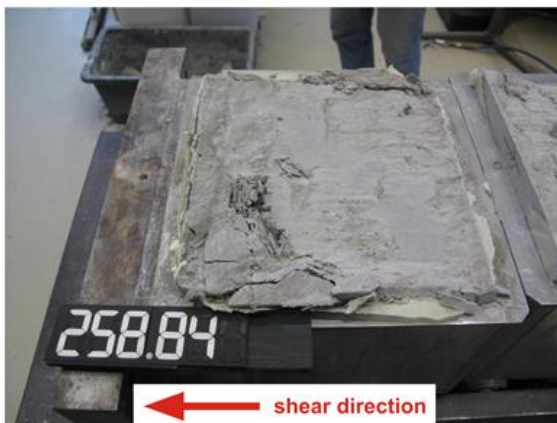


25% block proportion – 0° block orientation – shear in x-direction – test no. 1

(→ ---- trans.)



lower shear surface after the test

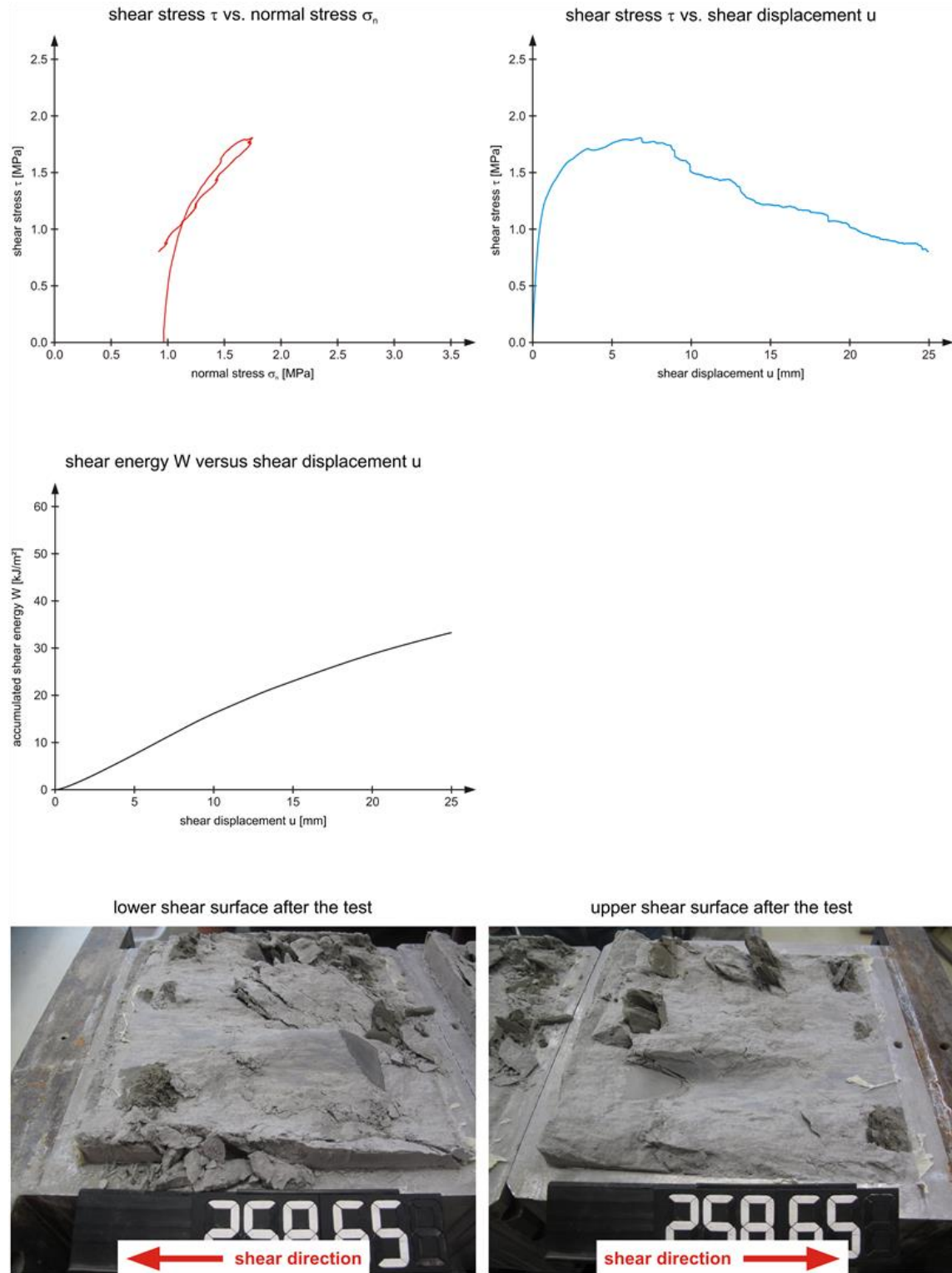


upper shear surface after the test



25% block proportion – 30° block orientation – inclined against shear direction – test no. 1

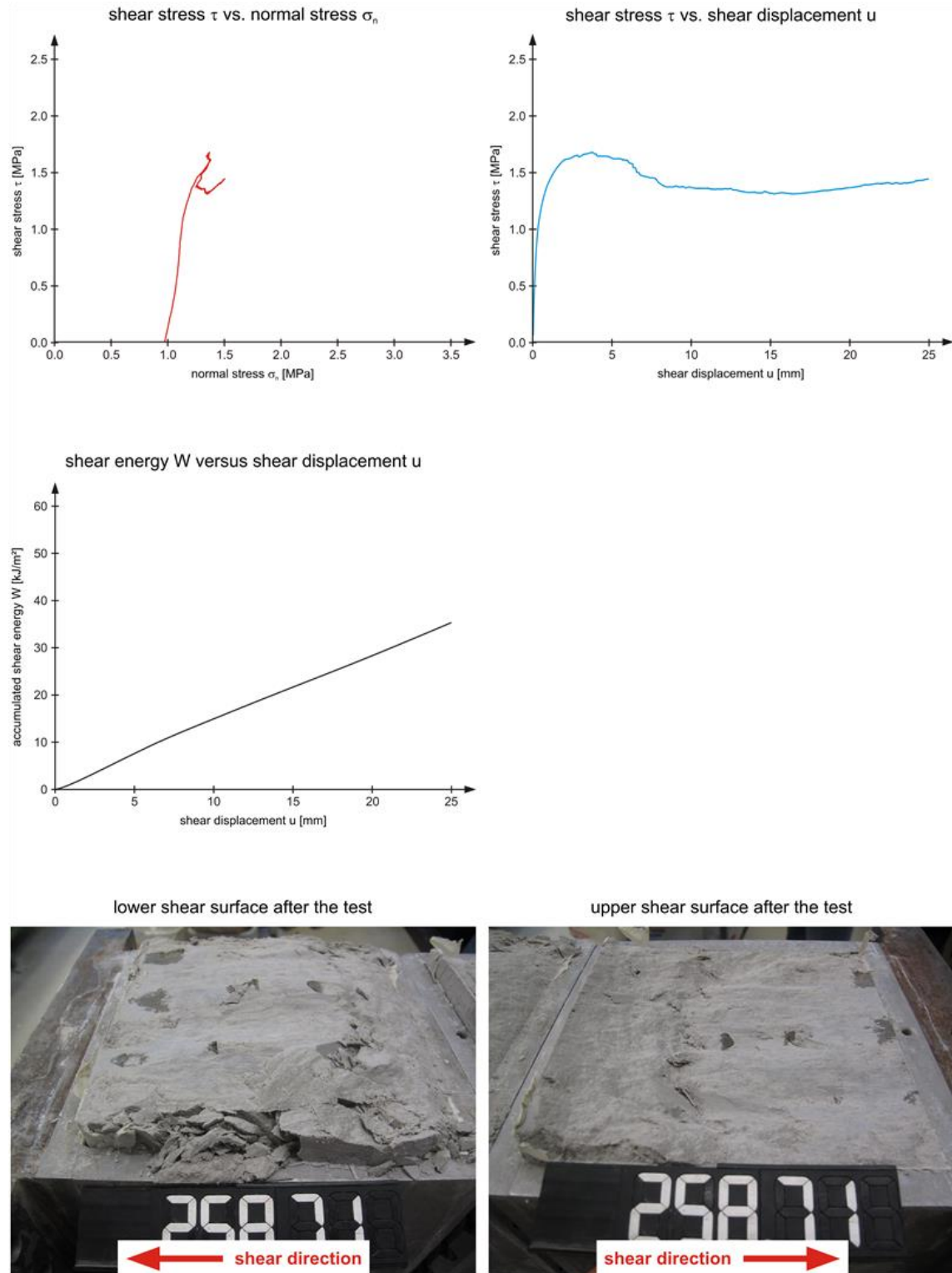
(→ ///)





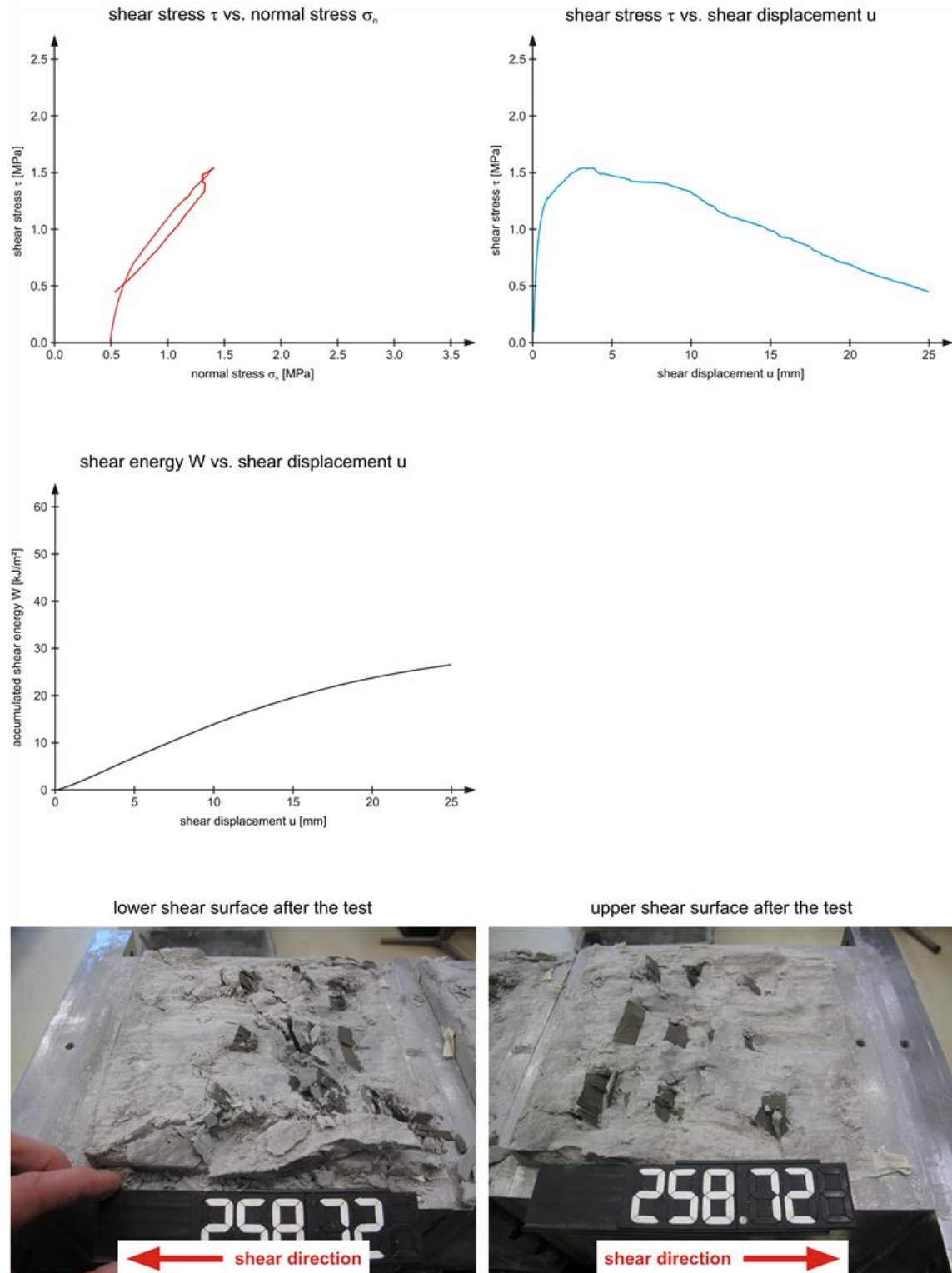
25% block proportion – 30° block orientation – inclined against shear direction – test no. 2

(→ ///)



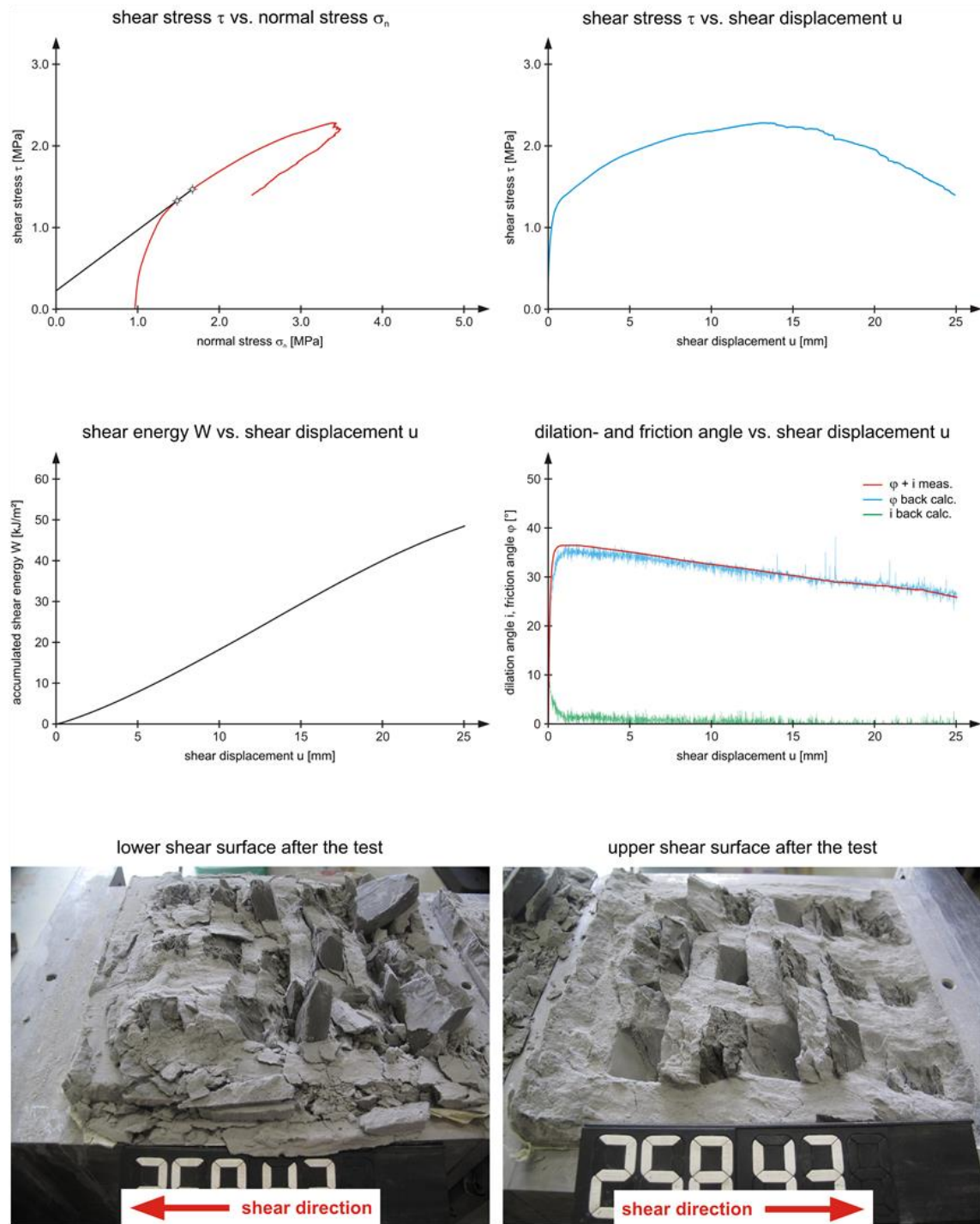
25% block proportion – 30° block orientation – inclined in shear direction – test no. 1

(→ \\\)



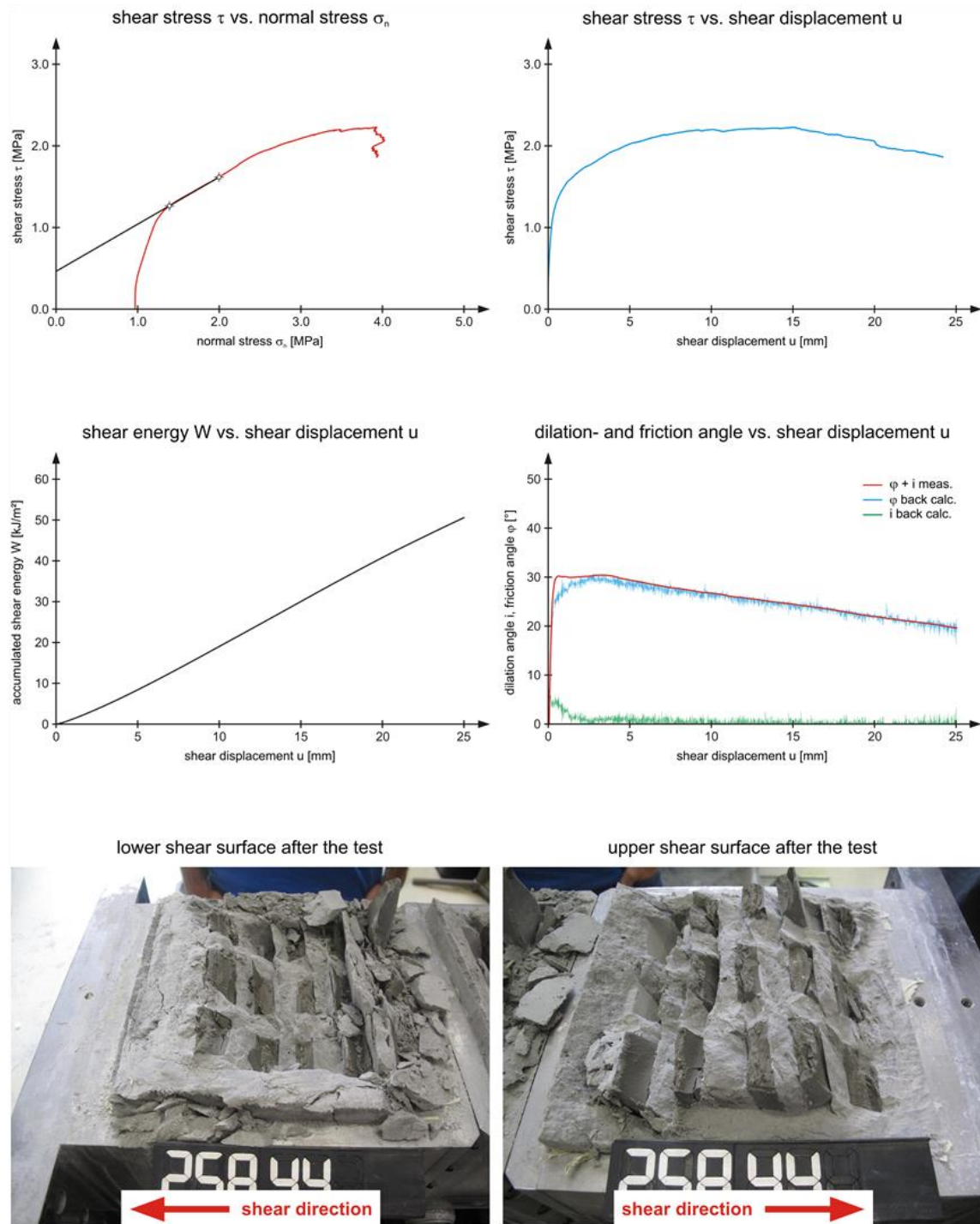
25% block proportion – 60° block orientation – inclined against shear direction – test no. 1

(→ ///)



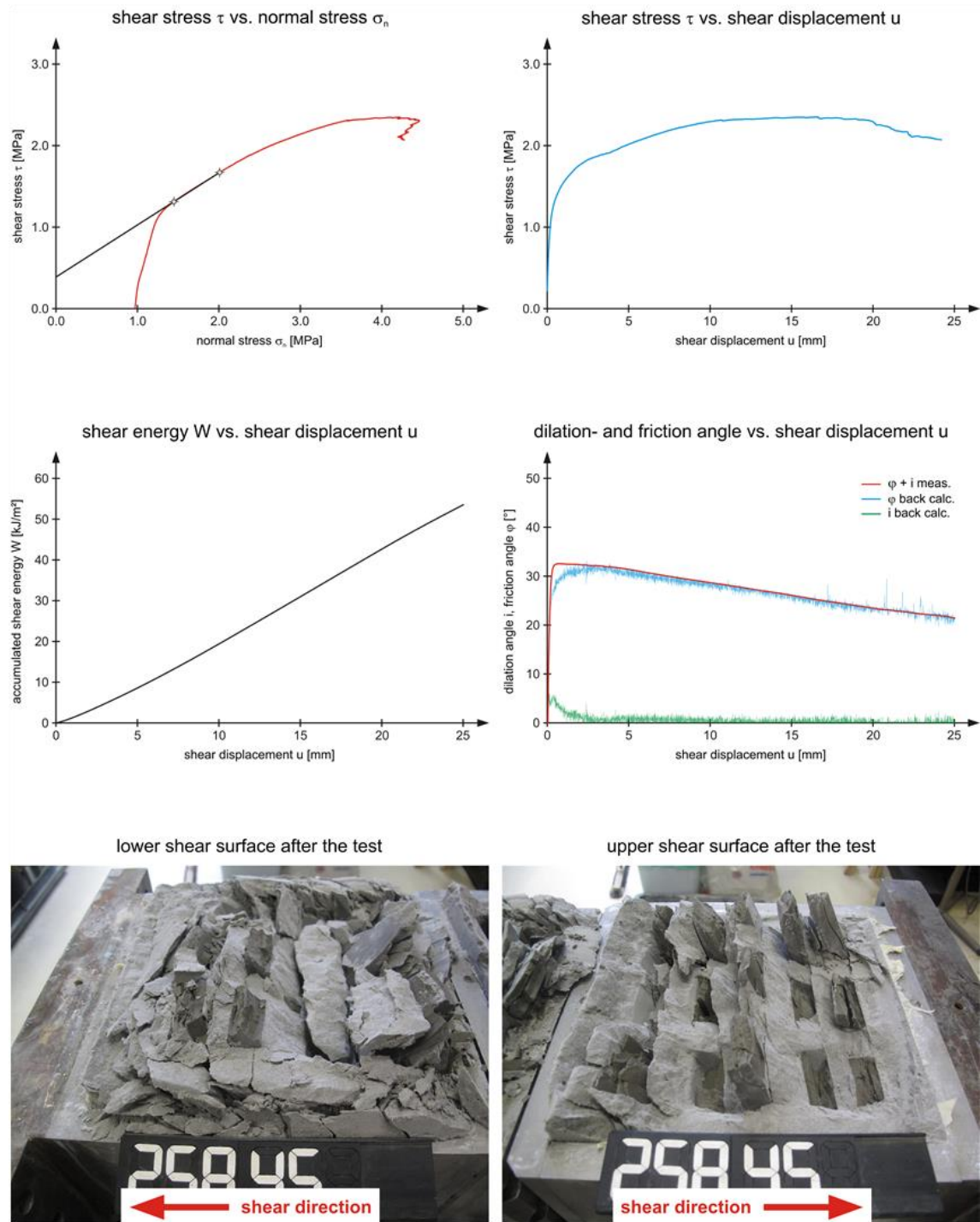
25% block proportion – 60° block orientation – inclined against shear direction – test no. 2

(→ ///)



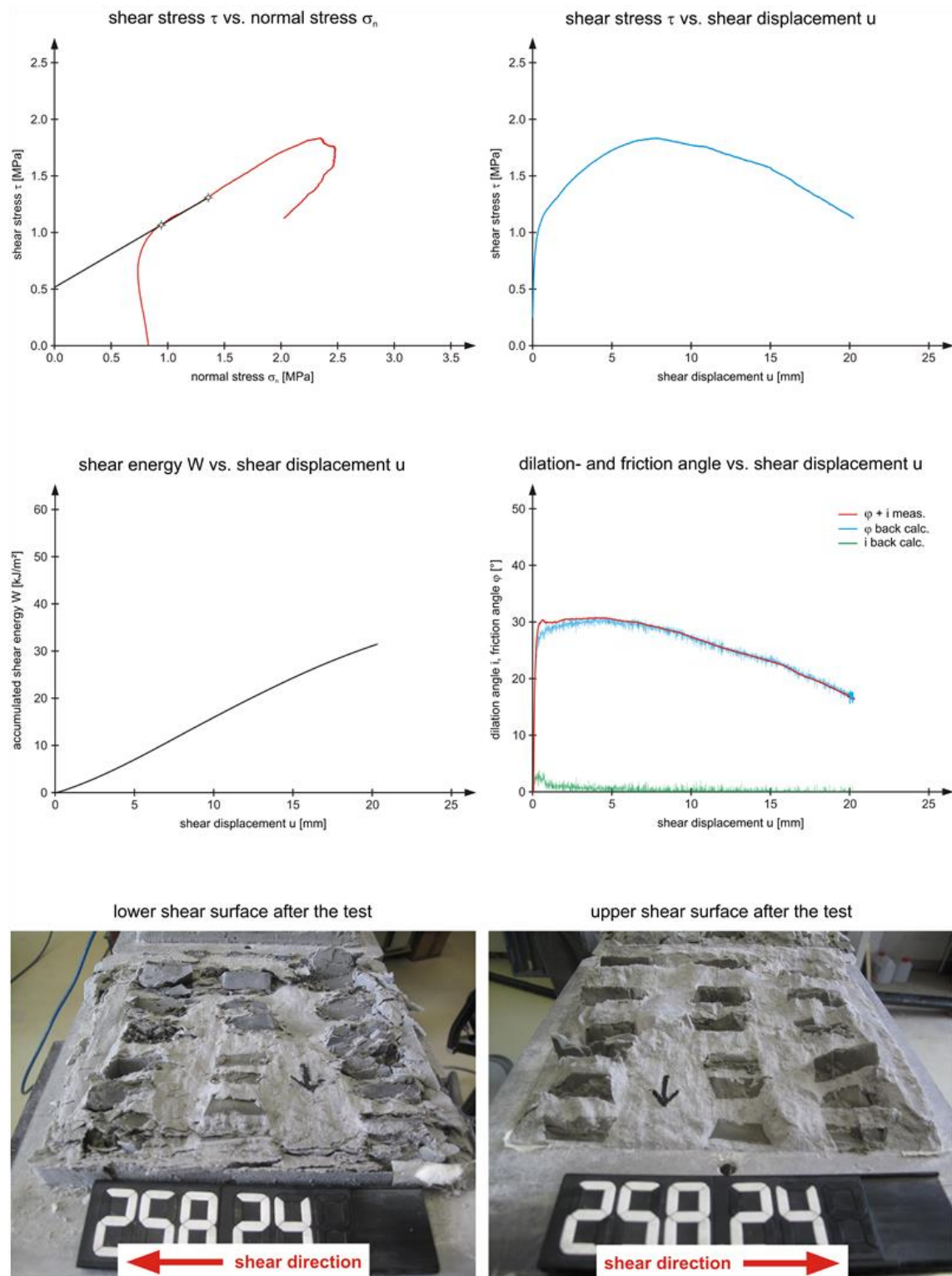
25% block proportion – 60° block orientation – inclined against shear direction – test no. 3

(→ ///)



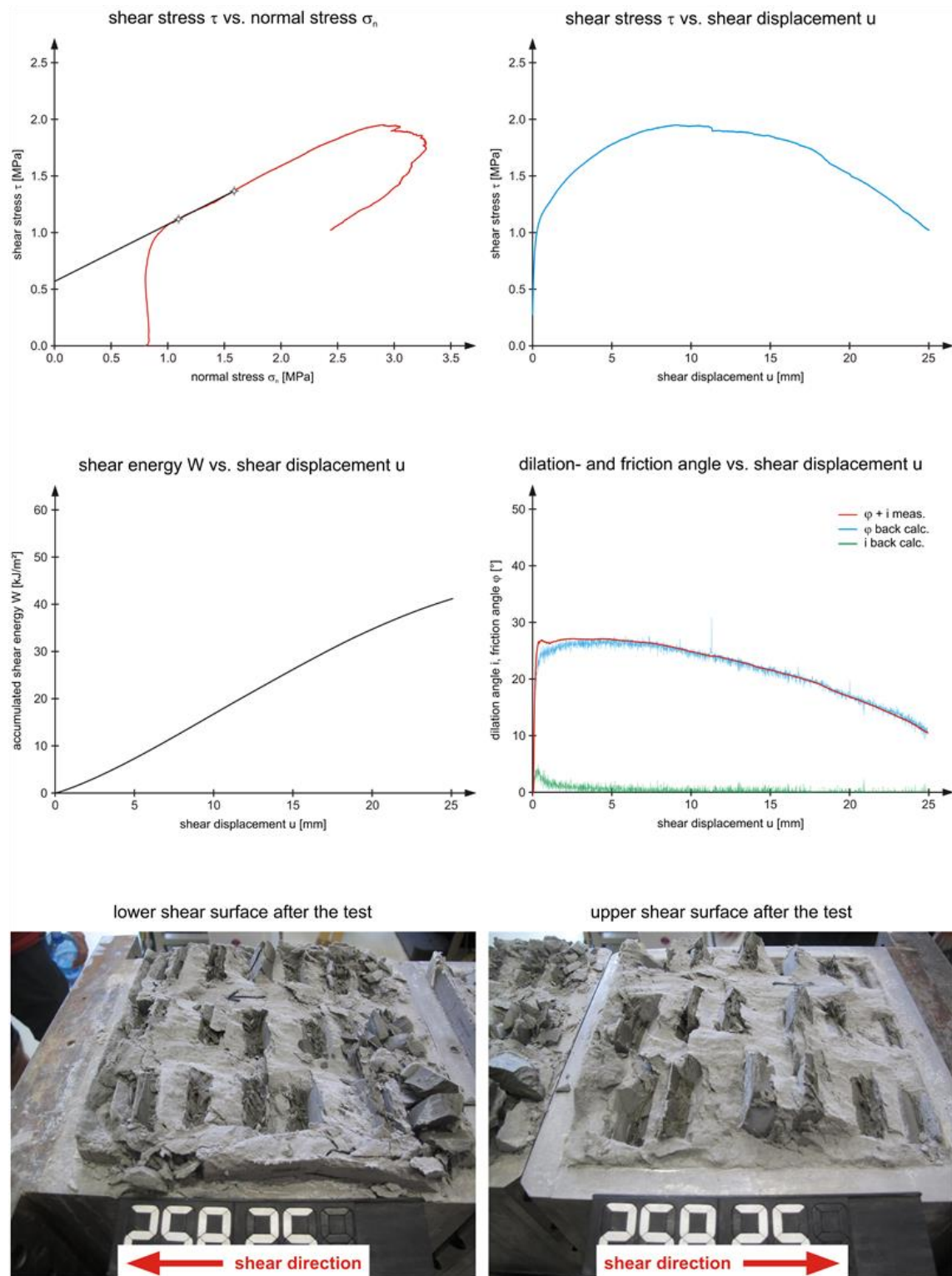
25% block proportion – 90° block orientation – shear in y-direction – test no. 1

(→ |||  $\sigma$  in z-dir.)



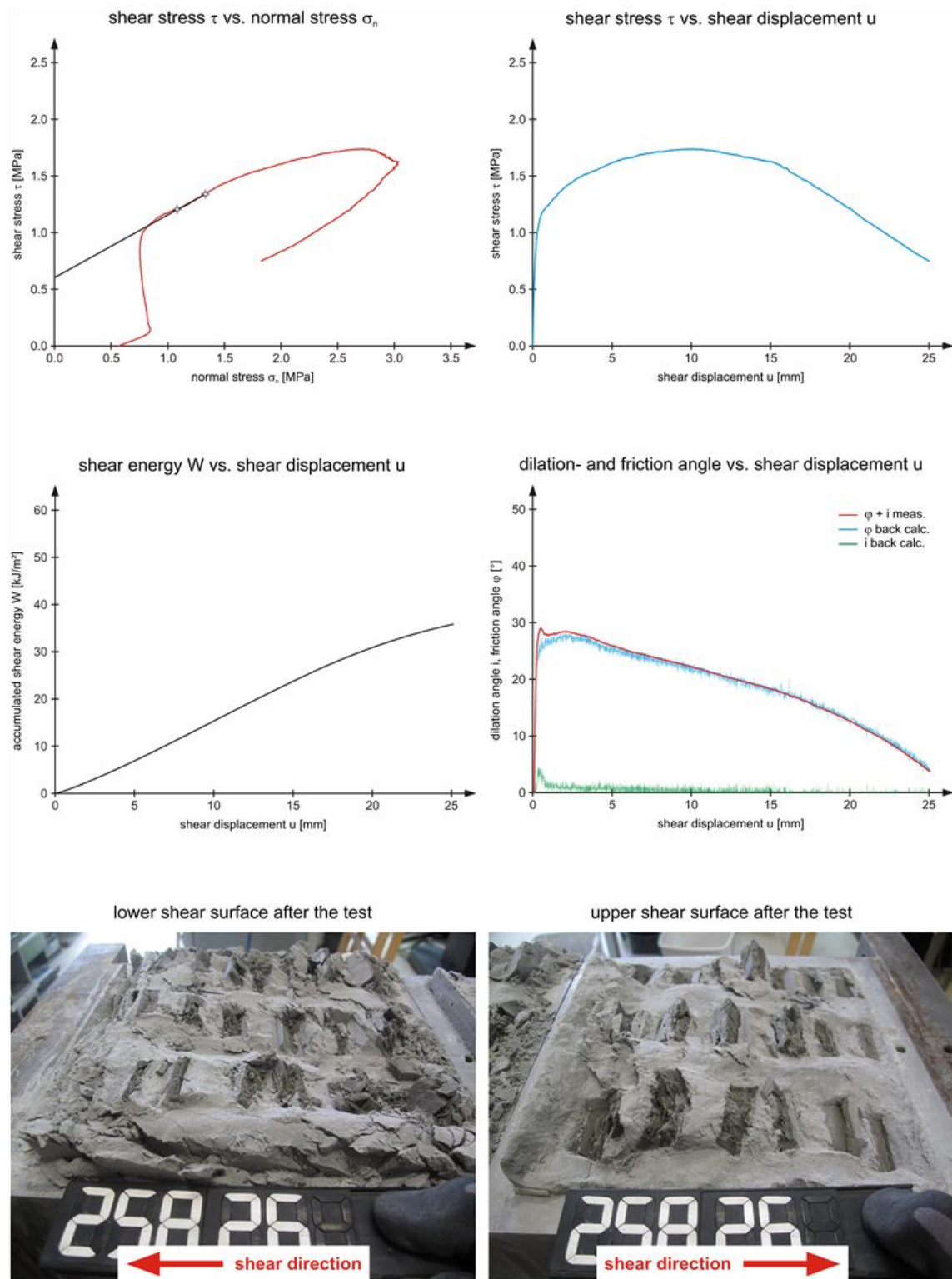
25% block proportion – 90° block orientation – shear in y-direction – test no. 2

(→ |||  $\sigma$  in z-dir.)



25% block proportion – 90° block orientation – shear in y-direction – test no. 3

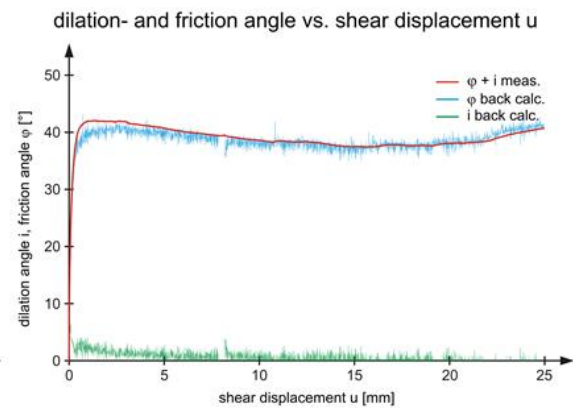
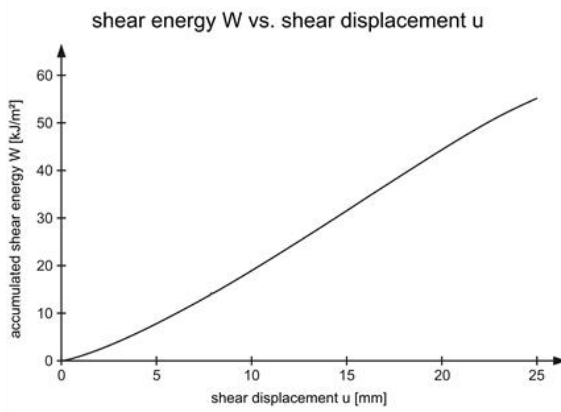
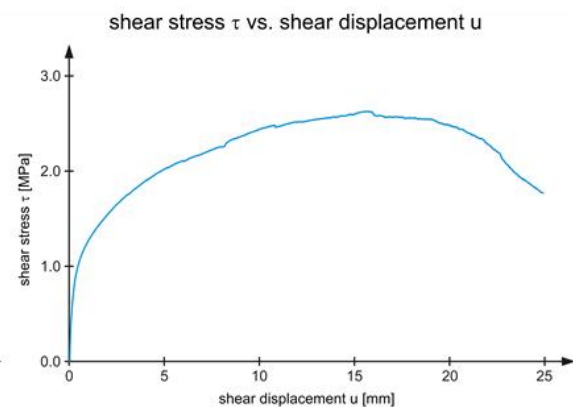
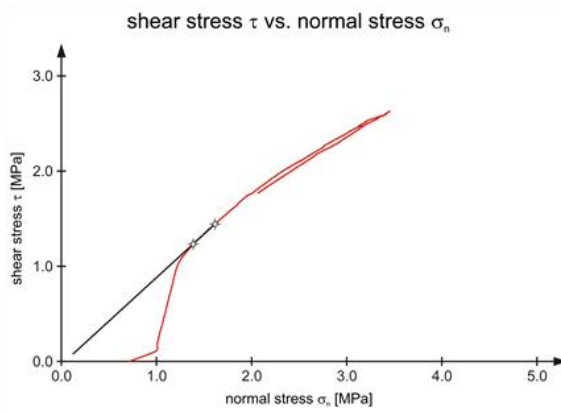
(→ |||  $\sigma$  in z-dir.)



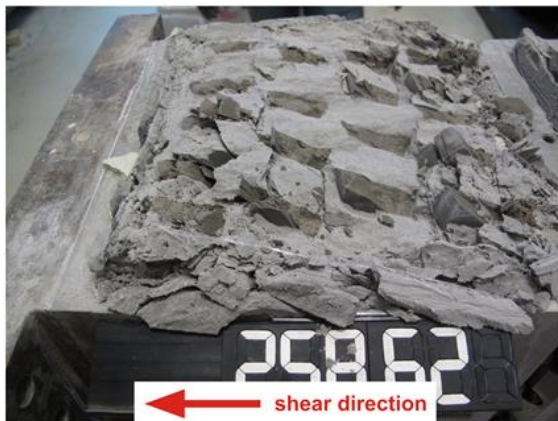


25% block proportion – 90° block orientation – shear in x-direction – test no. 1

(→ ||| par.  $\sigma$  in z-dir.)



lower shear surface after the test

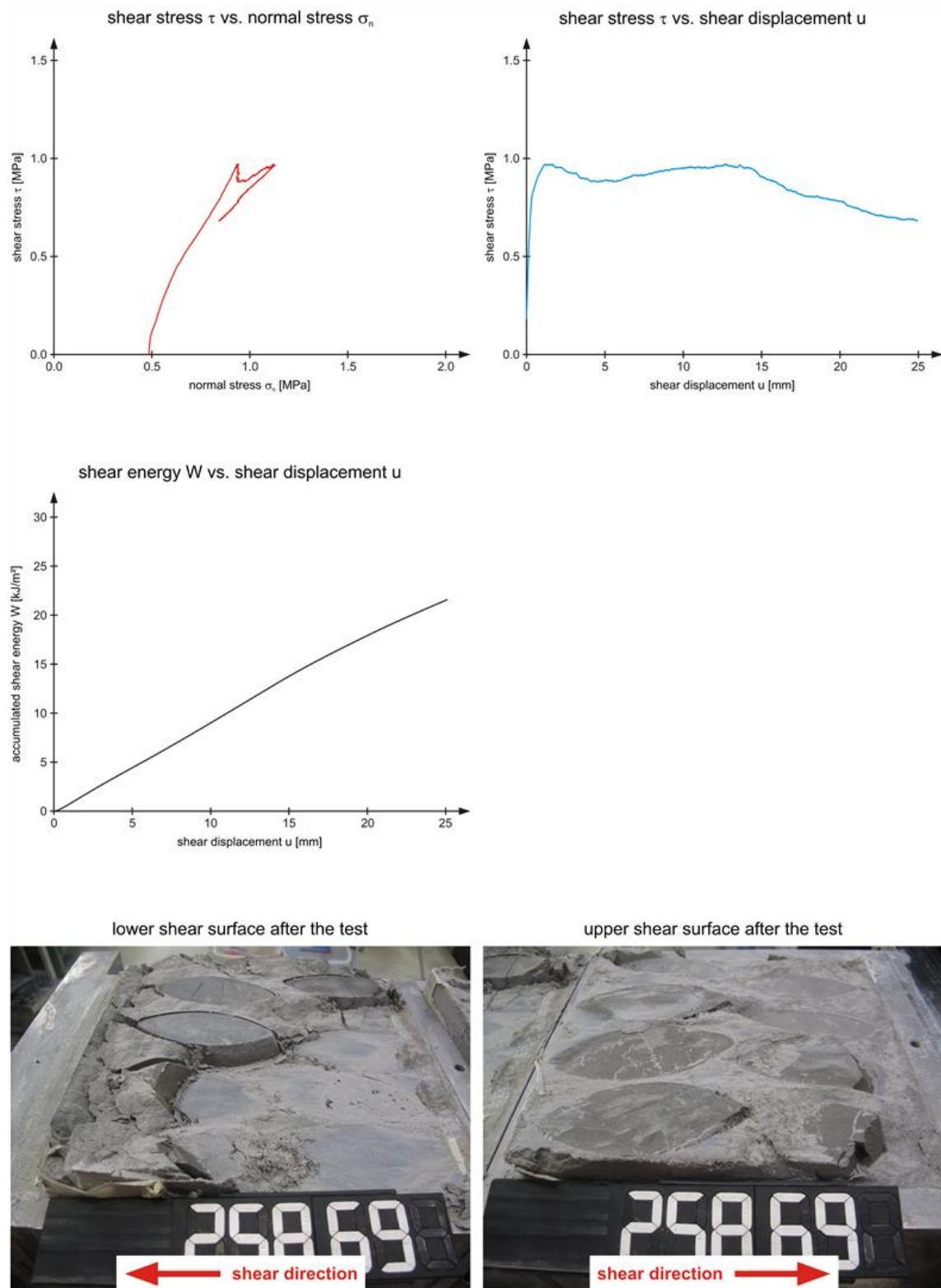


upper shear surface after the test



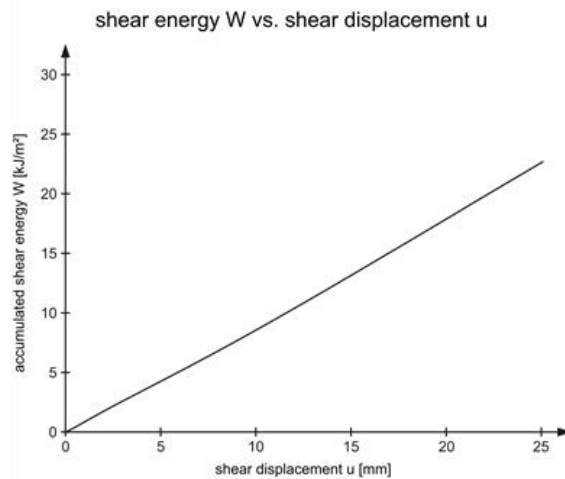
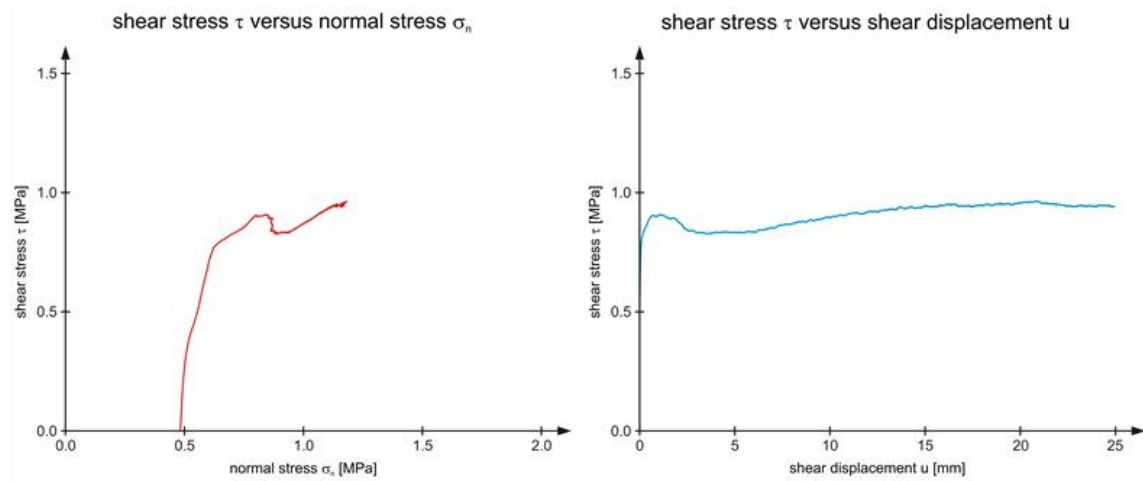
50% block proportion – 0° block orientation – shear in z-direction – test no. 1

(→ ---- long.)

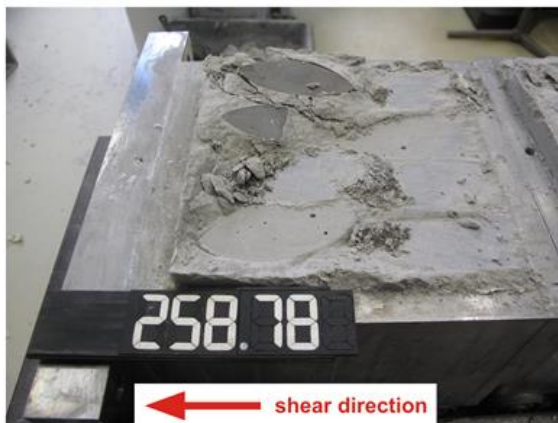


50% block proportion – 0° block orientation – shear in z-direction – test no. 2

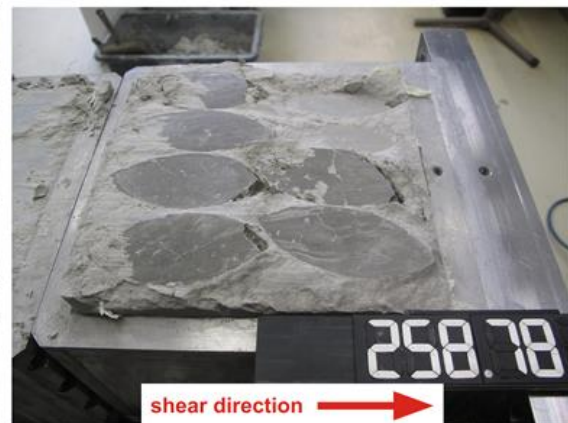
(→ ---- long.)



lower shear surface after the test

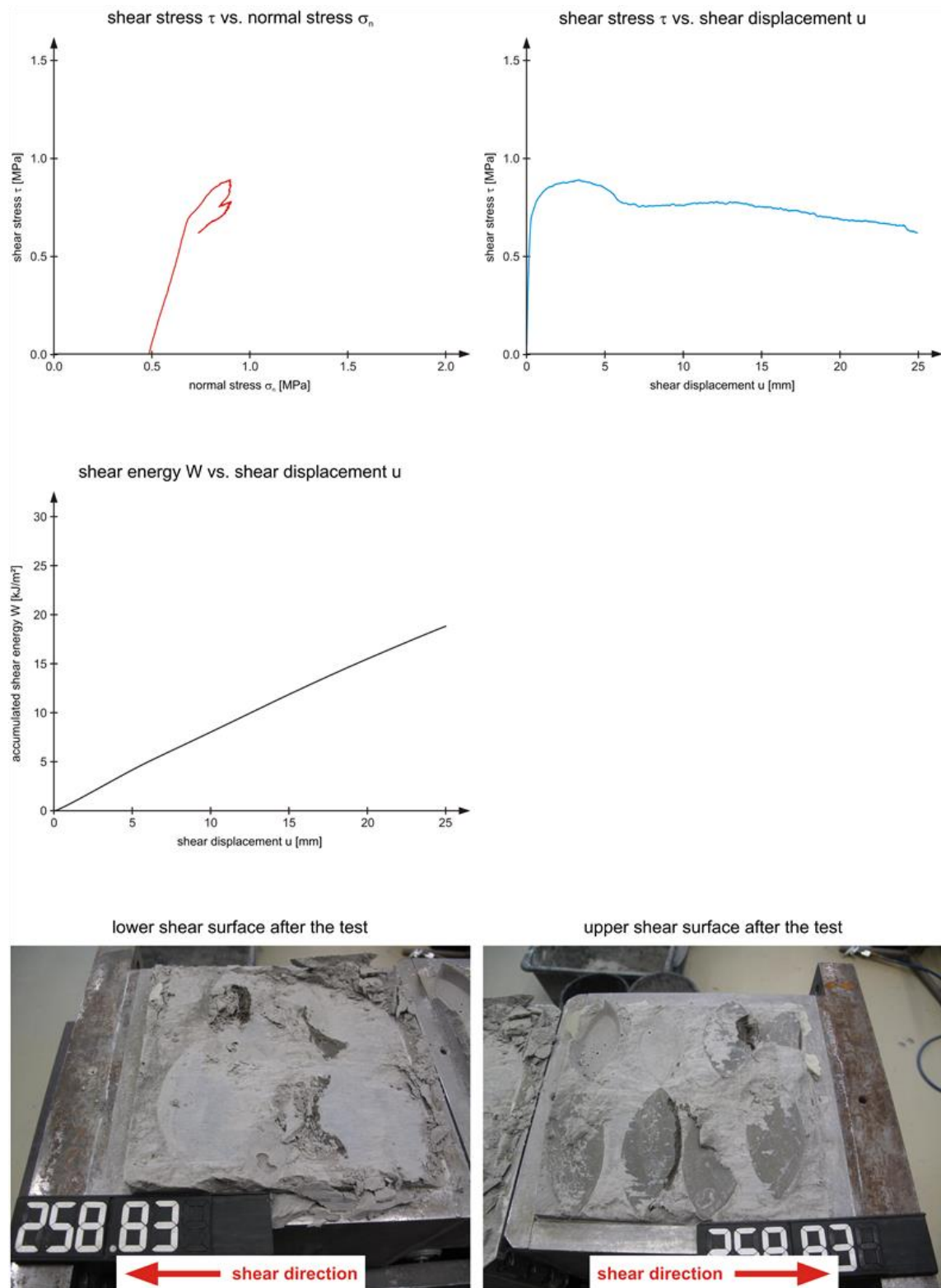


upper shear surface after the test



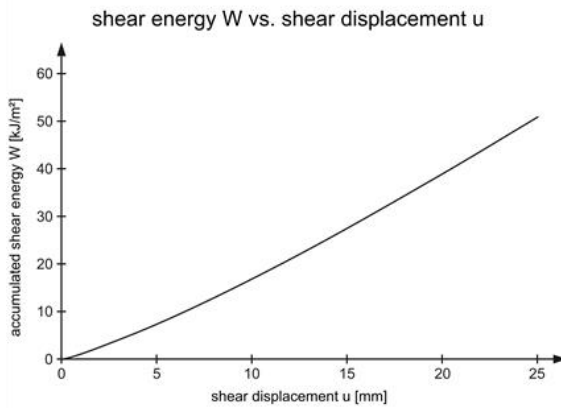
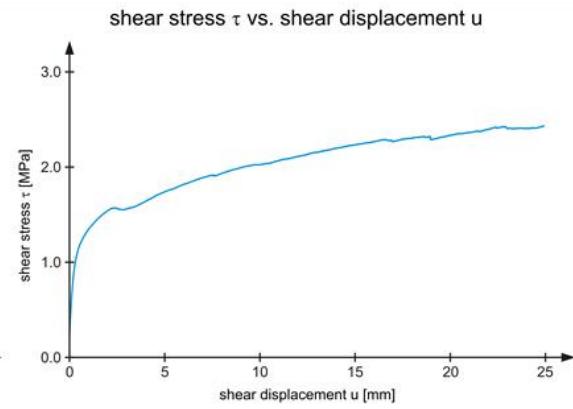
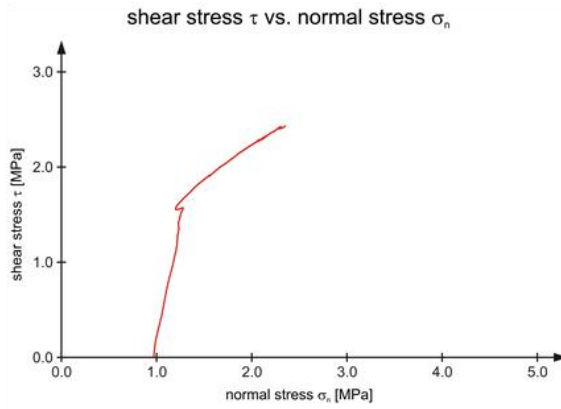
50% block proportion – 0° block orientation – shear in x-direction – test no. 1

(→ ---- trans.)



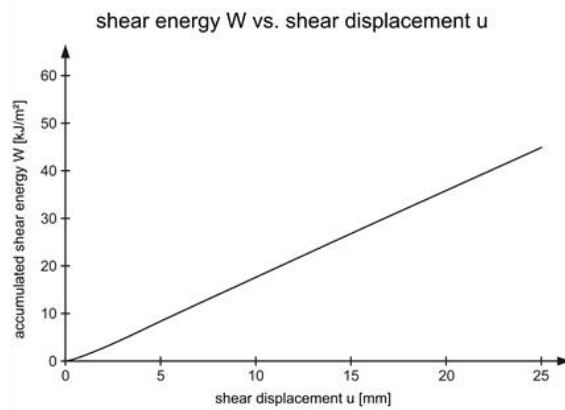
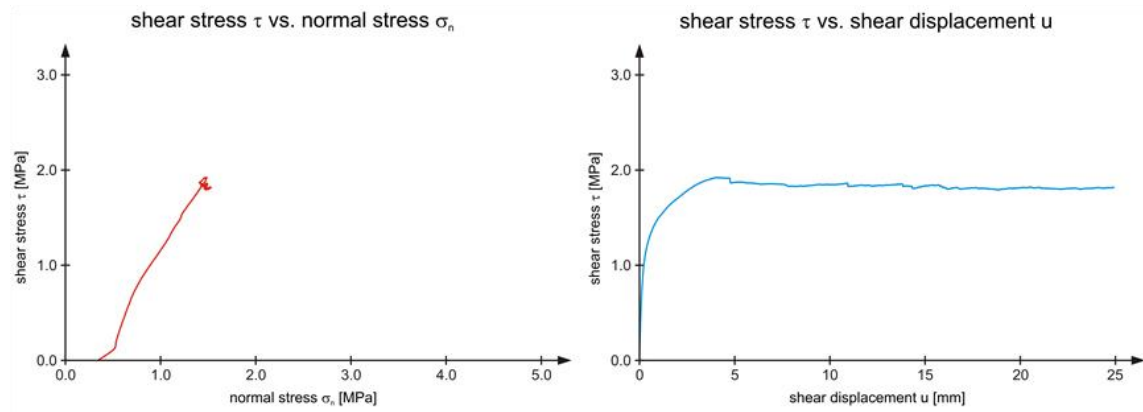
50% block proportion – 30° block orientation – inclined against shear direction – test no. 1

(→ ///)



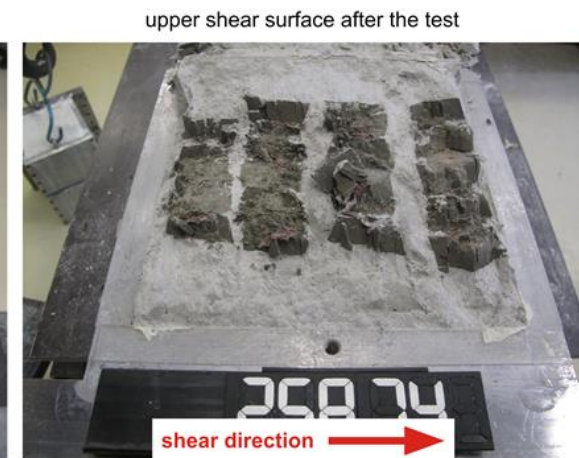
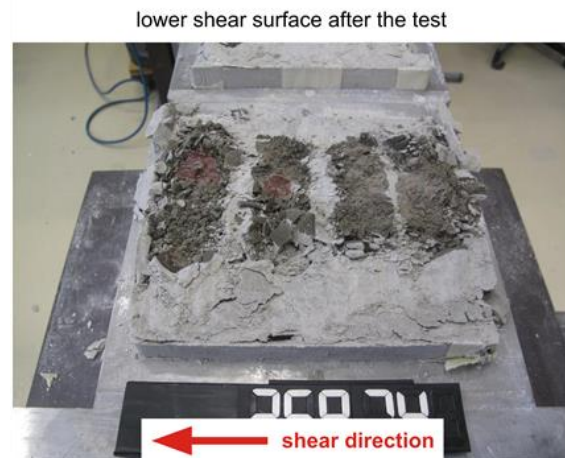
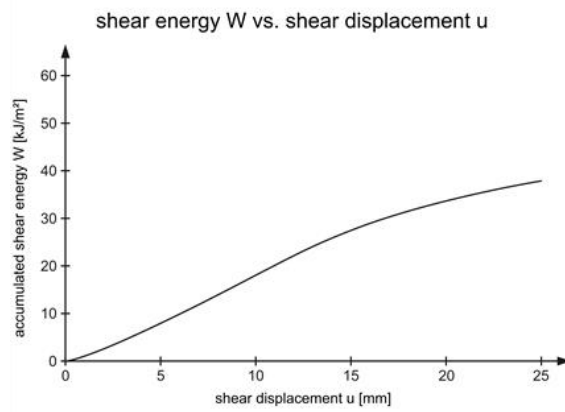
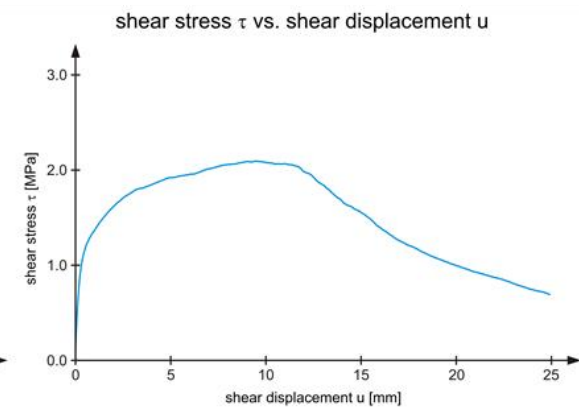
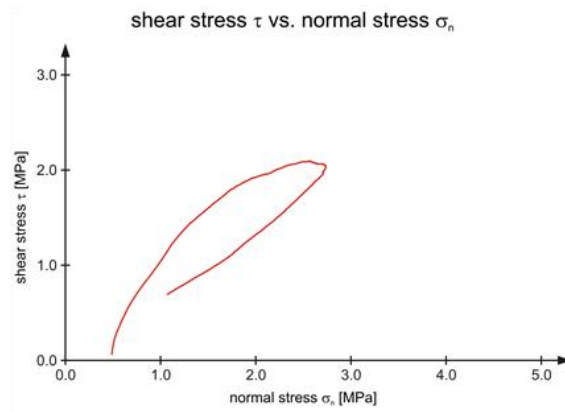
50% block proportion – 30° block orientation – inclined against shear direction – test no. 2

(→ ///)



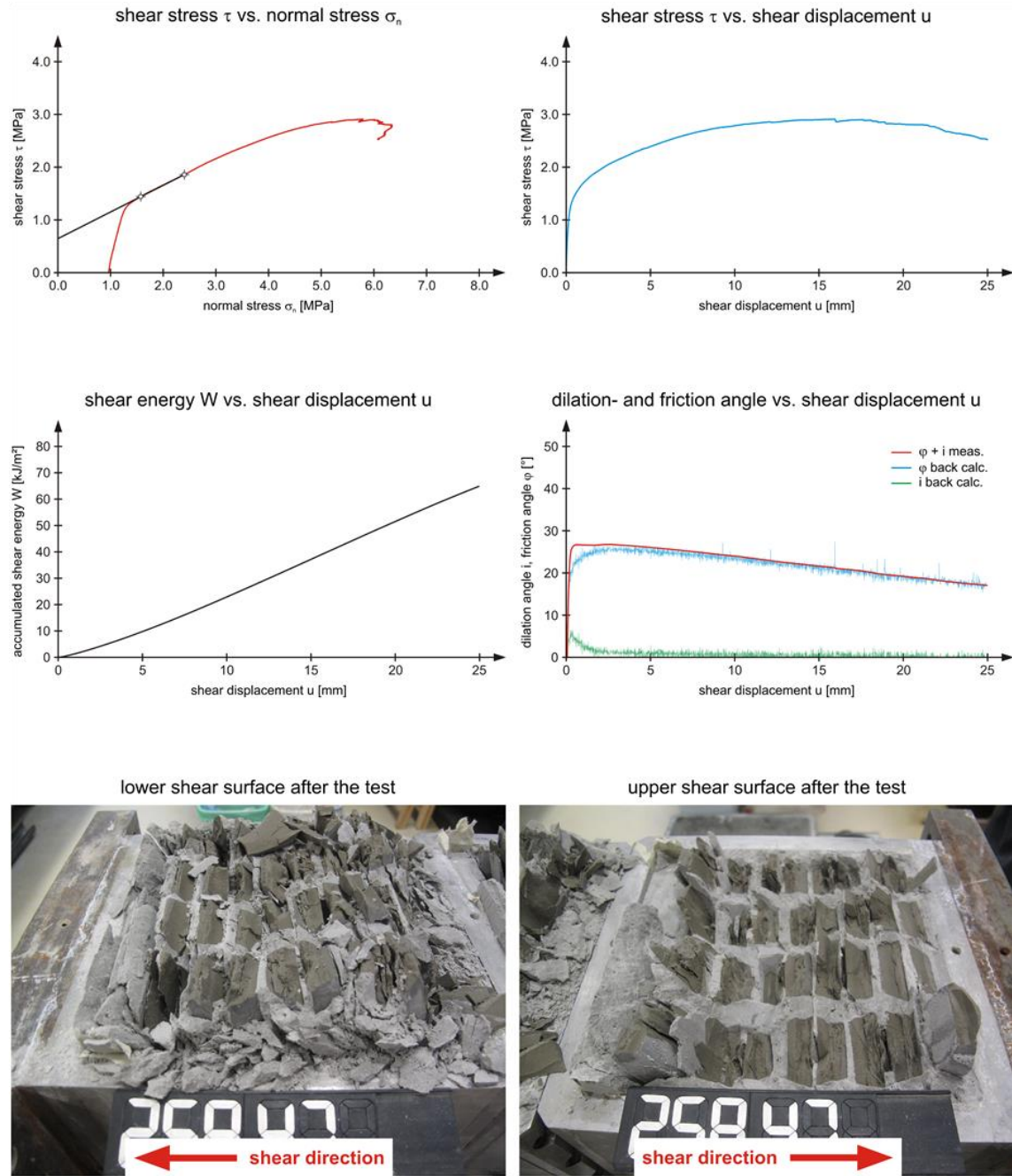
50% block proportion – 30° block orientation – inclined in shear direction – test no. 1

(→ \\\)



50% block proportion – 60° block orientation – inclined against shear direction – test no. 1

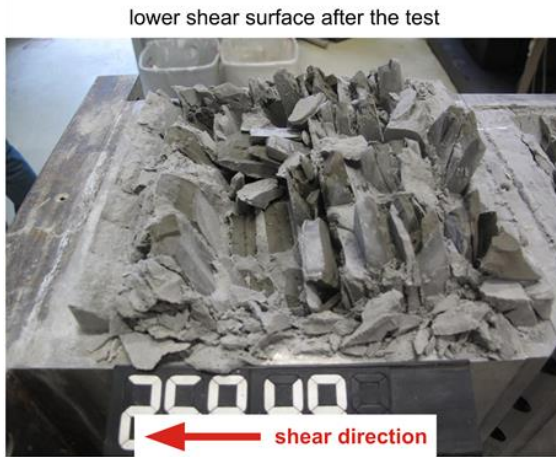
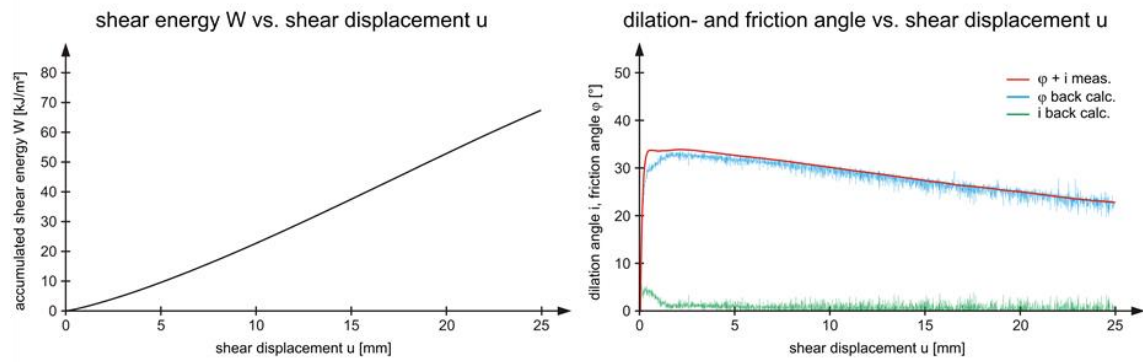
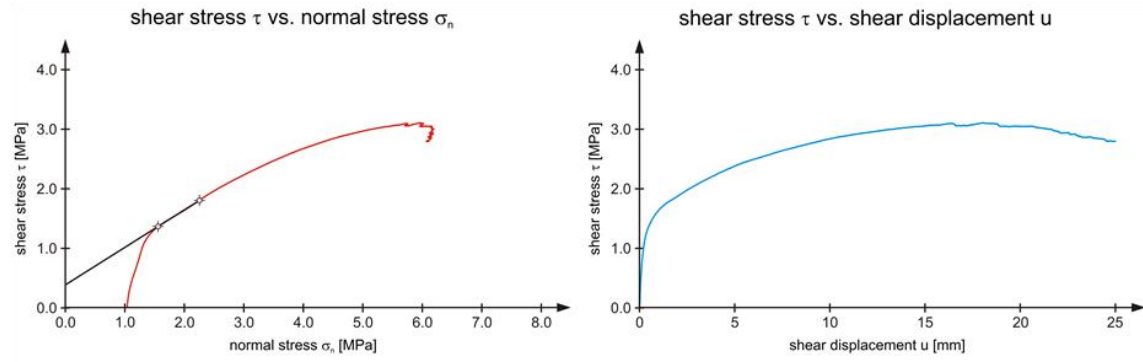
(→ ///)





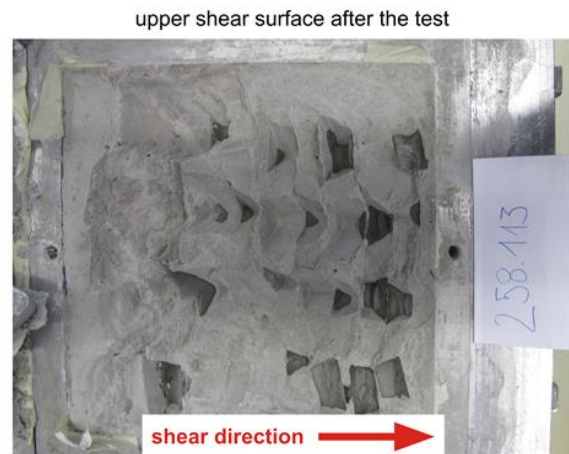
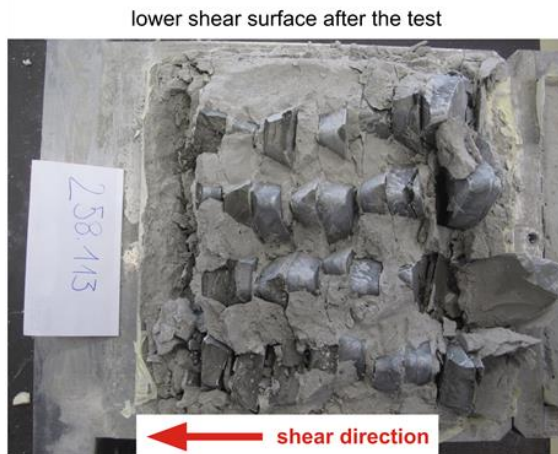
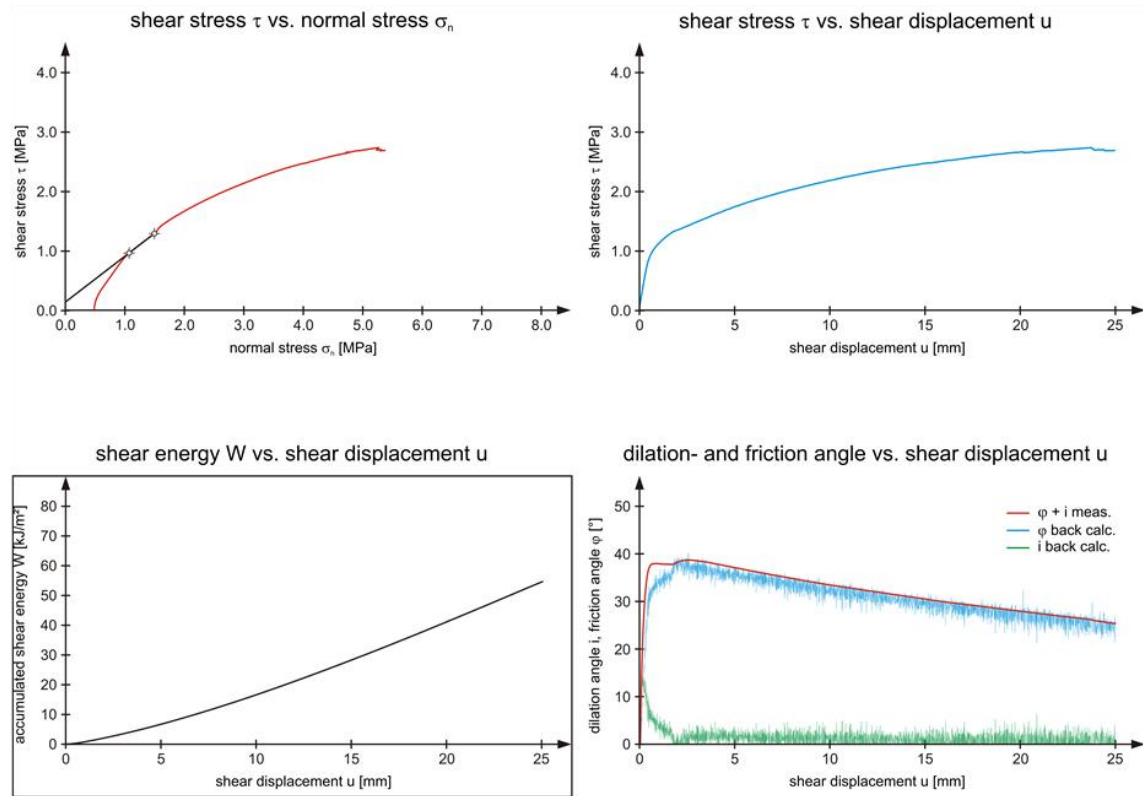
50% block proportion – 60° block orientation – inclined against shear direction – test no. 2

(→ ///)



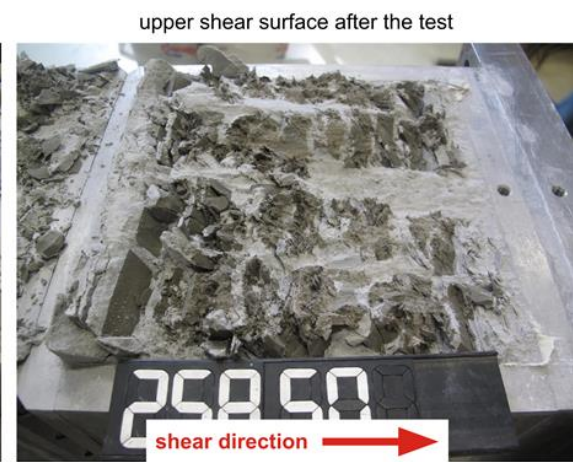
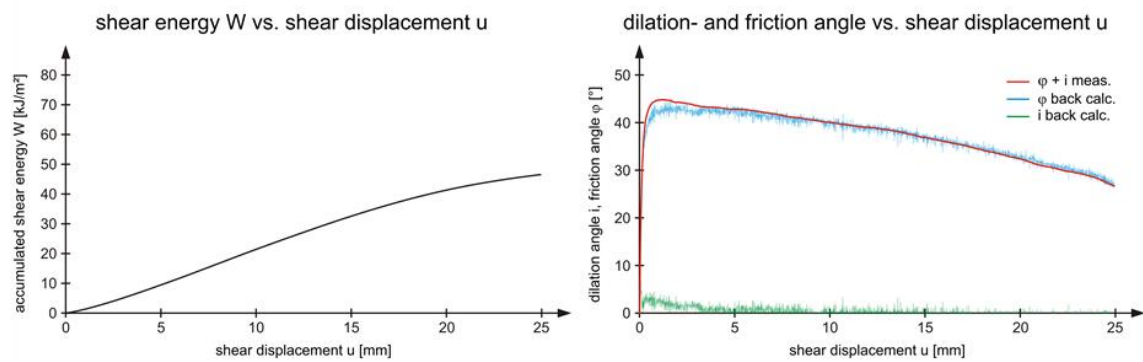
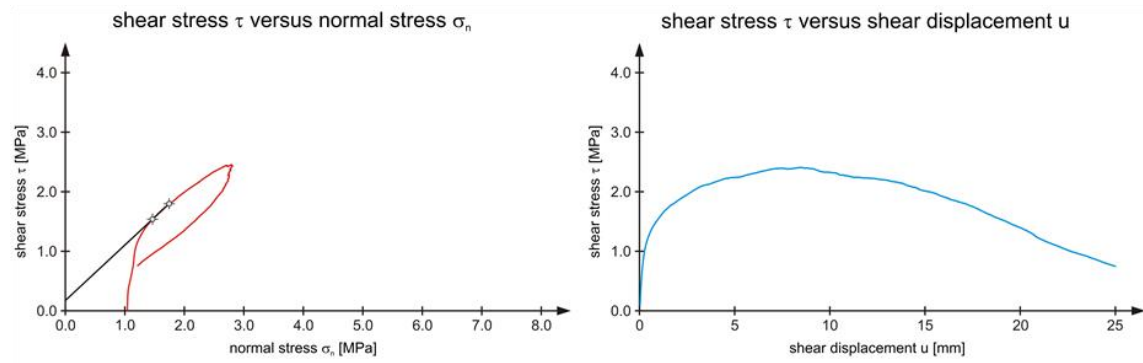
50% block proportion – 60° block orientation – inclined against shear direction – test no. 3

(→ ///)



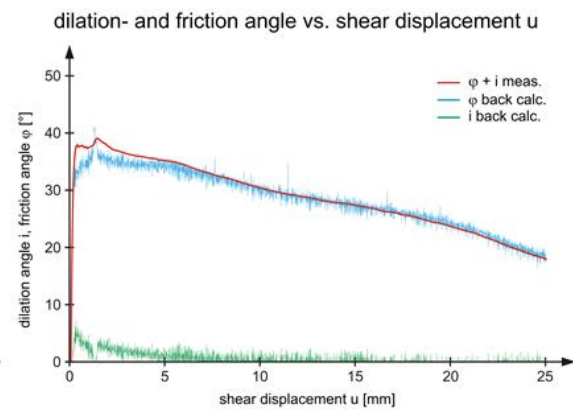
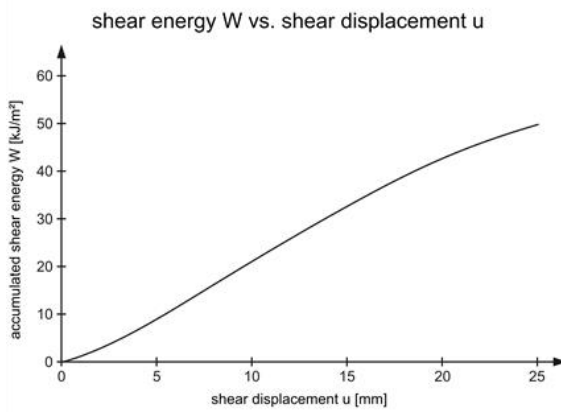
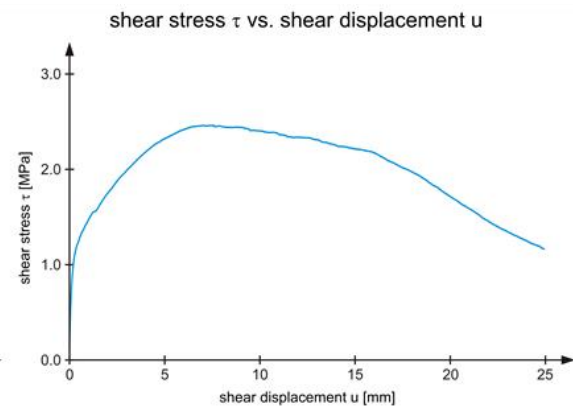
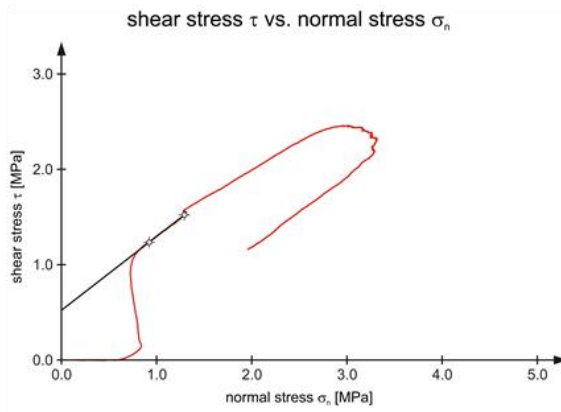
50% block proportion – 60° block orientation – inclined in shear direction – test no. 1

(→ \\\)



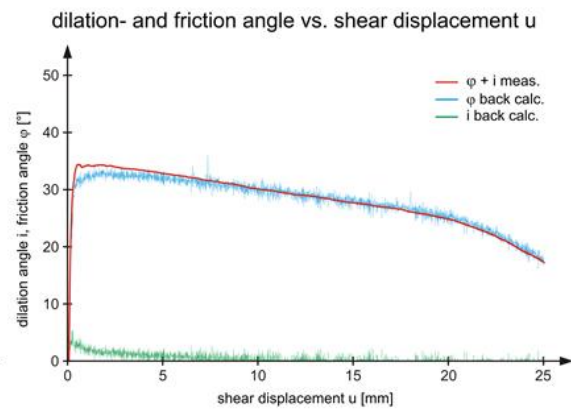
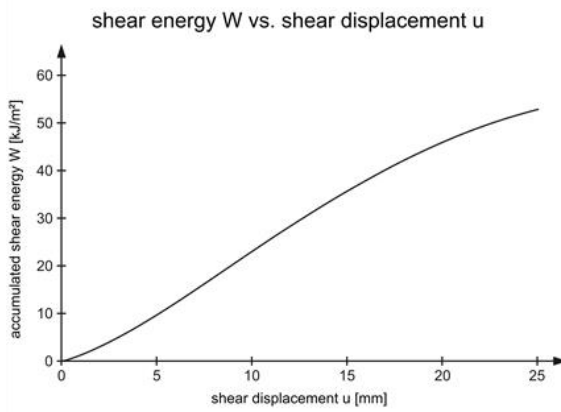
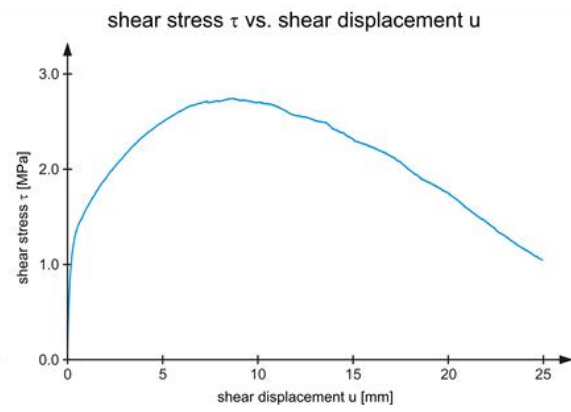
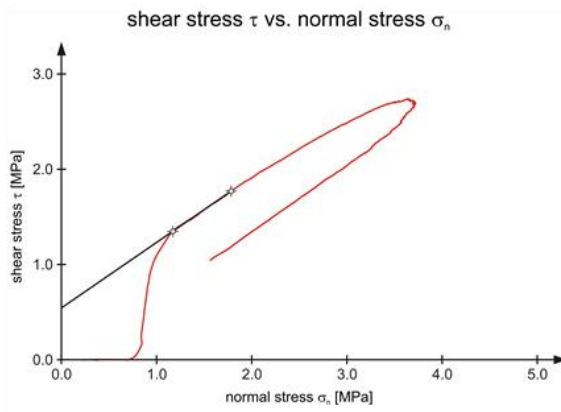
50% block proportion – 90° block orientation – shear in y-direction – test no. 1

(→ |||  $\sigma$  in z-dir.)



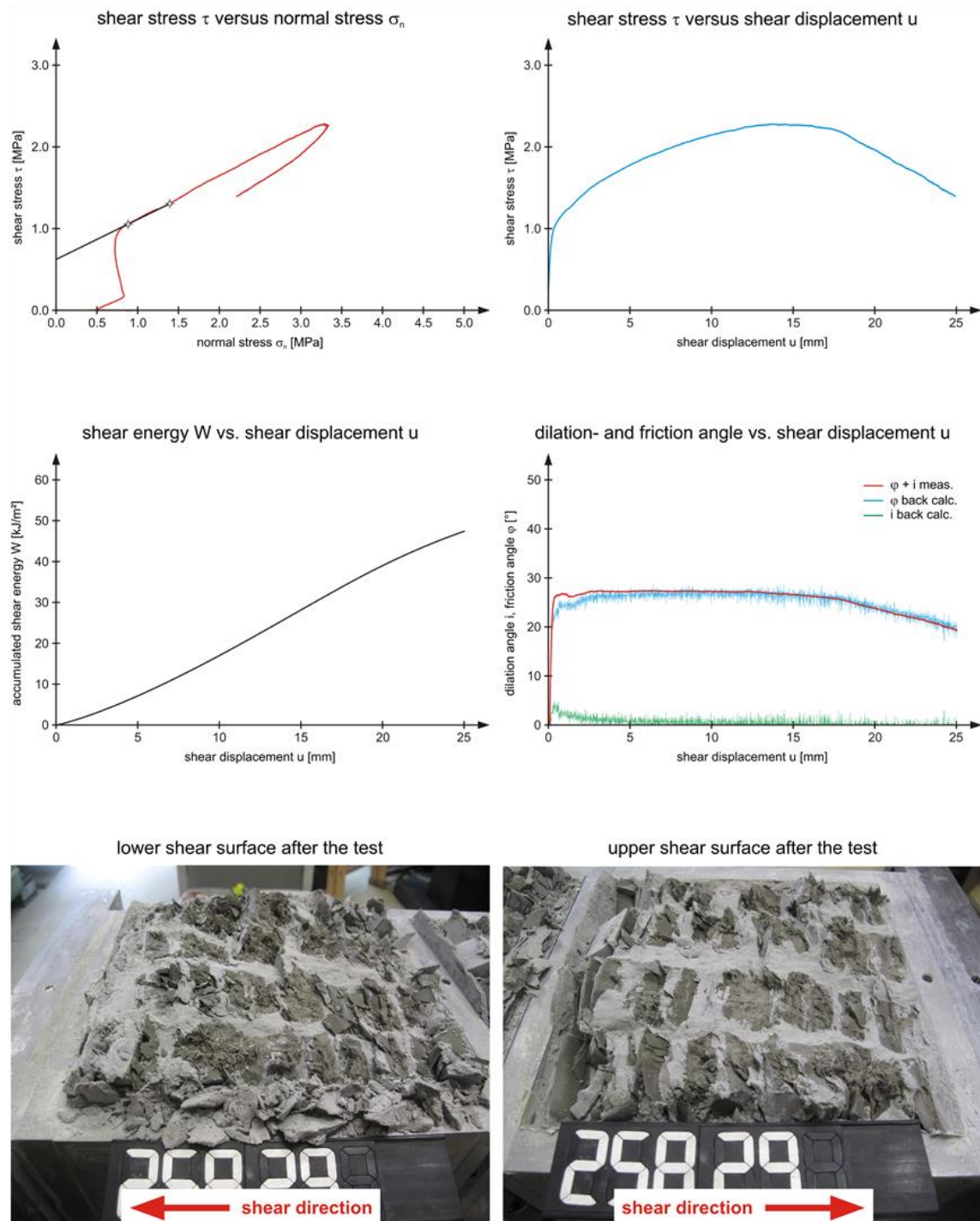
50% block proportion – 90° block orientation – shear in y-direction – test no. 2

(→ |||  $\sigma$  in z-dir.)



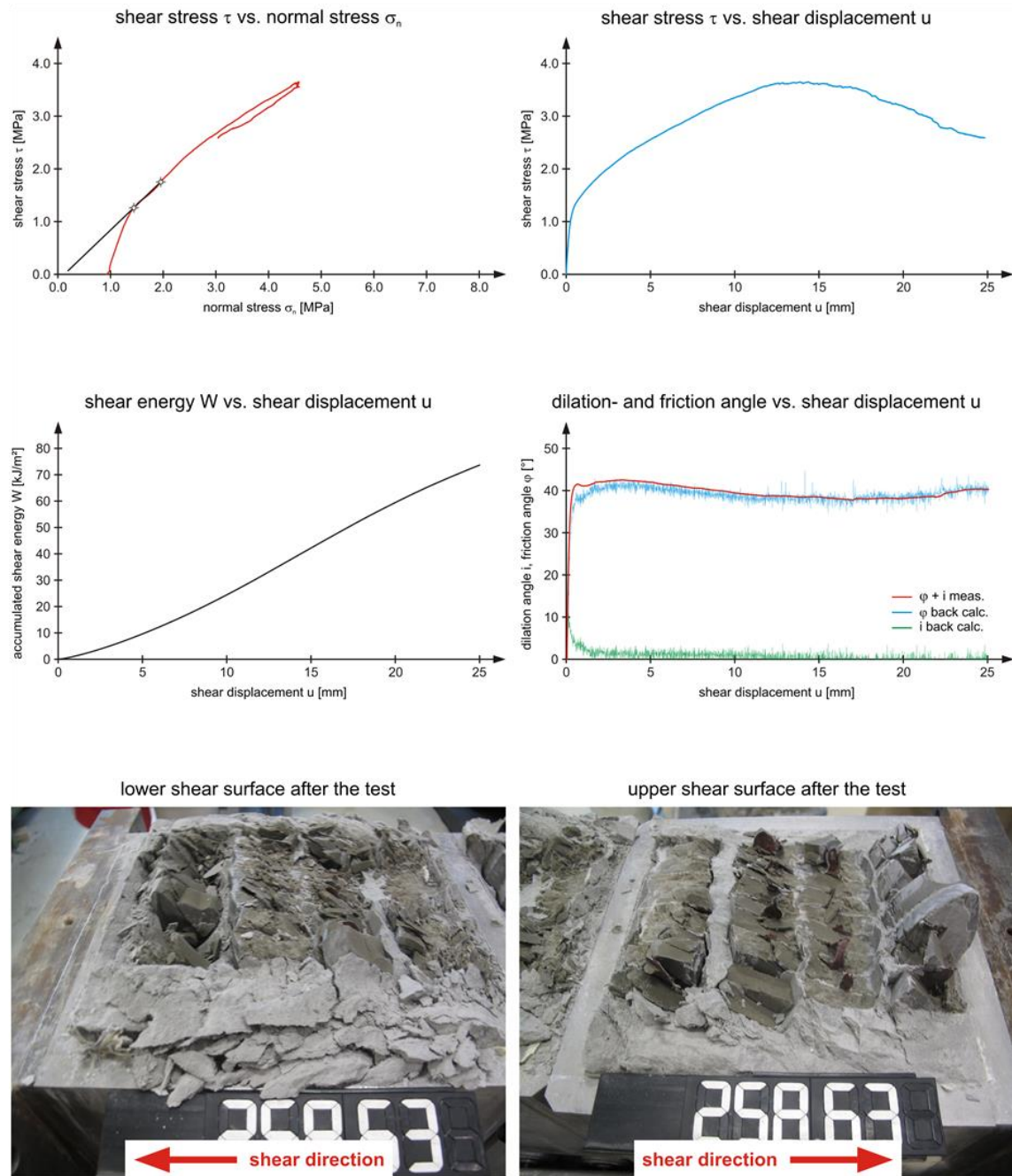
50% block proportion – 90° block orientation – shear in y-direction – test no. 3

(→ |||  $\sigma$  in z-dir.)



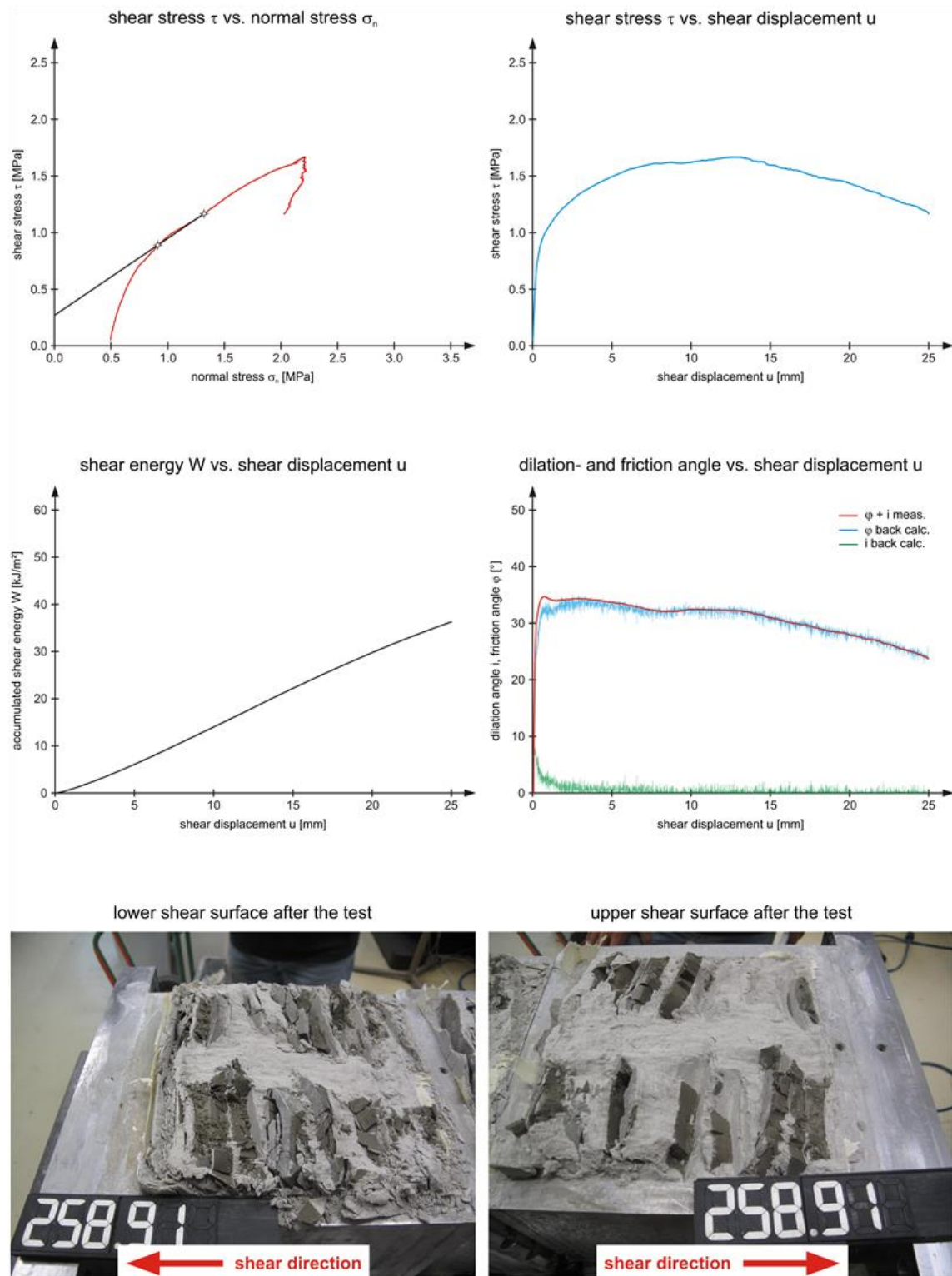
50% block proportion – 90° block orientation – shear in x-direction – test no. 1

(→ ||| par.  $\sigma$  in z-dir.)



50% block proportion – 90° block orientation – shear in y-direction – test no. 1

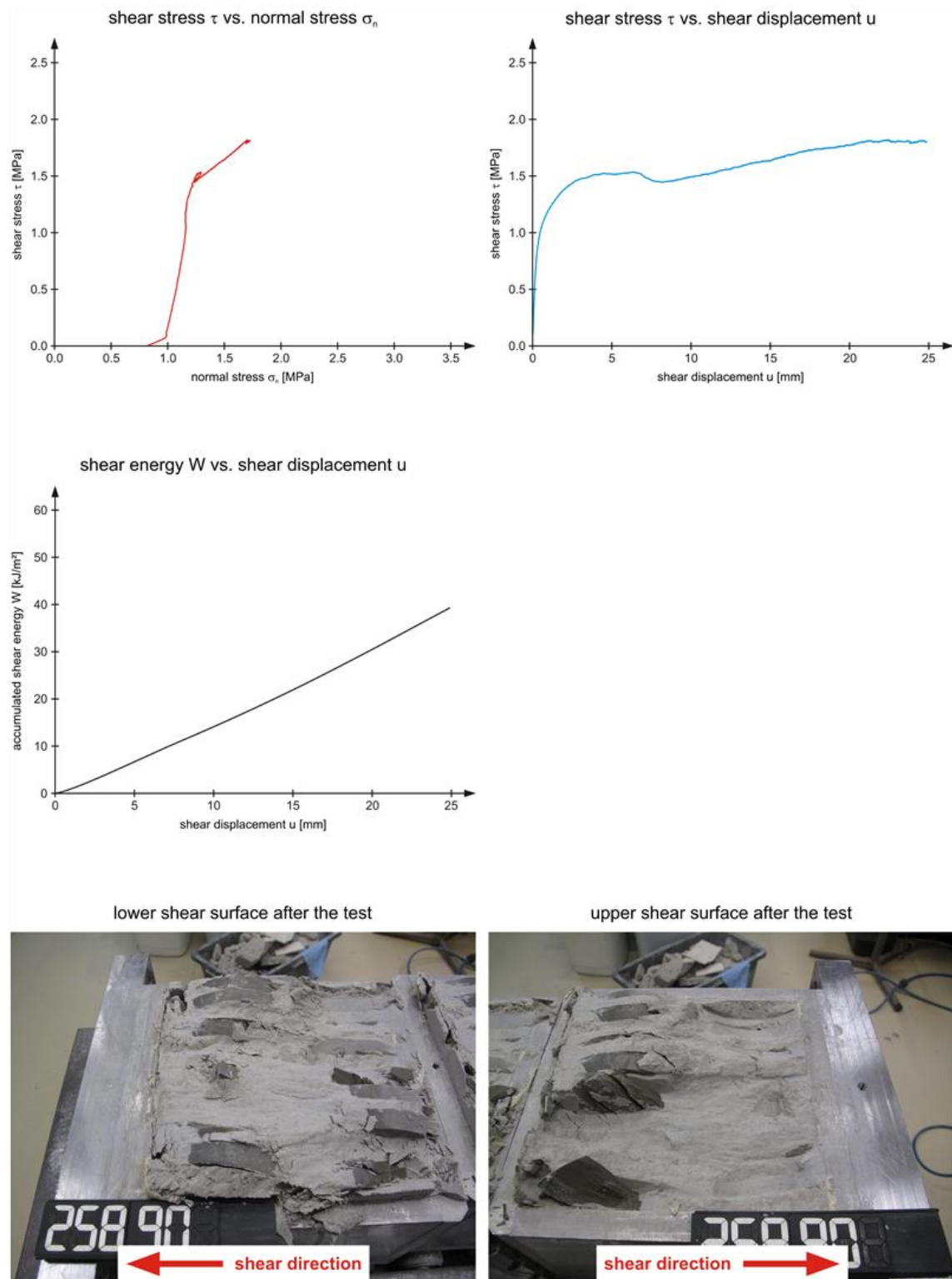
(→ |||  $\sigma$  in x-dir.)





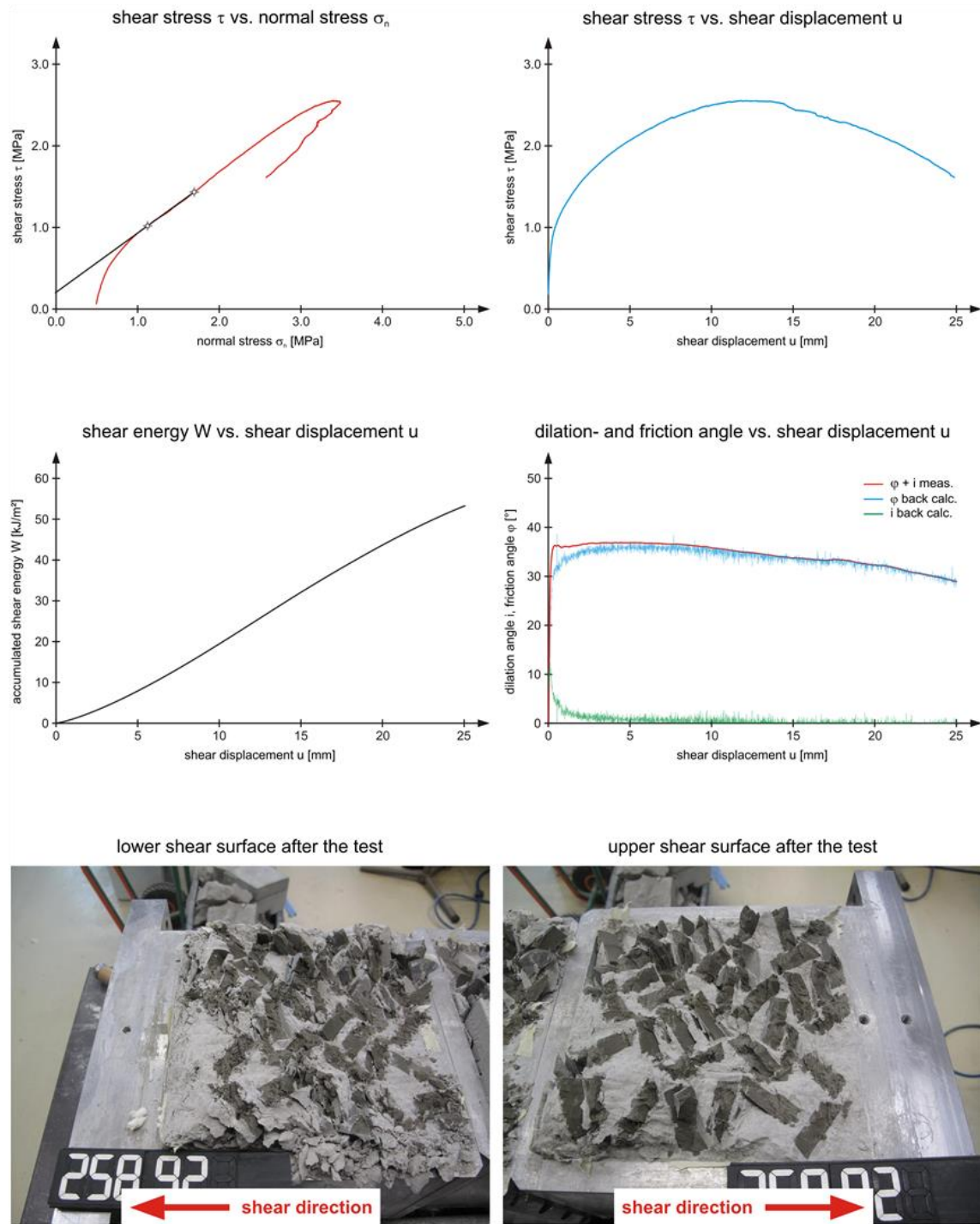
50% block proportion – 90° block orientation – shear in z-direction – test no. 1

(→ ||| par.  $\sigma$  in x-dir.)



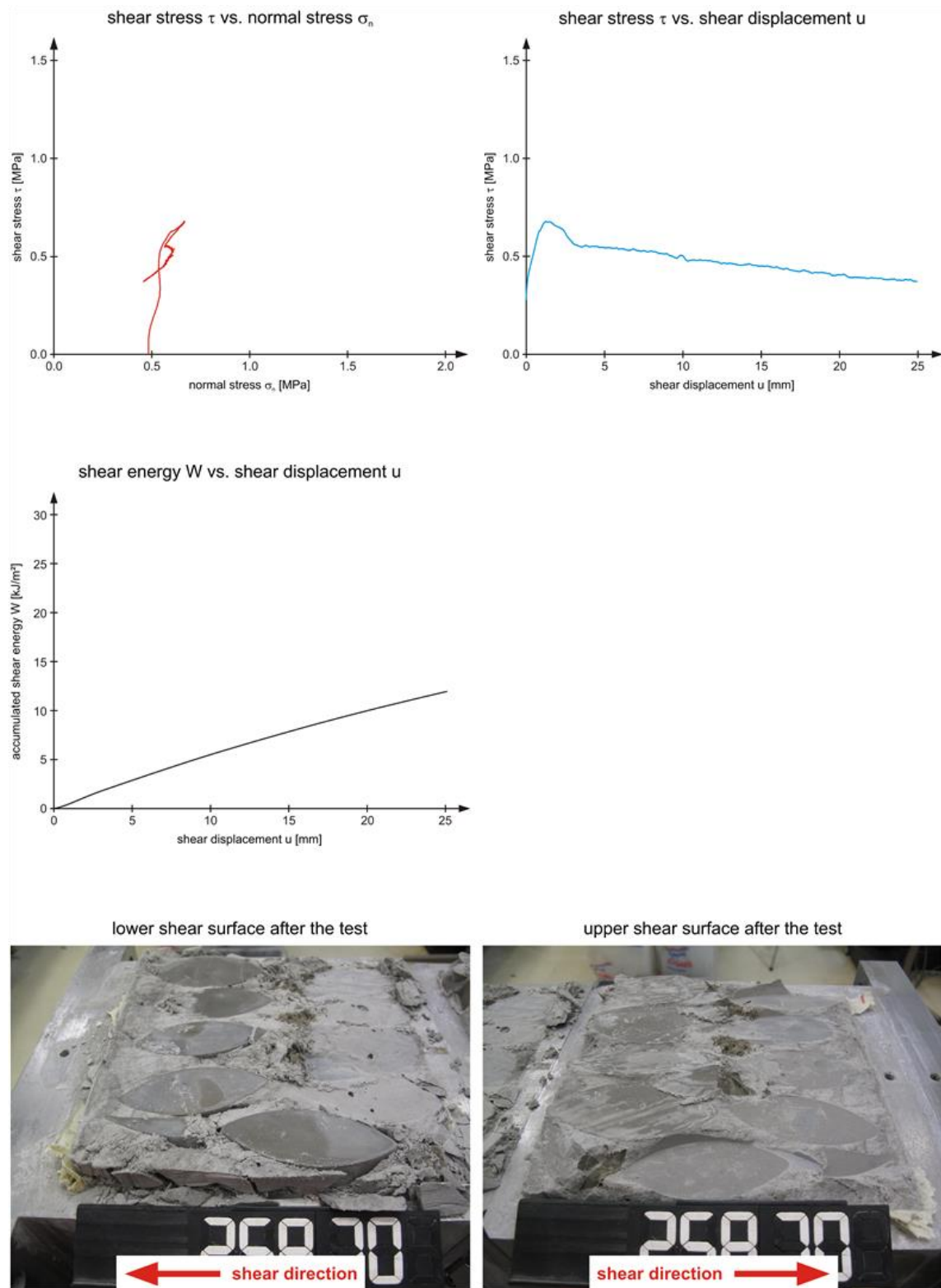
50% block proportion – 90° block orientation – shear in x- and y-direction – test no. 1

(random,  $\sigma$  in z-dir.)



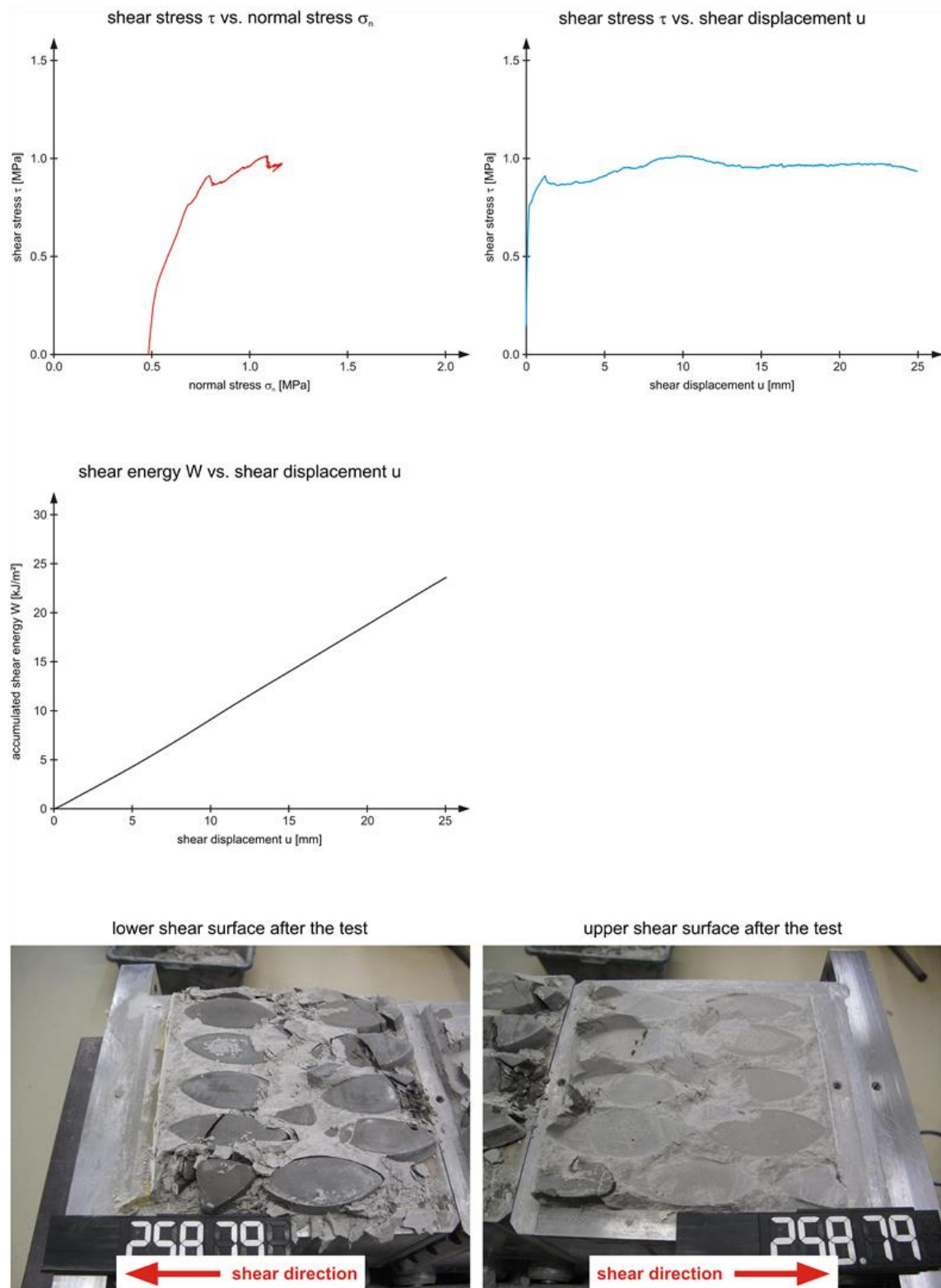
75% block proportion – 0° block orientation – shear in z-direction – test no. 1

(→ ---- long.)



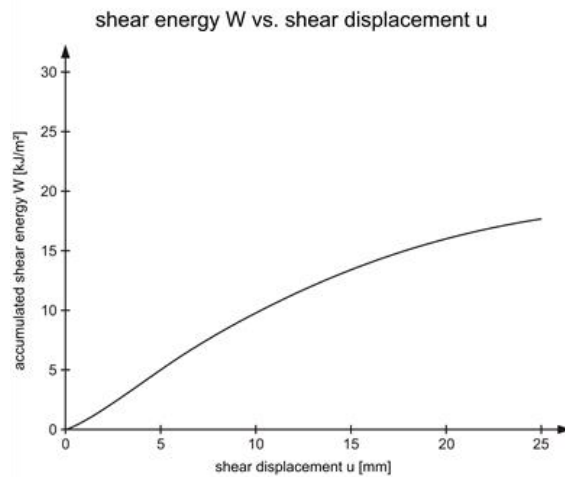
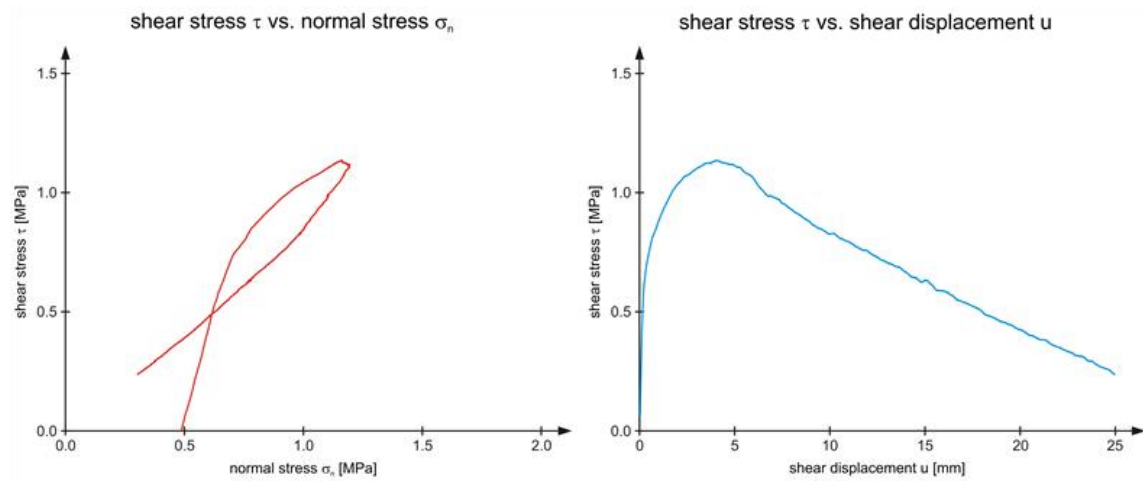
75% block proportion – 0° block orientation – shear in z-direction – test no. 2

(→ ---- long.)



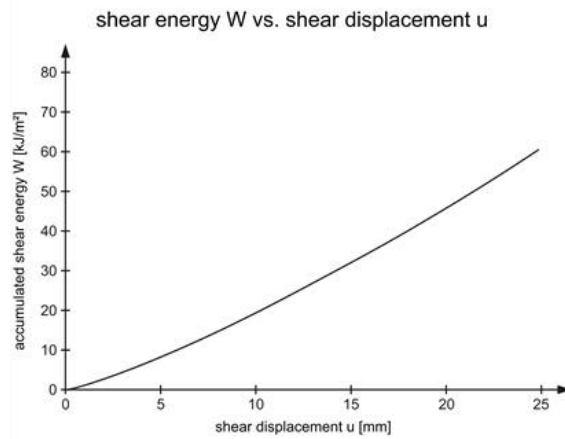
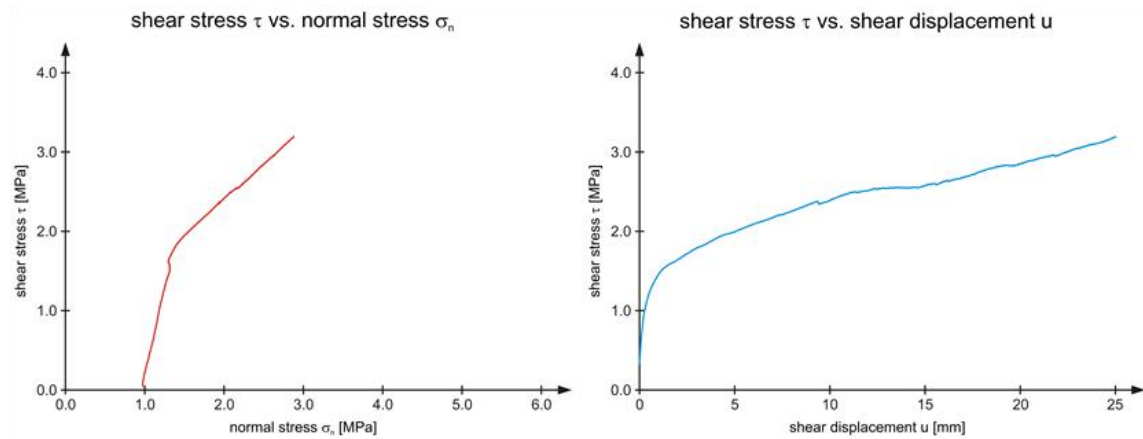
75% block proportion – 0° block orientation – shear in x-direction – test no. 1

(→ ---- trans.)



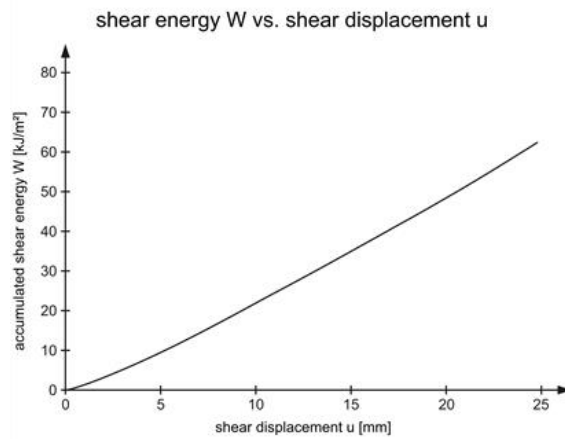
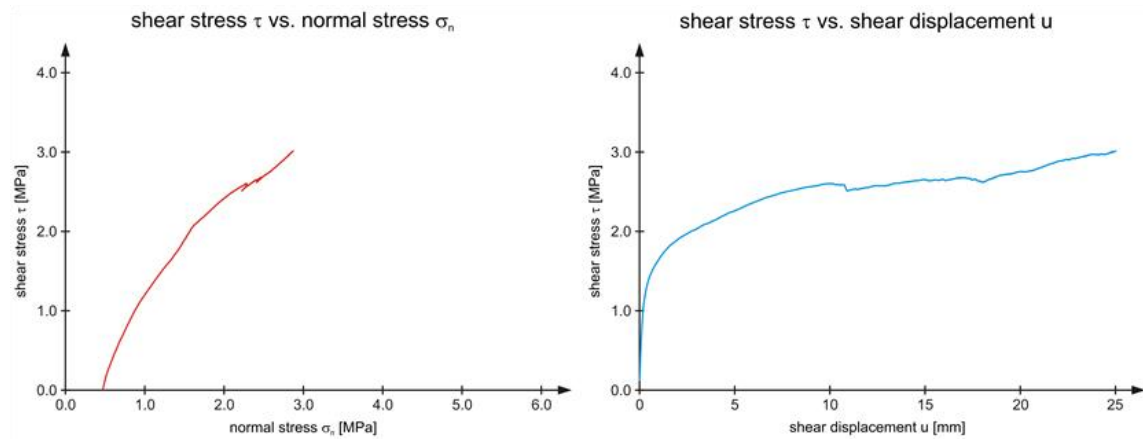
75% block proportion – 30° block orientation – inclined against shear direction – test no. 1

(→ ///)



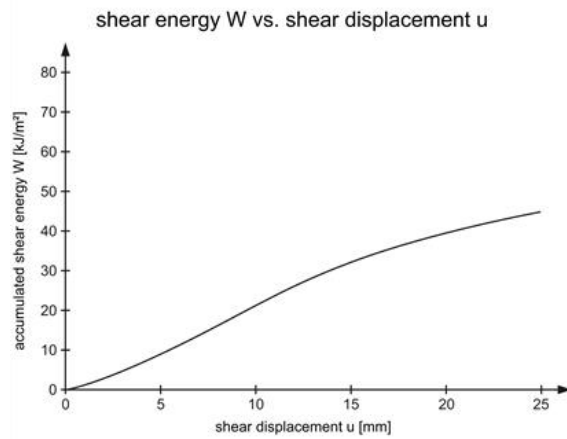
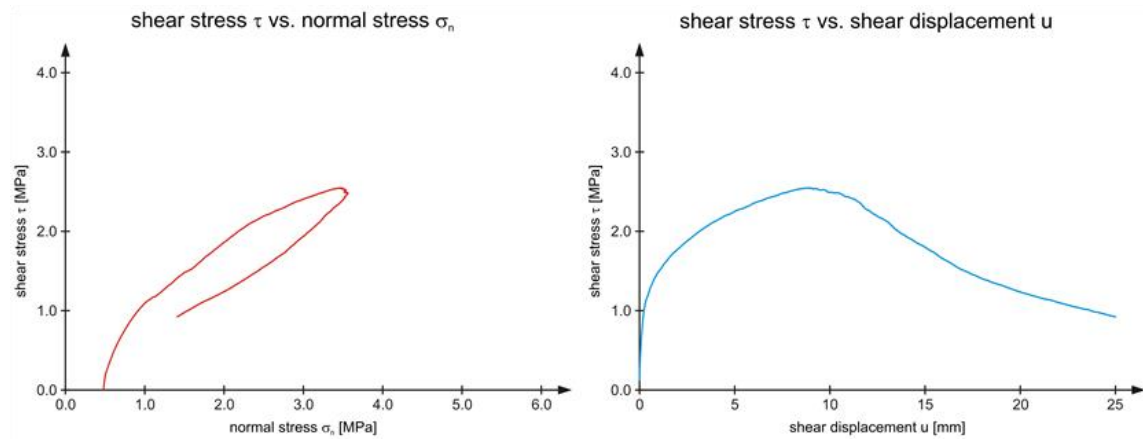
75% block proportion – 30° block orientation – inclined against shear direction – test no. 2

(→ ///)



75% block proportion – 30° block orientation – inclined in shear direction – test no. 1

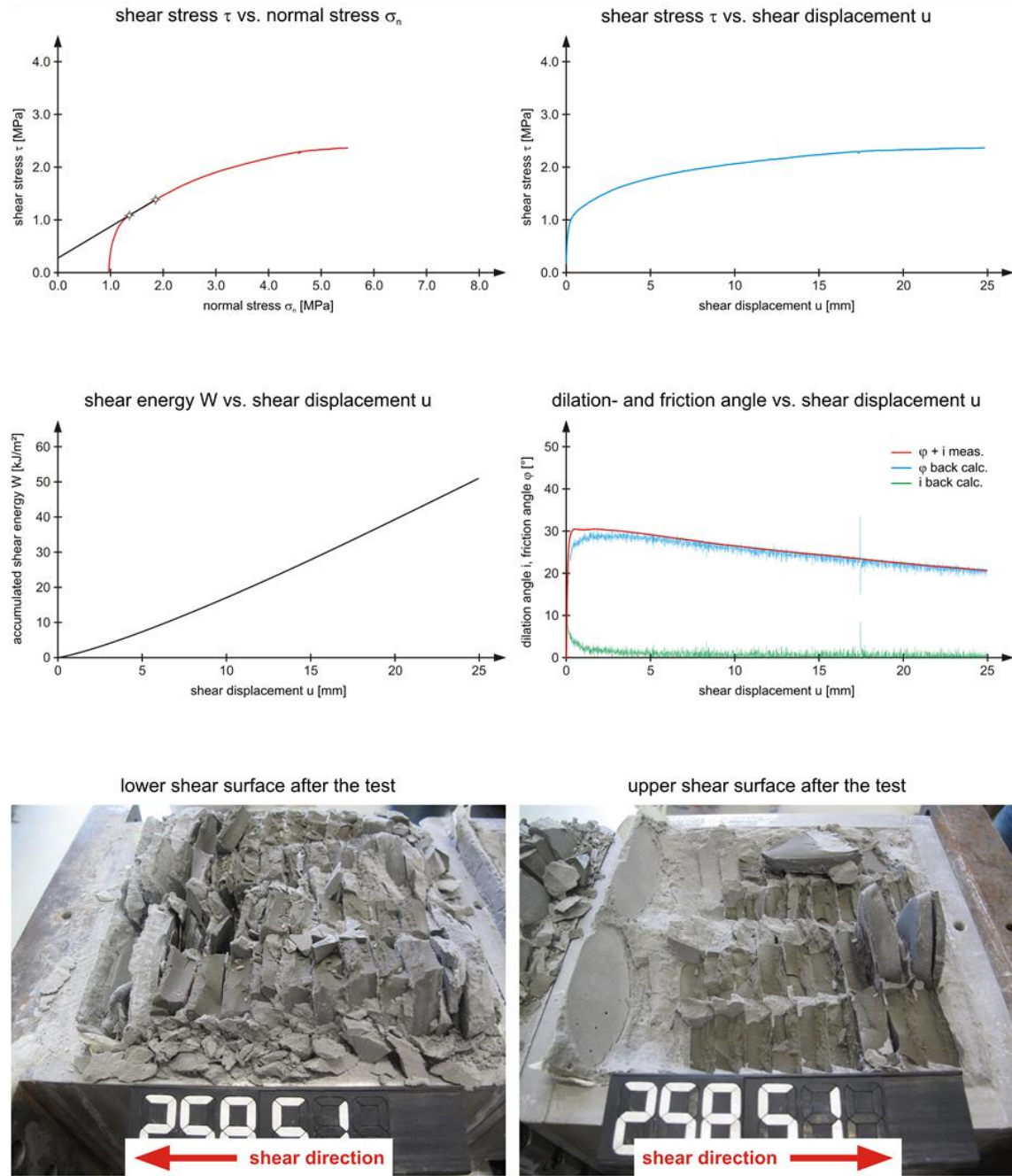
(→ \\\)





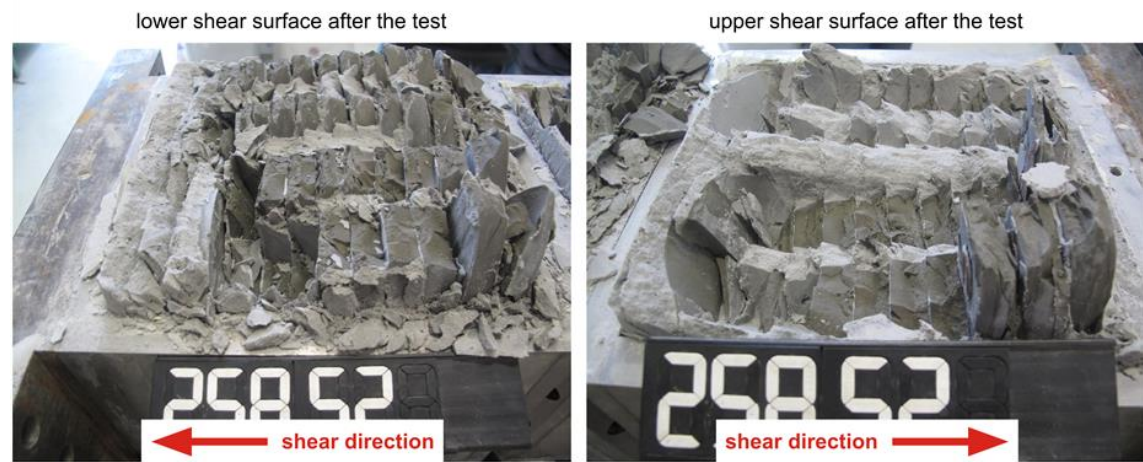
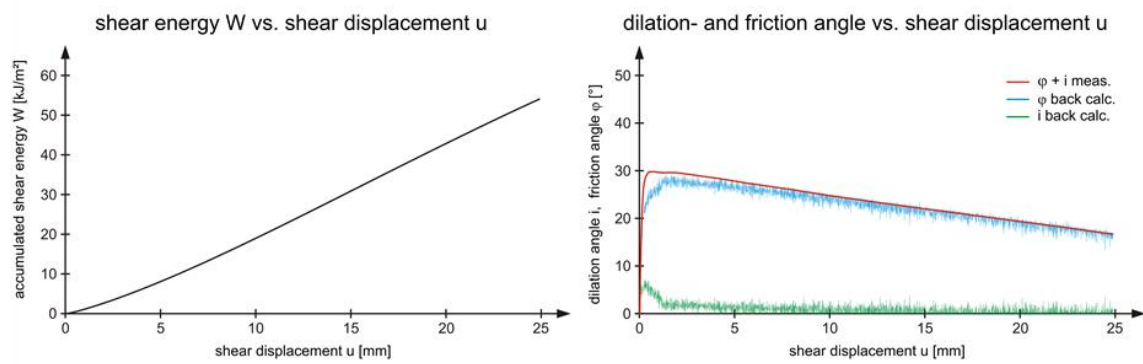
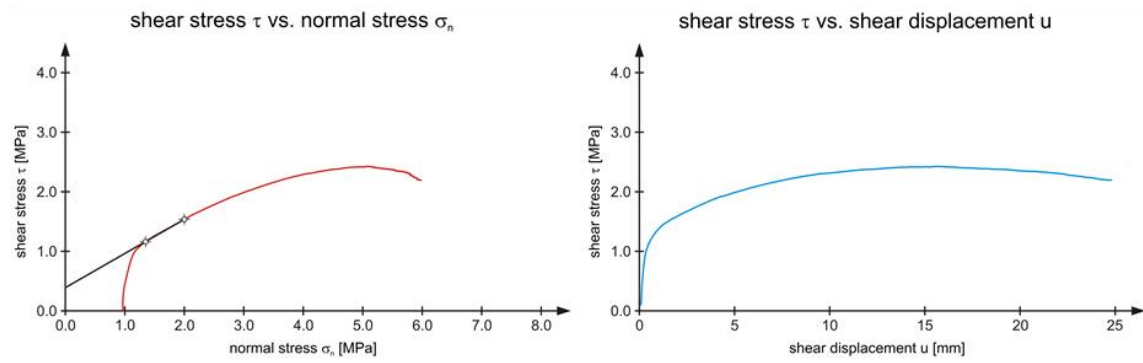
75% block proportion – 60° block orientation – inclined against shear direction – test no. 1

(→ ///)



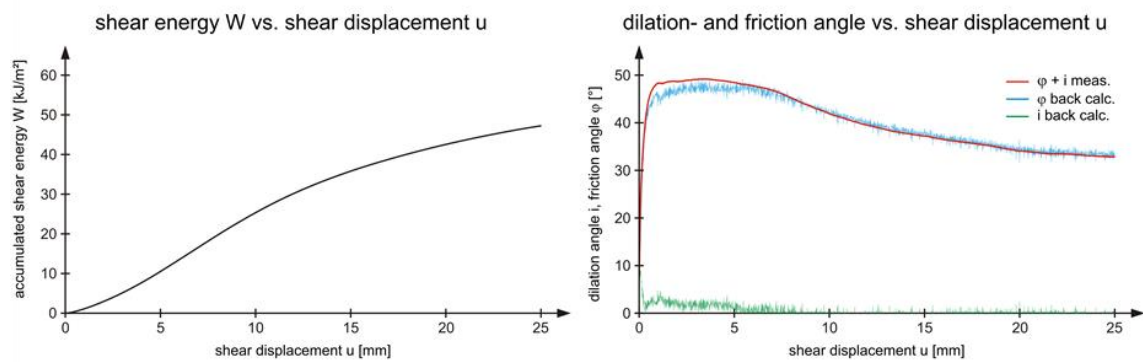
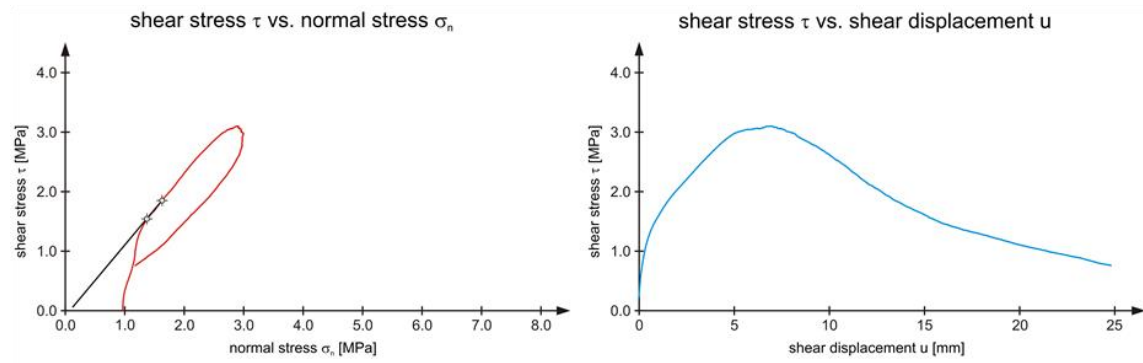
75% block proportion – 60° block orientation – inclined against shear direction – test no. 2

(→ ///)



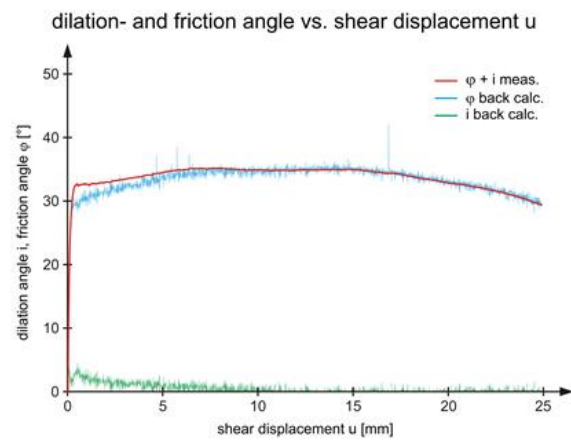
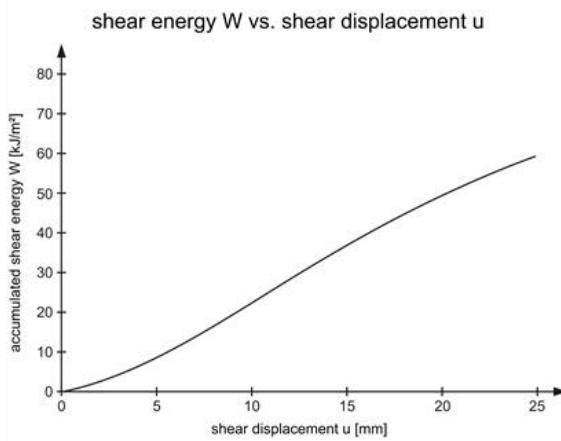
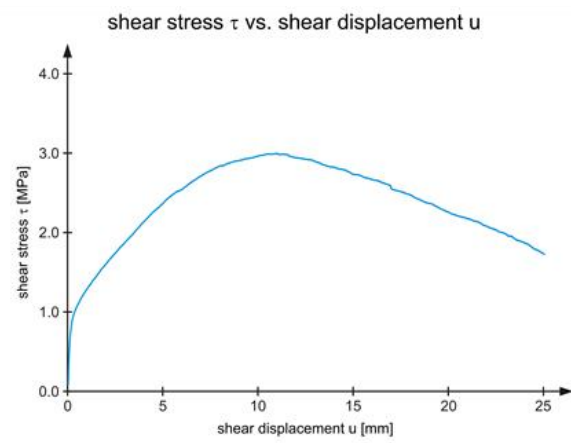
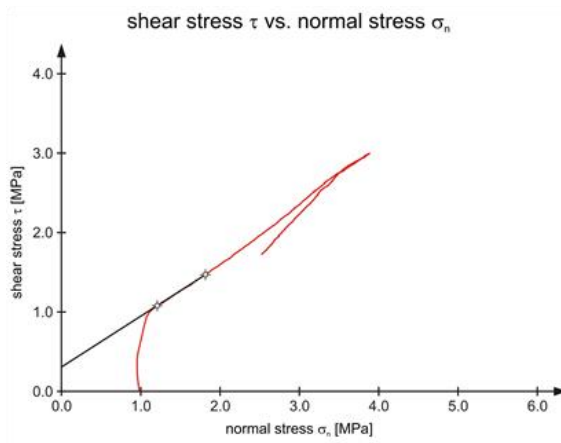
75% block proportion – 60° block orientation – inclined in shear direction – test no. 1

(→ \\\)



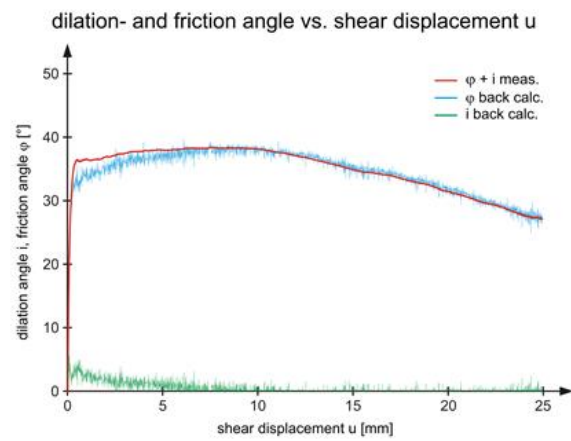
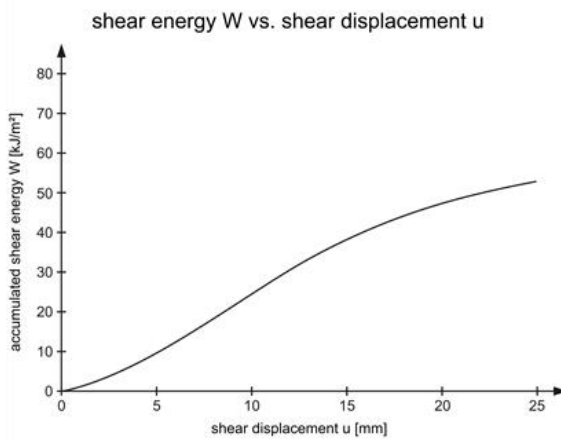
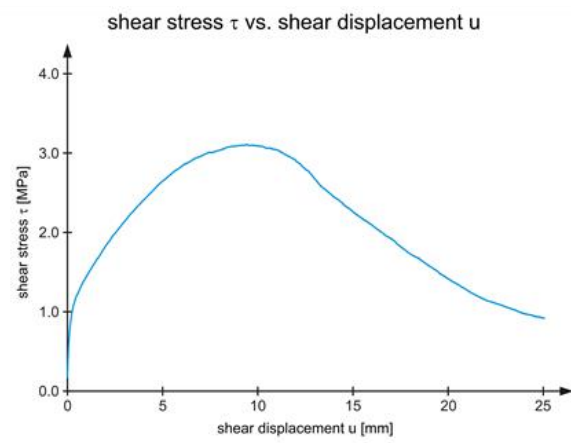
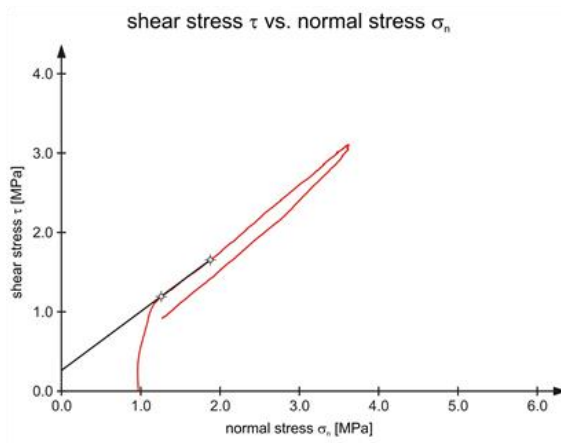
75% block proportion – 90° block orientation – shear in y-direction – test no. 1

( $\rightarrow$  |||  $\sigma$  in z-dir.)



75% block proportion – 90° block orientation – shear in y-direction – test no. 2

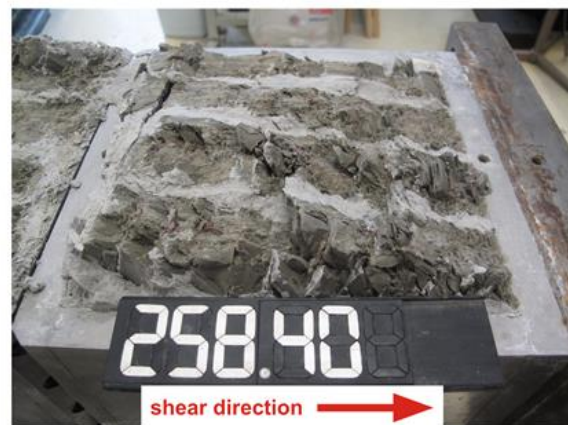
(→ |||  $\sigma$  in z-dir.)



lower shear surface after the test

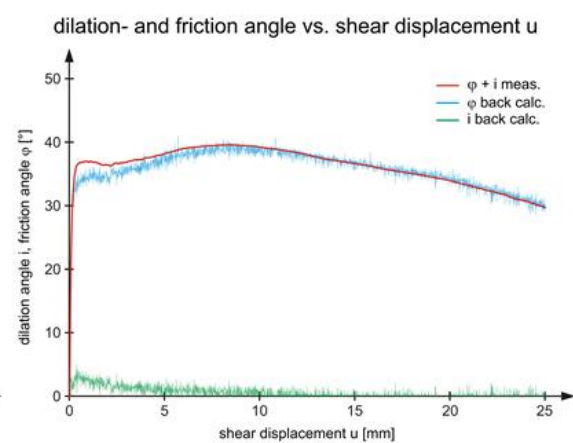
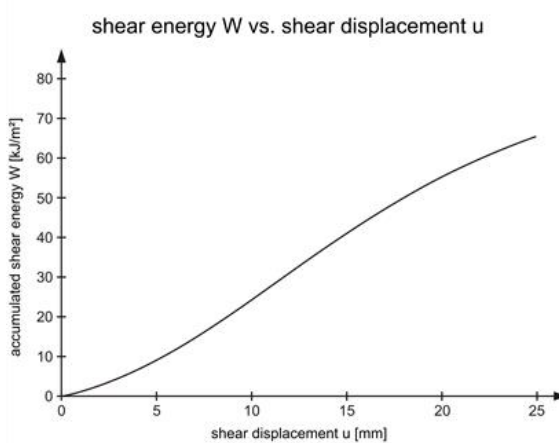
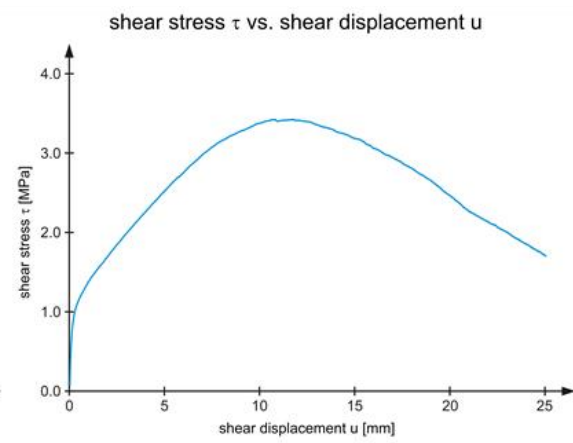
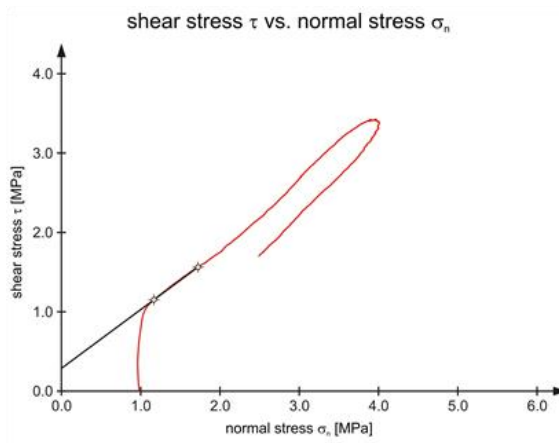


upper shear surface after the test



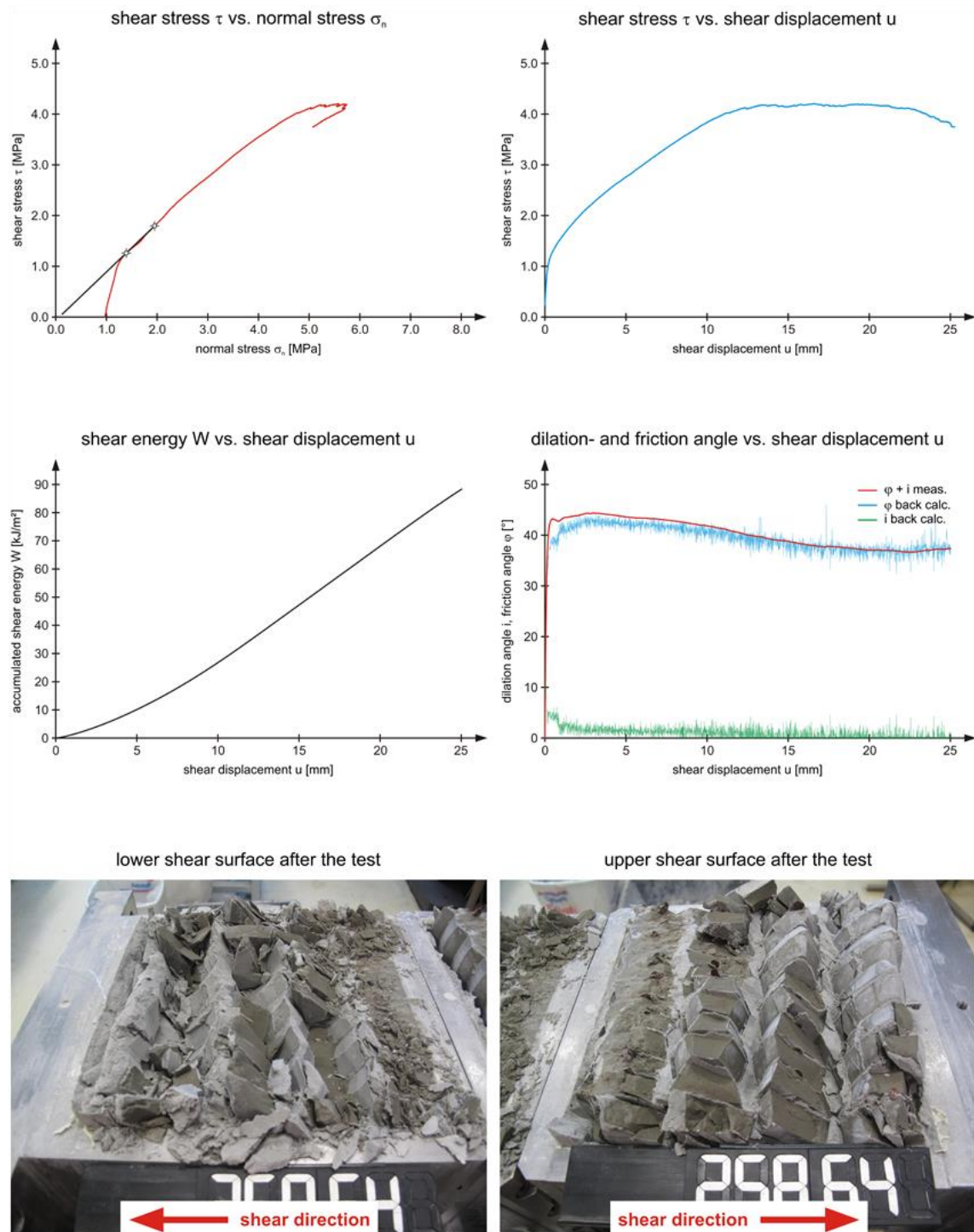
75% block proportion – 90° block orientation – shear in y-direction – test no. 3

(→ |||  $\sigma$  in z-dir.)



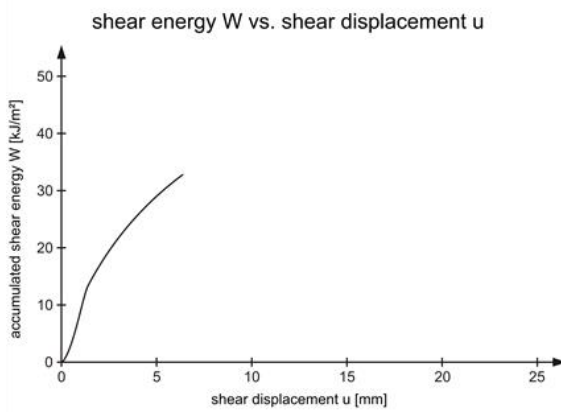
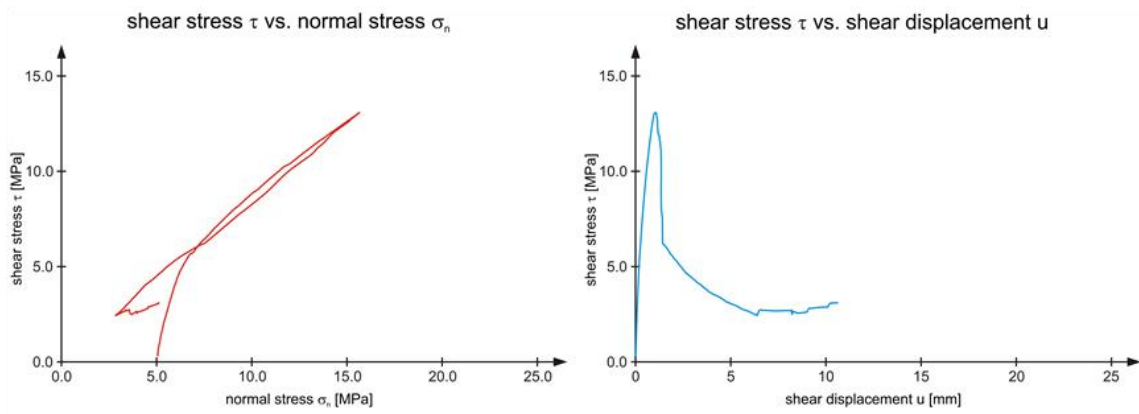
75% block proportion – 90° block orientation – shear in x-direction – test no. 1

(→ ||| par.  $\sigma$  in z-dir.)



100% block proportion – pure block – shear in y-direction – test no. 1

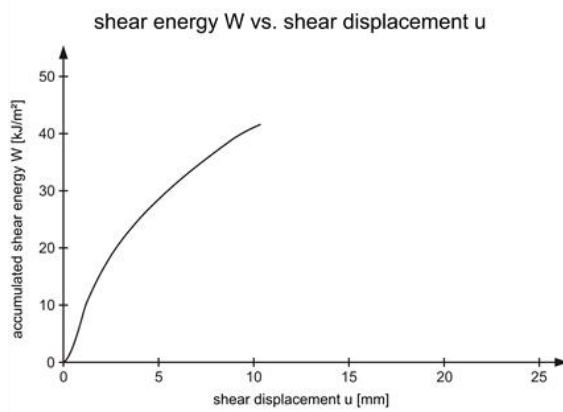
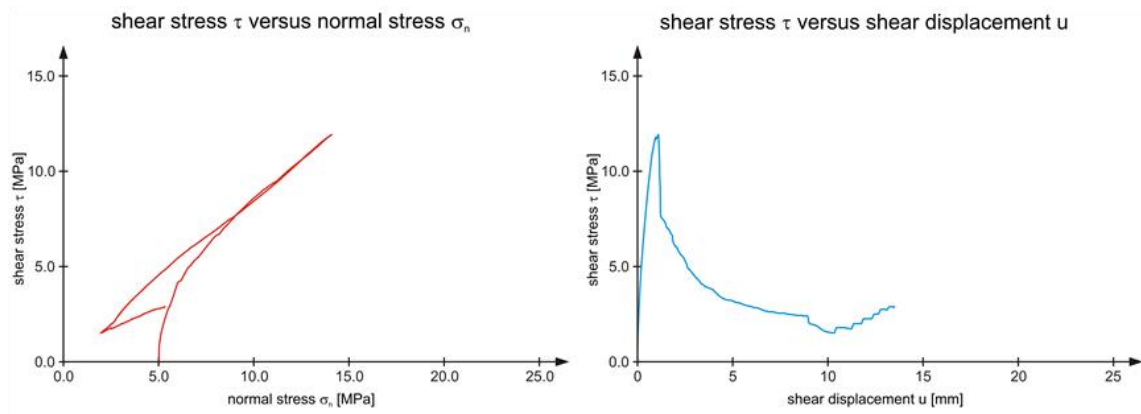
(n/a)





100% block proportion – pure block – shear in y-direction – test no. 2

(n/a)



lower shear surface after the test

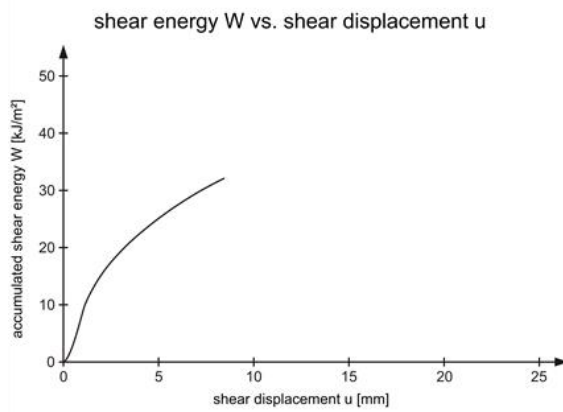
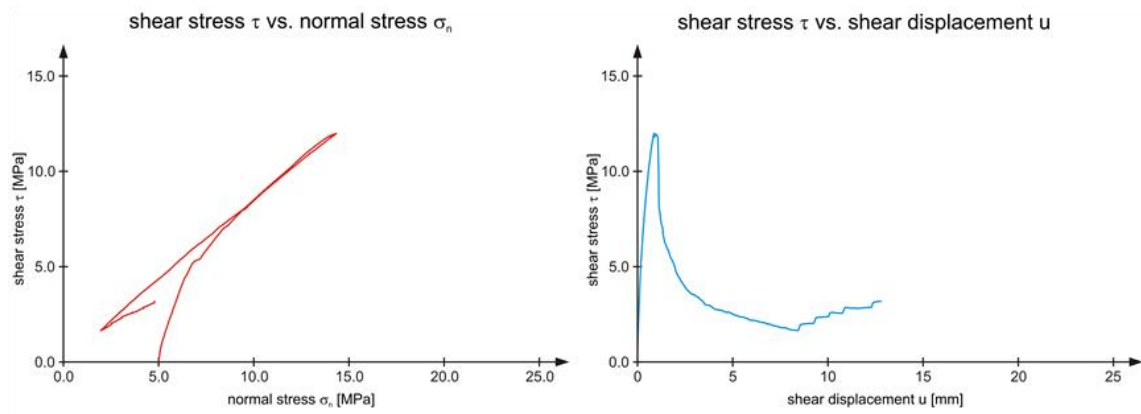


upper shear surface after the test



100% block proportion – pure block – shear in y-direction – test no. 3

(n/a)



lower shear surface after the test



upper shear surface after the test

